



THE HONG KONG
POLYTECHNIC UNIVERSITY

香港理工大學

Pao Yue-kong Library

包玉剛圖書館

Copyright Undertaking

This thesis is protected by copyright, with all rights reserved.

By reading and using the thesis, the reader understands and agrees to the following terms:

1. The reader will abide by the rules and legal ordinances governing copyright regarding the use of the thesis.
2. The reader will use the thesis for the purpose of research or private study only and not for distribution or further reproduction or any other purpose.
3. The reader agrees to indemnify and hold the University harmless from and against any loss, damage, cost, liability or expenses arising from copyright infringement or unauthorized usage.

IMPORTANT

If you have reasons to believe that any materials in this thesis are deemed not suitable to be distributed in this form, or a copyright owner having difficulty with the material being included in our database, please contact lbsys@polyu.edu.hk providing details. The Library will look into your claim and consider taking remedial action upon receipt of the written requests.

**VEHICLE QUEUE EFFECT ON THE CHARACTERISTICS
OF AIR FLOW, AND EXHAUST SCALAR DISPERSION
AND DISTRIBUTION FIELDS IN THE VEHICLE WAKE**

HUANG JIEFENG

Ph.D

The Hong Kong Polytechnic University

2013



The Hong Kong Polytechnic University
Department of Mechanical Engineering

**Vehicle Queue Effect on the Characteristics of
Air Flow, and Exhaust Scalar Dispersion and
Distribution Fields in the Vehicle Wake**

Huang Jiefeng

A thesis submitted in partial fulfillment of the requirements for
the Degree of Doctor of Philosophy

October 2011

Certificate of Originality

Certificate of Originality

I hereby declare that this thesis is my own work and that, to the best of my knowledge and belief, it reproduces no material previously published or written, nor material that has been accepted for the award of any other degree or diploma in any other University or Institute, except where due acknowledgement and reference have been made in the text of the thesis.

_____ (Signed)

Huang Jiefeng (Name of student)

Abstract

The characteristics of air flow, and vehicular exhaust scalar (i.e., pollutant) dispersion and distribution fields in the near-wake region of a scaled-down vehicle were experimentally investigated using the particle image velocimetry (PIV) and cold- and hot-wire anemometers for selected urban vehicle speeds. The studied vehicle was placed alone or behind preceding vehicle(s) inside a wind tunnel facility. The front and body of all studied vehicles are of the same shape except for different rear slant angles ($\alpha=25^\circ$ and 60°) in order to generate three-dimensional and quasi two-dimensional wake flows behind the vehicle, respectively. The structures of wake flow are almost independent of the studied vehicle speeds but the presence of the preceding vehicle(s) can change the wake structures especially in the recirculation zone.

The incoming flow toward the following vehicle can be blocked by the preceding vehicle(s). This blockage effect is more prominent with shorter vehicle spacing. For two-dimensional wake flow, the flow velocity behind the vehicle can be reduced by about 40% for $3.1H$ vehicle spacing, 20% for $9.3H$ and 10% for $15.5H$, respectively. The second preceding vehicle can further reduce no more than 10% of the flow velocity. Compared with the two-dimensional wake flow, the three-dimensional wake flow can double the blockage effect of preceding vehicle.

The vehicular exhaust scalar (i.e., pollutant) distribution pattern is found to mainly conform to the main flow structure behind the vehicle, whereas the flow turbulence velocity field can slightly expand the scalar dispersion and distribution

region. For the studied vehicle ($\alpha = 60^\circ$), the cross-section of exhaust scalar dispersion and distribution region behind the vehicle looks like an “n-shape” profile whose size is initially almost identical to vehicle rear. It will grow to about 2 times of the vehicle width and 1.5 times of the vehicle height near the end of near-wake region where the highest scalar region stays at about half of the vehicle height (i.e., close to the height level of human inhalation zone). With the presence of the preceding vehicle(s), the size and shape of the scalar profile will not change too much, but the highest scalar contour region will be lowered from half of the vehicle height toward ground surface.

On the other hand, for the studied vehicle ($\alpha = 25^\circ$), the cross-section of exhaust scalar distribution region behind the vehicle looks like an “m-shaped” profile. It is initially about 0.5 times of the vehicle height and 1.5 times of the vehicle width, and will grow to about 0.8 times of the vehicle height and 3 times of the vehicle width near the end of near-wake region. One side of the “m-shaped” profile which is right behind the tailpipe exit will share a larger portion of scalar jet exit, thus this side has a much higher scalar concentration, and its size is 50% taller than the other side of the “m-shaped” profile but not much wider. In addition, each side of the “m-shaped” profile has its highest concentration zone located very close to ground surface. With the presence of the preceding vehicle(s), the “m-shaped” profile of scalar distribution will not change too much, but the unbalance of scalar distribution between the two sides of “m-shaped” profile would be enhanced.

Acknowledgements

I wish to express my deep gratitude to my Chief Supervisor, Dr. T.L. Chan for his guidance, useful comments, encouragement and patience throughout my study. And I would also like to express my thanks to my Co-Supervisor, Prof. Y. Zhou for his guidance on my study of the air flow field.

I am grateful to the research personnel, Dr. K. Gosse who shared his knowledge about the experimental setup and the nature of this related scientific problems. My appreciations also go to the technical personnel, Dr. C.S. Tse (retired), Mr. K.H. Hui and Mr. Raymond Chan who provided the support for accessing the research facilities and measurement instruments. I also wish to thank Ir. K.K. Lo and the technicians of Project Lab who helped to build the studied model vehicles for the present research.

I would also like to express my appreciation to the financial support from the Central Research Grants and the research studentship granted by The Hong Kong Polytechnic University for accomplishing this research work.

Finally, I wish to give my deep thanks to my parents and brother for their love, support, help and encouragement during my PhD studying period.

Table of Contents

Abstract	i
Acknowledgements	iii
Table of Contents	iv
List of Figures	ix
List of Tables	xxi
Nomenclature	xxii
List of Publications	xxv
Chapter 1 Introduction	1
1.1 Research Background and Scope	1
1.2 Research Objectives of Present Study	9
1.3 Layout of Present Thesis	10
Chapter 2 Literature Review	12
2.1 The Wake of a Moving Vehicle	12
2.2 Characteristics of the Vehicle Wake and its Vehicular Exhaust Jet in the Wake Region	14
2.3 Stationary Vehicle in Still Ambient Air ($U_w \leq 0.1$ m/s)	18
2.4 Stationary Vehicle in Windy Ambient Air ($U_w > 0.1$ m/s)	21
2.5 Moving Vehicle in Still Ambient Air ($U_w \leq 0.1$ m/s)	22
2.6 Moving Vehicle in Windy Ambient Air ($U_w \gg 0.1$ m/s)	25

Table of Contents

2.7	Research Development of Analytical and Computational Approaches for the On-road Vehicle Aerodynamics and Pollutant Dispersion	27
2.7.1	Gaussian dispersion models for highway/ roadway air dispersion	31
2.7.2	General Motor model for highway/ roadway air dispersion	32
2.7.3	HIWAY model for highway air dispersion	33
2.7.4	CALINE model for highway air dispersion	35
2.8	Research Development of Experimental Approaches for Vehicle Aerodynamics and Pollutant Dispersion	36
2.9	Summary of Literature Review	47
Chapter 3	Experimental Methodology	48
3.1	Introduction	48
3.2	Experimental Methodology of Simulating the Moving Ground Vehicle Conditions in a Wind Tunnel	48
3.3	Studied Model Vehicles	51
3.4	Methodology of Using Particle Image Velocimetry (PIV) System for Flow Field Measurement	58
3.5	Methodology of Simulating the Vehicular Exhaust Tailpipe Conditions in a Wind Tunnel	72
3.6	Methodology of Hot-wire and Cold-wire Anemometers for Air Flow and Temperature Measurements	76
3.7	The Determination of the Sampling Frequency, Sample Number and Uncertainty Analysis	82
3.8	The Analogy between Vehicle Exhaust Temperature Dispersion and Exhaust Gas Dispersion	85

Table of Contents

Chapter 4	Vehicle Queue Effect on the Characteristics of Air Flow in the Vehicle Wake	89
4.1	Introduction	89
4.2	Experimental Set-up	93
4.3	Results and Discussion for Queue Effect of the Studied Vehicles ($\alpha = 25^\circ$) on the Flow Structures in the Vehicle Wake	95
4.3.1	Wake structure of one-, two- and three-vehicle cases ($\alpha = 25^\circ$) in X - Y plane at $Z/H = 0.5$ for different vehicle speeds	95
4.3.1.1	Velocity profiles, \bar{U}/U_∞ and u'/U_∞ for the vehicles ($\alpha = 25^\circ$) at 10 km/h	95
4.3.1.2	Velocity profiles, \bar{U}/U_∞ and u'/U_∞ for the vehicles ($\alpha = 25^\circ$) at 30 km/h	98
4.3.1.3	Velocity profiles, \bar{U}/U_∞ and u'/U_∞ for the vehicles ($\alpha = 25^\circ$) at 50 km/h	100
4.3.1.4	Streamwise velocity, \bar{U}/U_∞ and momentum, $u'v'/U_\infty^2$ contours for the vehicles ($\alpha = 25^\circ$) at different vehicle speeds	102
4.3.1.5	Wake structure in X - Z plane at $Y/H = 0$ for the vehicles ($\alpha = 25^\circ$) at different vehicle speeds	107
4.3.2	Wake structure of one-, two- and three-vehicle cases ($\alpha = 25^\circ$) in Y - Z planes for different vehicle speeds	117
4.3.2.1	Vorticity contours in Y - Z plane at $X/H = 1$ for the vehicles ($\alpha = 25^\circ$) at different vehicle speeds	117
4.3.2.2	Vorticity contours in Y - Z plane at $X/H = 3$ for the vehicles ($\alpha = 25^\circ$) at different vehicle speeds	122
4.3.3	Summary of the characteristics of maximum vorticity values for trailing vortices at different X/H locations and vehicle speeds for one-, two- and three-vehicle cases ($\alpha = 25^\circ$)	124
4.3.4	Summary conclusions of a queue of the vehicles ($\alpha = 25^\circ$)	125
4.4	Results and Discussion for Queue Effect of the Studied Vehicles ($\alpha = 60^\circ$) on the Flow Structures in the Vehicle Wake	126

Table of Contents

4.4.1	Wake structure in X - Y plane at $Z/H = 0.5$ for the vehicles ($\alpha = 60^\circ$) at different vehicle speeds	126
4.4.1.1	Velocity profiles, \bar{U}/U_∞ and u'/U_∞ for the vehicles ($\alpha = 60^\circ$) at 10 km/h	126
4.4.1.2	Velocity profiles, \bar{U}/U_∞ and u'/U_∞ for the vehicles ($\alpha = 60^\circ$) at 30 km/h	128
4.4.1.3	Velocity profiles, \bar{U}/U_∞ and u'/U_∞ for the vehicles ($\alpha = 60^\circ$) at 50 km/h	130
4.4.1.4	Streamwise velocity, \bar{U}/U_∞ contours for the vehicles ($\alpha = 60^\circ$) at different vehicle speeds	132
4.4.1.5	Wake structure in X - Z plane at $Y/H = 0$ for the vehicles ($\alpha = 60^\circ$) at different vehicle speeds	136
4.4.2	Wake structure of one-, two- and three-vehicle cases ($\alpha = 60^\circ$) in Y - Z planes for different vehicle speeds	142
4.4.2.1	Vorticity contours in Y - Z plane at $X/H = 1$ for the vehicles ($\alpha = 60^\circ$) at different vehicle speeds	142
4.4.2.2	Vorticity contours in Y - Z plane at $X/H = 3$ for the vehicles ($\alpha = 60^\circ$) at different vehicle speeds	144
4.4.3	Summary for the characteristics of maximum vorticity values for trailing vortices at different X/H locations and vehicle speeds for one-, two- and three-vehicle cases ($\alpha = 60^\circ$)	146
4.5	Summary of Chapter	147
Chapter 5	Vehicle Queue Effect on the Characteristics of Air Flow, and Exhaust Scalar Dispersion and Distribution Fields in the Vehicle Wake	149
5.1	Introduction	149
5.2	Experimental Set-up	152
5.3	Results and Discussion	157
5.3.1	Air flow characteristics, and exhaust scalar dispersion and distribution fields behind a queue of the studied vehicles ($\alpha = 25^\circ$) in the downstream	157

Table of Contents

5.3.2	Exhaust scalar dispersion and distribution fields behind a queue of the studied vehicles ($\alpha = 60^\circ$) in the downstream	181
5.4	Summary of Chapter	197
Chapter 6	Conclusions and Recommendations for Future Work	201
6.1	Conclusions for the Vehicle Queue Effect on the Characteristics of Air Flow in the Vehicle Wake	201
6.1.1	Conclusions for the characteristics of air flow around a single vehicle ($\alpha > 30^\circ$)	201
6.1.2	Conclusions for the characteristics of air flow around a queue of vehicle(s) ($\alpha > 30^\circ$)	203
6.1.3	Conclusions for the characteristics of air flow around a single vehicle ($\alpha < 30^\circ$)	206
6.1.4	Conclusions for the characteristics of air flow around a queue of vehicles ($\alpha < 30^\circ$)	207
6.2	Conclusions for the Vehicle Queue Effect on the Characteristics of Exhaust Scalar Dispersion and Distribution Fields in the Vehicle Wake	210
6.2.1	Conclusions for the characteristics of exhaust scalar dispersion and distribution fields behind a single vehicle ($\alpha > 30^\circ$)	211
6.2.2	Conclusions for the characteristics of exhaust scalar dispersion and distribution fields behind a queue of vehicles ($\alpha > 30^\circ$)	212
6.2.3	Conclusions for the characteristics of exhaust scalar dispersion and distribution fields behind a single vehicle ($\alpha < 30^\circ$)	212
6.2.4	Conclusions for the characteristics of exhaust scalar dispersion and distribution fields behind a queue of vehicles ($\alpha < 30^\circ$)	213
6.3	Recommendation for Future Work	214
Appendix	Equipment Specifications	216
References	221

List of Figures

Figure 2.1	The wake of single vehicle moving in air (Katz, 1995).	12
Figure 2.2	The near-wake region of a moving vehicle (Ahmed, 1981).	14
Figure 2.3	A typical snapshot of the temperature distribution of a ground vehicle ($\alpha = 25^\circ$) at the cross section plane for vehicle speed = 30 km/h (Chan et al. 2008a).	17
Figure 2.4	The typical flow profile of a jet at different axial distances.	18
Figure 2.5	A typical vehicular exhaust jet pollutant (in ppm) distribution behind the stationary ground vehicle in a still ambient air for $U_w = 0.1$ m/s (Dong and Chan, 2006).	20
Figure 2.6	A typical vehicular exhaust jet pollutant (in ppm) distribution behind the ground vehicle for an ambient wind speed, $U_w = 1$ m/s and yaw angle, $\theta = 45^\circ$ (Dong and Chan, 2006).	22
Figure 2.7	A typical turbulence intensity distribution of a ground vehicle ($\alpha = 25^\circ$) at vehicle speed = 30 km/h (Chan et al. 2008a).	24
Figure 2.8	Determination of motorway-induced turbulence for (a) the experimental setup and measurement area; (b) the measured and simulated turbulent kinetic energy against time of a full day; (c) measured and simulated vertical profile of CO concentration downstream of the motorway during neutral thermal stratification (Baumer et al., 2005).	37
Figure 2.9	Wind tunnel experiments for the dilution of tailpipe emissions from different types of vehicle models for (a) the experimental setup inside a wind tunnel; (b) the flow streamlines around a vehicle; (c) the concentration contours in a cross-section plane behind the vehicle (Kanda et al. 2006b).	38
Figure 2.10	Wind tunnel experiments for the dilution of tailpipe emissions from different types of vehicle models for (a) the main flow behind the vehicle (white arrow); (b) the dilution rate along the downstream distance of vehicle (Chang et al. 2009a).	39

List of Figures

Figure 2.11	(a) A simplified Ahmed vehicle body with 25° rear slant angle for wind tunnel study; (b) the friction line visualizations on the side of rear window of vehicle body (Gillieron et al. 2010).	40
Figure 2.12	A wind tunnel experimental study of a pickup truck's near wake for (a) the truck model in wind tunnel; (b) the setup of flow measurement instruments; (c) the measured streamlines in the center plane of truck; (d) the flow vectors and vorticity map in a cross-section plane behind the truck (Al-Garni and Bernal, 2010).	41
Figure 2.13	Measurement of nanoparticles in the wake of a moving vehicle at 20 km/h for (a) a map of on-board measurement points behind the vehicle; (b) the particle number concentrations at $x = 0.45$ m during the on-board measurement points; (c) the ground-fixed sampling measurements; (d) the normalized size distributions during evolution at $H = 0.1$ m (Carpentieri and Kumar, 2011).	42
Figure 2.14	(a) A 1:8 scale vehicle model setup in a wind tunnel for (b) measured velocity vectors along the centerline of X - Z plane behind the vehicle using the laser Doppler anemometer (LDA); (c) measured velocity vectors on the vehicle's horizontal tailpipe plane, (d) measured tracer gas concentration distribution along the centerline of X - Z plane behind the vehicle using the fast response flame ionization detector (FFID); (e) measured tracer gas concentration distribution on the vehicle's horizontal tailpipe (Carpentieri et al., 2012).	44
Figure 2.15	(a) The background concentration on the top of a light duty vehicle using the DustTrak measurement for the incoming airflow in a wind tunnel; (b) the normalized tracer gas distribution measured behind the vehicle for 30 km/h using the chemiluminescence detectors (Mathissen et al., 2012).	45
Figure 2.16	(a) Sketch of the experimental setup with the positions of four ultrasonic anemometers on the highway M-12; (b) the turbulence intensity components depending on downwind distance; (c) the turbulent kinetic energy depending on the vehicle speed for different kinds of vehicles (Alonso-Estebanez et al. 2012).	46

List of Figures

Figure 3.1	Closed circuit wind tunnel facility used for the present research. The circled yellow rectangular frames with transparent acrylic walls are the test section.	50
Figure 3.2	A driving fan for wind tunnel facility (http://www.nimr.org/systems/images/pwt.html).	51
Figure 3.3(a)	Schematic drawing of two types of scaled model vehicles, $\alpha = 25^\circ$ (vehicle A) or 60° (vehicle B) (in mm).	52
Figure 3.3(b)	A heated air jet system of the model vehicle, V1 and (c) a single model vehicle setup inside the wind tunnel facility (Chan et al. 2008b).	53
Figure 3.4(a)	Experimental setup and coordinate system inside the wind tunnel facility for a three-vehicle queue arrangement at 10 km/h case (Not in scale).	54
Figure 3.4(b)	Experimental setup and coordinate system for a two-vehicle queue arrangement at 30 km/h case (Not in scale).	55
Figure 3.4(c)	Experimental setup and coordinate system for a two-vehicle queue arrangement at 50 km/h case (Not in scale).	55
Figure 3.5	Photo of a queue of model vehicles (i.e. V1 to V3) which was placed in-line on the designated flat plate inside the test section for the three-vehicle queue arrangement at 10 km/h case.	56
Figure 3.6	Measured boundary layer thickness over the center of the designated flat plate using the hot-wire anemometer.	58
Figure 3.7	Schematic drawing for a typical experimental setup using PIV and test model in wind tunnel (Dantec Dynamics A/S, 2008).	59
Figure 3.8	Working principle of PIV (a) one of the two captured images for the seeding particles in air flow is shown. A random interrogation area in frame I, is then marked out by a small white frame; (b) cross-correlation is applied to extract a vector from interrogation area I of the two particle images; (c) vector map and derived vorticity map are generated for the whole captured air field by repeating the sub-section cross-correlation for the full image frame (Dantec Dynamics A/S, 2008).	60

List of Figures

Figure 3.9(a)	Laser and optical arm used to deliver the light sheet into the wind tunnel for the illumination of seeding particles.	62
Figure 3.9(b)	A CCD camera was placed outside the test section of wind tunnel to capture the images of a two-dimensional flow field around the last vehicle, V1 (enclosed by the white circle) which was painted in black to minimize its noise laser reflection.	62
Figure 3.9(c)	Triangular laser light sheet was vertically shot down from laser arm to illuminate the flow field for the image capture of CCD camera.	63
Figure 3.9(d)	Safex 2010 smoke generator and its particle exit nozzle. The nozzle was inserted into the closed circuit wind tunnel through a hole on wall to inject the seeding particles into air flow.	63
Figure 3.10(a)	Pre-set of time interval, Δt in PIV control software (inside red frame).	64
Figure 3.10(b)	Dantec Dynamics' FlowMap System Hub (Dantec Dynamics A/S, 2008).	65
Figure 3.11(a)	A captured PIV image for the air flow around the vehicle front. The air flow is filled with smoke particles which are illuminated as the white dots by a laser sheet.	67
Figure 3.11(b)	Vector map generated from Figure 3.11(a) by a cross-correlation of 32×32 pixels with 50% overlap and an afterward validation. For the region under vehicle body, it is blank because down-shooting laser light cannot reach it.	67
Figure 3.11(c)	Streamline derived from the vector map of Figure 3.11(b) to illustrate the flow path around the vehicle front. For the region under vehicle body, it is blank because down-shooting laser light cannot reach it.	68
Figure 3.12(a)	A captured PIV image for the air flow around the vehicle rear.	69
Figure 3.12(b)	Vector map generated from Figure 3.12(a) by a cross-correlation of 32×32 pixels with 50% overlap and an afterward validation.	69

List of Figures

Figure 3.12(c)	Streamline can be derived from the vector map of Figure 3.12(b) to depict the flow path around the vehicle rear.	70
Figure 3.12(d)	Vorticity map can be derived from the vector map of Figure 3.12(b) to depict the flow structure around the vehicle rear.	70
Figure 3.13	Time-averaged streamlines in X - Z plane for one-vehicle ($\alpha = 25^\circ$) case (a) from the present experimental study and (b) from LES study (Figure 4(b) of Krajnovic and Davidson (2005a).	71
Figure 3.14(a)	Dantec StreamLine hot-wire anemometer (the bottom black box) and the cold-wire anemometer (the upper silver box) used in the present study.	78
Figure 3.14(b)	Flow chart of the Dantec StreamLine hot-wire anemometer (from left to right): hot-wire at the tip of probe dissipates heat, Q into flow; anemometer output probe's electrical consumption power, E to a A/D converter to be read and captured into computer; from linearized function gained from calibration, the values of E can be calculated to the flow velocity, U (Dantec Dynamics, 2008).	78
Figure 3.15	The schematic drawing of the custom-made three-wire probe.	81
Figure 3.16	Measured power spectrum in near-wake region of the vehicle ($\alpha = 25^\circ$) at $X/H = 2$ and $Z/H = 0.5$ using the hot-wire anemometer.	83
Figure 3.17	Comparison of the flow properties, \bar{U}/U_∞ , \bar{V}/U_∞ , $4u'/U_\infty$ and $4v'/U_\infty$, from the different number of PIV images ranging from 1 to 1200 at the check point (*) at $1H$ in front of the last vehicle, V1 ($\alpha = 25^\circ$) and $0.5H$ above the ground (Huang et al., 2009a).	85

List of Figures

Figure 3.18	<p>(a) The present studied model vehicle ($\alpha = 25^\circ$) and a tailpipe exhaust hot air; (b) Kanda et al. (2006a) studied the vehicle with a tailpipe exhaust tracer gas; (c) the normalized mean temperature excess, \bar{T}^* (i.e., scalar) contours in Y-Z plane at $X/H = 4$ behind the present studied vehicle ($\alpha = 25^\circ$) at 10 km/h, where $H = 0.081$ m; (d) Kanda et al. (2006a) measured mean gas concentration contours (solid line) in Y-Z plane at $X/H = 4.1$ behind their vehicle at 20 km/h, where $H = 0.072$ m.</p>	88
Figure 4.1	<p>Experimental setup and coordinate system inside the wind tunnel facility for one-, two- and three-vehicle cases (Huang et al. 2009a).</p>	94
Figure 4.2	<p>Horizontal cross-sectional profiles: (a) \bar{U}/U_∞ and (b) u'/U_∞ at $1H$ in front of the vehicle, $V1$ and $Z = 0.5H$ above the ground for one-, two- and three-vehicle cases ($\alpha = 25^\circ$) at 10 km/h (i.e., $3.1H$ vehicle spacing). The center of two curve valleys or where the two vortex centers are marked by +, while edges of the two vortices are marked by \times (Huang et al., 2009a).</p>	98
Figure 4.3	<p>Horizontal cross-sectional profiles: (a) \bar{U}/U_∞ and (b) u'/U_∞ at $1H$ in front of the vehicle, $V1$ and $Z = 0.5H$ above the ground for one- and two-vehicle cases ($\alpha = 25^\circ$) at 30 km/h (i.e., $9.3H$ vehicle spacing) (Huang et al., 2009a).</p>	100
Figure 4.4	<p>Horizontal cross-sectional profiles: (a) \bar{U}/U_∞ and (b) u'/U_∞ at $1H$ in front of the vehicle, $V1$ and $Z = 0.5H$ above the ground for one- and two-vehicle cases ($\alpha = 25^\circ$) at 50 km/h (i.e., $15.5H$ vehicle spacing) (Huang et al., 2009a).</p>	102
Figure 4.5	<p>Contours of \bar{U}/U_∞ in X-Y plane at $Z/H = 0.5$ for one-, two- and three-vehicle cases ($\alpha = 25^\circ$) at 10 km/h (Contour base line = 0.005, step = 0.005) (Huang et al., 2009a).</p>	104
Figure 4.6	<p>Averaged turbulent stress, $\overline{u'v'} /U^2$ contours in X-Y plane at $Z/H = 0.5$ for one-vehicle case ($\alpha = 25^\circ$) at (a) 10 km/h, (b) 30 km/h and (c) 50 km/h (Contour base line = 0.002, step = 0.002) (Huang et al., 2009a).</p>	106

List of Figures

Figure 4.7	(a) \bar{U}/U_∞ and (b) u'/U_∞ profiles in X - Z plane at $1H$ ahead of the last vehicle front, V1 for one-, two- and three-vehicle cases ($\alpha = 25^\circ$) at 10 km/h (Huang et al., 2009a).	108
Figure 4.8	(a) \bar{U}/U_∞ and (b) u'/U_∞ profiles in X - Z plane at $1H$ ahead of the last vehicle front, V1 for one- and two-vehicle cases ($\alpha = 25^\circ$) at 30 km/h (Huang et al., 2009a).	108
Figure 4.9	(a) \bar{U}/U_∞ and (b) u'/U_∞ profiles in X - Z plane at $1H$ ahead of the last vehicle front, V1 for one- and two-vehicle cases ($\alpha = 25^\circ$) at 50 km/h (Huang et al., 2009a).	109
Figure 4.10	Vorticity, $\bar{\omega}_z \cdot H/U_\infty$ contours in X - Z plane for (a) one-vehicle, (b) two-vehicle and (c) three-vehicle cases ($\alpha = 25^\circ$) at 10 km/h (Contour base line = 1, step = 1) (Huang et al., 2009a).	110
Figure 4.11	Vorticity, $\bar{\omega}_z \cdot H/U_\infty$ contours in X - Z plane for (a) one-vehicle, and (b) two-vehicle cases at 30 km/h (Contour base line = 1, step = 1)	111
Figure 4.12	Vorticity, $\bar{\omega}_z \cdot H/U_\infty$ contours in X - Z plane for (a) one-vehicle (Huang et al., 2009a) and (b) two-vehicle cases at 50 km/h (Contour base line = 1, step = 1)	112
Figure 4.13	Reynolds shear stress, $ \overline{u'w'} /U_\infty^2$ contours in X - Z plane for (a) one-vehicle, (b) two-vehicle and (c) three-vehicle cases ($\alpha = 25^\circ$) at 10 km/h (Contour base line=0.0025, step=0.0025) (Huang et al., 2009a).	115
Figure 4.14	Reynolds shear stress, $ \overline{u'w'} /U_\infty^2$ contours in X - Z plane for (a) one-vehicle and (b) two-vehicle ($\alpha = 25^\circ$) at 30 km/h (Contour base line = 0.0025, step = 0.0025)	116
Figure 4.15	Reynolds shear stress, $ \overline{u'w'} /U_\infty^2$ contours in X - Z plane for (a) one-vehicle and (b) two-vehicle ($\alpha = 25^\circ$) at 50 km/h (Contour base line = 0.0025, step = 0.0025)	117

List of Figures

Figure 4.16	Time-averaged vector map in Y - Z plane at the downstream distance $X/H = 1$ for one-vehicle ($\alpha = 25^\circ$) (a) black arrows from the present experimental study measured by PIV at 50km/h and (b) white arrows from Figure 5(d) of Gosse et al. (2011) measured by LDA at 45 km/h.	118
Figure 4.17	Vorticity, $\bar{\omega}_x \cdot H/U_\infty$ contours in Y - Z plane at $X/H = 1$ for one-vehicle case ($\alpha = 25^\circ$) at (a) 10 km/h; (b) 30 km/h and (c) 50 km/h (Contour base line = 0.2, step = 0.2) (Huang et al., 2009a).	120
Figure 4.18	Vorticity, $\bar{\omega}_x \cdot H/U_\infty$ contours in Y - Z plane at $X/H = 3$ for one-vehicle case ($\alpha = 25^\circ$) at (a) 10 km/h; (b) 30 km/h and (c) 50 km/h (Contour base line = 0.2, step = 0.2) (Huang et al., 2009a).	123
Figure 4.19	Horizontal cross-sectional profiles: (a) \bar{U}/U_∞ and (b) u'/U_∞ at $1H$ ahead of the last vehicle front, $V1$ and $Z = 0.5H$ above the ground for one-, two- and three-vehicle cases ($\alpha = 60^\circ$) at 10 km/h (i.e., $3.1H$ vehicle spacing).	128
Figure 4.20	Horizontal cross-sectional profiles: (a) \bar{U}/U_∞ and (b) u'/U_∞ at $1H$ ahead of the last vehicle front, $V1$ and $Z = 0.5H$ above the ground for one- and two-vehicle cases ($\alpha = 60^\circ$) at 30 km/h (i.e., $9.3H$ vehicle spacing).	129
Figure 4.21	Horizontal cross-sectional profiles: (a) \bar{U}/U_∞ and (b) u'/U_∞ at $1H$ ahead of the last vehicle front, $V1$ and $Z = 0.5H$ above the ground for one- and two-vehicle cases ($\alpha = 60^\circ$) at 50 km/h (i.e., $15.5H$ vehicle spacing).	131
Figure 4.22	Contours of \bar{U}/U_∞ in X - Y plane at $Z/H = 0.5$ for (a) one-, (b) two- and (c) three-vehicle cases ($\alpha = 60^\circ$) at 10 km/h (Contour base line = 0.005, step = 0.005), where the dashed lines represent the negative values.	133
Figure 4.23	Contours of \bar{U}/U_∞ in X - Y plane at $Z/H = 0.5$ for (a) one- and (b) two-vehicle cases ($\alpha = 60^\circ$) at 30 km/h (Contour base line = 0.005, step = 0.005), where the dashed lines represent the negative values.	134

List of Figures

Figure 4.24	Contours of \bar{U}/U_∞ in X - Y plane at $Z/H = 0.5$ for (a) one- and (b) two-vehicle cases ($\alpha = 60^\circ$) at 50 km/h (Contour base line = 0.005, step = 0.005), where dashed lines represent negative values.	135
Figure 4.25	(a) \bar{U}/U_∞ and (b) u'/U profiles in X - Z plane at $1H$ ahead of the last vehicle front, V1 for one-, two- and three-vehicle cases ($\alpha = 60^\circ$) at 10 km/h.	137
Figure 4.26	(a) \bar{U}/U_∞ and (b) u'/U_∞ profiles in X - Z plane at $1H$ ahead of the last vehicle front, V1 for one- and two-vehicle cases ($\alpha = 60^\circ$) at 30 km/h.	137
Figure 4.27	(a) \bar{U}/U_∞ and (b) u'/U_∞ profiles in X - Z plane at $1H$ ahead of the last vehicle front, V1 for one- and two-vehicle cases ($\alpha = 60^\circ$) at 50 km/h.	138
Figure 4.28	Vorticity, $\varpi_z \cdot H/U_\infty$ contours in X - Z plane for (a) one-vehicle, (b) two-vehicle and (c) three-vehicle cases ($\alpha = 60^\circ$) at 10 km/h (Contour base line = 0.5, step = 1).	139
Figure 4.29	Vorticity, $\varpi_z \cdot H/U_\infty$ contours in X - Z plane for (a) one-vehicle and (b) two-vehicle cases ($\alpha = 60^\circ$) at 30 km/h (Contour base line = 0.5, step = 1).	140
Figure 4.30	Vorticity, $\varpi_z \cdot H/U_\infty$ contours in X - Z plane for (a) one-vehicle and (b) two-vehicle cases ($\alpha = 60^\circ$) at 50 km/h (Contour base line = 0.5, step = 1)	141
Figure 4.31	Vorticity, $\varpi_x \cdot H/U_\infty$ contours in Y - Z plane at $X/H = 1$ for one-vehicle case ($\alpha = 60^\circ$) at (a) 10 km/h, (b) 30 km/h and (c) 50 km/h (Contour base line = 0.2, step = 0.1)	143
Figure 4.32	Vorticity, $\varpi_x \cdot H/U_\infty$ contours in Y - Z plane at $X/H = 3$ for one-vehicle case ($\alpha = 60^\circ$) at (a) 10 km/h, (b) 30 km/h and (c) 50 km/h (Contour base line = 0.2, step = 0.1)	145

List of Figures

Figure 5.1	Two studied scale-model vehicles of a rear slant angle, $\alpha = 25^\circ$ (vehicle A) and 60° (vehicle B) where the dimension is normalized by the vehicle height, $H = 81$ mm, respectively (Chan et al. 2008b). The small circle on the backside of the vehicle, V1 represents the location of exhaust tailpipe.	154
Figure 5.2	Experimental setup and coordinate system inside the wind tunnel facility for a queue vehicle arrangement at the speed of 10 and 30 km/h.	156
Figure 5.3	Normalized mean temperature excess, \bar{T}^* and normalized mean vector, \overrightarrow{VW}^* in $Y-Z$ plane at $X/H = 2$ behind the vehicle(s) ($\alpha = 25^\circ$) at 10 km/h for (a) one-vehicle, (b) two-vehicle (c) three-vehicle cases.	158
Figure 5.4	Normalized mean temperature excess, \bar{T}^* and normalized mean vector, \overrightarrow{VW}^* in $Y-Z$ plane at $X/H = 2$ behind the vehicle(s) ($\alpha = 25^\circ$) for (a) one-vehicle at 30 km/h and (b) one-vehicle at 45 km/h (Figure 5(e) of Gosse et al. (2011)).	164
Figure 5.5	Normalized mean temperature excess, \bar{T}^* and normalized mean vector, \overrightarrow{VW}^* in $Y-Z$ plane at $X/H = 2$ behind the vehicle(s) ($\alpha = 25^\circ$) at 30 km/h for (a) one-vehicle and (b) two-vehicle cases.	166
Figure 5.6	Normalized mean temperature excess, \bar{T}^* and normalized mean vector, \overrightarrow{VW}^* in $Y-Z$ plane at $X/H = 4$ behind the vehicle(s) ($\alpha = 25^\circ$) at 10 km/h for (a) one-vehicle, (b) two-vehicle (Huang et al. 2009b) and (c) three-vehicle cases.	167
Figure 5.7	Normalized mean temperature excess, \bar{T}^* and normalized mean vector, \overrightarrow{VW}^* in $Y-Z$ plane at $X/H = 4$ behind the vehicle(s) ($\alpha = 25^\circ$) at 30 km/h for (a) one-vehicle and (b) two-vehicle cases (Huang et al. 2009b).	169
Figure 5.8	Normalized mean temperature excess, \bar{T}^* and normalized mean vector, \overrightarrow{VW}^* in $Y-Z$ plane at $X/H = 6$ behind the vehicle(s) ($\alpha = 25^\circ$) at 10 km/h for (a) one-vehicle, (b) two-vehicle and (c) three-vehicle cases.	170

List of Figures

Figure 5.9	Normalized mean temperature excess, \bar{T}^* and normalized mean vector, \overrightarrow{VW}^* in $Y-Z$ plane at $X/H = 6$ behind the vehicle(s) ($\alpha = 25^\circ$) at 30 km/h for (a) one-vehicle and (b) two-vehicle cases.	172
Figure 5.10	Normalized mean temperature excess, \bar{T}^* and normalized mean vector, \overrightarrow{VW}^* in $Y-Z$ plane at $X/H = 8$ behind the vehicle(s) ($\alpha = 25^\circ$) at 10 km/h for (a) one-vehicle, (b) two-vehicle (Huang et al. 2009b) and (c) three-vehicle cases.	173
Figure 5.11	Normalized mean temperature excess, \bar{T}^* and normalized mean vector, \overrightarrow{VW}^* in $Y-Z$ plane at $X/H = 8$ behind the vehicle(s) ($\alpha = 25^\circ$) at 30 km/h for (a) one-vehicle and (b) two-vehicle cases (Huang et al. 2009b).	175
Figure 5.12	Peak scalar, \bar{T}_{\max}^* behind the vehicle(s) ($\alpha = 25^\circ$) for the left- and right-hand regions along the downstream distance, X/H at 10 km/h and 30 km/h.	176
Figure 5.13	Normalized mean temperature excess, \bar{T}^* and normalized mean vector, \overrightarrow{VW}^* in $Y-Z$ plane at $X/H = 2$ behind the vehicle(s) ($\alpha = 60^\circ$) at 10 km/h for (a) one-vehicle, (b) two-vehicle and (c) three-vehicle cases.	183
Figure 5.14	Normalized mean temperature excess, \bar{T}^* and normalized mean vector, \overrightarrow{VW}^* in $Y-Z$ plane at $X/H = 2$ behind the vehicle(s) ($\alpha = 60^\circ$) at 30 km/h for (a) one-vehicle and (b) two-vehicle and three-vehicle cases.	184
Figure 5.15	Normalized mean temperature excess, \bar{T}^* in $Y-Z$ plane at $X/H = 4$ behind the vehicle(s) ($\alpha = 60^\circ$) at 10 km/h for (a) one-vehicle, (b) two-vehicle (Huang et al. 2009b) and (c) three-vehicle cases.	186
Figure 5.16	Normalized mean temperature excess, \bar{T}^* in $Y-Z$ plane at $X/H = 4$ behind the vehicle(s) ($\alpha = 60^\circ$) at 30 km/h for (a) one-vehicle and (b) two-vehicle (Huang et al. 2009b).	187
Figure 5.17	Normalized mean temperature excess, \bar{T}^* in $Y-Z$ plane at $X/H = 6$ behind the vehicle(s) ($\alpha = 60^\circ$) at 10 km/h for (a) one-vehicle, (b) two-vehicle and (c) three-vehicle cases.	189

List of Figures

Figure 5.18	Normalized mean temperature excess, \bar{T}^* in Y - Z plane at $X/H = 6$ behind the vehicle(s) ($\alpha = 60^\circ$) at 30 km/h for (a) one-vehicle and (b) two-vehicle cases.	190
Figure 5.19	Normalized mean temperature excess, \bar{T}^* in Y - Z plane at $X/H = 8$ behind the vehicle(s) ($\alpha = 60^\circ$) at 10 km/h for (a) one-vehicle, (b) two-vehicle (Huang et al. 2009b) and (c) three-vehicle cases.	192
Figure 5.20	Normalized mean temperature excess, \bar{T}^* in Y - Z plane at $X/H = 8$ behind the vehicle(s) ($\alpha = 60^\circ$) at 30 km/h for (a) one-vehicle and (b) two-vehicle cases (Huang et al. 2009b).	193
Figure 5.21	Peak scalar value, \bar{T}_{\max}^* behind the vehicle(s) ($\alpha = 60^\circ$) along the downstream distance, X/H at 10 km/h and 30 km/h.	194

List of Tables

Table 1.1	Registered vehicles operating in Hong Kong (Hong Kong Transport Department, 2011)	2
Table 3.1	Exhaust conditions of a typical on-road light-duty vehicle (Chan et al. 2007; Chan et al. 2008a and 2008b).	75
Table 3.2	The simulation parameters of the studied vehicle cases.	75
Table 4.1	Average longitudinal peak vorticity behind the last vehicle, $V1$ ($\alpha = 25^\circ$) for different vehicle speeds and arrangements of the preceding model vehicle(s) (Huang et al., 2009a).	124
Table 4.2	Average longitudinal peak vorticity behind the last vehicle, $V1$ ($\alpha = 60^\circ$) for different vehicle speeds and arrangements of the preceding vehicle(s).	147
Table 5.1	Fitted values of variables in the dual finite line source Gaussian equation (5-4) for the studied vehicles ($\alpha = 25^\circ$).	180
Table 5.2	Fitted values of variables in the single finite line sources Gaussian equation (5-2) for the studied vehicles ($\alpha = 60^\circ$).	196

Nomenclature

B	width of a real on-road vehicle, m
C	concentration of jet flow
C_D	coefficient of drag
D	diameter of a real on-road vehicle exhaust tailpipe, m
H	height of a real on-road vehicle, m
L	length of a real on-road vehicle, m
Q_i	strength of a finite temperature line source ($i = 0, 1$ or 2), $\text{K} \cdot \text{m}^3/\text{s}$
Re_H	Reynolds number, $Re_H = U_\infty H/\nu$
R	radius of jet flow, m
Rms	root mean square
T	local temperature behind the vehicle, K
T_j	initial temperature excess difference from an exhaust jet, K
T_∞	ambient temperature, K
\bar{T}^*	normalized mean temperature excess, $\bar{T}^* = \bar{T}/T_j$
\bar{T}_{\max}^*	peak normalized mean temperature excess, $\bar{T}_{\max}^* = \bar{T}_{\max}/T_j$
U	streamwise velocity in x direction, m/s
U_j	vehicular exhaust jet exit velocity, m/s
$U_{\text{real vehicle}}$	on-road real vehicle speed, m/s
U_∞	free stream velocity, m/s

Nomenclature

\bar{U}^*	normalized streamwise velocity, $\bar{U}^* = \bar{U}/U_\infty$
U_{def}	the wake velocity deficit, m/s
X_{NW}	length of the near-wake separation bubble region
X_{SL}	flow separation and reattachment region
d_0	diameter of exhaust tailpipe for the studied models, m
h_0	height of plume center, m
k	constant for the concentration of jet flow in Equation 2-3
$\dot{m}_{j(\text{real vehicle})}$	mass flow rate of a real vehicular exhaust gas jet, $\dot{m}_{j(\text{real vehicle})} = \rho_{\text{exhaust gas}} U_{j(\text{real vehicle})} \left(\frac{\pi D^2}{4} \right), \text{ kg/s}$
$\dot{m}_{j(\text{model vehicle})}$	mass flow rate of a model vehicular exhaust hot air jet, $\dot{m}_{j(\text{model vehicle})} = \rho_{\text{hot air}} U_{j(\text{model vehicle})} \left(\frac{\pi d^2}{4} \right), \text{ kg/s}$
$\dot{m}_{\text{real vehicle}}$	mass flow rate of a real vehicle, $\dot{m}_{\text{real vehicle}} = \rho_{\text{ambient air}} U_{\text{real vehicle}} (BH)_{\text{real vehicle}}, \text{ kg/s}$
$\dot{m}_{\text{model vehicle}}$	mass flow rate of a model vehicle, $\dot{m}_{\text{model vehicle}} = \rho_{\text{ambient air}} U_\infty (bh)_{\text{model vehicle}}, \text{ kg/s}$
u	streamwise velocity, m/s
\bar{u}	mean value of streamwise velocity u , m/s
u'	root mean square of streamwise velocity, m/s
v	transverse velocity, m/s
w	spanwise velocity, m/s
x	streamwise coordinate, m
y	transverse coordinate, m

Nomenclature

z	spanwise coordinate, m
*	dimensionless
ΔX	displacement in X axis, m
ΔY	displacement in Y axis, m

Greek symbols

α	rear slant angle of the scale-model vehicle, °
β	angular coefficient of the pollutant dispersion
γ	power exponent of the pollutant dispersion
θ	yaw angle, °
ρ	density, kg/m ³
ν	kinematic viscosity of fluid, m ² /s
σ	dispersion parameter, m
λ	length coefficient for the lateral length of wake, m
σ_y	horizontal dispersion parameter of crosswind Finite Line Source (FLS) Gaussian formula, m
σ_z	vertical dispersion parameter of crosswind FLS Gaussian formula, m
σ_{z_a}	vertical dispersion parameter for the contribution from ambient turbulence, m
σ_{z_w}	vertical dispersion parameter for the contribution from wake-induced turbulence, m

List of Publications

1. Chan T.L., Gosse K., Zhou Y., Lee S.C., Wang X.W., **Huang J.F.**, 2008. Effect of rear slant angle on flow structures and pollutant dispersion in the wake of the studied model vehicle. *International Journal of Heat and Fluid Flow*, Vol. 51 (25-26), pp. 6180-6193.
2. **Huang J.F.**, Chan T.L., Zhou Y., 2009a. Three-dimensional flow structure measurements behind a queue of studied model vehicles. *International Journal of Heat and Fluid Flow*, Vol. 30 (4), pp. 647-657.
3. **Huang J.F.**, Chan T.L., Zhou Y., 2009b. Flow structures, and pollutant dispersion and concentration fields from a queue of studied model vehicles. *Environment and Transport-Transport and Air Pollution 2009 (ETTAP 2009)*, Paper No.: 063. Proceedings of the 17th Transport and Air Pollution Symposium and 3rd Environment and Transport Symposium, June 2-4, 2009, Toulouse, France.

Chapter 1 Introduction

1.1 Research Background and Scope

In many urban cities, air quality problems have attracted growing public concerns in the past decades (Mayer, 1999). Pacione (2003) presented that the concern over the quality of modern life, for example the quality of urban environment, has become a characteristic of modern society. Many governments in the world have attempted to identify and control the source of air pollutants (Kukkonena et al. 2003). For instance, the automobile emissions (i.e., motor vehicles) have been identified to contribute at least 70 to 75% of the total amount of air pollutants during the past 5 years in Malaysia (Rafia et al, 2003). Similarly, the automobile emissions have also been identified as the major contributing source of urban air pollution by the Hong Kong government. This can be attributed to the large number of vehicles which are running daily on the roads of Hong Kong, as shown in Table 1.1. There are on average 331 vehicles distributed on every kilometer of Hong Kong road (Hong Kong Transport Department, 2011). The contribution of vehicle exhaust emissions is an important factor affecting the daily life quality of more than 7.1 million people (Hong Kong Census and Statistics Department, 2011)

Number of Vehicles	Year 2003	Year 2011
Private car	382,880	467,327
Motor-cycles	41,128	55,059
Taxi	18,138	18,088
Public light buses	4,350	4,350
Private light buses	490	2,200
Public buses	1,979	3887
Private buses	490	506
Goods vehicle	121,587	114775
Government vehicles	6,654	6315
Others	13,806	13165
Total	591,502	685,672
Motor vehicles per 1000 human population	77	96

Table 1.1 Registered vehicles operating in Hong Kong
(Hong Kong Transport Department, 2011).

As the major source of air pollution has been identified as the on-road vehicle exhaust emissions in most urban cities and due to their serious impacts on urban air quality and public health (Mayer, 1999), many experiments and numerical models for the pollutant dispersion of on-road vehicles or the pollutant dispersion in urban street canyons have been performed for the monitoring and improvement of urban air quality in the past decade. For example, Sharma and Khare (2001) reviewed the research works for the modeling of vehicle exhausts; Xia and Leung (2001) studied the pollutant dispersion in urban street canopies; Chan et al. (2002a) validated a developed two-dimensional pollutant dispersion model in an isolated street canyon; Hallmark et al. (2003) characterized the on-road variables that may affect the vehicle exhaust pollutant dispersion models; Harrison et al. (2004) studied the influence of meteorological factors and traffic volumes upon suspended particle mass in urban area; Gillies et al. (2005) studied the effect of vehicle characteristics on unpaved road dust emissions; Silva et al. (2006) evaluated the effect of catalytic converter on the spark ignition engine

exhaust gas emissions; Chan et al. (2007) studied the gaseous and particle emission factors from the selected on-road petrol/gasoline, diesel and liquefied petroleum gas vehicles; Nelson et al. (2008) studied the effects of vehicle type and fuel quality on the toxic emissions; Chang et al. (2009a) measured the dilution of tailpipe emissions from different types of model vehicle; Luo et al. (2010) studied the fraction of vehicle exhaust emissions in Hong Kong; Carpentieri and Kumar (2011) measured the nanoparticles in the wake of a moving vehicle; Liu et al. (2010) studied the mechanism of air pollutant re-entrainment in two-dimensional idealized street canyons; Amato et al. (2011) studied the inhalable road dust particles in three European cities.

On the contrary, the pollution in close vicinity of on-road vehicles (e.g., the vehicular exhaust pollutant dispersion and concentration in a relatively short distance behind vehicle(s)) has received less attention. This kind of pollutant dispersion behavior not only has a direct impact on human health in urban microenvironments, particularly to those high peak exposures of ground vehicle drivers and passengers, bicyclists, motorcyclists, pedestrians and people passing, working or living nearby but also constitutes a major fraction of the total pollutant dispersion problem (Venkatram et al., 1999). For example, Wang et al. (2006a) studied numerically a three-dimensional pollutant concentration dispersion of a vehicular exhaust plume; Wang et al. (2006b) also studied the roadside measurement and prediction of CO and PM_{2.5} dispersion from on-road vehicles in Hong Kong. Esber et al. (2007) studied numerically the different ventilation modes for in-vehicle carbon monoxide exposure; Claudia et al. (2009) examined the roadside particle emission factors of individual vehicles under the conventional

driving conditions; and Kumar et al. (2009) measured the dispersion of nanoparticles in a vehicle wake and a street canyon.

Richards et al. (2000) studied numerically the pollution dispersion in the near wake of a vehicle. Chan et al. (2001) developed a two-dimensional nitrogen oxides dispersion from a vehicular exhaust plume and its sensitivity studies. Wang et al. (2006b) have developed a three-dimensional pollutant (i.e., carbon monoxide) concentration dispersion from a vehicular exhaust plume in the real atmosphere. Kanda et al. (2006a & 2006b) have investigated the velocity and concentration fields behind vehicle model(s) and have found that the concentration field of exhaust gas has strong relationship to the flow behavior behind the vehicle(s). Dong and Chan (2006) and Chan et al. (2008a) have developed a three-dimensional large eddy simulation of flow structures and pollutant dispersion in the near-wake regions of a ground vehicle for different urban driving conditions. Sahlodin et al. (2007) incorporated vehicle induced turbulence together with atmosphere-induced turbulence into simple Gaussian dispersion modeling for his predictive model on the dispersion near roadways. Uhrner et al. (2007) developed a physical model by combining a computational fluid dynamics model with an aerosol fine particle model to account for the effects of dilution, nucleation, condensation and coagulation on particle formation and growth in the exhaust plume of a diesel fuelled vehicle. Chan et al. (2008b) have also investigated the effect of rear slant angle on the flow structures, and pollutant dispersion and concentration fields in the wake of a scaled model vehicle. Albriet et al. (2010) coupled a computational fluid dynamics code to a modal aerosol model to simulate the tailpipe plume of a vehicle with emissions corresponding to urban driving

conditions. These literatures have well documented the pollutant dispersion and concentration fields. But the majority of them limited their scope to the pollutant dispersion of a single vehicle leaving the corresponding knowledge about multiple vehicles almost blank.

On the other hand, urban traffic density has been increasing significantly with shortened interval distance between the consecutive vehicles (i.e., vehicle spacing) especially for the most dense urban areas which have considerably slower average vehicle speeds or encountered slow traffic under the road congestion. Watkins and Vino (2008) have recently discussed the application of modern traffic technologies (i.e., intelligent transport systems) for further reducing on the vehicle spacing. Here rises a question: how much of our knowledge gained from a single vehicle can still be applied to the case like a queue of multiple vehicles? Up to now, very few research works concerning the interaction effect of flow structures and pollutant dispersion from a queue of multiple vehicles have been performed. Clifford et al. (1996) identified that 75% of the total received pollution for a following vehicle comes from the preceding one. Kanda et al. (2006b) found that the pollutant dispersion for a queue of vehicles is dominated by the symmetric vehicle wake other than the offset positioned exhaust tailpipe. It can be concluded that the wake flow of a queue of vehicles affects not only their aerodynamic properties but also the pollutant dispersion and concentration field behind the vehicles. A better understanding of the interaction effect of flow structures, pollutant dispersion and concentration fields from a queue of vehicles becomes necessary.

Baker (2001b) stated clearly that the vehicle wakes have a significant effect on the vehicular exhaust pollutant dispersions, but is over simplified by most vehicle pollutant dispersion models. He also pointed out that most of the wake studies serve for vehicle drag reduction, but provide less attention to the interaction between the wake development and vehicular exhaust pollutant dispersion. Similar point of view has been shared by Kanda et al. (2006b) that “Traffic produced turbulence plays an important role in the dispersion of automobile exhaust gas. However, the nature of traffic-produced turbulence is poorly understood, and the existing air pollution models adopt various empirical schemes that are difficult to verify”. Consequently Kanda et al. (2006b) have made an assumption in their vehicle exhaust concentration test that three preceding vehicles are sufficient to produce wake turbulence equivalent to that of an infinite queue. In addition to the experimental investigations, the numerical simulations also have to stem from a base weakened by the lack of knowledge about the flow around a moving vehicle queue, “although exploratory works are emerging” (Kanda et al. 2006b). The lack of information has become a bottle neck for both experimental and numerical research works.

As the wake flow behind the ground vehicles plays an important role in the dispersion and concentration fields of vehicular exhaust pollutants (Chang et al. 2009b), it has long been studied by researchers and engineers using different measurement techniques such as flow visualization, pressure sensor, Pitot tube, multi-hole sensor, hot wire anemometer (HWA), laser Doppler velocimetry (LDV), particle image velocimetry (PIV) etc. as well as the computational fluid dynamics (CFD) techniques. A lot of papers and reports have been documented in the related

areas. As mentioned above, so far our knowledge gained from the experimental and numerical approaches is mainly about a single ground vehicle/scale-down model vehicle either running on road or in a testing facility (e.g. wind tunnel). On the other hand, the automobile population is ever increasing in most urban cities, which leads to the growing traffic density with a shortened interval distance (i.e., vehicle spacing, safety distance etc.) between the consecutive running vehicles on the traffic lanes. And the application of modern technologies such as intelligent transport systems will further reduce the traffic/vehicle spacing (Watkins and Vino 2008). It has been clearly known that the moving ground vehicle may alter the incoming flow structures for the following vehicle(s). Up to now, very few research works concerning the flow structures, and pollutant (i.e., scalar) dispersion and concentration fields behind multiple ground vehicles have been reported. Particular research attention has only been drawn in recent years.

In recent years, the time-averaged wake flow has been extensively studied by either traditional experimental fluid dynamics (EFD) or thriving computational fluid dynamics (CFD) methods to explain the details of aerodynamics or pollutant dispersion around vehicles, for example Khalighi et al. (2001) studied experimentally and computationally the unsteady wake flow behind a vehicle body; Vino et al. investigated the relationship between the passenger vehicle wake and upstream turbulence (2003); Gosse et al. (2006a and b) studied the scalar dispersion in the near wake of a simplified model vehicle while Dong and Chan (2006) studied numerically the flow structures and pollutant dispersion in the near-wake region of vehicle using a large eddy simulation (LES) approach; Watkins and Vino (2008) investigated the relationship between vehicle spacing

and vehicle aerodynamics; Chan et. al. (2008a and 2008b) studied numerically and experimentally the flow structures and pollutant dispersion in the near-wake region of a vehicle, respectively; Al-Garni and Bernal (2010) studied experimentally the near wake of a pickup truck (2010). A rear slant angle of vehicle less than the critical angle 30° is expected to generate a complex of three-dimensional vehicle wake (Ahmed et al. 1984; Chan et al., 2008a and 2008b). Krajnovic and Davidson (2004) pointed out that the variety in the turbulent length scales in combination with very unsteady reattachment of separated flow in this region are possible reasons for failure of Reynolds-averaged Navier-Stokes (RANS) simulations to predict the flow around simplified car model with a rear slant angle less than the critical 30° . A hybrid large eddy simulation - Reynolds-averaged Navier-Stokes (LES-RANS) or detached eddy simulation (DES) is still not fully developed and several problems remain to be solved for this particular rear slant angle (Krajnovic and Davidson, 2005a). Nevertheless, the flow around an Ahmed body with a 25° rear slant angle was successfully simulated by using large eddy simulation (LES) (Krajnovic and Davidson, 2004, 2005a and 2005b). Recently, Guilmineau (2008) has investigated numerically for the flow around a simplified car body with different rear slant angles (i.e., 25° and 35°) and compared his results with the experimental data of Lienhart and Becker (2003). He concluded that the flow around the car body with 25° rear slant angle is still considered an open challenge for turbulence modeling. Guilmineau et al. (2011) have used a detached eddy simulation (DES) approach to investigate the main flow features of an Ahmed vehicle body. They have found that the DES can give a better solution compared with the solution from Reynolds-Averaged Navier–Stokes (RANS) though the DES failed to predict a vortex bubble on the rear slant surface of the vehicle body.

On the other hand, the EFD approaches could still provide the important flow properties for our studied vehicle(s) with a rear slant angle of 25° and become a promising tool to gain our still lacked information.

1.2 Research Objectives of Present Study

As the scientific knowledge about the vehicle queue effect on the characteristics of air flow, and exhaust scalar dispersion and distribution fields in the vehicle wake is still very limited, the present study is going to firstly investigate the time-averaged wake flow around a queue of vehicles to fill the knowledge gap. An intensive experimental investigation will be performed in a well controlled wind tunnel testing facility to have a better understanding of the flow structures for different vehicle queue cases. Air flows passing through the selected representative planes of the studied model vehicle(s) will be measured by using particle image velocimetry (PIV) technique. The air flow structures and properties in the vehicle wake region for one-, two- and three-vehicle cases (i.e., a queue of vehicles) will then be revealed.

Secondly, the present study will also investigate the time-averaged wake flow and exhaust scalar dispersion around a queue of vehicles. This experimental investigation will be performed in the wind tunnel testing facility to have a better understanding of the flow structures for different vehicle queue cases. Heat (i.e. scalar) and air flow passing through the selected representative planes of the vehicle(s) will be measured by using the cold-wire and hot-wire techniques. The characteristics of air flow and exhaust scalar dispersion and distribution fields in

the vehicle wake for one-, two- and three-vehicle cases will then be revealed. The following research objectives will be accomplished:

- (i) to investigate experimentally the vehicle queue effect on the characteristics of air flow of a scale-down vehicle with different rear slant angles which is placed alone or behind the preceding vehicle(s) in a wind tunnel facility for the selected urban vehicle speeds using the particle image velocimetry. Two different rear slant angle categories (i.e., $\alpha = 25^\circ$ and 60°) will be used to generate the three-dimensional and quasi two-dimensional vehicle wake flows behind the vehicle, respectively.
- (ii) to investigate experimentally the vehicle queue effect on the characteristics of exhaust scalar dispersion and distribution fields of the studied vehicle (i.e., $\alpha = 25^\circ$ or 60°) which is placed alone or behind the preceding vehicle(s) in a wind tunnel facility for the selected urban vehicle speeds using the cold-wire and hot-wires anemometers.

The scientific findings generated from the above comprehensive experiments will provide the essential information to enrich our limited knowledge in the vehicle queue effect on the characteristics of air flow, and exhaust scalar dispersion and distribution fields in the vehicle wake.

1.3 Layout of Present Thesis

Chapter 1 introduces an overview of the background and scope related to the present study, indicating that the knowledge gap of the vehicle queue effect on

the characteristics of air flow, and exhaust scalar dispersion and distribution fields in the vehicle wake should be investigated. The objectives of the present study are intended to fill this knowledge gap.

Chapter 2 provides a more detailed literature survey of the research work performed in the related research areas using PIV, cold-wire and hot-wire techniques, and analytical and numerical modeling approaches, the knowledge and understanding that the researchers have acquired, and the shortcomings of these research areas and where the knowledge gap lies.

Chapter 3 provides our experimental arrangements and the proposed measurement techniques (i.e. PIV, cold-wire and hot-wire sensors) together with their methodology, merits and successful applications.

Chapter 4 provides the experimental PIV results of air flow passing through the selected representative planes around and behind the studied vehicle with two different rear slant angle categories (i.e., 25° and 60°) under the different vehicle queue conditions.

Chapter 5 provides the experimental cold-wire and hot-wire results of heat (i.e., scalar) and air flow passing through the selected representative planes behind the model vehicle with two different rear slant angle categories (i.e., 25° and 60°) under different vehicle queue conditions.

Chapter 6 provides the conclusions and major scientific findings revealed by the present study, and some recommendations for future work.

Chapter 2 Literature Review

2.1 The Wake of a Moving Vehicle

The wake of a moving vehicle can be defined as a trace of disturbed air left by a moving vehicle in air. When a bluff body moves in fluid, the fluid is pushed aside and separates from the ending surface of bluff body generating a velocity deficit behind the body and extends some distance in the downstream. The region filled by the separated fluid is defined as wake (Ahmed 1981). Figure 2.1 shows a bluff body vehicle moving at a relative speed U to the originally uniform air and its disturbance left behind. The rear shape of the bluff body is important to the beginning point of wake, the main structure of the wake and how far the wake will remain behind the bluff body.

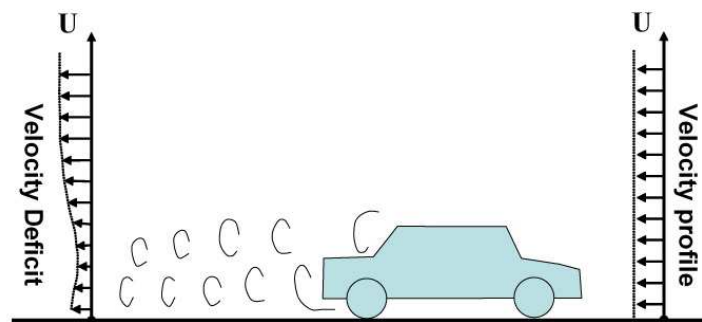


Figure 2.1 The wake of single vehicle moving in air (Katz, 1995).

The whole wake behind a moving vehicle can be divided into two regions: a near-wake region and a far-wake region (Ahmed 1981; Baker 2001). The near-wake region of a ground vehicle starts from the rear of vehicle body. According to past research works (e.g. Ahmed 1981; Khalighi et al. 2001;

Chan et al. 2008a), this near-wake region is found to contain two distinguishable large scale structures: one is a recirculation region right behind vehicle rear and the other one is two counter-rotating trailing vortices (also called longitudinal vortices), and the wake structure and flow characteristics are related to the shape of vehicle rear which defines shear layer separation point and wake pumping. Because the near- wake region has direct link to vehicle's drag force, life force, dispersion of gaseous and particle pollutants, therefore it has received extensive experimental investigations. For instance, the Ahmed (1981) introduced the Ahmed vehicle bodies which are categorized into the generation of two- and three-dimensional vehicle wake flow structures; Ahmed et al. (1984) further studied the relationship between the wake flow category and rear shape of vehicles; Onorato et al. (1986) made a more detailed experimental analysis of the vehicle wakes; Sims-Williams et al. (2001) investigated the large scale unsteady flow structures in the wake of real and idealized vehicle hatchback; Baker (2001) reviewed the studies of the flow and dispersion in ground vehicle wakes; Depardon et al. (2006) studied the near-surface air flow around a scaled-down vehicle; Song et al. (2006) measured the characteristics of air flow behind a passenger vehicle; and Pino et al. (2011) investigated theoretically and experimentally the structure of trailing vortices behind the vehicle. The extension of near-wake region is about ten times the height of its ground vehicle and may vary with its vehicle body shape, as defined by Ahmed (1981). Further the flow downstream, there exists a far-wake region which is a region of cascading flow turbulence with no discernable flow structure, and the ensemble-averaged velocity gradually decays at a relatively steady step (Baker, 2001b; Richards, 2002). The main flow structures in the near-wake region are shown in Figure 2.2.

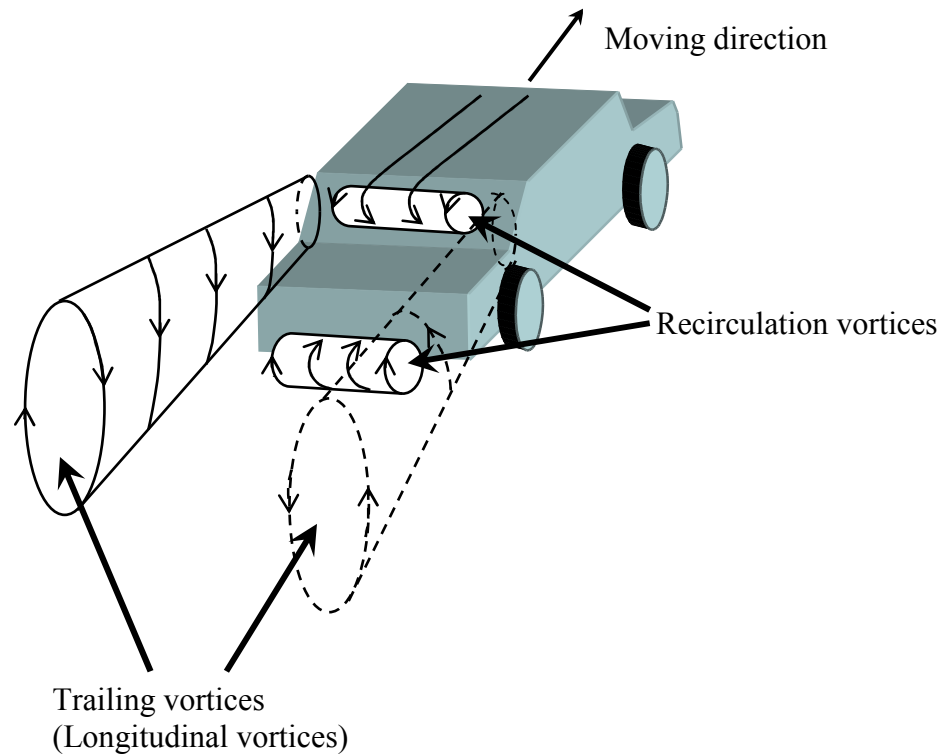


Figure 2.2 The near-wake region of a moving vehicle (Ahmed, 1981).

2.2 Characteristics of the Vehicle Wake and its Vehicular Exhaust Jet in the Wake Region

Compared with the dispersion of gaseous pollutants, the dispersion of particle pollutants is quite different because the exhausted particles have a small but significant mass and volume. The gravity and dynamic force of local air flow cause these particles to behave differently from gaseous components in the vehicle wake (Hider et al., 1997). Therefore it is necessary to study the behavior of particle pollutants and gaseous pollutants separately in the wake of a moving vehicle in order to have a detailed understanding of their dispersion patterns and flow structures. Many past studies concentrated on the monitoring of mass and number-size distribution of particle pollutants near roadsides or in test facilities. For example, Melvin and Robert (1982) studied the pollutant concentration from

the mobile sources in the ambient air; Hider et al. (1997) developed a numerical model to predict the particulate dispersion in the wake of a vehicle; Harrison et al. (1999) measured the physical properties of particles in urban atmosphere; Namdeo et al. (1999) investigated the dispersion of fine and coarse particulates in an urban street canyon; Vignati et al. (1999) studied the transformation of size distributions of vehicle emitted particles in streets; Charron and Harrison (2003) investigated the primary particle formation from vehicle exhaust emissions in the roadside atmosphere; Longley et al. (2003) measured the aerosol number and mass size distribution in a busy street canyon; Harrison et al. (2004) studied the influence of meteorological factors and traffic volumes on the suspended particle mass at urban roadside sites; Zhang et al. (2004a and 2004b) analyzed the aerosol dynamics and its implications for engine emission measurement (2004a) and the evolution of particle number distribution near the roadways, respectively; Gillies et al. (2005) studied the effect of vehicle characteristics on unpaved road dust emissions; Uhrner et al. (2007) performed a numerical simulation for the dilution and aerosol dynamics within a diesel car exhaust plume of on-road measurement conditions; Claudia et al. (2009) developed a new approach for the in-situ determination of roadside vehicular particle emission factors; Kumar et al. (2009) used a fast response measurements of nanoparticles in a vehicle wake and a street canyon; Chang et al. (2009a and 2009b) measured the dilution of tailpipe emissions in downstream for the multiple types of vehicles and the effects of vehicle shape, tailpipe position and exhaust velocity on the dilution rates for tailpipe emissions, respectively; Zhang et al. (2011) compared the vehicle emissions for different work zone, rush hour and free-flow conditions; Carpentieri and Kumar (2011)

measured concentration of nanoparticles in the wake of a moving vehicle with the ground-fixed and on-board sensors.

On the other hand, some other studies put their emphasis on detecting and modeling the dispersion of gaseous pollutants in the wake of the real vehicles or model vehicles. For example, Eskridge et al. (1979a and 1979b) developed a highway model to predict the velocity and turbulence fields, and the advection and diffusion of tracer gas in the wake of vehicles, respectively; Baker (1996) developed a novel method for the prediction of pollution dispersal from road vehicles; Pearce and Baker (1997) investigated the effect of vehicle motion on exhaust dispersion in urban canyons; Baker and Hargreaves (2001) developed and evaluated a vehicle pollution dispersion model; Sotiris et al. (2002) analyzed the model sensitivity and uncertainty using the data from the roadside air quality measurement; Kanda et al. (2006a and 2006b) performed a wind tunnel study on the exhaust gas dispersion for a single vehicle and the multiple road vehicles, respectively; Uhrner et al. (2007) used CFD simulations for the dilution within a diesel car exhaust plume; Chan et al. (2008 a & b) numerically and experimentally investigated the flow structures and pollutant dispersion behind a scaled model vehicle. Recently, Chan et al. (2010a) have first investigated numerically the effects of the aerosol characteristics and behavior in the wake of a ground vehicle for stationary and lower vehicle speed conditions. Furthermore, Chan et al. (2010b) have investigated the interaction effects of different sulfur contents, relative humidities, driving modes and vehicular exhaust tailpipe exit conditions on the three-dimensional exhaust gas-to-nanoparticle conversion and concentration distribution in the wake region of a typical bus-shaped vehicle. Liu et al. (2011b)

have simulated numerically the three-dimensional exhaust particle dispersion and concentration fields in the near-wake region of a ground vehicle. Figure 2.3 provides a snapshot of the dispersion of hot exhaust jet in the vehicle wake. The above studies are dedicated to either the vehicle exhaust pollutant dispersion or the vehicle wake and have fruitful insights for the present study. Most of the above studies, however, overlooked the interaction between vehicle exhaust pollutant dispersion and vehicle wake. Many factors play their roles in the dilution rate of exhausted pollutants in a vehicle wake, such as the shape of vehicle rear (i.e., fastback, estate or square back, notchback as described by Ahmed, 1981), the vehicle type (i.e., car, truck, bus, tractor etc.), the driving conditions of vehicle(s), the position of vehicular exhaust tailpipe exit, and the ambient conditions (i.e., wind speed and direction) etc. The sections below will discuss the role of different driving and ambient wind conditions on the dispersion and concentration fields of the vehicle exhaust gases.

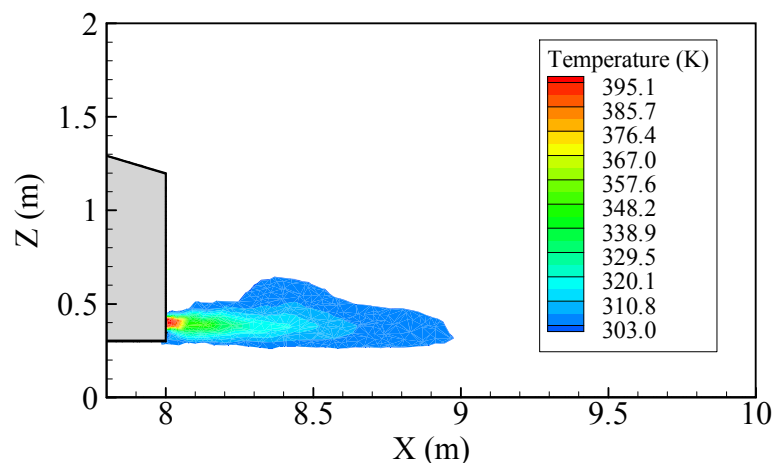


Figure 2.3 A typical snapshot of the temperature distribution of a ground vehicle ($\alpha = 25^\circ$) at the cross section plane for vehicle speed = 30 km/h (Chan et al. 2008a).

2.3 Stationary Vehicle in Still Ambient Air ($U_w \leq 0.1$ m/s)

This section is to study the case that a stationary vehicle exhausts jet into calm ambient air. This case is quite similar to the situation where a free shear jet comes out from a vehicular exhaust tailpipe (diameter d_0) of a stationary vehicle with an exit velocity (U_0) and moves into idle ambient air, as shown in Figure 2.4. The concept of ‘free shear jet’ means that the jet flow is away from the effects from walls or confined space etc., and the turbulence in flow is purely induced by shear force due to the differences in the velocity of moving jet and idling ambient air. Jet plume may expand because of the turbulence which is produced by the shear force rising from the velocity difference between the jet flow and the ambient air. Viscous dissipation and diffusion in space will decrease the turbulent kinetic energy when jet moves forward axially. The interface between the turbulent jet flow and ambient flow will gradually expand outwards as the jet inhales more ambient air through the interface when moving. The mass of jet flow will gradually increase with the axial distance due to the inhaling, but the velocity of jet will decrease along the distance because the total momentum of jet flow will remain its conservation.

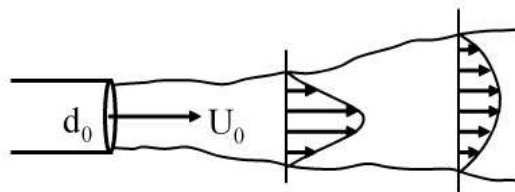


Figure 2.4 The typical flow profile of a jet at different axial distances.

For the region within four or five times the pipe diameter downstream from the mouth of exhaust tailpipe, this region is called potential wake. In this region, the inhaled mass from ambient air can be negligible because of jet's high velocity and low diffusion rate into ambience. As a consequence, the dilution volume is almost negligible in this potential region. The jet flow will go further and grow in size and inhale ambient air but decreases in velocity along downstream direction.

Let the concentration of jet flow, C be the concentration of jet flow at a downstream distance x and initially $C = C_0$ at the mouth of tailpipe. Assume that the jet flow enters the still ambient air with an initial density, ρ_0 at an initial velocity U_0 . Let R be the radius and U be the speed of jet flow at downstream distance x . For a circular jet flow, the conservation of mass flow rate (kg/s) can be expressed as:

$$2\pi \int_0^{\infty} R U_0 \rho_0 dr = \rho \pi R^2 U \quad (2-1)$$

and the momentum mass flux (kg·m/s²) can be expressed as:

$$\frac{d}{dx} \rho \pi R^2 U^2 = 0 \quad (2-2)$$

Within potential region where $x = 4 \sim 5d_0$, $U \approx U_0$. Put this condition in equations (2-1) and (2-2) and after some algebra we can have

$$C = k C_0 \frac{d_0}{x} \quad (2-3)$$

where k is a constant and Pope (2000) gave a value for it that $k = 5$. Now the dilution rate of a jet flow in idle ambient air can be expressed as:

$$C = C_0 \frac{5d_0}{x} \quad (2-4)$$

The exhaust pollutant transport and concentration field in the wake region of a stationary ground vehicle for a still ambient air condition have been simulated by Dong and Chan (2006) as shown in Figure 2.5. It has shown that the thermally induced upward motion by the buoyancy force causes the scalar (i.e., pollutant) dispersion in upward direction.

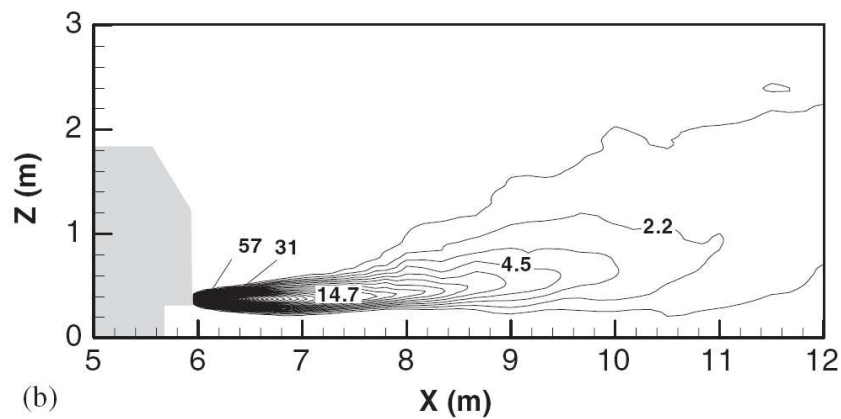


Figure 2.5 A typical vehicular exhaust jet pollutant (in ppm) distribution behind the stationary ground vehicle in a still ambient air for $U_w = 0.1$ m/s (Dong and Chan, 2006).

2.4 Stationary Vehicle in Windy Ambient Air ($U_w > 0.1$ m/s)

This case can be considered as a point source at the ground level withstanding an incoming wind speed, U_w ($U_w > 0.1$ m/s). The Gaussian equation can be applied for this point source to calculate the pollutant concentration in its downstream region. For the ground level at $z = 0$,

$$C = \frac{Q}{\pi U \sigma_y \sigma_z} \exp\left(-\frac{z_0^2}{2\sigma_z^2}\right) \quad (2-5)$$

The downwind dispersion parameters, σ_y and σ_z can be expressed as:

$$\sigma_y = \sigma_{y_0} + ax^p \quad \text{and} \quad \sigma_z = \sigma_{z_0} + bx^q \quad (2-6)$$

where a , b , p and q are the coefficients related to the stability of atmospheric air and the roughness of ground, and σ_{y_0} and σ_{z_0} are the initial spread of jet flow due to entrainment. For example, Pasquill-Gifford atmospheric stability categories provide the values as $\sigma_{y_0} = 0.219x^{0.764}$ and $\sigma_{z_0} = 0.14x^{0.727}$ respectively for a typical atmospheric stability in neutral class D (Gifford, 1968). The exhaust pollutant transport and concentration field in the wake region of a ground vehicle for a windy air condition have been simulated by Dong and Chan (2006) as shown in Figure 2.6. It has shown that shortly after the exhaust plume, the direction of exhaust jet pollutant dispersion is parallel to the same direction of oblique ambient wind.

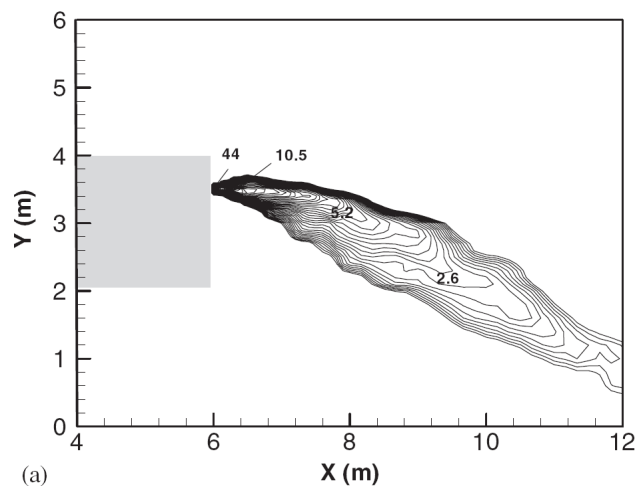


Figure 2.6 A typical vehicular exhaust jet pollutant (in ppm) distribution behind the ground vehicle for an ambient wind speed, $U_w = 1$ m/s and yaw angle, $\theta = 45^\circ$ (Dong and Chan, 2006).

2.5 Moving Vehicle in Still Ambient Air ($U_w \leq 0.1$ m/s)

As discussed in Section 2.1, the wake region can be divided into the near-wake and far-wake regions based on local turbulence cascade and flow structures. However, the effective factors for the pollutant mixing in the near-wake and far-wake regions of a vehicle moving at velocity, V can be assumed to be the same as to a stationary vehicle experiencing an incoming wind at a speed, $U_w = V$ where the relative velocities between the ambient wind and moving vehicle in these two cases are exactly the same. The turbulence generated behind the moving vehicle will exceed natural atmospheric turbulence in almost still air. In the potential wake region, the dilution of the vehicular exhaust jet is negligible as the changes in the axial and cross sectional velocities of jet exit are still small. Further behind the potential wake region, the dilution process will be enhanced by jet turbulence, and the wake cannot remain in a simple self preserving form. However, the turbulence will decrease when the jet flow moves away from the vehicle due to

the viscous dissipation and diffusion of turbulent kinetic energy. Consequently the turbulent kinetic energy will decay in the volume of the mixing process, as in a simple exhaust jet case of a stationary vehicle in still ambient air. Some models proposed by Benson (1979), Sliggers (1991) and Baker (1996) for the prediction of atmospheric pollution dispersion around on-road vehicles are based on Gaussian dispersion theory. Hence the traffic flow is simply represented by the stationary points placed at the intervals along the road lane rather than in moving point sources. It has the defect that the effects of vehicle velocity cannot be simulated. Eskridge and Hunt (1979a) developed a Gaussian model for the wake region by assuming that a vehicle was fixed in space over the roadway while the road and air are passing the vehicle at speed U . The U is the relative speed between a moving vehicle and calm ambient air (i.e., ambient wind speed, $U_w < 0.1$ m/s). Their simulated results show that the velocity and length scale in wake vary as $(x/H)^{-3/4}$ and $(x/H)^{1/4}$ respectively, where 'x' is the downstream distance along the X-direction and 'H' is the height of vehicle. Based on an assumption for simplification that the lateral length equals to vertical length in wake which is not exact to real situation, the vertical scale length of velocity deficit is given as:

$$l(x) = ABH \left(\frac{x}{H} \right)^{1/4} \quad (2-7)$$

where $A = 0.095$; $B = \left(\frac{C_D}{32\pi e^{1/2} \lambda A^3} \right)^{1/4}$; $\lambda = 1.14$; and C_D is the coefficient of drag.

Based on the Equation (2-7), Eskridge and Thomson (1982) further developed the wake theory and expressed the vertical (l_{vertical}) and lateral (l_{lateral}) length scales respectively as:

$$l(x) = l_{\text{vertical}} \quad \text{and} \quad l_{\text{lateral}} = \lambda \left(\frac{W}{H} \right) l(x) \quad (2-8)$$

where W is the width of vehicle.

The turbulence intensity behind a ground vehicle at 30 km/h in still ambient air has been simulated by Chan et al. (2008) as shown in Figure 2.7. The relatively large values of turbulence intensity at **M** and **N** points have been found in the lower part of the near-wake region where the separated flow is caused by the studied vehicle slanted surface and underbody.

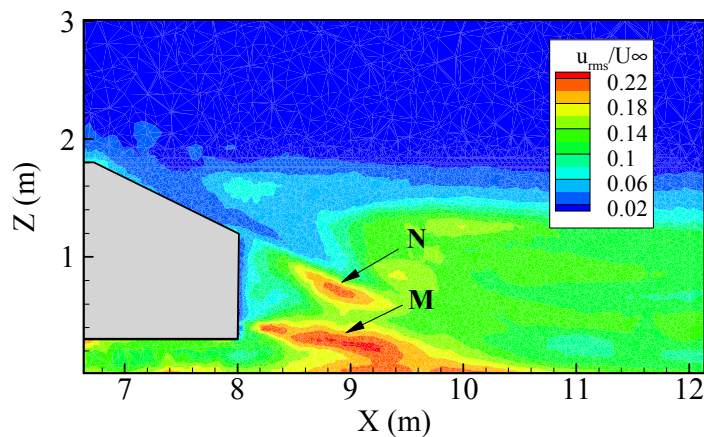


Figure 2.7 A typical turbulence intensity distribution of a ground vehicle ($\alpha = 25^\circ$) at vehicle speed = 30 km/h (Chan et al. 2008a).

2.6 Moving Vehicle in Windy Ambient Air ($U_w \gg 0.1$ m/s)

In case of a moving vehicle experiencing ambient wind, the decay rate of turbulent kinetic energy will be different in the near-wake and far-wake regions. The dispersion of pollutants in the wake region will vary with local flow structure and local turbulence generated by the moving vehicle and the turbulence in windy atmosphere (Kim et al., 2001). Accordingly pollutant dispersion and concentration fields from a single vehicle or multiple vehicles will be quite different in these two sub-regions.

Eskridge and Hunt (1979) expressed that for the “zero” ambient wind condition ($U_w = 0$ m/s) in the near-wake region,

$$\frac{U_{\text{def}}}{U_{w-v}} = \left(\frac{x}{H}\right)^m, \quad \frac{W_h}{H} = \left(\frac{x}{H}\right)^n, \quad \text{and} \quad \frac{W_w}{W_{EF}} = \left(\frac{x}{H}\right)^n \quad (2-9)$$

where U_{def} is wake velocity deficit, U_{w-v} is the relative velocity between the wind and moving vehicle, x is the downstream distance, H is vehicle height, W_h is the wake height, W_w is the width of wake, and W_{EF} is the effective vehicle width. If the velocity of a moving vehicle is much higher than that of ambient wind, then the power coefficients $m = -0.75$ and $n = 0.25$ can be used. For a stationary vehicle in ambient wind $m = -1.5$ and $n = 0.5$ should be used.

Based on Eskridge and Hunt’s work (1979), Baker (1996) further extended the theory for the angled wind cases by considering a vehicle of length, l and width, b is moving along the y -axis at a velocity, V m/s and the wind is blowing along

x -axis at a speed of U m/s, then the wake centerline is inclined at a yaw angle, θ to the direction of vehicle movement,

$$W_{EF} = l \sin \theta + b \cos \theta; \quad \tan \theta = U / V; \quad \sin \theta = U / U_{WRV} = U / (U^2 + V^2) \quad (2-10)$$

In the far-wake region where vehicle generated turbulence has faded away and natural atmospheric turbulence is almost constant, the dispersion coefficients can be considered as proportional to the off-source distance and turbulent intensity (Baker 1996). In this far wake windy case the downwind dispersion parameters σ_y and σ_z can be expressed as:

$$\sigma_x = \sigma_y = T_y (X - X_w) \quad (2-11)$$

$$\sigma_z = T_z (X - X_w) \quad (2-12)$$

where X_w is the distance that far wake begins, T_y and T_z are turbulent intensity defined as:

$$T_y = 2.0 \left(\frac{u'}{u} \right) \left\{ 1 + \left[0.138 \left(-\frac{H}{L} \right)^{2/3} \right] \right\}^{1/2} (X - X_w) \quad (2-13)$$

$$T_z = 1.3 \left(\frac{u'}{u} \right) \left\{ 1 + \left[1.547 \left(-\frac{H}{L} \right)^{2/3} \right] \right\}^{1/2} (X - X_w) \quad (2-14)$$

where u' is friction velocity, u is wind velocity, H is the thickness of atmospheric boundary layer, and L is the Monin-Obukhov length.

2.7 Research Development of Analytical and Computational Approaches for the On-road Vehicle Aerodynamics and Pollutant Dispersion

Since 1970s, the analytical and computational approaches such as line source modeling and computational fluid dynamics (CFD) have become the common tools to describe the analysis of systems involving fluid flow, heat transfer and associated phenomena, for example the chemical reactions by means of computer-based numerical methods (Vardoulakis et al., 2002). It has been widely used for industrial and more recently for environmental and biomedical applications (Gosman, 1999). Accumulated experimental works during past decades have built a large pool of data source for the validation and verification of CFD results, for example, Chok et al. (1994) investigated numerically the effects of base slant on the wake pattern and drag of three-dimensional bluff bodies with a rear blunt end; Khalighi et al. (2001) studied experimentally and computationally the unsteady wake flow behind a bluff body with a drag reduction device; Krajnovic and Davidson (2005a) performed a LES simulation for the flow around a simplified car; Uhrner et al. (2007) also performed CFD simulations for the dilution and aerosol dynamics within a diesel car exhaust plume; Albriet et al. (2010) developed a CFD model for the aerosol number distributions from a vehicle exhaust; Chan et al. (2010a) have first investigated numerically the effects of the aerosol characteristics and behavior in the wake of a ground vehicle for stationary and lower vehicle speed conditions. Furthermore, Chan et al. (2010b) have investigated the interaction effects of different sulfur contents, relative humidities, driving modes and vehicular exhaust tailpipe exit conditions on the three-dimensional exhaust gas-to-nanoparticle conversion and concentration distribution in the wake region of a typical bus-shaped vehicle. Guilmineau et al.

(2011) performed a DES simulation for the air flow around a vehicle; Liu et al. (2011b) have simulated numerically the three-dimensional exhaust particle dispersion and concentration fields in the near-wake region of a ground vehicle. CFD has advantage over other prediction models in their capability to deal with the complex boundary conditions by using the flexible fine-scale grids on the shaped walls, for example in the design of aircraft and automobile. Because the real-world automobiles are often complex in shape and difficult to study experimentally, CFD has increasingly become an important tool for the study of three-dimensional flow around a ground vehicle for the optimization of body shape to reduce aerodynamic drag and improve fuel economy. CFD is also valuable in providing insight of facts that are difficult to gain from experiments.

CFD modeling is a numerical approach for solving the governing equations for mass, momentum, energy and any additional constituents (i.e., pollutant species) which are difficult to have an analytical solution. These equations can be derived from the basic conservation and transport principles: (a) the mass conservation (continuity) equation, (b) the three momentum conservation (Navier–Stokes) equations in x , y , z , directions and (c) the energy conservation equation. In addition, the equations of thermodynamic equilibrium and the Newtonian model of the viscous stresses are often utilized to solve the defined model system numerically. All initial and boundary conditions have to be pre-set before starting the numerical processing.

Many general-purpose CFD packages like PHOENICS, STAR-CD and FLUENT codes have been commercially available and widely applied in a number

of vehicle emissions modeling studies such as the flow and dispersion around a simple cube, the modeling of dense gas dispersion in tunnels and a two-dimensional pollutant dispersion model in an isolated street canyon (Scanlon, 1997; Hall, 2001 and Chan et al, 2002a). Some other numerical models like MERCURE (Carissimo et al., 1995), CHENSI (Levi and Sini, 1992) and MISKAM (Eichhorn, 1995) were specifically developed for the pollutant dispersion at local scale. Alexander and Walter (2003) conducted a series of CFD simulations to evaluate the relative impacts of several forced ventilation configurations on vehicle pollutant dispersion in a covered roadway. Dong and Chan (2006) performed a three-dimensional large eddy simulation (LES) of pollutant dispersion in near wake for the combined effects of driving modes and ambient wind conditions. Recently, Chan et al. (2008a) have investigated comprehensively a three-dimensional large eddy simulation (LES) of the flow structure, pollutant dispersion and concentration field in the near-wake region of their studied vehicles (i.e., $\alpha = 25^\circ$ and 60°), stationary (i.e., low and high idling modes) and moving vehicle conditions, vehicular exhaust jet exit conditions, and ambient wind conditions (i.e., with wind speed and direction) within the urban road microenvironment.

Line source emission modeling has become an important tool in control and management of vehicular exhaust emissions in urban environment (Sharma and Khare, 2001). Chock (1978) established a simple line-source GM (General Motor) model for the description of the downwind pollutant dispersion near roadway. Besides, several other traffic/highway air pollution models have also been developed by the US Environmental Protection Agency (EPA) which includes

CALINE (California Line Source Model) and EPA-HIWAY (Highway Air Pollution Model) as described in Zimmerman and Thompson (1975). Both models are based on the Gaussian equation. But the more simple and popular HIWAY model adopts an assumption of a series of finite line sources while CALINE model includes a set of equations to calculate the pollutant dispersion under crosswind and parallel windy conditions. Chock (1977) and Noll et al. (1977) reviewed these models with the conclusion that the EPA-HIWAY model has a shortage of overestimating the pollutant concentrations adjacent to the highway. A micro-scale dispersion model was adopted by Shozo and Hitoshi (1990) to estimate the vehicular exhaust gaseous concentration within an urban area that locates within 200 m aside from a road. Based on the India Delhi traffic conditions, Khare and Sharma (1999) presented a model namely Delhi Finite Line Source Model (DFLSM). Matsui and Karim (1998a and 1998b) incorporated some more parameters such as wind distributions, emission dispersion and modified Gaussian equations in a numerical model to evaluate the effects of street canyon and vehicle wake on the transport of air pollution from road to urban environment. Sivacoumar and Thanasekaran (1999) employed a Gaussian-based Finite Line Source Model which can handle all orientations of wind direction in relation to the road though there was a slight over prediction when wind direction was parallel to the road. Sharma and Khare (2001) presented their review on analytical modeling techniques including deterministic and statistical modeling approaches which were developed for vehicle exhaust emissions. Vardoulakis et al. (2002) made an attempt to combine three dispersion models in an exploration for the best carbon monoxide (CO) and benzene estimation. Nagendra and Khare (2002) evaluated a few line source emission models with the conclusion that Gaussian model is

generally accepted for the prediction of long-term average vehicular exhaust concentrations and numerical models are more desirable so long as adequate data and theory of dispersion phenomenon and enough computational resources are available. Hallmark et al. (2003) released a methodology specialized for signalized intersections, where the elevated emissions due to specific vehicle operating modes are expected to occur by the emission rate models, and further improved vehicle exhaust predictions. Kukkonen et al (2003) verified an operational street pollution model (OSPM) which incorporated an urban background with the data measured in 1997 at the Runeberg street of Helsinki, Finland. Carpentieri et al. (2011) reviewed literature on the vehicle wake and nanoparticle dispersion contributed from field measurements, wind tunnel experiments and numerical approaches with a conclusion that the interaction between nanoparticles and the flow and turbulence fields immediately behind the vehicle is important for mixing process but has not been well analyzed.

2.7.1 Gaussian dispersion models for highway/roadway air dispersion

In the past numerical modeling studies, a few Gaussian line source dispersion models for predicting vehicular gaseous pollutants have been developed. The common idea in various Gaussian line-source models is based on the superposition principle that the concentration at a receptor can be considered as the sum of contributions from all the infinitesimal point sources in the line source. The mechanism of diffusion from each point source is assumed to be irrelevant to the presence of other point sources. Three typical Gaussian line source models for traffic/highway/roadway air dispersion will be briefly discussed in Sections 2.7.2 to 2.7.4.

2.7.2 General Motor model for highway/roadway air dispersion

Chock (1978) in his modeling work developed a simple line-source model named as General Motor model (GM) to describe the downwind dispersion of pollutants near the roadway. For normal Gaussian models, however, the validity of the point source assumption becomes questionable when the line source is accompanied by self-generated turbulence, for example the case for a roadway with traffic. In addition, the approximation of superposition degrades when the angle between the directions of wind and road becomes small. To resolve the problems, it would be useful to avoid the point source assumption. Therefore the GM model could be expressed as:

$$C(x, z) = \frac{Q}{\sqrt{2\pi U \sigma_z}} \left\{ \exp\left[-\frac{1}{2} \left(\frac{z+h_0}{\sigma_z}\right)^2\right] + \exp\left[-\frac{1}{2} \left(\frac{z-h_0}{\sigma_z}\right)^2\right] \right\} \quad (2-15)$$

where $C(x, z)$ is the concentration at point (x, z) relative to the line source at $x = 0$; Q is the emission rate per unit length; U is the effective crossroad wind; σ_z is the vertical dispersion parameter and h_0 is the plume center height at distance x from the road. On the condition that the above parameters are valid at different cross-road wind speeds, the effect of plume rise can be predicted with certain accuracy at low crossroad winds.

The dispersion characteristics are affected by the angle between directions of wind and road. When wind direction is almost parallel to road, it can be expected that the pollutants from the upstream portion of the line source will significantly disperse before they arrive at the receptor. Hence, σ_z would increase when the wind is almost parallel to road. An improved σ_z is expressed as:

$$\sigma_z = (a + b \cdot f(\theta) \cdot x)^c \quad (2-16)$$

where a , b and c are constants need to be determined and

$$f(\theta) = 1 + \beta |(\theta - 90^\circ)/90^\circ|^\gamma \quad (2-17)$$

where β and γ are to be determined by the least square sense, and θ is the angle between wind and road.

Hence, the GM model is used to predict the downwind dispersion of pollutants near the roadway which requires relatively simple calculations and is potentially more accurate than some other non-Gaussian models.

2.7.3 HIWAY model for highway air dispersion

The HIWAY model was developed by Zimmerman and Thompson in 1975. Later Chock (1977) pointed out that the EPA-HIWAY model has a shortage of overestimating the pollutant concentrations adjacent to the highway. Then Rao and Keenan (1980) made some improvements to the original HIWAY model.

The HIWAY line source dispersion model equation is expressed as follows:

$$C = \frac{\sqrt{2}}{\sqrt{\pi}} \frac{Q}{\bar{u} \sin \theta \sigma_z} \exp\left(-\frac{1}{2} \frac{Z^2}{\sigma_x^2}\right) \quad (2-18)$$

where C is the observed concentration; \bar{u} is the mean wind speed; θ is the angle between the directions of wind and road ($60^\circ \leq \theta \leq 90^\circ$); Z is the height of the receptor; and σ_z is the vertical diffusion parameter. At every receptor location, the Gaussian plume model assumes that σ_z is not a function of height and the wind is

uniform in the researched atmospheric layer. Past experimental results show that σ_z is affected by not only atmospheric stability but also the wind speeds crossing the road. Under low crossing wind speeds to the road, the plume spends a longer time on the way from the source region to a receptor. As a consequence, the local turbulence mechanism will act on the plume for a longer time and spread the plume wider than under higher wind speeds.

From the knowledge gained from the influence of the local turbulence over the naturally generated turbulence, the vertical dispersion parameter is defined as:

$$\sigma_z^2 = \sigma_{z_w}^2 + \sigma_{z_a}^2 \quad (2-19)$$

where σ_{z_w} and σ_{z_a} are the contributions from wake-induced turbulence and ambient turbulence, respectively. The contribution of the wake effects to the initial dispersion is given as:

$$\sigma_{z_w} = 3.57 - 0.53U_{\perp} \quad (2-20)$$

where U_{\perp} is the wind speed crossing the road.

Petersen (1980) released an improved version of the HIWAY model, namely HIWAY-2. The difference between the first and second versions is that the latter model gives lower but more realistic estimation on the pollutant concentration due to the improved dispersion algorithm as described by Sharma and Khare (2001).

2.7.4 CALINE model for highway air dispersion

The California State Department of Transportation (CalTrans) of USA has issued a series of CALINE models. The first dispersion model of line source for inert gaseous pollutants was issued in 1972. Model verification against the data from the field observations was inconclusive. Later in 1975, the original model was replaced by a second version, CALINE2 (Ward et al., 1977). The second model can be applied in a wider application range than the first version as verified by CalTrans. In 1979, the third version, CALINE3, was developed by Benson. This model was still based on Gaussian dispersion methodology but employed new vertical and horizontal dispersion curves variable to surface roughness, averaging time and turbulence induced by passing vehicle. In 1989, the fourth version, CALINE4 was also issued by CalTrans. It is still based on the Gaussian diffusion equation, but adopts a new concept of mixing zone to characterize pollutant dispersion over roadway.

In CALINE4 model, individual highway sections are considered as a series of elements with incremental concentrations, and then they are summed to a total estimated concentration for a particular receptor. The first element is in square shape with side length equal to highway width. Its location is determined by the angle θ between the directions of wind and roadway. For $\theta > 45^\circ$, the center of first element is located upwind of the receptor. For $\theta < 45^\circ$, the location of first element remains the same to its position at $\theta = 45^\circ$. This positional adjustment for first element has the advantage to achieve the smooth model response for receptors locating very near the link. Every element is considered as a finite line source (FLS) at the element midpoint and normal to wind direction.

Crosswind FLS Gaussian formula is applied to calculate the downwind concentrations from source elements as follows:

$$C = \frac{Qy}{2\pi\sigma_y\sigma_z u} \left[\exp\left(\frac{-y^2}{2\sigma_y^2}\right) \right] \left\{ \exp\left[\frac{-(z-H)^2}{2\sigma_z^2}\right] + \exp\left[\frac{-(z+H)^2}{2\sigma_z^2}\right] \right\} \quad (2-21)$$

where C is the concentration; y is the lateral distance between receptor and line source; Q is the strength of line source; u is wind speed; H is the height of source; and σ_y and σ_z are horizontal and vertical dispersion parameters, respectively.

More detailed review and insight on the generation and application of CALINE3 and CALINE4 models can be referred to Benson (1992) and Sharma (2004).

2.8 Research Development of Experimental Approaches for Vehicle Aerodynamics and Pollutant Dispersion

As moving vehicle in still ambient air ($U_w \leq 0.1$ m/s) or an equivalent reverse is a common situation in real traffic and an ideal case, it leads to many experiments that have been devoted to either laboratory or field studies. These experiments cover from the fundamental studies to the real world studies and build a solid knowledge base for establishing the present experimental study.

Baumer et al. (2005) developed and integrated the parameterisation of motorway-induced turbulence in a diffusion model to simulate the transport and the chemical reactions of air pollutants in the vicinity of a motorway as shown in Figure 2.8. Their findings show that two effects have to be taken into account for modeling. The first one is the production of turbulent kinetic energy by the

vehicles. The second one is the production of turbulent kinetic energy by the flow over the dam on which the motorway is located.

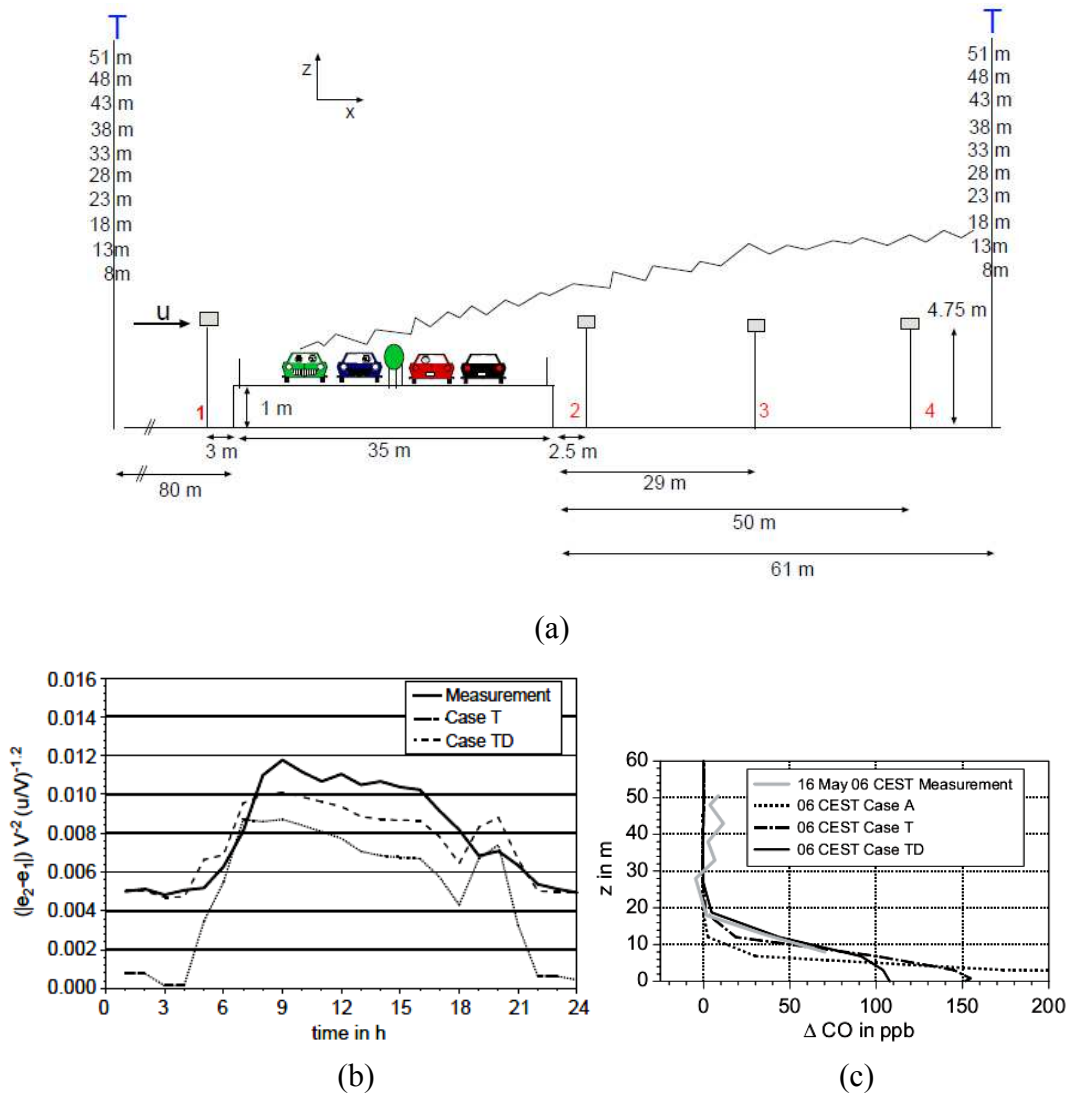


Figure 2.8 Determination of motorway-induced turbulence for (a) the experimental setup and measurement area; (b) the measured and simulated turbulent kinetic energy against time of a full day; (c) measured and simulated vertical profile of CO concentration downstream of the motorway during neutral thermal stratification (Baumer et al., 2005).

Kanda et al. (2006b) investigate the dispersion behavior of exhaust gas from a queue of passenger cars and small-size trucks by a reduced-scale wind tunnel as shown in Figure 2.9. They analyzed tracer gas concentrations and wake

fields, and found that the distribution of the mean and the fluctuation velocity fields conform to the exhaust-gas concentration field.

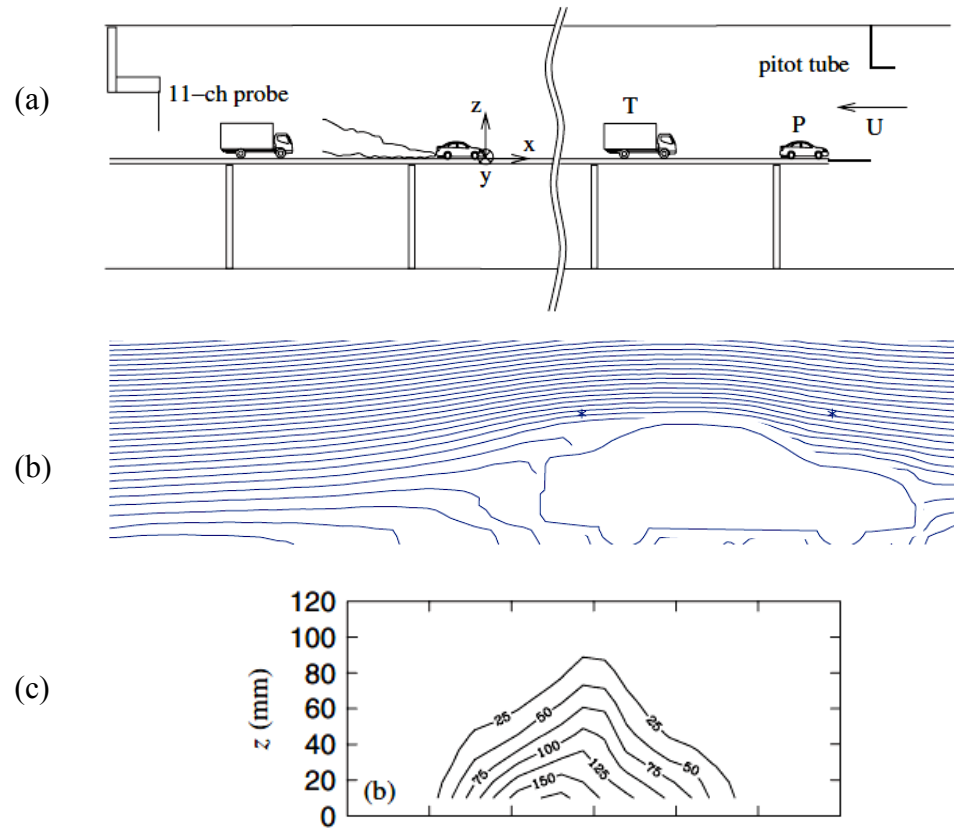


Figure 2.9 Wind tunnel experiments for the dilution of tailpipe emissions from different types of vehicle models for (a) the experimental setup inside a wind tunnel; (b) the flow streamlines around a vehicle; (c) the concentration contours in a cross-section plane behind the vehicle (Kanda et al. 2006b).

Chang et al. (2009a) studied the dilution ratios of tailpipe emissions using model vehicles representing a light-duty truck, a passenger car, and a heavy-duty tractor head in a wind tunnel as shown in Figure 2.10. They found that the vehicle shape strongly influences the flow fields and dilution profiles in the near-wake region but is much less important in the far-wake region.

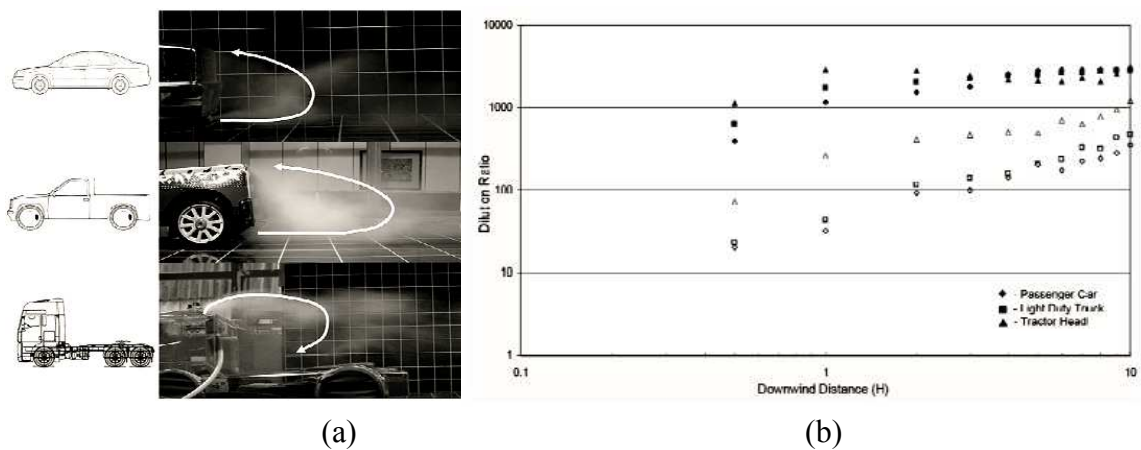


Figure 2.10 Wind tunnel experiments for the dilution of tailpipe emissions from different types of vehicle models for (a) the main flow behind the vehicle (white arrow); (b) the dilution rate along the downstream distance of vehicle (Chang et al. 2009a).

Gillierion et al. (2010) have recently presented that the static pressure distributions and skin friction line visualizations on both sides of the edge where the swirling structure was generated on the rear window of an Ahmed body for different slant angles. Their results have shown the influence of the slant angle on the swirling structure formation. The vortex bursting process can be promoted by small rear window angles. Typical friction line visualizations on the side of rear window of an Ahmed vehicle body with 25° rear slant angle inside a closed-circuit wind tunnel are shown in Figure 2.11.

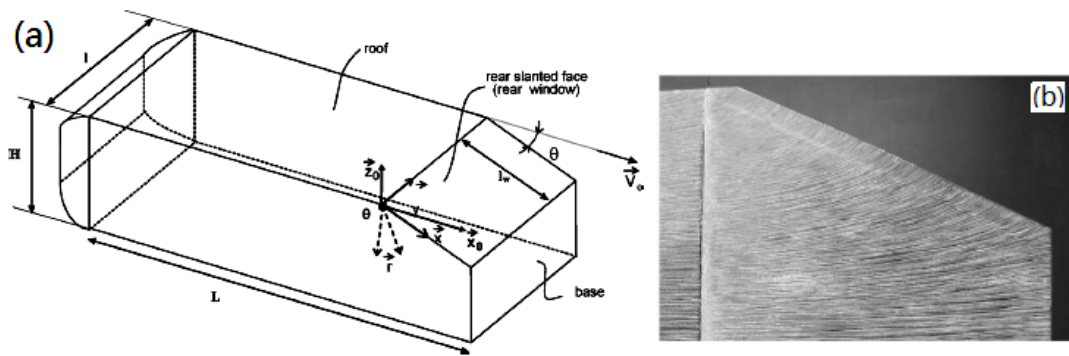
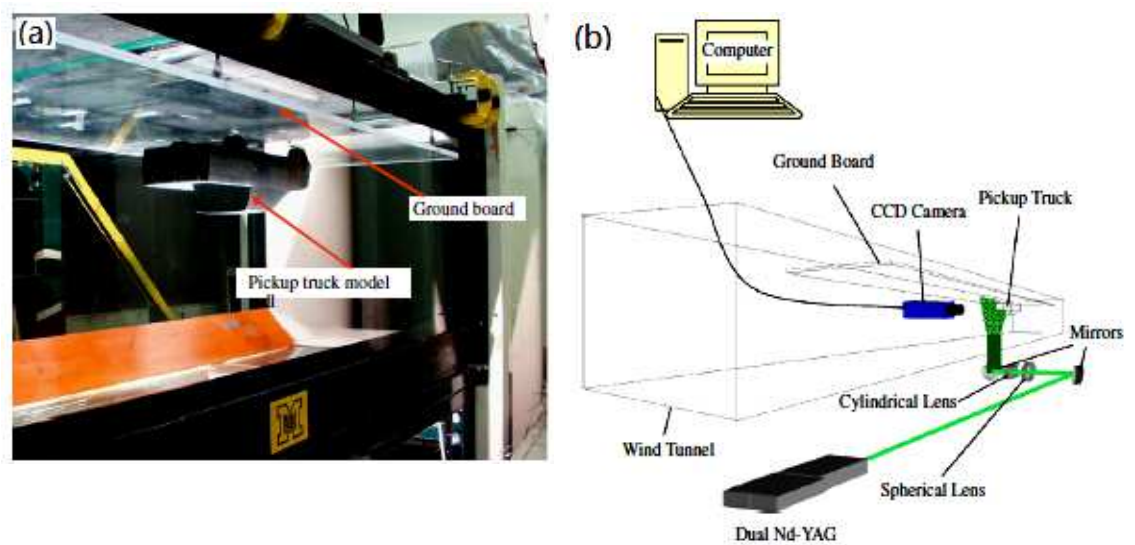


Figure 2.11 (a) A simplified Ahmed vehicle body with 25° rear slant angle for wind tunnel study; (b) the friction line visualizations on the side of rear window of vehicle body (Gillieron et al. 2010).

Al-Garni and Bernal (2010) experimentally studied the detailed flow field of a generic pickup truck using particle image velocimetry (PIV) as shown in Figures 2.12(a) and (b). Velocity field measurements of the near wake flow show a relatively quiet region behind the cab and no recirculating flow region in the symmetry plane behind the tailgate. Instead there is a strong downwash at the symmetry plane behind the tailgate (in Figure 2.12c), which is due to the existence of a pair of counter-rotating vortices downstream of the tailgate (Fig. 2.12d).



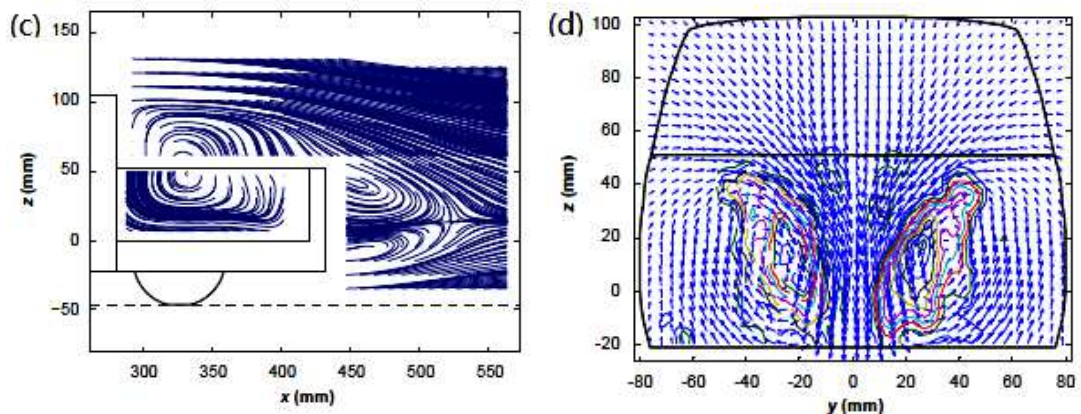


Figure 2.12 A wind tunnel experimental study of a pickup truck's near wake for (a) the truck model in wind tunnel; (b) the setup of flow measurement instruments; (c) the measured streamlines in the center plane of truck; (d) the flow vectors and vorticity map in a cross-section plane behind the truck (Al-Garni and Bernal, 2010).

Carpentieri and Kumar (2011) performed both ground-fixed and on-board measurements to obtain the number and size distributions of nanoparticles using a fast response differential mobility spectrometer in the wake of a diesel car running at different speeds as shown in Figure 2.13. The results were analysed to understand the dynamics, dispersion and transport of nanoparticle emissions in the wake of a moving vehicle. Results from their experimental datasets clearly confirm the presence of two separate groups of particles: (i) new particles, which are freshly emitted and come directly from the tailpipe and (ii) relatively aged particles, which are entrained within the recirculation vortices of the vehicle wake and reside there for a longer time. Immediately after exhaust plume emissions, the particle number concentrations and particle number distributions change rapidly due to nucleation processes driven by quickly increasing dilution. Then the complex interactions between the flow in vehicle wake and exhaust emissions start to affect the dispersion and transformation of nanoparticles.

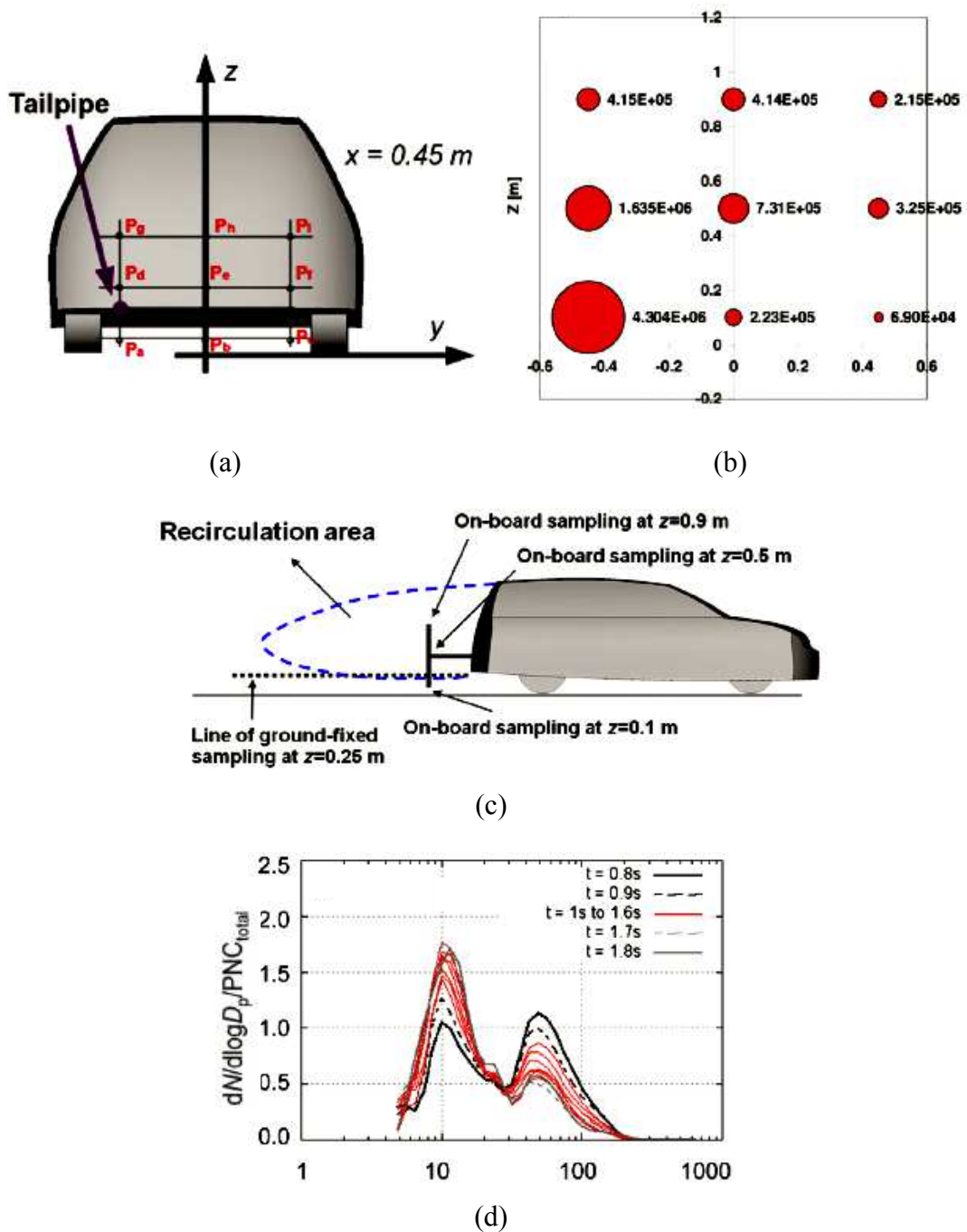
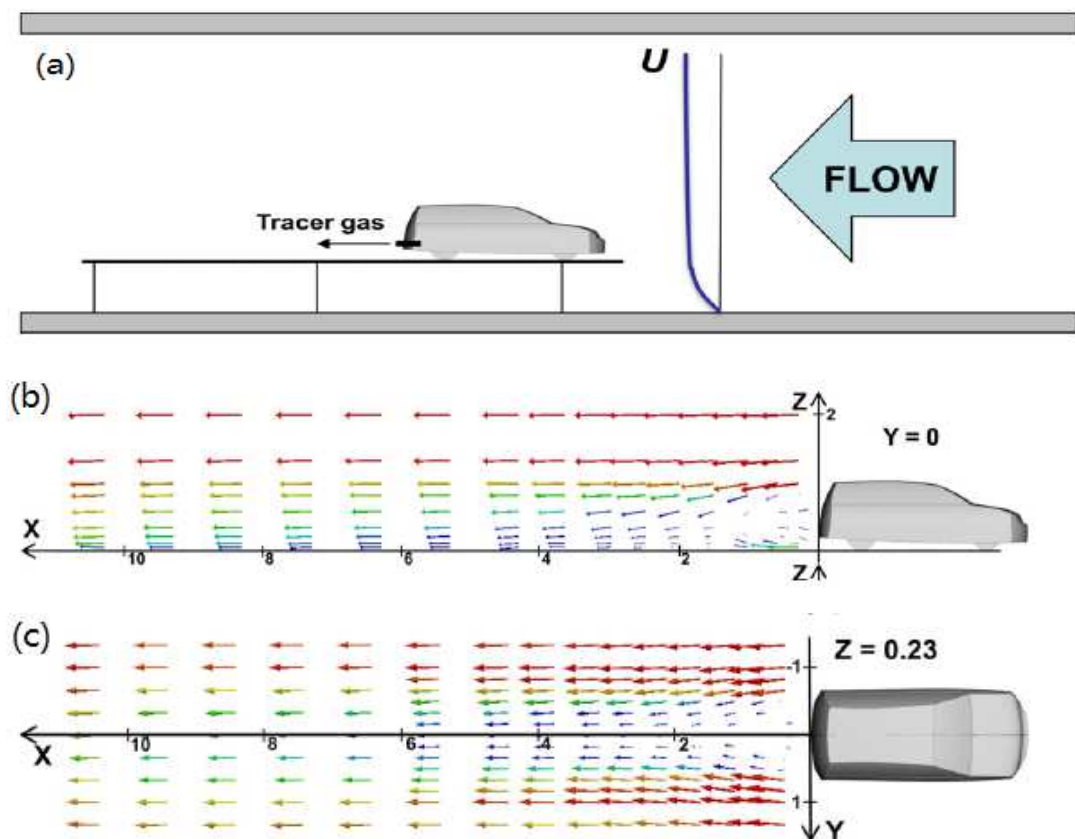


Figure 2.13 Measurement of nanoparticles in the wake of a moving vehicle at 20 km/h for (a) a map of on-board measurement points behind the vehicle; (b) the particle number concentrations at $x = 0.45$ m during the on-board measurement points; (c) the ground-fixed sampling measurements; (d) the normalized size distributions during evolution at $H = 0.1$ m (Carpentieri and Kumar, 2011).

Recently, Carpentieri et al. (2012) have performed wind tunnel measurements downwind of reduced scale car models to study the flow, turbulence and concentration fields in both near and far wake regions as shown in Figure 2.14. Experimental results were also compared with the estimates from two existing vehicle wake models. It was found that these models can adequately describe the far-wake of a vehicle in terms of velocities, but a better characterisation in terms of turbulence and pollutant dispersion is still needed. It was found that the parameterized models which are able to predict velocity and concentrations with fine enough details in near-wake region do not exist yet.



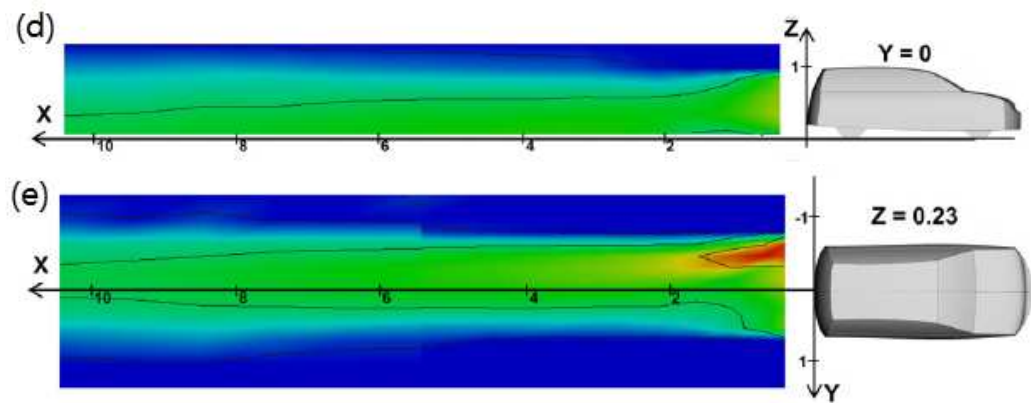


Figure 2.14 (a) A 1:8 scale vehicle model setup in a wind tunnel for (b) measured velocity vectors along the centerline of X - Z plane behind the vehicle using the laser Doppler anemometer (LDA); (c) measured velocity vectors on the vehicle's horizontal tailpipe plane; (d) measured tracer gas concentration distribution along the centerline of X - Z plane behind the vehicle using the fast response flame ionization detector (FFID); (e) measured tracer gas concentration distribution on the vehicle's horizontal tailpipe (Carpentieri et al., 2012).

Mathissen et al. (2012) have performed a trailer-based mobile measurement approach for analyzing non-exhaust particle emissions of a light duty vehicle as shown in Figure 2.15. They also estimated emission factors based on a tracer gas experiment in a wind tunnel which allowed a mapping of the particle dispersion within the wake of the vehicle, assuming that the particles and the tracer gas are dispersed equally. Such assumption was also adopted into the present study.



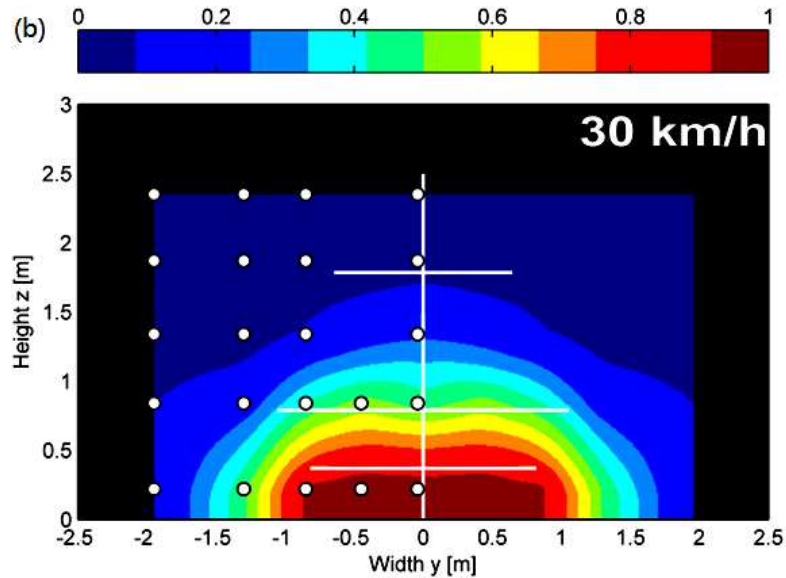


Figure 2.15(a) The background concentration on the top of a light duty vehicle using the DustTrak measurement for the incoming airflow in a wind tunnel; (b) the normalized tracer gas distribution measured behind the vehicle for 30 km/h using the chemiluminescence detectors (Mathissen et al., 2012).

Alonso-Estebanez et al. (2012) have also performed a traffic-induced turbulence analysis from a field campaign using ultrasonic anemometers deployed in a highway as shown in Figure 2.16. They found that both the turbulent momentum fluxes and the turbulent kinetic energy values correlated well with the vehicle speed for the lorry and the van, but not for the car where the turbulence produced is much lower. In Chapter 4, the two-dimensional vehicle wake generated by the lorry and van, and the three-dimensional vehicle wake generated by our studied vehicle, may help to explain their discrepancy.

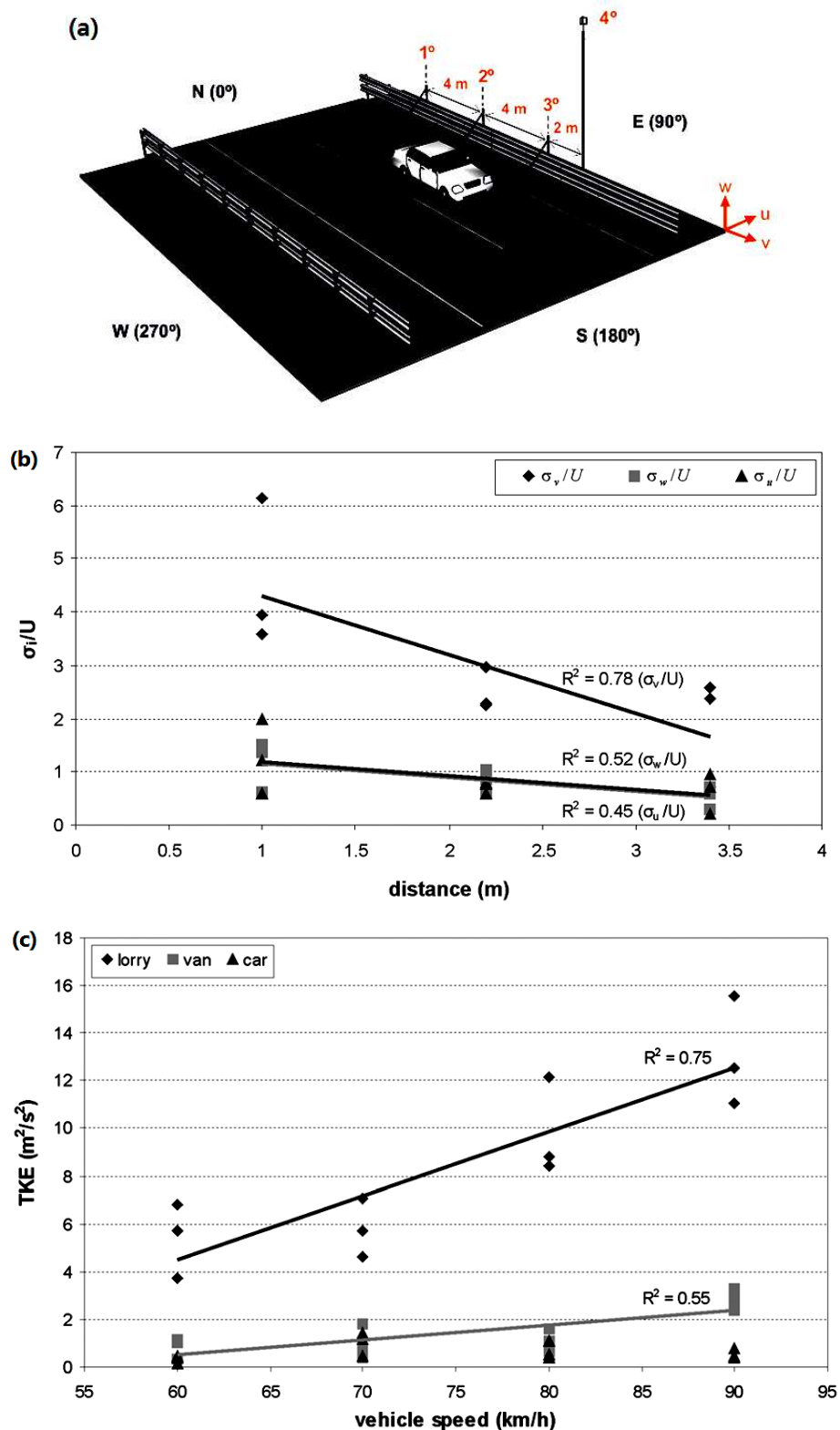


Figure 2.16 (a) Sketch of the experimental setup with the positions of four ultrasonic anemometers on the highway M-12; (b) the turbulence intensity components depending on downwind distance; (c) the turbulent kinetic energy depending on the vehicle speed for different kinds of vehicles (Alonso-Estebanez et al. 2012).

2.9 Summary of Literature Review

Relevant technical information on the flow field and exhaust pollutant dispersion generated by vehicle are reviewed in this chapter. The above-mentioned literatures shed light on the flow field, and vehicle exhaust pollutant dispersion and concentration, provide insights from different aspects research methodologies (e.g. field measurements, wind tunnel experiments and numerical modeling approaches), and establish a solid foundation for our understanding of the basic physical processes which are of primary concern.

A lot of wind tunnel experiments have been performed and contributed a large portion of our understanding of the air flow around a moving single vehicle. On the contrary, the acquired information about a queue of vehicles is disproportionately insufficient. In mega/urban cities, the traffic congestion conditions of the vehicles waiting in long or short queues frequently occur. The understanding about the basic physical processes that took place as a result of the vehicle queue effect on the characteristics of air flow, and exhaust scalar dispersion and distribution fields in the vehicle wake is still insufficient and the scientific knowledge gap needs to be filled.

Chapter 3 Experimental Methodology

3.1 Introduction

In the present study, how the air flow structure and exhaust heat (i.e. scalar) dispersion and distribution fields behind the vehicle are, and how they can be altered by a queue of the preceding vehicle(s) will be investigated. For this research purpose, three scaled down model vehicles categorized into two rear slant angle groups (i.e., $\alpha = 25^\circ$ and 60°) according to the characteristics of vehicle wake formation were placed in a closed circuit wind tunnel for well controlled study environment. Two- or three-dimensional flow velocity components and air temperature distributions for the selected representative planes in front of and behind the last vehicle of each vehicle group will be measured.

3.2 Experimental Methodology of Simulating the Moving Ground Vehicle Conditions in a Wind Tunnel

Due to the complexities and difficulties of aerodynamic research, the fluid flow studies which are exposed to wind have heavily relied on the experimental investigations conducted in wind tunnel rather than in fields to acquire reliable databases. These fluid flow studies range from buildings and bridges to moving ground vehicles, trains, vessels, aircrafts and rockets etc. In real life, on-road moving ground vehicle conditions are difficult to control, regulate and repeat. The effect of natural wind and vehicle(s) induced turbulences on the exhaust pollutant dispersion of moving ground vehicles cannot be separated easily (Clifford et al. 1997). These problems bring difficulties to the induction of physical phenomena. Therefore, the queue effect of vehicles on the flow structures, and scalar

(i.e., pollutant) dispersion and distribution fields in the vehicle wake will be performed in a closed circuit wind tunnel under well controlled environment to avoid the disadvantages of field studies (Chan et al., 2008b; Huang et al., 2009a and 2009b). The wind tunnel is a facility to reverse the usual movement relationship: contrary to that the air stays still and the object moves at a speed in still air, the object stays still and the air moves at a certain speed passing the object, with the presumption that the same aerodynamic phenomena would happen. Therefore, the stationary observers can easily study the still object which is “running in air”, and the instruments can easily measure the aerodynamic phenomena on or around the object. Compared with open circuit wind tunnel, the closed circuit wind tunnel has the benefits of low level of background noise, negligible intervention with laboratory air, and some testing materials can be recycled within duct thus lower supply rate and less consumption quantity are required for experiments. Because some of the flow measurements for the present study would require certain density of seeding particles which is difficult to maintain in an open circuit wind tunnel, the last merit of closed circuit wind tunnel is essential. Figure 3.1 shows the closed circuit wind tunnel facility used for the present study which is located at the Department of Mechanical Engineering, The Hong Kong Polytechnic University (Wang et al. 2004 ; Wang et al. 2005; Huang et al. 2006; Choy et al. 2007; Chan et al. 2008; Huang et al. 2009; Zhou et al. 2010; Alam et al. 2011).



Figure 3.1 Closed circuit wind tunnel facility used for the present research. The circled yellow rectangular frames with transparent acrylic walls are the test section.

The air inside this closed circuit wind tunnel facility is blown or sucked by the rotating fans through a duct which is equipped with a test section where the test model(s) is/are mounted for the study. The air flow driven by the fans is normally high turbulent flow before entering the test section due to the motion of fan blades. The high turbulence is disadvantageous for many accurate flow measurements which require low turbulent and laminar air flow. In order to minimize this turbulence problem, narrow air channels are often used between fans and test section to smooth down the turbulent air flow before it reaches the test section. At the upper left part of Figure 3.1, the white rectangular section lying above the red frames contains the fan blades and driving motor whose rotation speed is adjustable from the motor controller via the frequency inverter. The white rectangular fan section is the section of narrow air channels in gray color.



Figure 3.2 A driving fan for wind tunnel facility (<http://www.nimr.org/systems/images/pwt.html>).

This closed circuit wind tunnel has an effective velocity range between 0.2 and 55 m/s, and a test section of $0.6 \times 0.6 \times 2$ m (Width \times Height \times Length) enclosed by smooth acrylic plates with a wall thickness of 10 mm. Background turbulence intensity was measured by a hot-wire anemometer around 0.5% over the middle point of flat plate for the free stream velocities, $U_\infty = 8.3$ m/s (Huang et al. 2006 and 2009a).

3.3 Studied Model Vehicles

For easier comparison and continual research development, the studied model vehicles are in exactly the same shape and dimension of a 1/22 scaled-down light duty vehicle used in Chan et al. (2008a and 2008b) and Huang et al. (2009a and 2009b). The bodies of the vehicles were all made of smooth acrylic plates with a 5 mm thickness. The front and body of all studied vehicles are of the same shape, but have different vehicle rear slant angles because previous studies indicated that the structure of wake flow is mainly determined by the vehicle rear other than its vehicle front and body (Ahmed 1981, Ahmed et al. 1984). The dimensions of the

vehicle body (i.e., $W \times H \times L = 90 \times 81 \times 180$ mm) have a rear slant angle, $\alpha = 25^\circ$ or 60° as shown in Figure 3.3(a). The identical vehicle for $\alpha = 25^\circ$ or 60° was used in Chan et al. (2008b) for investigating the interaction of the vehicular exhaust jet plume on flow structures, and scalar (i.e., pollutant) dispersion and distribution fields in the wake of a single vehicle. The vehicular exhaust tailpipe pollutant concentration of on-road vehicle was simulated by using a heated air jet at certain temperature and velocity through a small tailpipe exit of 3 mm in diameter from the vehicle. The vehicular exhaust tailpipe exit was located at the vehicle rear (i.e., $X/H = 0$, $Y/H = 0.278$, $Z/H = 0.22$) as shown in Figure 3.3(b). Two studied rear slant angle categories are either smaller or larger than the critical angle 30° . Hence it is expected to generate two categories of vehicle wake, namely a complex three-dimensional wake flow with $\alpha = 25^\circ$ and a relatively simple two-dimensional wake flow with $\alpha = 60^\circ$ (Ahmed et al. 1984).

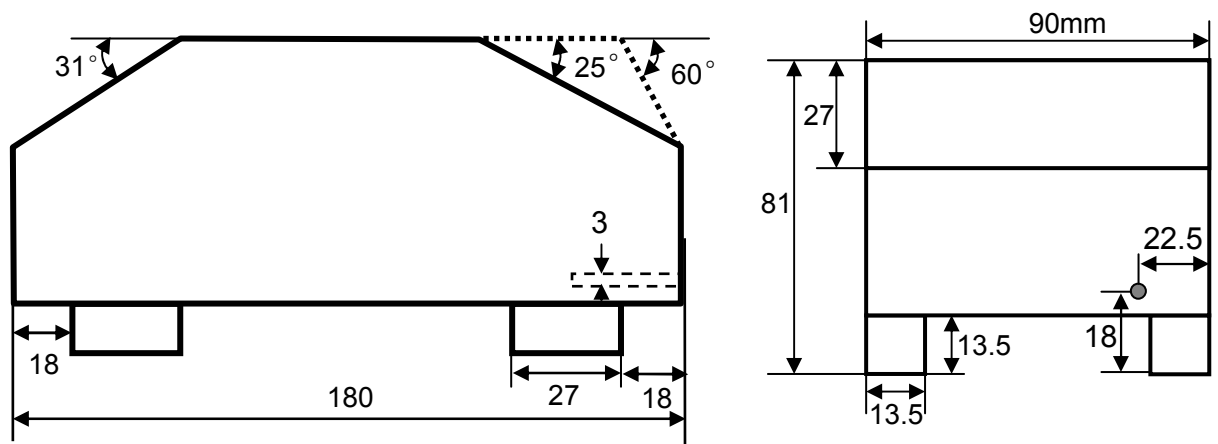


Figure 3.3(a) Schematic drawing of two types of scaled model vehicles, $\alpha = 25^\circ$ (vehicle **A**) or 60° (vehicle **B**) (in mm).

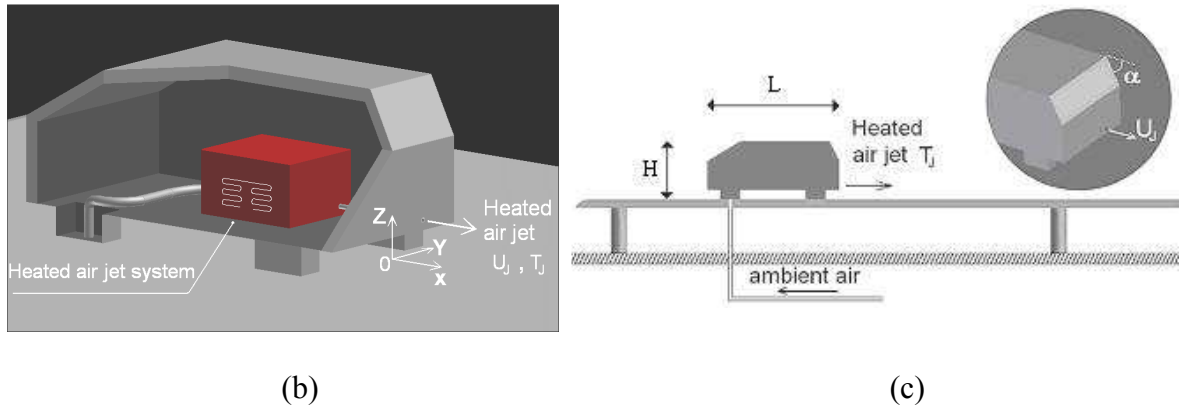


Figure 3.3(b) A heated air jet system of the model vehicle, V1 and (c) a single model vehicle setup inside the wind tunnel facility (Chan et al. 2008b).

For the experimental investigations conducted in a wind tunnel, the flow blockage induced by test models is one of the precautions for relatively large test models if they are placed in a wind tunnel due to the limited size of testing section. Blockage ratio is defined as the ratio of the cross-section of the test model to the cross-section of wind tunnel test section, $B = \frac{S_{\text{model}}}{S_{\text{tunnel}}}$ where S stands for the size of cross-section. Generally, the blockage ratio less than 7% is usually acceptable for engineering investigations or less than 5% for research investigations (Farell et al. 1977), otherwise the pressure distribution on test model surface will be severely distorted to alter flow pattern. In the present study, the blockage ratio induced by the model vehicle was 2%, which was well below the 5% research limit suggested by Farell et al. (1977), therefore no additional blockage correction is needed for the present study.

A single model vehicle or a queue of model vehicles was placed in-line on a designated horizontal $2000 \times 590 \times 20$ mm (Length \times Width \times Thickness) flat plate (Chan et al., 2008b) which was supported by six small stands of 130 mm in height

each on the bottom of the test section as shown in Figure 3.4. In the present study, three typical urban driving speeds of 10, 30 and 50 km/h (i.e., three free stream velocities, U_∞ of 2.78, 8.33 and 13.89 m/s in wind tunnel) were used. Their corresponding Reynolds numbers, $Re_H = U_\infty \times H / \nu$ were equal to 1.48×10^4 , 4.44×10^4 and 7.40×10^4 , respectively. For all queue of vehicle cases, the vehicle spacing between the rear of the preceding vehicle and the front of the following one was fixed to allow for 2 seconds of the vehicle movement (i.e. vehicle spacing = $U_\infty \times 2s$). The corresponding vehicle spacing was $3.1 H$, $9.3 H$ and $15.5 H$ in respect to the vehicle speeds of 10, 30 and 50 km/h, as shown in Figures 3.4(a) to (c). The origin point of Cartesian coordinate system was fixed on the ground of the designated flat plate under the center point of the rear side of vehicle No. 1 (hereafter referred to as V1). The X -axis was in the direction of main stream flow, Y -axis was in the direction of the width of the vehicle, and Z -axis was in the direction of the height of the vehicle. The velocities, U , V and W correspond to the velocity components in X , Y and Z directions, respectively.

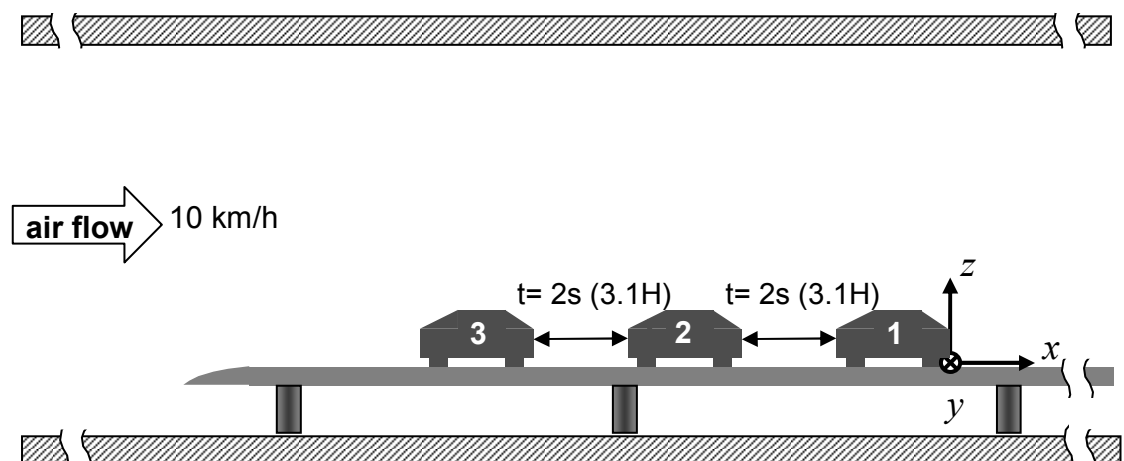


Figure 3.4(a) Experimental setup and coordinate system inside the wind tunnel facility for a three-vehicle queue arrangement at 10 km/h case (Not in scale).

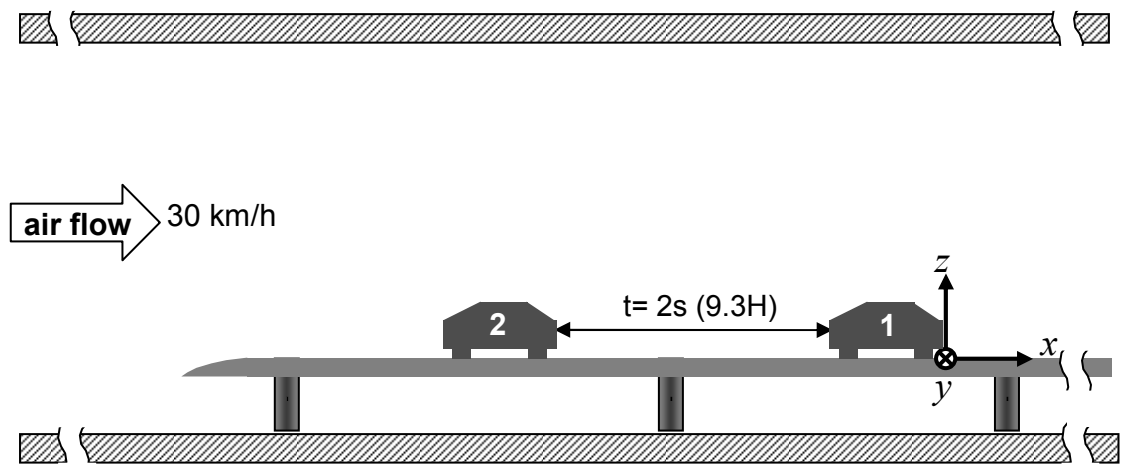


Figure 3.4(b) Experimental setup and coordinate system for a two-vehicle queue arrangement at 30 km/h case (Not in scale).

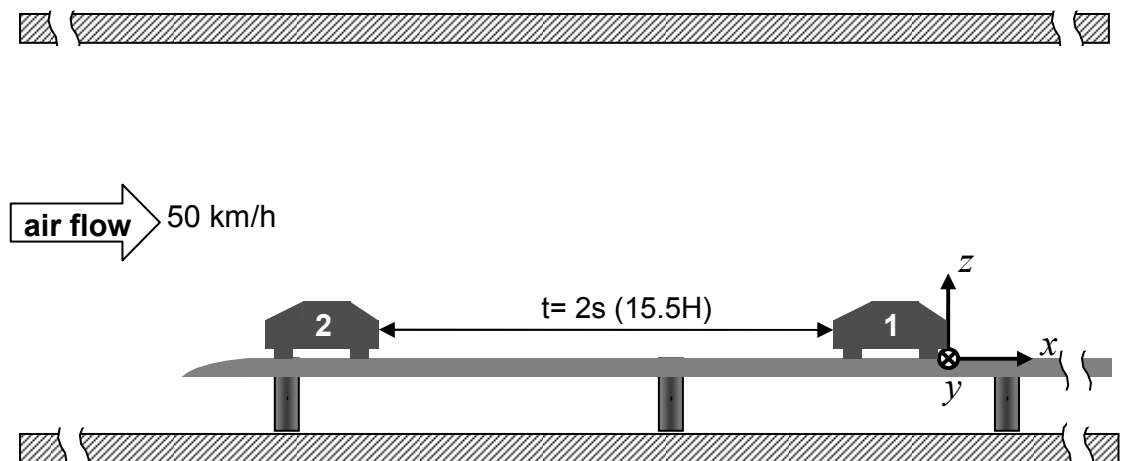


Figure 3.4(c) Experimental setup and coordinate system for a two-vehicle queue arrangement at 50 km/h case (Not in scale).

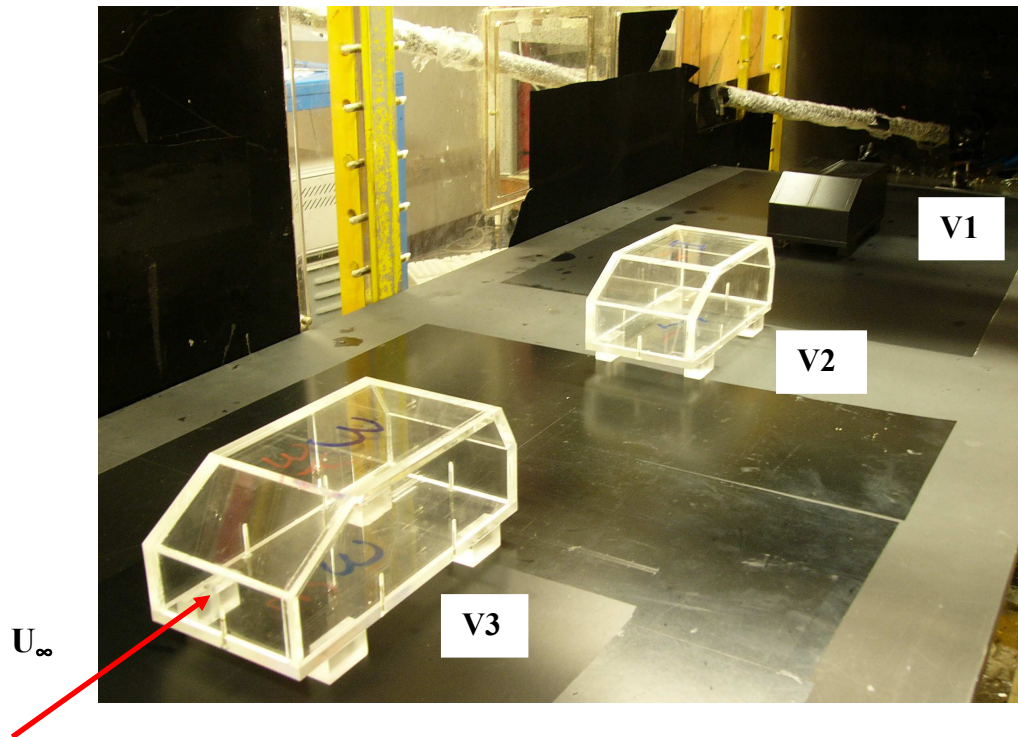


Figure 3.5 Photo of a queue of model vehicles (i.e. V1 to V3) which was placed in-line on the designated flat plate inside the test section for the three-vehicle queue arrangement at 10 km/h case.

One difference between the real road condition and wind tunnel simulation is the existence of a boundary layer over the ground for the latter case. If the ‘ground’ inside the wind tunnel does not move at the same speed as air flow, the boundary layer over ground will have two effects on experimental simulation: (i) the modification of the near-ground air flow structure; and (ii) the mixing of jet flow in the boundary layer (Krajnovic and Davidson 2005c). Lajos et al. (1986) compared the difference between the effects of a stationary “ground” and a moving “ground” for relatively high-profiled vehicles (e.g. a model bus) and found that the stagnation point of roll-up flow is lower for the latter case. However, Hackett et al (1987) used a model car to study the relative low-profiled vehicle and found that a moving “ground” has insignificant effects on the vehicle wake flow. Krajnovic and Davison (2005) found that the largest difference between the moving and

stationary ground effects for an Ahmed body with a rear slant angle, 25° does not occur in the wake region behind the vehicle rear but on the rear slant surface of the vehicle body. Similar insensitivity of vehicle wake to the ground motion was also observed by Bearman et al. (1989). Therefore, the wake flow of the vehicle(s) could be considered to be insensitive to the fixed ground and the relatively low-profiled model vehicle in the present study. The boundary layer over the designated flat plate is considered to have a minor effect on the experimental simulation of the studied regions. However, the shape of the leading edge of the flat plate (Chan et al., 2008b) was designed to reduce the thickness of boundary layer by delaying the flow separation according to the research work of Narasimha and Prasad (1994). The boundary layer at the center point of the flat plate was measured by a one-dimensional hot-wire probe at 8.33 m/s without placing the model vehicle. Figure 3.6 demonstrates that the thickness of boundary layer over the center of the flat plate was measured to be less than $0.1H$. Hence, it is considered to be acceptable for the present study of which the investigated area was up to the height of $Z = 2H$. Due to the existence of boundary layer on the flat plate, the measured data in the near-ground region (i.e., $Z \leq 0.1H$) should be examined with certain caution because they are more or less affected by the boundary layer. For other higher regions (i.e., $Z > 0.1H$), the measured data should not be affected at all.

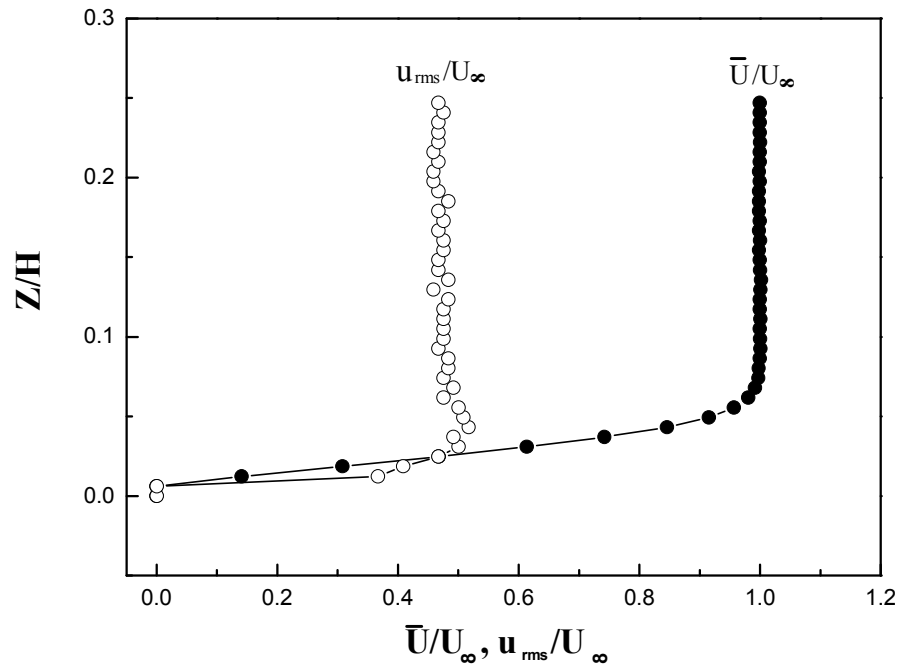


Figure 3.6 Measured boundary layer thickness over the center of the designated flat plate using the hot-wire anemometer.

3.4 Methodology of Using Particle Image Velocimetry (PIV) System for Flow Field Measurement

Particle image velocimetry (PIV) is an optical non-intrusive and a diagnostic technique providing a two-dimensional instantaneous velocity vector measurement for a flow region which is very suitable for the present study of flow structure. PIV has been widely used by many researchers, for example, Baroud et al. (2003) investigated the quasi-two-dimensional and three-dimensional rotating turbulent flows; Shridhar et al. (2004) studied the structure of a jet in a cross flow; Matsuda and Sakakibara (2005) investigated the vortical structure in a round jet; Geers et al. (2005) studied the coherent structures of multiple jets; Camussi and Felice (2006) investigated the vortical structures in turbulent boundary layers; Ganapathisubramani et al. (2006) investigated the vortex properties in a turbulent boundary layer; Recktenwald et al. (2007) studied the

rotating turbulent channel flow; Casarsa and Giannattasio (2008) studied a three-dimensional turbulent sudden expansion flow; Amatya and Longmire (2010) measured simultaneously the velocity and deformation in flows through diaphragms; Feng et al. (2010) studied the effect of synthetic jet on wake vortex shedding modes of a circular cylinder; Singha and Balachandar (2011) investigated the wake structure of a sharp-edged bluff body in a channel flow; Pino et al. (2011) studied the structure of bluff body trailing vortices and compared with the theoretical models; Mouhammad et al. (2011) investigated the flow in the near-field of a cross-shaped orifice jet etc. A typical experimental setup of using PIV and test model in wind tunnel is shown in Figure 3.7.

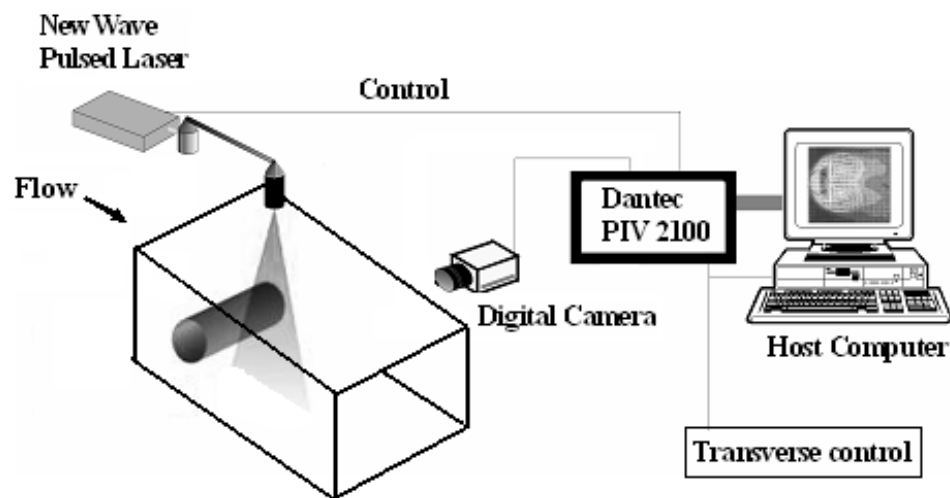


Figure 3.7 Schematic drawing for a typical experimental setup using PIV and test model in wind tunnel (Dantec Dynamics A/S, 2008).

The working principle of PIV is simple. It determines the velocity components by tracing the movement of small and light seeding particles which are dispersed into air. PIV measures the displacement, ΔX in X -axis of a moving particle between two consecutive camera images that were taken with a pre-set

interval, Δt . Then one air velocity component, U can be calculated by the equation,

$$U = \frac{\Delta X}{\Delta t} \quad \text{which does likewise for another air velocity component, } V = \frac{\Delta Y}{\Delta t} .$$

Thus the two velocity components of this particle can be determined. Based on the assumption that the small and light particle is moving along with the air flow stream, the velocity components of a particle can be considered as the velocity components of local air flow.

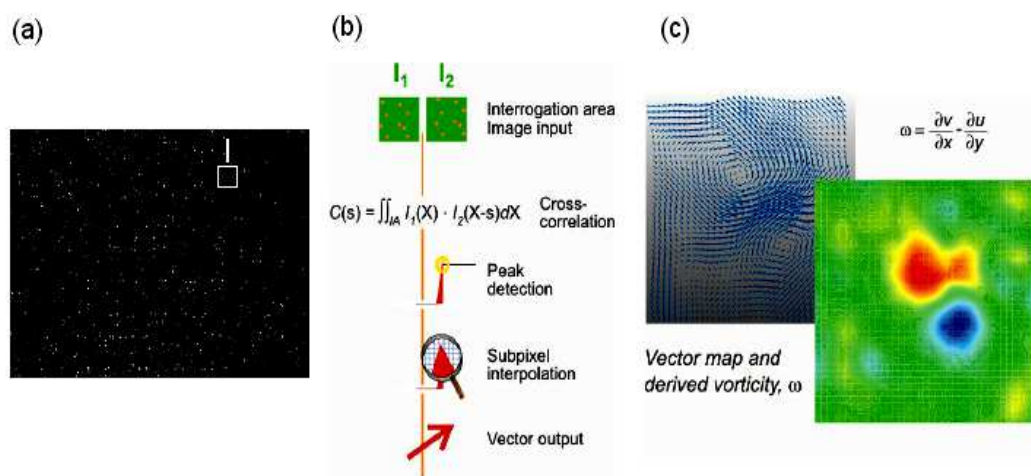


Figure 3.8 Working principle of PIV (a) one of the two captured images for the seeding particles in air flow is shown. A random interrogation area in frame I, is then marked out by a small white frame; (b) cross-correlation is applied to extract a vector from interrogation area I of the two particle images; (c) vector map and derived vorticity map are generated for the whole captured air field by repeating the sub-section cross-correlation for the full image frame (Dantec Dynamics A/S, 2008).

A set of PIV instrument purchased from the Dantec Dynamics A/S was used for determining two-dimensional velocity components of air flow in the present study. The studied flow field was filled with small seeding particles at a concentration density of around 0.1% to attain a good imaging density as shown in Figure 3.8(a). Large particles are relatively too heavy to exactly follow air flow stream due to their large inertial force and will induce considerable disagreement

between the velocity of a particle and the velocity of local air flow. But if particles are too small they are almost invisible to the CCD (charge coupled device) camera. For the present study, a smoke generator, Safex 2010 model was used to yield smoke particles with a mean diameter of $0.3 \mu\text{m}$ for PIV seeding. Particles of this size can well follow local air flow and leave clear images on CCD camera's frame records. Then the flow in the studied area is illuminated twice with the preset time interval, Δt by the laser light sheets. A CCD camera is able to capture the reflection light from the studied area twice in the separate image frames. Once a sequence of two light pulses is recorded, the images are divided into the small sub-sections called interrogation areas. The interrogation areas from each image frame, I_1 and I_2 are cross-correlated with each other pixel by pixel. The correlation produces a peak signal, and identify the particle displacement, ΔX and ΔY . An accurate measured displacement is achieved with a sub-pixel interpolation. A velocity vector map over the whole target flow area is then obtained by repeating the cross-correlation for each interrogation area over the two image frames captured by the CCD camera. Figures 3.9(a) to (d) show the actual PIV arrangement with the present wind tunnel facility.



Figure 3.9(a) Laser and optical arm used to deliver the light sheet into the wind tunnel for the illumination of seeding particles.



Figure 3.9(b) A CCD camera was placed outside the test section of wind tunnel to capture the images of a two-dimensional flow field around the last vehicle, V1 (enclosed by the white circle) which was painted in black to minimize its noise laser reflection.

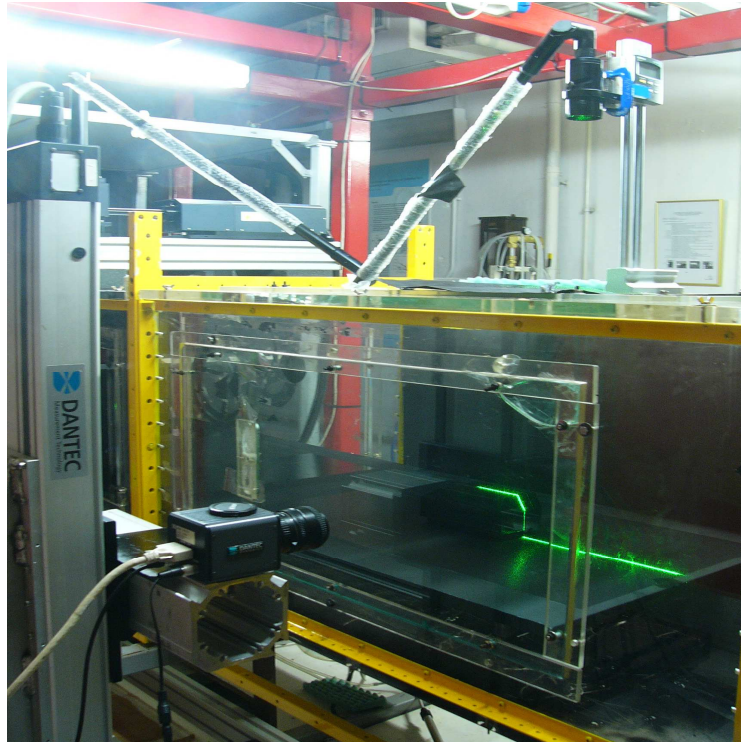


Figure 3.9(c) Triangular laser light sheet was vertically shot down from laser arm to illuminate the flow field for the image capture of CCD camera.



Figure 3.9(d) Safex 2010 smoke generator and its particle exit nozzle. The nozzle was inserted into the closed circuit wind tunnel through a hole on wall to inject the seeding particles into air flow.

In practice, the determination of Δt between two light pulses is a critical issue for the successful PIV acquisitions. The Δt should be neither too long that the particle displacement, ΔX is too large often resulting in a low

cross-correlation value, nor too short that the particle displacement, ΔX is so small that the error of ΔX determination becomes comparable. As suggested by the PIV user manual of Dantec Dynamics, the ideal range of ΔX should be around 6-10 pixels long. Therefore, the Δt can be estimated by $\Delta t = \frac{\Delta X}{U}$ where U is the velocity component in X -direction. PIV processor which is named as Flowmap System Hub in the current PIV system will accordingly generate two electronic pulse signals to trigger two laser light pulses with the time interval, Δt . When sending to trigger signals to laser for flash, the Flowmap System Hub will also send them to CCD camera to open shutter to capture images simultaneously as shown in Figures 3.10(a) and (b).

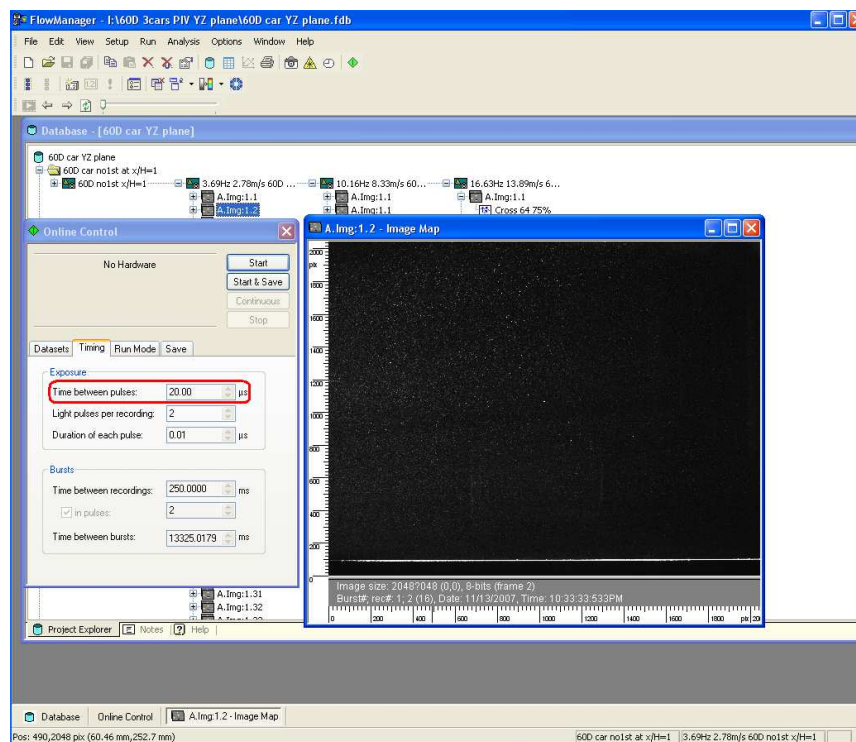


Figure 3.10(a) Pre-set of time interval, Δt in PIV control software (inside red frame).

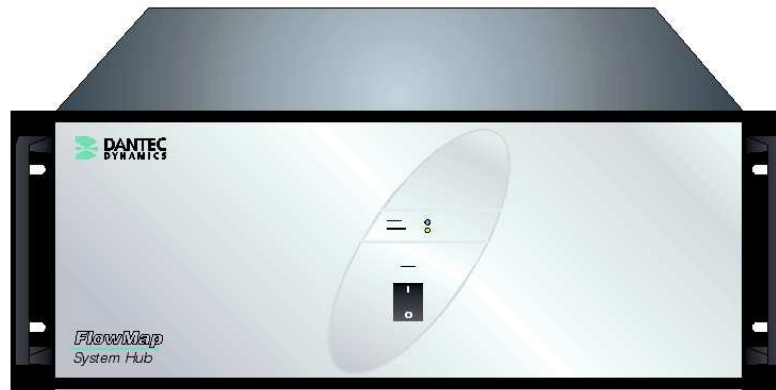


Figure 3.10(b) Dantec Dynamics' FlowMap System Hub (Dantec Dynamics A/S, 2008).

The PIV system manufactured by the Dantec Dynamics has a dual-cavity 200 mJ Nd-YAG laser to illuminate the studied flow field, and a double-image HiSense 4M CCD camera (2048×2048 pixels) was used to shoot the illuminated flow areas which were seeded by smoke particles with a mean diameter of around $0.3\mu\text{m}$ produced by Safex 2010 smoke generator. The double images captured by the CCD camera were stored in the computer for later cross-correlation analysis in order to determine the velocity vectors. The 32×32 pixels and 50% overlap cross-correlation arithmetic were applied to every pair of stored images to yield $127 \times 127 = 16,129$ vectors for each captured flow field. As the area of the camera's field of view was maintained to be $3H \times 3H$ (i.e., $H = 81$ mm), therefore the spatial resolution of vector was $3H/127 = 0.0236H$ (i.e., 1.913 mm for vector spacing). All investigated PIV planes were positioned either in front of or behind the model vehicle (i.e., Vehicle 1) as an example in Figure 3.9(c). If there is no preceding vehicle (i.e., Vehicle 1, V1), it will be considered as one-vehicle case. When other model vehicles (i.e., only the preceding vehicle No. 2, V2 or both preceding vehicles Nos. 2 and 3, V2 and V3 are taken into consideration by arranging one by

one in the upstream region, in that case V1 will be acting as the second or third vehicle in a traffic queue of multiple vehicles. For all measurements taken at the same target area, no further position adjustment of instrument is needed to cover the arrangements of these three vehicle queue cases (i.e., one-, two- and three-vehicle cases), therefore it would still maintain a high repetition accuracy for the studied cross-sectional flow fields.

Because there are often noise signals in the camera images such as the reflection light from objects other than the seeding particles, for example either the bright line on the top of the vehicle or the black shadow beneath as shown in Figure 3.11(a), certain measures should be taken to filter out the false velocity vectors generated from these noise signals. Range validation is often adopted to remove false vectors which have abnormal magnitude as long as the velocity of main stream is known. In the present study, a valid range for velocity is set e.g. $-3 \sim +3$ m/s. Any velocity outside this validation range will be considered as false velocity vector. The second correction step is the validation of moving average to filter out vectors which have abnormal moving directions. This is done by comparing a vector's direction with all its surrounding vectors. If the direction is too different from its surroundings, this vector will be considered as a false one, based on the continuity presumption of fluid. After the above correction steps are taken, the vector map can be considered as of good quality and can be used for the present study (FlowMap System Hub PIV User Manual from Dantec Dynamics A/S).

Figures 3.11(a) to (c) show a normal routine of PIV image processing step by step to illustrate how to understand the studied flow field from a pair of dotted

images. It should be noted that all these processing steps are based on a pair of clean and clear images and a proper choice of Δt between two light pulses, otherwise the same processing routine may generate meaningless results from the poor quality of the captured images.

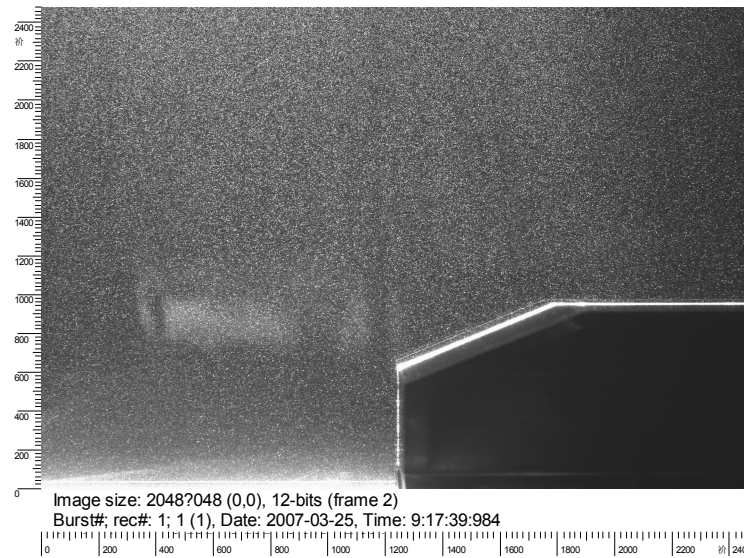


Figure 3.11(a) A captured PIV image for the air flow around the vehicle front. The air flow is filled with smoke particles which are illuminated as the white dots by a laser sheet.

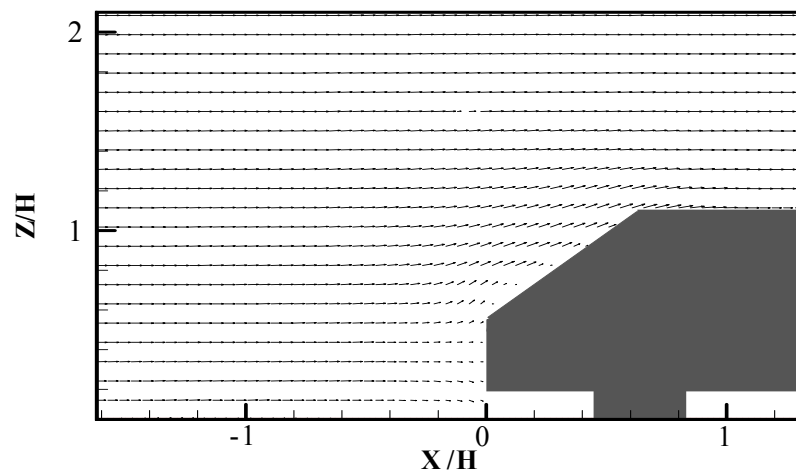


Figure 3.11(b) Vector map generated from Figure 3.11(a) by a cross-correlation of 32×32 pixels with 50% overlap and an afterward validation. For the region under vehicle body, it is blank because down-shooting laser light cannot reach it.

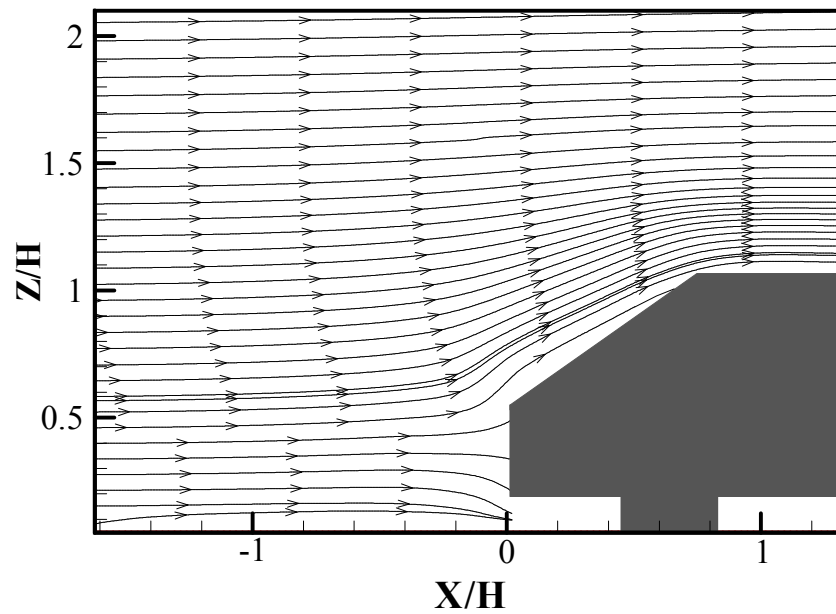


Figure 3.11(c) Streamline derived from the vector map of Figure 3.11(b) to illustrate the flow path around the vehicle front. For the region under vehicle body, it is blank because down-shooting laser light cannot reach it.

Figures 3.12(a) to (d) show another normal routine of PIV image processing step by step. It should be noted that for one-vehicle, two-vehicle and three-vehicle cases, their induced difference in air flow is more prominent for presenting in the vorticity contour as shown in Figure 3.12(d) than the vector map of Figure 3.12(b) and the streamline of Figure 3.12(c) therefore the experimental results of vorticity contours will be the main focus in Chapter 4.

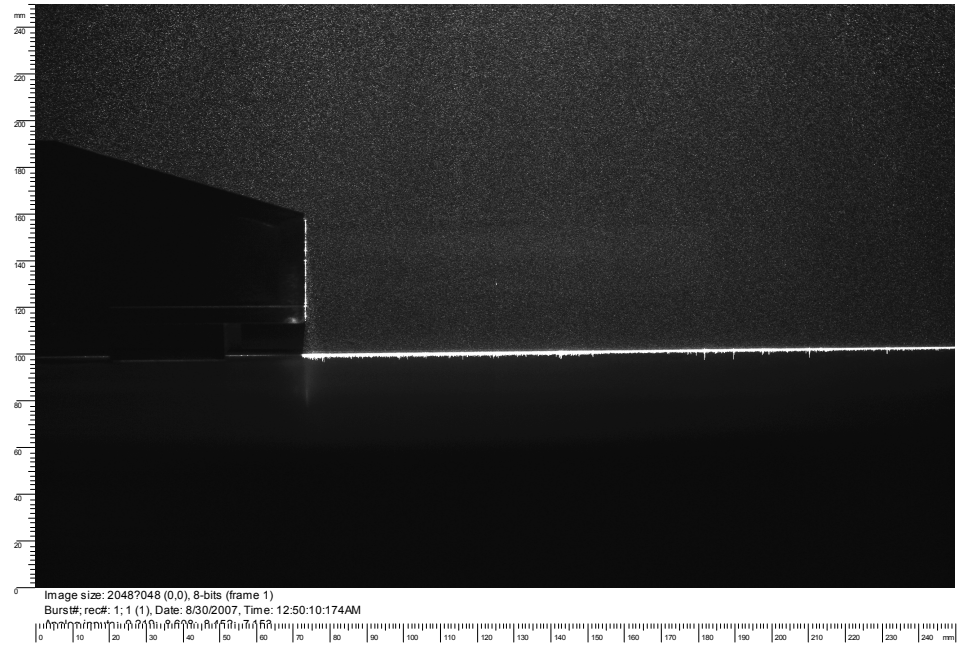


Figure 3.12(a) A captured PIV image for the air flow around the vehicle rear.

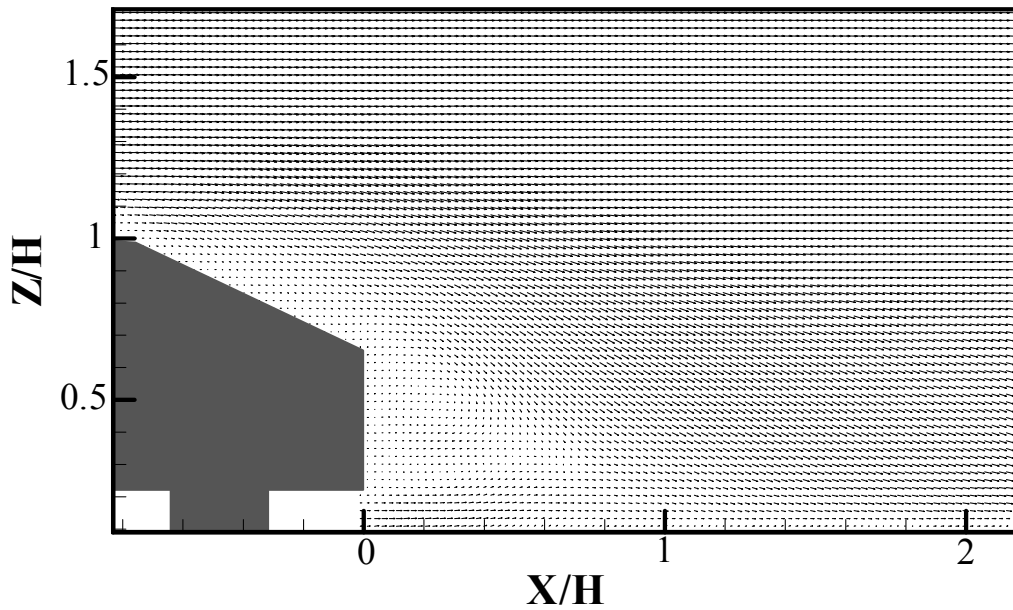


Figure 3.12(b) Vector map generated from Figure 3.12 (a) by a cross-correlation of 32×32 pixels with 50% overlap and an afterward validation.

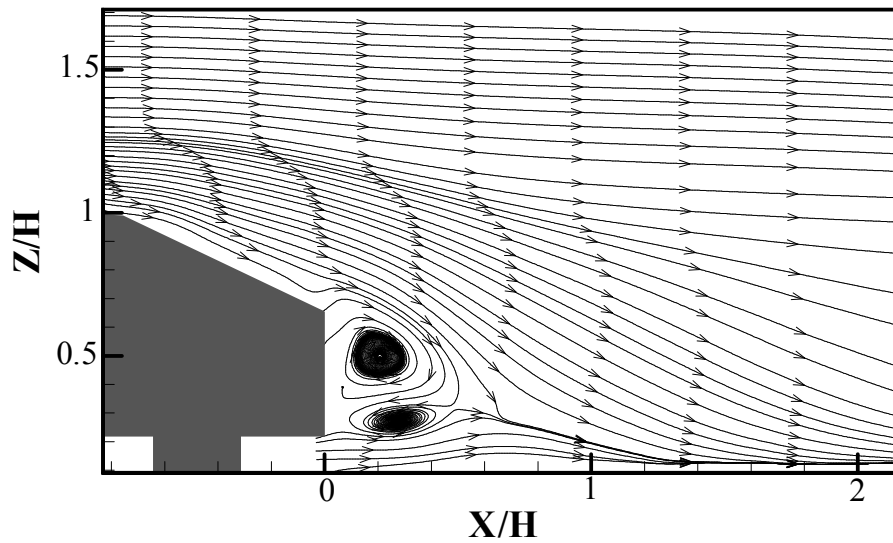


Figure 3.12(c) Streamline can be derived from the vector map of Figure 3.12(b) to depict the flow path around the vehicle rear.

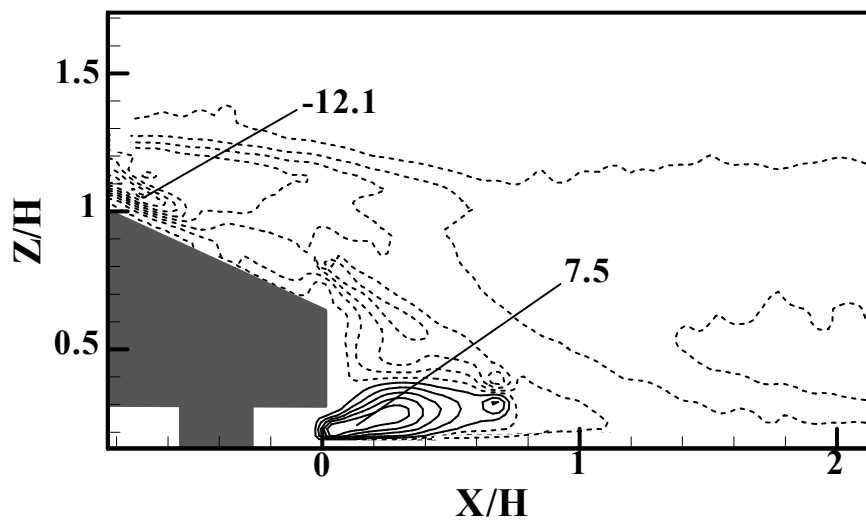


Figure 3.12(d) Vorticity map can be derived from the vector map of Figure 3.12(b) to depict the flow structure around the vehicle rear.

Figure 3.13 shows the comparison of time-averaged streamlines between the present experimental study and the LES study (Krajnovic and Davidson 2005a) for one-vehicle ($\alpha = 25^\circ$) case. Despite the Reynolds number difference (i.e., $Re_H = 1.48 \times 10^4$ for the present experimental study and $Re_H = 2.0 \times 10^5$ for LES

study), they both show close similarity between two interesting regions in length, X_{SL} and X_{NW} as shown in Figures 3.13(a) and (b). It should be noted that X_{NW} is the length of the near-wake separation bubble and X_{SL} is the length between flow separation and reattachment. This similarity rationalizes that both studies reveal the same flow phenomenon because the possibility of random overlap of these two interesting regions in length is very slim. Hence, it is quite certain that both figures correctly reveal the real flow patterns behind a single vehicle. The present study was further extended from a single vehicle to a queue of vehicles.

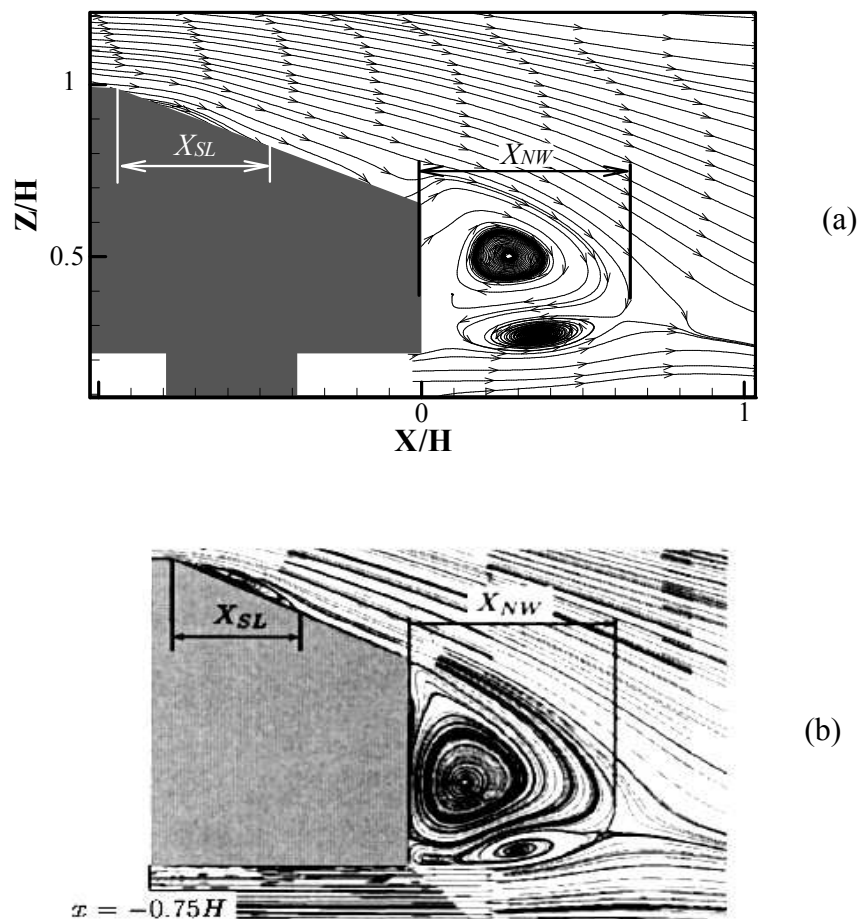


Figure 3.13 Time-averaged streamlines in X - Z plane for one-vehicle ($\alpha = 25^\circ$) case (a) from the present experimental study and (b) from LES study (Figure 4(b) of Krajnovic and Davidson (2005a)).

3.5 Methodology of Simulating the Vehicular Exhaust Tailpipe Conditions in a Wind Tunnel

The vehicular exhaust tailpipe pollutant concentration of on-road vehicle was simulated using a heated air jet at certain temperature T_j and velocity U_j through a small tailpipe exit (diameter $d = 3\text{mm}$) for the model vehicle. The exhaust tailpipe exit was located on the rear side of vehicle (i.e., $X/H = 0$, $Y/H = 0.278$, $Z/H = 0.22$) as shown in Figure 3.3(a). In order to avoid the possible perturbation of the flow by the heated air injection system, the ambient air tube was inserted through the left front tire of vehicle and connected to the heating element device and produced the necessary hot air jet exit condition as shown in Figure 3.3(c). The temperature difference between the potential core of the heated air jet, T_j and the wind tunnel background temperature, T_∞ was maintained constantly using a dedicated temperature feedback control system (Chan et al. 2008b). The heating element device was placed inside the vehicle as shown in Figure 3.3(b). The studied parameters of vehicle conditions were summarized in Table 3.1, which shows the exit conditions of a vehicular exhaust tailpipe from a typical on-road light-duty diesel vehicle of the exhaust tailpipe diameter, $D = 0.054\text{ m}$ for different driving modes.

In order to study the effect of the vehicular exhaust tailpipe exit conditions for different driving modes, the experiments were performed based on the different exhaust gas flow rates from these two model vehicles **A** and **B**.

As described by Kanda et al. (2006), the exit jet velocity, U_j could not be directly linked to its Reynolds number, Re_j :

$$Re_j = \frac{U_{j(\text{real vehicle})} \times D}{\nu_{\text{exhaust gas}}} = \frac{U_{j(\text{model vehicle})} \times d}{\nu_{\text{hot air}}} \quad (3-1)$$

$$U_{j(\text{model vehicle})} = \frac{\nu_{\text{hot air}}}{\nu_{\text{exhaust gas}}} \left(\frac{D}{d} \right) U_{j(\text{real vehicle})} \quad (3-2)$$

For example, if the driving mode of a real world on-road vehicle is 30 km/h, then the respective vehicular tailpipe exit jet velocity for the model vehicle would be equal to $U_{j(\text{model vehicle})} = 98$ m/s which is too high.

The exit jet velocity, U_j of the scale-model was then determined by the conservation of the mass flow rates from the vehicular exhaust tailpipe conditions of the real and scale-model vehicles as follows:

$$\frac{\dot{m}_{j(\text{real vehicle})}}{\dot{m}_{\text{real vehicle}}} = \frac{\dot{m}_{j(\text{model vehicle})}}{\dot{m}_{\text{model vehicle}}} \quad (3-3)$$

where the real vehicle's exhaust tailpipe mass rate $\dot{m}_{j(\text{real vehicle})}$ can be expressed as

$$\dot{m}_{j(\text{real vehicle})} = \rho_{\text{exhaust gas}} U_{j(\text{real vehicle})} \left(\frac{\pi D^2}{4} \right) \quad (3-4)$$

where $\rho_{\text{exhaust gas}}$ is the density of exhaust jet and determined from

Silva et al. (2006), $U_{j(\text{real vehicle})}$ is the exit velocity of exhaust jet as summarized in

Table 3.1, and D is the diameter of tailpipe.

The real vehicle's air flow mass rate $\dot{m}_{\text{real vehicle}}$ can be expressed as

$$\dot{m}_{\text{real vehicle}} = \rho_{\text{ambient air}} U_{\text{real vehicle speed}} (BH)_{\text{real vehicle}} \quad (3-5)$$

where $\rho_{\text{ambient air}}$ is the density of ambient air, $U_{\text{real vehicle}}$ is the moving speed of real vehicle, $(BH)_{\text{real vehicle}}$ is the cross section area of real vehicle. The height, H and width, B of a typical on-road light-duty diesel vehicle are 1.8 m and 2.0 m, respectively.

The model vehicle's exhaust tailpipe mass rate $\dot{m}_{j(\text{model vehicle})}$ can be expressed as:

$$\dot{m}_{j(\text{model vehicle})} = \rho_{\text{hot air}} U_{j(\text{model vehicle})} \left(\frac{\pi d^2}{4} \right) \quad (3-6)$$

where $\rho_{\text{hot air}}$ is the density of hot air exhausted from model vehicle, $U_{j(\text{model vehicle})}$ is the exit velocity of the hot air, and d is the diameter of tailpipe.

The model vehicle's air flow mass rate, $\dot{m}_{\text{model vehicle}}$ can be expressed as:

$$\dot{m}_{\text{model vehicle}} = \rho_{\text{ambient air}} U_{\infty} (bh)_{\text{model vehicle}} \quad (3-7)$$

where $\rho_{\text{ambient air}}$ is the density of ambient air, U_{∞} is the flow velocity in wind tunnel, $(bh)_{\text{model vehicle}}$ is the cross section area of model vehicle.

Hence the equation (3-1) can be expressed as:

$$\frac{\rho_{\text{exhaust gas}} U_{j(\text{real vehicle})} \left(\frac{\pi D^2}{4} \right)}{\rho_{\text{ambient air}} U_{\text{real vehicle speed}} (BH)_{\text{real vehicle}}} = \frac{\rho_{\text{hot air}} U_{j(\text{model vehicle})} \left(\frac{\pi d^2}{4} \right)}{\rho_{\text{ambient air}} U_{\infty} (bh)_{\text{model vehicle}}} \quad (3-8)$$

Finally, the ratio U_j/U_{∞} of the model vehicle can be expressed as:

$$\frac{U_{j(\text{model vehicle})}}{U_{\infty}} = \frac{(bh)_{\text{model vehicle}}}{(BH)_{\text{real vehicle}}} \frac{U_{j(\text{real vehicle})}}{U_{\text{real vehicle speed}}} \times \frac{\rho_{\text{exhaust gas}}}{\rho_{\text{hot air}}} \times \frac{D^2}{d^2} \quad (3-9)$$

The simulation parameters of model vehicle conditions are summarized in Table 3.2. Since the ratios of $\dot{m}_{j(\text{real vehicle})}/\dot{m}_{\text{real vehicle}}$ and U_j/U_{∞} for the driving modes at 30 and 50 km/h are quite similar hence only the driving modes of 10 and 30 km/h were studied.

Driving mode	$T_{j(\text{real vehicle})}$ (K)	$U_{j(\text{real vehicle})}$ (m/s)
10 km/h	371.9	7.7
30 km/h	395.1	8.1
50 km/h	419.2	13.9

Table 3.1 Exhaust conditions of a typical on-road light-duty vehicle (Chan et al. 2007; Chan et al. 2008a and 2008b).

Driving mode	$\dot{m}_{j(\text{real vehicle})}/\dot{m}_{\text{real vehicle}}$	$U_{j(\text{model vehicle})}/U_{\infty}$
10 km/h	1.802×10^{-3}	4.395
30 km/h	5.950×10^{-4}	1.452
50 km/h	5.768×10^{-4}	1.407

Table 3.2 The simulation parameters of the studied vehicle cases.

3.6 Methodology of Hot-wire and Cold-wire Anemometers for Air Flow and Temperature Measurements

The measurement technique of hot-wire anemometer has been established for many years and adopted by many researchers, for example, Hall et al. (2003) studied the vortex-shedding from a single cylinder and the tandem cylinders in the presence of applied sound; Park and Lee (2003 and 2004) investigated the flow structure around two side-by-side finite circular cylinders located in an atmospheric boundary layer and the effects of free-end corner shape on flow structure around a finite cylinder, respectively; Jung and Park (2005) studied the vortex-shedding characteristics in the wake of an oscillating airfoil; Chan et al. (2008b) investigated the effect of rear slant angle on flow structures in the wake of a scaled model vehicle; Iungo and Buresti (2009) investigated the wake flow features of triangular prisms under different wind directions, etc. The measurement principle of hot-wire anemometer is shown in Figure 3.14(b). If a sensor is heated by the electrical current and is positioned in a relatively cold air flow, it will dissipate heat into the passing air flow. When the sensor reaches the thermal equilibrium with its surrounding air flow, the heat dissipation, P from the heated hot-wire sensor to the cold air flow will equal to the power supplied by the electrical current and resistance:

$$P = I^2 R = k \cdot S \cdot (T_{wire} - T_{flow}) \quad (3-10)$$

where I is the electrical current, R is the resistance of the heated hot-wire sensor, k is heat dissipation coefficient, S is heat dissipation area, T_{wire} is the working temperature of hot-wire sensor, T_{flow} is the temperature of air flow. All

parameters are constants except the variables of I and k , for a fixed working condition. Therefore a relationship between I and k can be established:

$$k = \frac{R}{S \cdot (T_{\text{wire}} - T_{\text{flow}})} \cdot I^2 = m \cdot I^2 \quad (3-11)$$

where m is a constant for given conditions.

From King's law, the heat dissipation coefficient, k can be expressed as:

$$k = a + b \cdot U^{\frac{1}{2}} \quad (3-12)$$

where a and b are coefficients and U is the air flow velocity. Hence,

$$k = a + b \cdot U^{\frac{1}{2}} = m \cdot I^2 \quad (3-13)$$

or

$$U = \sqrt{(m \cdot I^2 - a) / b} \quad (3-14)$$

where a , b and m are constants which can be determined from on-site calibration.

Now the air flow velocity, U is reduced to a function of electrical current, I only and can be easily calculated from the reading of I .

A Dantec StreamLine constant temperature hot-wire anemometer was used in the present study. It is an improved version of the conventional hot-wire anemometer which puts the hot-wire sensor among one arm of a Wheatstone bridge circuit. Due to the high gain of the Wheatstone servo loop, the Streamline hot-wire anemometer can make faster response to the fluctuations in the air flow than the conventional one.



Figure 3.14(a) Dantec StreamLine hot-wire anemometer (the bottom black box) and the cold-wire anemometer (the upper silver box) used in the present study.

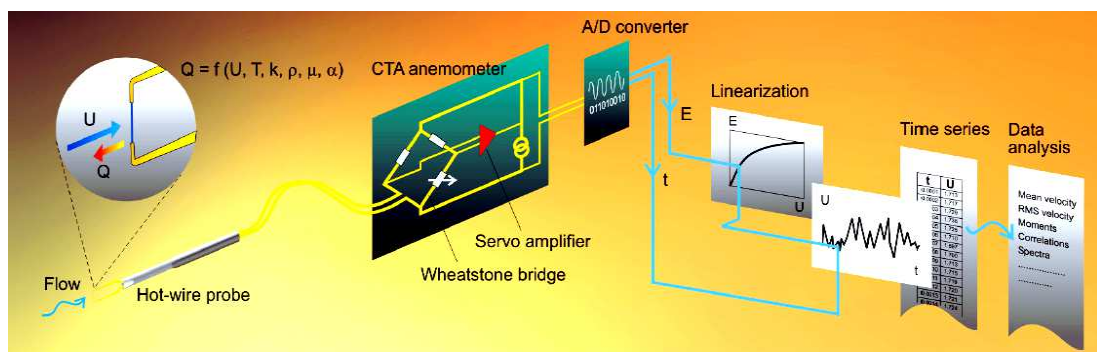


Figure 3.14(b) Flow chart of the Dantec StreamLine hot-wire anemometer (from left to right): hot-wire at the tip of probe dissipates heat, Q into flow; anemometer outputs probe's electrical consumption power, E to an A/D converter to be read and captured into computer; from linearized function gained from calibration, the values of E can be calculated to the flow velocity, U (Dantec Dynamics, 2008).

The measurement principle of cold-wire anemometer is based on the fact that wire resistance is dependent on temperature. Therefore, from the variation of wire resistance, the fluctuation in temperature can be detected:

$$R_T = R_0[1 + \alpha(T - T_0)] \quad (3-15)$$

where R_T is the wire resistance at temperature T , R_0 is the reference resistance at the reference temperature, α is the resistance-temperature coefficient of wire, T is the detected temperature and T_0 is the reference temperature.

In the present study the applied 90% platinum and 10% rhodium Wollaston wire has a resistance-temperature coefficient, $\alpha_T = 0.003926/^\circ\text{C}$ (Sigmund Cohn, 2011). The reference temperature, T_0 is the background temperature in the wind tunnel. The reference resistance, R_0 is dependent on the probe manufacturing and may vary within range $10 \pm 1 \Omega$. Supplying a constant current I to the cold-wire, it will generate a voltage E_T dependent on the temperature, T .

$$E_T = IR_T = IR_0[1 + \alpha(T - T_0)] \quad (3-16)$$

The E_T will be transmitted to an analog-to-digital (A/D) converter, and it will be read and captured into the computer for the analysis. The I in the present study was set to be 0.1mA which is the similar methodology used in Wang and Tong (2002) for the study of scalar dissipation and diffusion in a turbulent jet; Paranthoen et al. (2004) for the investigation of a counter diffusion temperature profile; Gosse et al. (2006b) for the study of scalar dispersion in the near wake of a

simplified model car; Chan et al. (2008b) for the study of pollutant dispersion in the wake of a scaled model vehicle, etc.

A custom-made three-wire probe consisting of the X-type hot-wire and cold-wire sensors was positioned in the air flow behind the vehicle (i.e. Vehicle No. 1, V1) to simultaneously measure the air flow velocity and temperature in the vehicle wake region. For its versatile function, this combined hot-wire and cold-wire probes have been widely used by many researchers, for example, Schacher and Fairall (1979) measured the atmospheric turbulence in the marine environment; Rahai and LaRue (1992) studied the decay of temperature variance in the presence of nonhomogeneous strain; Ball et al. (1999) used it for velocity measurements in non-isothermal flows; Wang and Tong (2002) investigated the scalar dissipation and diffusion, and air velocity in a turbulent jet; Rajagopalan and Tong (2003) studied the scalar-dissipation function and transport equation; Brillant et al. (2008) studied the blowing impact on a hot turbulent boundary layer; Mi and Nathan (2005) used it for statistical analysis of the velocity field in a mechanical processing jet flow; Nagata et al. (2011) studied the small-scale freestream turbulence on turbulent boundary layers with and without thermal convection; Berajeklian and Mydlarski (2011) simultaneously measured the velocity-temperature distribution in the heated wake of a cylinder, etc.

In the present study, the structure of this combined 3-wire probe is shown in Figure 3.15. Six thin metal prongs are extended from the ceramic probe body. These prongs act as not only sensors supports but also signal transmitting cables. The two longest prongs support a piece of cold-wire sensor at their tips. The

Wollaston cold-wire sensor is made of platinum (90%)-rhodium (10%) and was 5 mm in total length with 1 mm effective length in center and 1 μm in diameter. The other four prongs, each pair supports a piece of platinum (90%)-rhodium (10%) hot-wire sensor which is 5 mm in total length with 2.5 mm effective length in center and 5 μm in diameter. The two hot-wire sensors were positioned to form a X-shape and to measure the two velocity components in their formed plane. The hot-wire sensors were supplied with electrical energy by a Wheatstone servo loop to maintain a constant working temperature at T_{wire} while the background temperature of air flow, T_{flow} is also determined inside the wind tunnel facility.

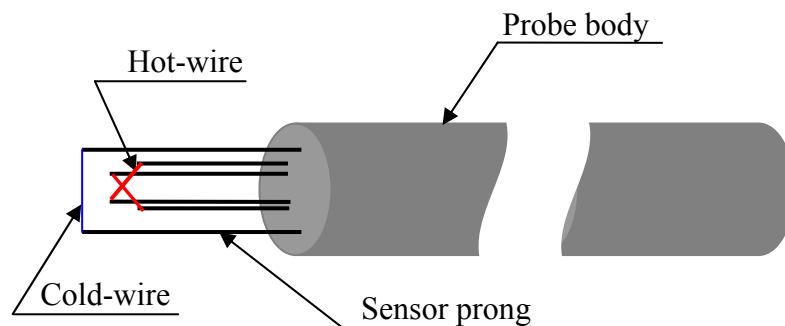


Figure 3.15 The schematic drawing of the custom-made three-wire probe.

The cold-wire sensor was located in the upstream of hot-wire sensors, and the distance between cold-wire and the center of X-wire is 3 mm to avoid the heat dissipated from the hot-wire going into cold-wire to generate noise signal. It should be noted that though the cold-wire sensor is too thin to noticeably alter the air flow attacking hot-wire, its two prongs may to some extent shield or alter the air flow under high turbulent circumstance. Thus the hot-wire sensors may not detect the actual air flow but more or less distorted by the prongs. For this reason our quantitative information about air flow mainly comes from PIV measurement. The

information about air flow that comes from hot-wire measurement will only serve as qualitative flow reference for better understanding the heat distribution field which is dispersed by air flow.

3.7 The Determination of the Sampling Frequency, Sample Number and Uncertainty Analysis

The next question is choosing the sampling frequency for hot-wire and cold-wire anemometers for the present study. To find out the answer a hot-wire measurement was arranged to detect the natural frequencies in air flow. The hot-wire sensor was position behind the vehicle, V1 at $X/H = 2$, $Y/H = 0$ and $Z/H = 0.5$ to measure the power spectrum of vehicle wake where high turbulence is expected among all tested cases. Acquisition time was taken to be 30 seconds long with a 10 kHz sampling frequency. The power spectrum curve for the vehicle speed at 30 km/h (i.e., $U_{\infty} = 8.3$ m/s) consistently descends with increasing of the frequency and shows no obvious peak in the whole studied frequency range as shown in Figure 3.16. It reveals that there is no strong periodic flow structure in the wake region of the studied vehicle. For the other two studied vehicle speeds (i.e., $U_{\infty} = 2.78$ and 13.89 m/s), the power spectrum curves show similar patterns. Similar results were also obtained from their studied vehicle(s) on a fixed floor by Krajnovic and Davison (2005c) and Kanda et al. (2006a and 2006b). The finding confirms that the random sampling and time averaging is applicable for the present study. No phase-locked acquisition technique is required for a flow without distinguishable periodic structures, so long as the number of random samples is large enough to obtain high averaging confidence. For later measurements, hot-wire and cold-wire acquisitions were set to be 5 seconds long with a 1 kHz

sampling frequency, yielding 5000 samples for each tested point. With such a number of samples, the true mean velocity has 95% confidence to fall within the interval $(1\pm 0.0011)\bar{U}$ or 99% confidence within $(1\pm 0.0013)\bar{U}$ where \bar{U} is the mean velocity using sampled datasets (Benedict and Gould, 1996).

The similarity for using hot wire and cold wire measurements in the present study, ‘Variance’ was statistically calculated to be 0.15 of mean \bar{U} and 0.21 of mean \bar{T} based on 10,000 samples. Therefore true mean velocity has 95% confidence to fall within the interval $(1\pm 0.0030)\bar{U}$ or 99% confidence within $(1\pm 0.0039)\bar{U}$, where the \bar{U} was the measured mean velocity using the sampled hot-wire datasets while the true mean temperature has 95% confidence to fall within the interval $(1\pm 0.0041)\bar{T}$ or 99% confidence within $(1\pm 0.0054)\bar{T}$, where the \bar{T} was the measured mean velocity using the sampled cold-wire datasets

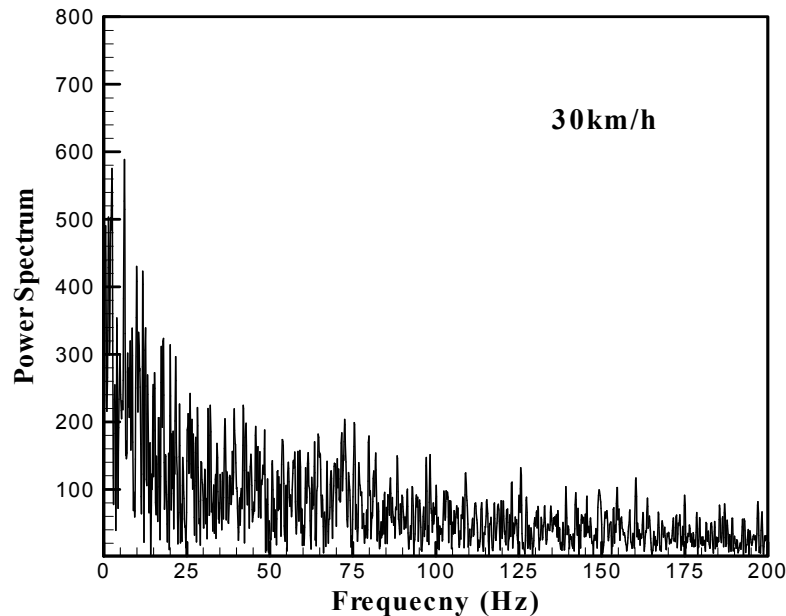


Figure 3.16 Measured power spectrum in near-wake region of the vehicle ($\alpha = 25^\circ$) at $X/H = 2$ and $Z/H = 0.5$ using the hot-wire anemometer.

The expected highest number of PIV images was then evaluated for the two-vehicle case at the vehicle speed of 10 km/h (i.e., $U_\infty = 2.78$ m/s) because the following vehicle is being exposed to the highest turbulence generated by the preceding one due to the shortest vehicle spacing (i.e., $3.1H$) among all studied vehicle cases. The flow field between two vehicles was selected for evaluation purpose. A check point in the selected PIV plane was located at $1H$ upstream in the centerline of V1 and $Z = 0.5H$ above the ground of flat plate. This point was chosen because the air flow passing this selected location is an indicator for the turbulent wake of the vehicle, V2 and also for the incoming flow of the vehicle, V1 as shown in Figure 3.17. A total of 1200 PIV images were acquired and a direct comparison was performed to show the convergence of averaged flow properties against the number of images for the selected check point which is marked by * in the left-up corner of Figure 3.17. It can be concluded from Figure 3.17 that the averaged flow properties become stable if the number of PIV images is more than 800 in the present study. Hence, the number of PIV images was chosen to be 1200 and the results were averaged from about 1080 PIV images based on a 10% rejection rate. In the present study, the true mean velocity has 95% confidence to fall within the interval $(1 \pm 0.0014)\bar{U}$ or 99% confidence within $(1 \pm 0.0019)\bar{U}$ where \bar{U} is the mean velocity using the sampled PIV datasets (Benedict and Gould, 1996).

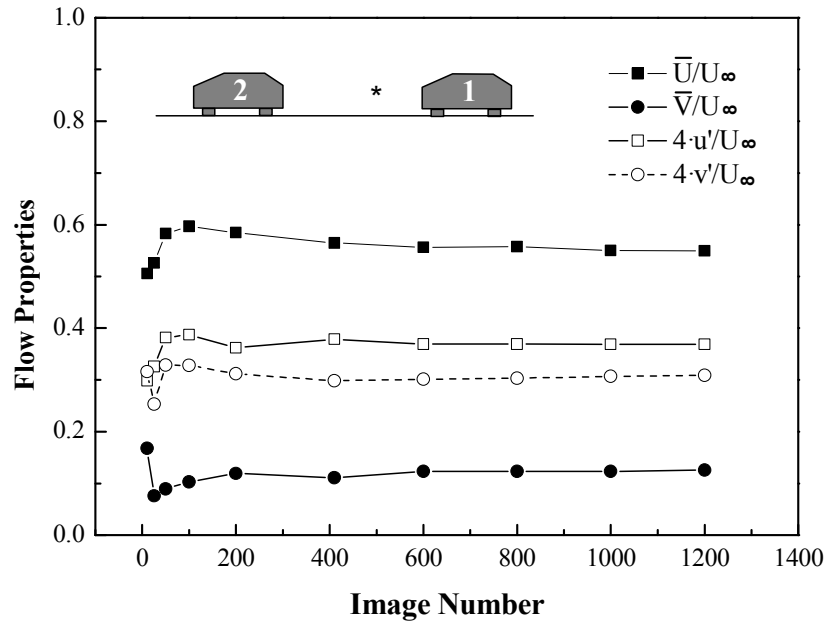


Figure 3.17 Comparison of the flow properties, \bar{U}/U_∞ , \bar{V}/U_∞ , $4\bar{u}'/U_\infty$ and $4\bar{v}'/U_\infty$, from the different number of PIV images ranging from 1 to 1200 at the check point (*) at $1H$ in front of the last vehicle, V1 ($\alpha = 25^\circ$) and $0.5H$ above the ground (Huang et al., 2009a).

3.8 The Analogy between Vehicle Exhaust Temperature Dispersion and Exhaust Gas Dispersion

The governing equation of heat transfer in a fluid flow follows the diffusion-convection equation:

$$\frac{\partial T}{\partial t} = \mu \nabla^2 T + \nabla \cdot (vT) + aT \quad (3-17)$$

where T is temperature, μ is diffusivity, v is fluid velocity vector, and a is a constant for the heat generated by friction which can be considered as zero for the present studied velocities.

The governing equation of mass transfer in a fluid flow also follows the diffusion-convection equation:

$$\frac{\partial C}{\partial t} = \mu \nabla^2 C + \nabla \cdot (vC) + bC \quad (3-18)$$

where C is chemical species concentration, μ is diffusivity, v is fluid velocity vector, and b is reaction rate which can be considered as zero for present passive gas.

Though differ in boundary conditions and coefficients, it can be inferred from similar expression of Equations 3-17 and 3-18 that there may be some analogies between the scalar dispersion patterns of the vehicle exhaust hot air temperature and gas which come out from the same source, i.e. the tailpipe. Figure 3.18 compares the present vehicle exhaust scalar dispersion patterns against the vehicle exhaust gas concentration patterns of Kanda et al. (2006a).

The above two studied vehicles, though different in body shapes, are expected to generate similar three-dimensional wake flows behind them for their rear angles both below 30° (Ahmed et al. 1984), and thus form the base for scalar contour comparison. These two scalar contours in Figures 3.18(c) and (d) are not exactly the same in their boundaries due to the difference in vehicle shapes, locations of tailpipe exit, the studied physical objectives, test conditions, etc. The key points in these two contours, however, are very similar, i.e. peak scalar contour regions are both located behind the tire which is the nearest to the tailpipe exit and its contour gradient is higher on the side of the vehicle tailpipe exit than the other. The scenario that there may be some analogies between the dispersion patterns of

the vehicle exhaust hot air temperature and exhaust gas thus is verified. This approach has been widely accepted and used in Gosse et al. (2006a & 2006b); Chan and Dong (2005); Chan et al. (2008a and 2008b); Gosse et al. (2011); Huang and Chan (2012) and Mohamed (2013). It has been further justified by Sideridis et al. (2011) who also studied heat transfer in wind tunnel. They concluded that “This (eddy diffusivity of heat) is of the same order of magnitude as the eddy diffusivity of mass due to the fact that the Prandtl and Schmidt numbers for gases are both close to one. The experimentally determined eddy diffusivity can provide a reliable assessment of the flux of a gaseous substance from ground level into the atmosphere”. Moreover, due to the small size of cold-wire probe and high spatial resolution in the present study, the exhaust hot air temperature contours can reveal more internal details of vehicle exhaust scalar dispersion region, e.g. the dual peak contour regions behind each tire of vehicle. The main limitations of this approach are that as temperature is a passive physical characteristic of air flow, it can only represent the dispersion of passive pollutants (i.e., non-reactive gas) and the pollutants should be either gaseous or light/fine particles which can well follow the movement of air flow. For heavy particles whose gravity force cannot be ignored in comparison with the drag and lift forces of air, the heavier the pollutant particle is, the larger the deviation of its behavior from the behavior of heat.

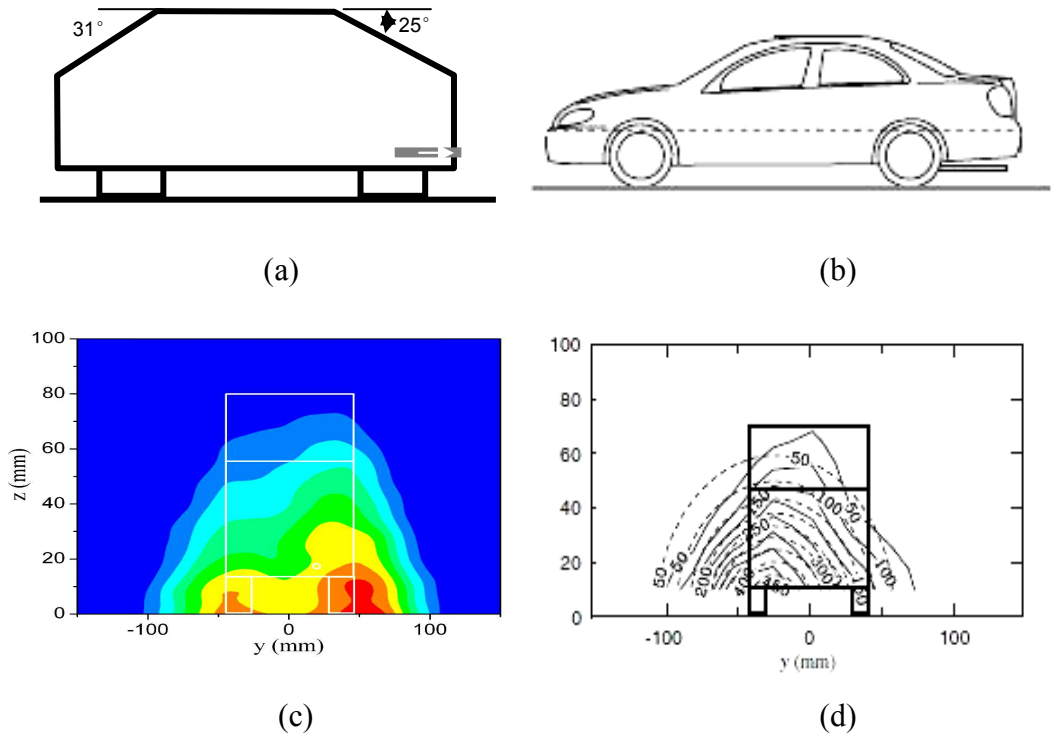


Figure 3.18 (a) The present studied vehicle ($\alpha = 25^\circ$) and a tailpipe exhaust hot air; (b) Kanda et al. (2006a) studied vehicle with a tailpipe exhaust tracer gas; (c) the normalized mean temperature excess, \bar{T}^* (i.e., scalar) contours in Y-Z plane at $X/H = 4$ behind the present studied vehicle ($\alpha = 25^\circ$) at 10 km/h where $H = 0.081$ m; (d) Kanda et al. (2006a) measured mean gas concentration contours (solid line) in Y-Z plane at $X/H = 4.1$ behind their vehicle at 20 km/h where $H = 0.072$ m.

Chapter 4 Vehicle Queue Effect on the Characteristics of Air Flow in the Vehicle Wake

4.1 Introduction

The three-dimensional wake flow behind the ground vehicles plays an important role in the dispersion and concentration fields of vehicle exhaust pollutants (Chang et al. 2009b). The flow fields or wake structures have long been studied by many researchers and engineers using different measurement techniques such as flow visualization, pressure sensor, Pitot tube, multi-hole sensor, hot-wire anemometer (HWA), laser Doppler velocimetry (LDV), particle image velocimetry (PIV) etc. as well as the computational fluid dynamics (CFD) techniques. Many papers and reports have been documented in the related areas. So far, our knowledge gained from the experimental and numerical approaches is mainly on a single ground vehicle/ scale-down model vehicle either running on roadway or in a testing facility (e.g. wind tunnel). On the other hand, the automobile population is ever increasing in most urban cities. It leads to the growing traffic density with a shortened vehicle spacing between the consecutive running vehicles on the traffic lanes, and the application of modern technologies such as intelligent transport systems will further reduce the traffic/vehicle spacing (Watkins and Vino 2008). It is clearly known that the moving ground vehicle may alter the incoming flow structures for the following vehicle(s). Here raises a question: how much of our knowledge gained from a single moving ground vehicle can still be applied to the case among a queue of moving ground vehicles? Particular research attention has only been drawn in recent years. Up to now, very few research works concerning

the flow structures, and pollutant (i.e., scalar) dispersion and concentration fields behind multiple ground vehicles have been reported.

One of the early research works concerning the vehicle queue (Clifford et al. 1996) was entirely devoted to the vehicle pollutant dispersion. They identified that 75% of the total received pollution for a following vehicle comes from the preceding one. Recently, Kanda et al. (2006a) have revealed that the exhaust pollutant dispersion in a queue of vehicles is dominated by the symmetric vehicle wake other than the offset positioned exhaust tailpipe. It can be concluded that the wake flow between vehicles moving in line affects not only their aerodynamic properties but also the vehicle exhaust pollutant dispersion patterns, if these ground vehicles are not sparsely distributed. Therefore a better understanding of the wake region between multiple moving ground vehicles is essential.

Baker and Hargreaves (2001) and Baker (2001) stated clearly the vehicle wakes have a significant effect on the vehicular exhaust pollutant dispersions but is over simplified by most vehicle pollutant dispersion models. They also pointed out that most of the wake studies serve for vehicle drag reduction whereas provide less attention to the interaction between the wake development and vehicle exhaust pollutant dispersion. Similar point of view has been shared by Kanda et al. (2006a) that “traffic-produced turbulence plays an important role in the dispersion of automobile exhaust gas. However, the nature of traffic-produced turbulence is poorly understood, and the existing air pollution models adopt various empirical schemes that are difficult to verify”. Consequently, they have made an assumption in their vehicle exhaust concentration study that three preceding

vehicles are sufficient to produce wake turbulence equivalent to that of an infinite queue. Despite of the experimental investigations, numerical simulations also have to stem from a base weakened by the lack of knowledge about the flow around a queue of moving vehicles, “although exploratory works are emerging” (Kanda et al. 2006b). This has become a bottle neck for both experimental and numerical research works of vehicle exhaust pollutant dispersion and concentration fields in a close vicinity of roadway.

In recent years, the time-averaged wake flow has been extensively studied by either traditional experimental fluid dynamics (EFD) or thriving computational fluid dynamics (CFD) methods in order to have a better understanding of the flow structures and aerodynamic characteristics around vehicles, and the exhaust pollutant dispersion and concentration fields behind vehicles. Khalighi et al. (2001) studied experimentally and computationally the unsteady wake flow behind a vehicle body; Vio et al. (2003) investigated the relationship between the passenger vehicle wake and upstream turbulence; Al-Garni (2004) experimentally investigated the flow around a generic sport utility vehicle; Gosse et al. (2006a and b) studied the scalar dispersion in the near wake of a simplified model vehicle while Dong and Chan (2006) studied numerically the flow structures and pollutant dispersion in the near-wake region of vehicle using a large eddy simulation (LES) approach; Watkins and Vio (2008) investigated the relationship between vehicle spacing and vehicle aerodynamics; Chan et. al. (2008a and 2008b) studied numerically and experimentally the flow structures and pollutant dispersion in the near-wake region of a scaled model vehicle, respectively; Huang et al. (2009a and 2009b) investigated the flow structures and pollutant dispersion of a queue of

vehicles, respectively; Al-Garni and Bernal (2010) studied experimentally the near wake of a pickup truck; Chan et al. (2010a) investigated numerically the particle formation and evolution processes in the wake of the vehicle using the direct quadrature method of moments approach; Liu et al. (2011a) performed a three-dimensional simulation of exhaust particle dispersion and concentration fields in the near-wake region of a ground vehicle, etc. Since the rear slant angle, $\alpha = 25^\circ$ of the present studied vehicles is smaller than the critical angle, 30° , it is expected that a complex three-dimensional wake flow will be generated (Ahmed et al. 1984; Chan et al., 2008a and 2008b; Huang et al., 2009a). Krajnovic and Davidson (2004) pointed out that the variety in the turbulent length scales in combination with very unsteady reattachment of separated flow in this region are possible reasons for the failure of Reynolds-averaged Navier-Stokes (RANS) simulations in the prediction of the flow around a simplified car model ($\alpha = 25^\circ$) case. The hybrid large-eddy simulation-Reynolds-averaged Navier-Stokes (LES-RANS) or detached eddy simulation (DES) is still not fully developed and several problems remain to be solved for this particular rear slant angle (Krajnovic and Davidson, 2005a; Guilmineau, 2008; Guilmineau et al., 2011). The flow around Ahmed body ($\alpha = 25^\circ$) was better simulated using large eddy simulation (LES) (Krajnovic and Davidson, 2004, 2005a and 2005b). Guilmineau (2008) has investigated numerically the flow around a simplified car body with different rear slant angles (i.e., 25° and 35°) and compared with the experimental data of Lienhart and Becker (2003). He concluded that the flow around the car body ($\alpha = 25^\circ$) is still considered an open challenge for turbulence modeling. Recently, Guilmineau et al. (2011) have performed a DES simulation with a result superior to that from

RANS. But the DES failed to predict a vortex bubble on the rear slant back of the studied vehicle. It implies that DES is still unable to provide a very reliable computational tool for solving the complex three-dimensional vehicle wake flow. On the other hand, the EFD approaches can still provide the important and reliable flow properties for the vehicles ($\alpha = 25^\circ$), therefore the present study mainly focuses on the EFD approaches.

The present study is to investigate the three-dimensional wake flow behind a queue of model vehicles (i.e., $\alpha = 25^\circ$ or 60°) in a closed-circuit wind tunnel testing facility using PIV for typical urban vehicle speeds in order to fill this knowledge gap. An intensive experimental investigation was performed in well controlled wind tunnel testing facility (Chan et al., 2008b; Huang et al., 2009a and 2009b) to understand the queue effect of the vehicles on the flow structures in the vehicle wake because the effects from traffic vehicle movements and natural ambient wind are difficult to separate in real world. Measurement by PIV in a wind tunnel facility of the vehicles will reveal the structures and properties of the air flow in the vehicle wake region for one-, two- and three-vehicle cases (i.e., a queue of vehicles), especially for the scarcely research works in the latter one.

4.2 Experimental Set-up

Detailed experimental set-up was given in Section 3.3. The seven measurement planes around the studied vehicle, V1 for using particle image velocimetry (PIV) are illustrated at the upright corner of Figure 4.1. All PIV measurement planes were maintained to be $3H \times 3H$ in dimension. PIV

measurement planes of No. 1 and No.7 were located at $Z/H = 0.5$ where one is in front of and one behind the vehicle, V1. The PIV measurement planes of Nos. 2 and 3 were located at $Y/H = 0$ where one was in front of and one behind the vehicle, V1. PIV measurement planes of Nos. 4, 5 and 6 were located at $X/H = 1, 2$ and 3 behind the vehicle, V1, respectively. By studying the air flow passing through all these seven representative planes, a better understanding of the three-dimensional flow field around the vehicle, V1 can be obtained.

The same arrangement of PIV measurement planes was applied to all studied vehicle cases ($\alpha = 25^\circ$ or 60°) at 10 km/h, 30 km/h and 50 km/h. Measured PIV data will be summarized and discussed in Section 4.3.

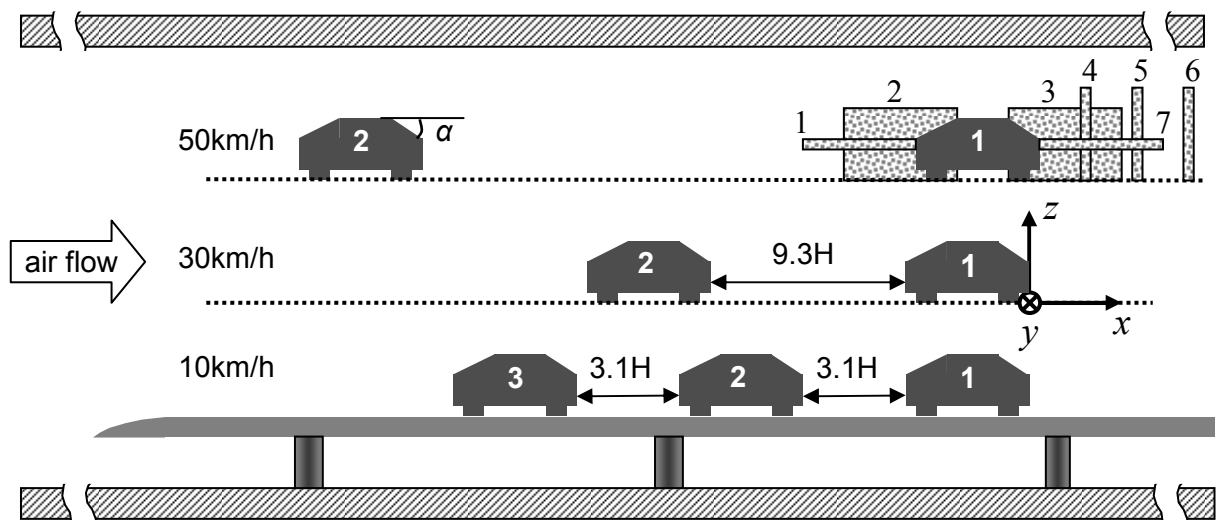


Figure 4.1 Experimental setup and coordinate system inside the wind tunnel facility for one-, two- and three-vehicle cases (Huang et al. 2009a).

4.3 Results and Discussion for Queue Effect of the Studied Vehicles ($\alpha = 25^\circ$) on the Flow Structures in the Vehicle Wake

4.3.1 Wake structure of one-, two- and three-vehicle cases ($\alpha = 25^\circ$) in X - Y plane at $Z/H = 0.5$ for different vehicle speeds

4.3.1.1 Velocity profiles, \bar{U}/U_∞ and u'/U_∞ for the vehicles ($\alpha = 25^\circ$) at 10 km/h

Figures 4.2 (a) and (b) show the cross-sectional normalized velocity, \bar{U}/U_∞ and turbulence, u'/U_∞ profiles at $1H$ upstream from the vehicle, V1 and $Z = 0.5H$ above the ground. In Figure 4.2(a), the profile of \bar{U}/U_∞ for one-vehicle case at 10 km/h shows a shallow valley in the middle. The maximum \bar{U}/U_∞ deficit is 12% due to the blockage effect from the vehicle, V1 downstream. For two-vehicle case, the curve shape is significantly altered in the wake region of the preceding vehicle, V2 within $-0.9 \leq Y/H \leq 0.9$. A hill is observed in between two valleys which are caused by two counter rotating longitudinal vortices (or known as trailing vortices in some literatures). At $2.1H$ downstream from the vehicle, V2, the diameter of the vortices equals to the width of valley which is around $0.4H$ and the distance between two vortex centers is around $0.8H$. Ahmed (1981), and Lienhart and Becker (2003) also found that the distance between two centers of longitudinal vortices is around $0.8H$ at the downstream $2H$ for their single vehicle studies. Moreover, the curve of two-vehicle case also indicates that the center part of longitudinal vortices moves along the downstream at an average velocity of $0.55U_\infty$ (i.e., the height of two curve valleys, marked by +) while the surrounding air moves at a speed of no less than $0.75U_\infty$ (i.e., the height of center hill, marked by \times). Since Figure 4.2(a) is an averaged result of about 1080 PIV images, two possible reasons may contribute to the shape of \bar{U}/U_∞ curve. One

reason may be caused by the effect of statistical averaging of \bar{U}/U_∞ . The instantaneous \bar{U}/U_∞ values inside the trailing vortices where the flow is highly turbulent may have large variation thus resulting in a lower mean value of \bar{U}/U_∞ than that for the more stable outside region. Another reason is that there is not much difference between the instantaneous and averaged \bar{U}/U_∞ values as shown in Figure 4.2(a). The \bar{U}/U_∞ profiles obtained from several instantaneous vector maps (figures not shown) were examined one by one instead of using the statistical averaging approach. The results showed more or less a similar curve to the one in Figure 4.2(a). Therefore they justify the second reason. The longitudinal vortices are discovered to have two flow behaviors which are different from their surrounding air in vehicle wake namely counter rotating as found by other researchers and moving downstream at relatively low velocity. It should also be noted that as the rotation axis of the longitudinal vortices is in line with their downstream movement, therefore the downstream velocities for different circles of the trailing vortices are not uniform but increase with their radius from the vortex center.

The \bar{U}/U_∞ profiles of two- and three-vehicle cases at 10 km/h in Figure 4.2(a) also show that two preceding vehicles case (i.e., both V2 and V3) has some minor changes in the wake structure or in the size of longitudinal vortices if compared with the single preceding vehicle case (i.e., V2 only). Some weak effects of the expanded wake from the second preceding vehicle, V3 (i.e., three-vehicle case), can be observed at the two far sides of the curve. The value of mean velocity, \bar{U}/U_∞ for two longitudinal vortex centers is reduced from 0.87 to 0.52 (i.e., 38%

reduction) which is caused by the single blockage effect of V2 alone (i.e., two-vehicle case), and further reduced to 0.35 (i.e., 30% reduction from 0.5) by the double blockage effects of both preceding vehicles, V2 and V3 (i.e., three-vehicle case). On the other hand, the value of mean turbulence, u'/U_∞ for these two longitudinal vortex centers is increased from 0.01 (i.e., background level) to 0.108 (i.e., 1070% increment) by V2 alone, and further up to 0.124 (i.e., 15% increment from 0.108) by both preceding vehicles, V2 and V3.

Furthermore, as the shape of curve depicts local flow structure (e.g., the position and diameter of longitudinal vortices are reflected by the position and width of the four valleys in curves (in the curves of 2- and 3-vehicle cases), the spatial coincidence of curves for 2- and 3-vehicle cases in Figures 4.2(a) and (b) reveals that the preceding vehicle, V3 (i.e., 3-vehicle case) does not have obvious effect on the wake structure of the following vehicle, V2 because the position and width of the four valleys in curves are almost unchanged even though the downstream velocity U/U_∞ of two longitudinal vortex centers can be considerably slowed down. It can be inferred that the curve for 4-vehicle case will not be distinctive from the curves of 2- and 3-vehicle cases except that the curve of 4-vehicle case will locate a bit deeper. Hence, it can be concluded that the wake structure behind a vehicle will be significantly altered by a preceding vehicle, but will not be significantly further altered by the second or even more preceding vehicles.

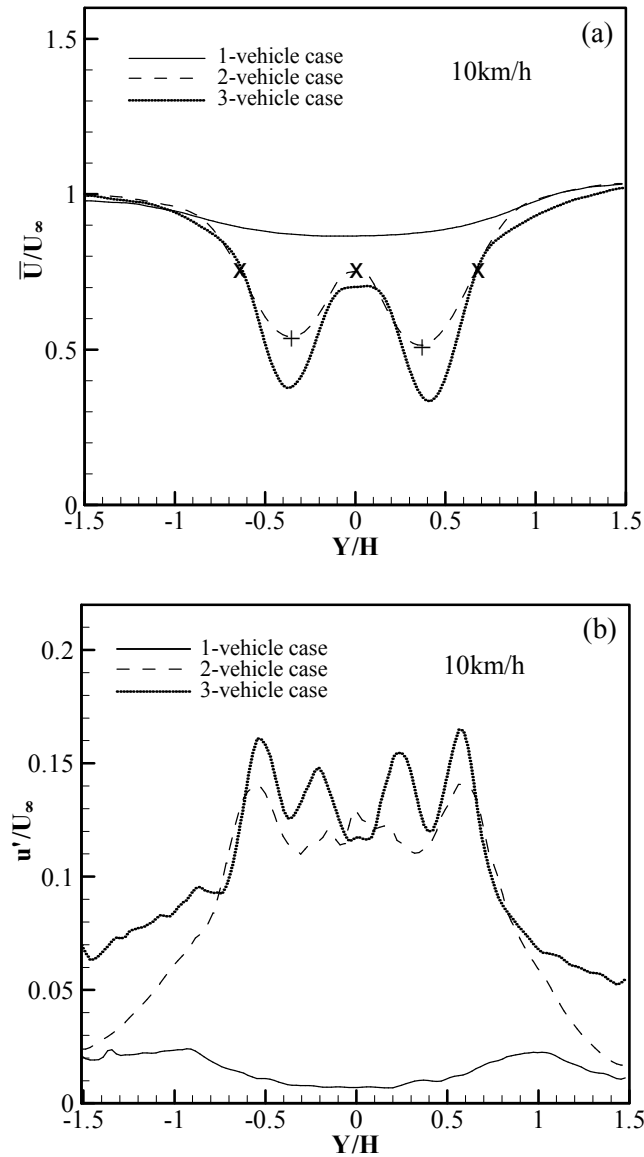


Figure 4.2 Horizontal cross-sectional profiles: (a) \bar{U}/U_∞ and (b) u'/U_∞ at $1H$ in front of the vehicle, $V1$ and $Z = 0.5H$ above the ground for one-, two- and three-vehicle cases ($\alpha = 25^\circ$) at 10 km/h (i.e., $3.1H$ vehicle spacing). The center of two curve valleys or where the two vortex centers are marked by +, while edges of the two vortices are marked by \times (Huang et al., 2009a).

4.3.1.2 Velocity profiles, \bar{U}/U_∞ and u'/U_∞ for the vehicles ($\alpha = 25^\circ$) at 30 km/h

Figures 4.3(a) and (b) show the cross-sectional velocity, \bar{U}/U_∞ and turbulence u'/U_∞ profiles at $1H$ upstream from the last following vehicle, $V1$ and $Z/H = 0.5$ for the vehicle speed at 30 km/h . In Figure 4.3(a), the maximum

normalized mean velocity, \bar{U}/U_∞ deficit is decreased from 12% (for 10 km/h case) to 5% (for 30 km/h case) due to the suppression of blockage effect by the faster incoming flow. For the two-vehicle case, the two valleys induced by the longitudinal vortices from the preceding vehicle, V2 are observed to be wider and shallower if they are compared with the valleys for two-vehicle case at 10 km/h. It might be because the vehicle spacing has been increased from $3.1H$ to $9.3H$. According to the description of Baker (2001), the near-wake region is characterized by the large-scale flow structures from 0 to $10H$ behind the vehicle, and the far-wake region is characterized by the gradual decay beyond $10H$. Supported by the Baker's conclusion and eddy energy cascade theory, it is believed that the two wide and shallow valleys are not induced by the weak longitudinal vortices but by many small-scaled eddies broken from the longitudinal vortices. Several \bar{U}/U_∞ curves from the instantaneous vector maps (figures not shown) are checked. Each curve has a few valleys which are small, shallow and almost randomly positioned. None of these checked curves show a symmetric pattern or any valley as wide as these two valleys in Figure 4.3(a). Therefore, it can be concluded that contrary to the case of 10 km/h, the two shallow valleys in the \bar{U}/U_∞ curve for 30 km/h are the averaging effect of many small sized eddies, and the two longitudinal vortices of $0.4H$ in diameter have already been broken apart along the way between $X/H = 2.1$ and 8.3 . In Figure 4.3(b), the distance between two averaged valley centers can be more accurately determined from the two peaks in the curve of u'/U_∞ to be about $1.5H$ at $X/H = 8.3$, in contrast to the about $0.8H$ at $X/H = 2.1$ in Figure 4.2(a).

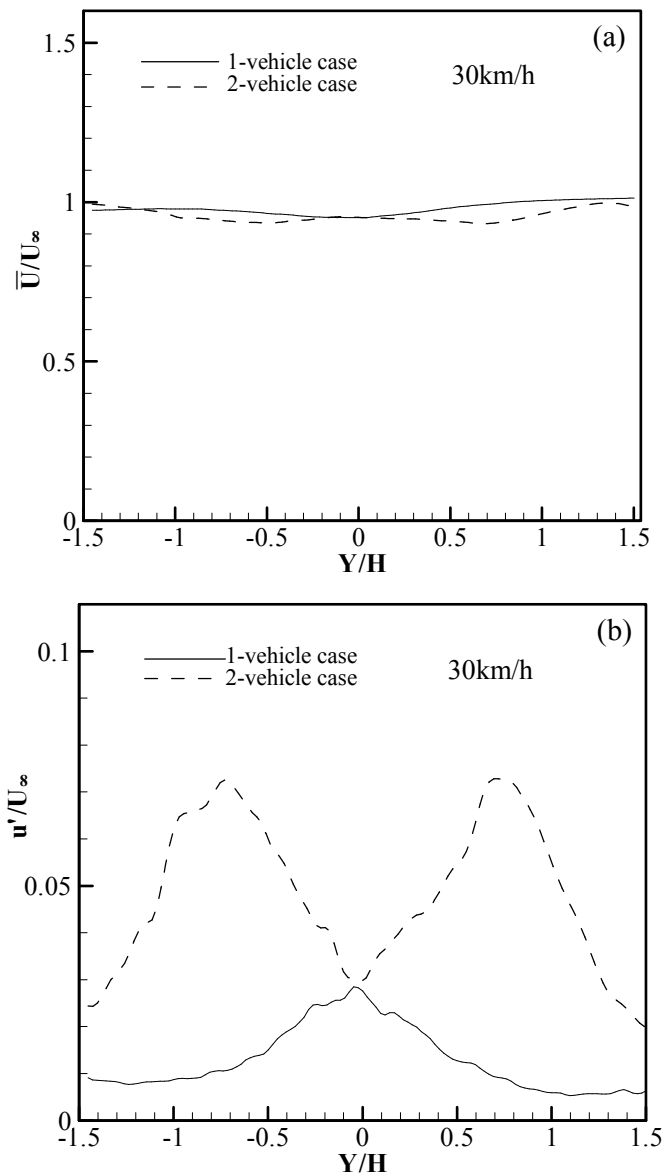


Figure 4.3 Horizontal cross-sectional profiles: (a) \bar{U}/U_∞ and (b) u'/U_∞ at $1H$ in front of the vehicle, $V1$ and $Z = 0.5H$ above the ground for one- and two-vehicle cases ($\alpha = 25^\circ$) at 30 km/h (i.e., $9.3H$ vehicle spacing) (Huang et al., 2009a).

4.3.1.3 Velocity profiles, \bar{U}/U_∞ and u'/U_∞ for the vehicles ($\alpha = 25^\circ$) at 50 km/h

Figures 4.4(a) and (b) show the cross-sectional velocity, \bar{U}/U_∞ and turbulence, u'/U_∞ profiles at $1H$ upstream from the last following vehicle, $V1$ and $Z/H = 0.5$ for the vehicle speed at 50 km/h . The differences between the curves of

\bar{U}/U_∞ and u'/U_∞ with and without a preceding vehicle are both within 5%. No large flow structure can be found in the far-wake region at $14.5H$ and $Z/H = 0.5$ behind the preceding vehicle, V2 for two-vehicle case. Interestingly, the center part of vehicle wake has the lowest turbulence intensity which is close to the background level, in sharp contrast to the presence of two preceding vehicles at 10 km/h. Since the differences between the magnitudes of flow properties of \bar{U}/U_∞ and u'/U_∞ with and without a preceding vehicle cases are 0.95 against 0.90 and 0.01 against 0.05, respectively, they can be considered to be small magnitude variations of the studied flow properties. It can be inferred that the difference in incoming flow caused by the preceding vehicle on the following vehicle, V1 can be ignored in most engineering applications if the vehicle separation is larger than $15H$.

However, an unexpected phenomenon is observed in Figure 4.4(b) where the turbulence, u'/U_∞ profile is still quite non-uniform even in the far-wake region, i.e. $14.5H$ downstream from the preceding vehicle, V2. The lowest turbulence, $u'/U_\infty = 0.012$ still occurs at the center part of wake while the highest turbulence, $u'/U_\infty = 0.048$ occurs at the two far sides. Such high turbulence is believed to be induced by the broken eddies from the trailing vortices. Comparing with the turbulence, u'/U_∞ profiles at $X/H = 8.3$ and $X/H = 14.5$ in Figures 4.3(b) and 4.4(b), it can be observed that from the near-wake region to the far-wake region of the vehicles, the turbulence in wake decreases in intensity for the whole cross-section profile, but the width of turbulent wake in the Y -direction has considerably expanded along the downstream distance.

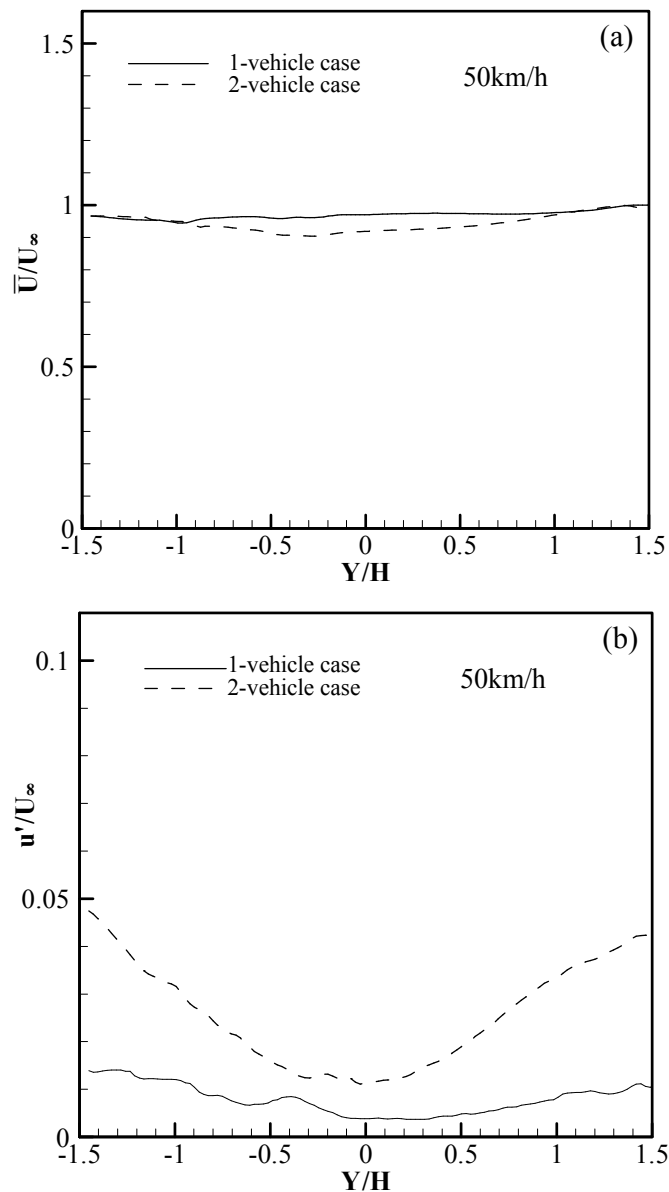


Figure 4.4 Horizontal cross-sectional profiles: (a) \bar{U}/U_∞ and (b) u'/U_∞ at $1H$ in front of the vehicle 1, $V1$ and $Z = 0.5H$ above the ground for one- and two-vehicle cases ($\alpha = 25^\circ$) at 50 km/h (i.e., $15.5H$ vehicle spacing) (Huang et al., 2009a).

4.3.1.4 Streamwise velocity, \bar{U}/U_∞ and momentum, $u'\hat{v}'U_\infty^2$ contours for the vehicles ($\alpha = 25^\circ$) at different vehicle speeds

Figure 4.5 shows the contours of \bar{U}/U_∞ in X - Y plane at $Z/H = 0.5$ behind the last vehicle, $V1$ for one-vehicle case at 10 km/h . Two “hills” occur shortly

behind the vehicle rear (i.e., $X/H \approx 0.3$), and then they converge to form a “ridge” at $X/H \approx 1$. The height of hill does not change with the addition of preceding vehicles but the height of ridge does. The heights of hill and ridge are (0.30, 0.78) for one-vehicle case and (0.30, 0.82) for two-vehicle case and (0.30, 0.85) for three-vehicle cases. For the other two vehicle speeds (i.e., 30 and 50 km/h), their contours are in similar patterns but just different in values. Hence only the different values are presented. Their heights of hill and ridge are (0.39, 0.86) for one-vehicle case and (0.43, 0.94) for two-vehicle case at 30 km/h, or (0.45, 0.91) for one-vehicle case and (0.48, 0.97) for two-vehicle case at 50 km/h, respectively.

In Figure 4.5, the most noticeable difference induced by preceding vehicles is the height of ‘ridge’, 0.78, 0.82 and 0.85 for one-, two- and three-vehicle cases at 10 km/h, respectively. It should be noted that the height of \bar{U}/U_∞ rises with the increasing upstream blockages (i.e., number of the preceding vehicles). An explanation can be referred to the vorticity contours in Figure 4.10. The absolute vorticity value (i.e., the changing rate of movement direction) over the rear slant of V1 will be decreased from 12.1 to 9.9 or 9.8 if one or two preceding vehicle(s) is/are arranged in the upstream of V1, thus resulting in less down-washing flow over the rear slant and producing a higher \bar{U}/U_∞ value in the near-wake region. This phenomenon may also explain why the \bar{U}/U_∞ values are increased by a preceding vehicle from 0.86 to 0.94 and 0.91 to 0.97 for 30 km/h and 50 km/h cases, respectively.

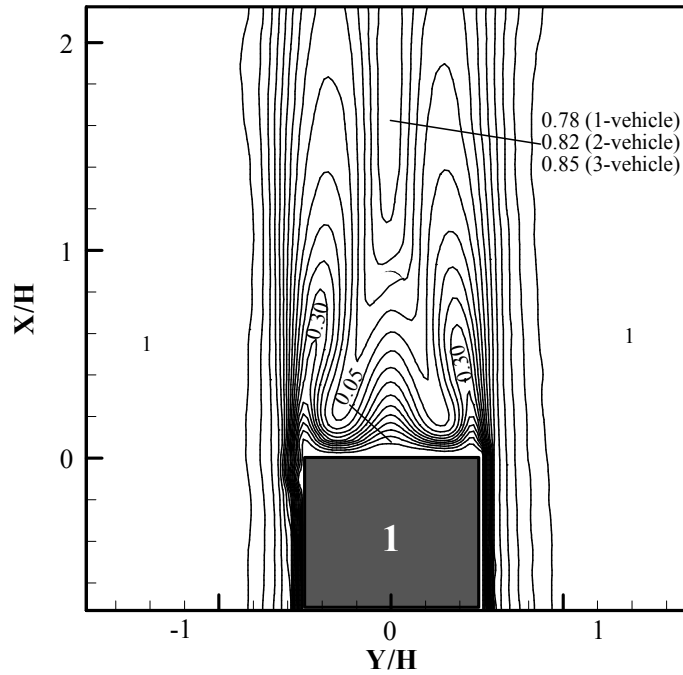


Figure 4.5 Contours of \bar{U}/U_∞ in X - Y plane at $Z/H = 0.5$ for one-, two- and three-vehicle cases ($\alpha = 25^\circ$) at 10 km/h (Contour base line = 0.005, step = 0.005) (Huang et al., 2009a).

Watkins and Vino (2008) have recently found that the relationship between the vehicle spacing and aerodynamics which both lift and drag coefficients vary remarkably within the vehicle spacing ranging from 0.1 to $1.0L$ ($1L = 3.6H$). Beyond a turning point at $1.0L$, both studied coefficients become relatively stable especially for the drag which is maintained at 88% of their values for one-vehicle case. Figure 4.5 shows that the flow properties such as \bar{U}/U_∞ in very near-wake region (i.e., $X/H \leq 1$) change drastically with downstream distance. Beyond this very near-wake region where the 'ridge' is formed, both the shape and values of \bar{U}/U_∞ become stable. It can be inferred that the resulting aerodynamics forces will follow similar trend of the flow properties.

The averaged turbulent stress, $|\overline{u'v'}|/U_\infty^2$ contours in X - Y plane are shown in Figures 4.6(a) to (c) for one-vehicle cases at 10, 30 and 50 km/h, respectively. In Figure 4.6(a), two peaks of $|\overline{u'v'}|/U_\infty^2$ with the height around 0.0134 can be observed at $X/H=0.6$ and $Y/H= \pm 0.45$. One or two preceding vehicles cannot obviously change the contour of $|\overline{u'v'}|/U_\infty^2$ behind the vehicle V1 because the peak values always occur in the same region (i.e., around $0.5-0.6H$) regardless of the presence of the preceding vehicle(s). For 10 km/h case, the peak value of $|\overline{u'v'}|/U_\infty^2$ is raised up to 0.0147 by one preceding vehicle, V2 alone or up to 0.0155 by two preceding vehicles, V2 and V3. For one preceding vehicle, V2 may also increase the peak value of $|\overline{u'v'}|/U_\infty^2$ by 17% for the 30 km/h case or 13% for the 50 km/h case when compared with 10 km/h case. On the other hand, one preceding vehicle only increases the turbulent intensity, u'/U_∞ value by 6% for 30 km/h case or 2% for 50 km/h case. Clearly, the preceding vehicle has more effect on $|\overline{u'v'}|/U_\infty^2$ than on u'/U_∞ . The distribution pattern of $|\overline{u'v'}|/U_\infty^2$, is not sensitive to either the vehicle speed or the presence of the preceding vehicle(s).

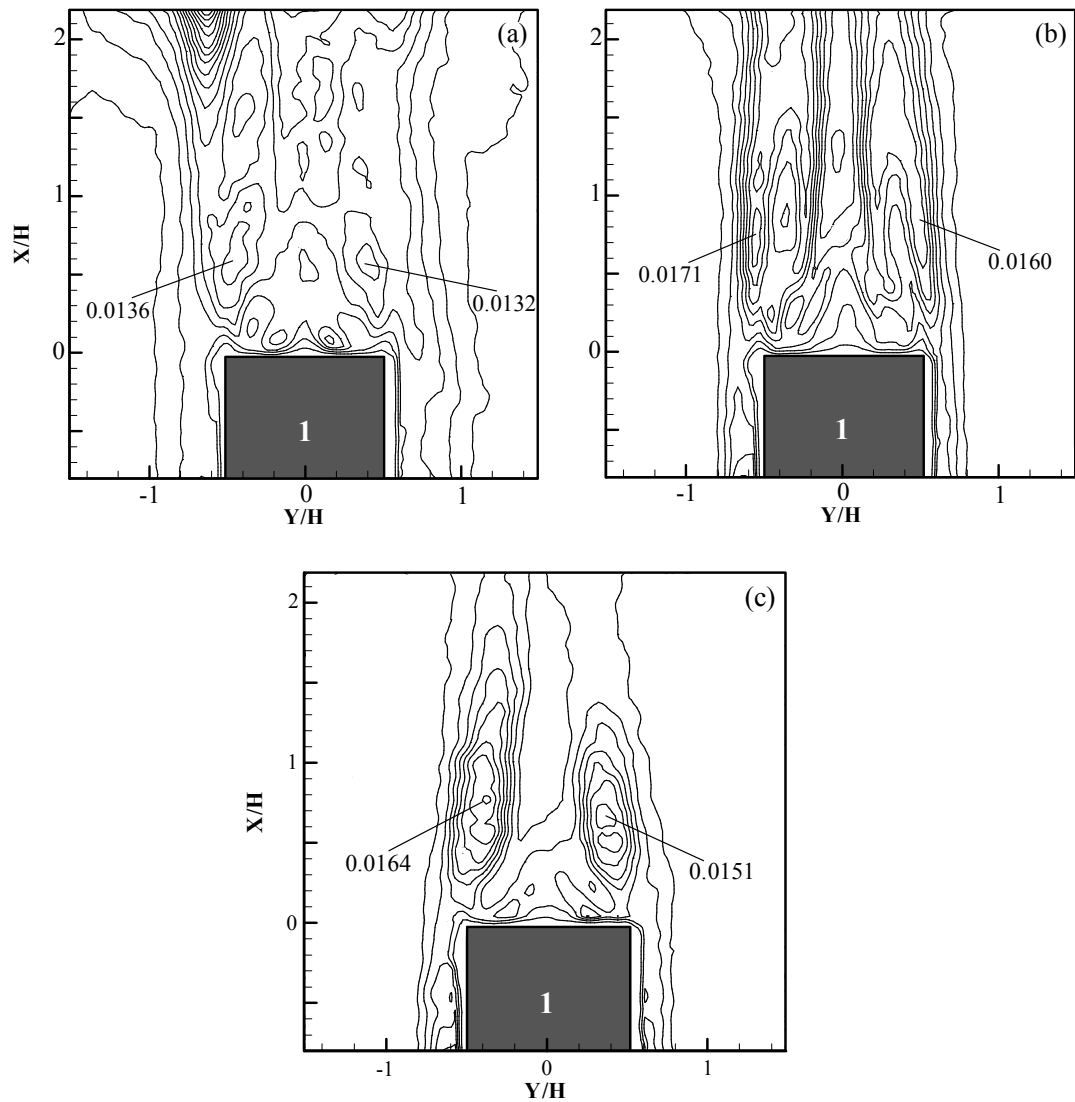


Figure 4.6 Averaged turbulent stress, $|\overline{u'v'}|/U_\infty^2$ contours in X - Y plane at $Z/H = 0.5$ for one-vehicle case ($\alpha = 25^\circ$) at (a) 10 km/h, (b) 30 km/h and (c) 50 km/h (Contour base line = 0.002, step = 0.002) (Huang et al., 2009a).

4.3.1.5 Wake structure in X - Z plane at $Y/H = 0$ for the vehicles ($\alpha = 25^\circ$) at different vehicle speeds

Normalized \bar{U}/U_∞ and u'/U_∞ profiles along the Z -direction at $1H$ in front of the last vehicle, V1 for one-, two- and three- vehicle cases at 10 km/h are shown in Figures 4.7(a) and (b). The preceding vehicle, V2 of two-vehicle case may decrease \bar{U}/U_∞ by 15% and increase u'/U_∞ by 8% at most for the incoming flow toward the following vehicle, V1. The blockage effect of V2 is obvious for the flow region lower than $Z/H = 1$ but still noticeable at $Z/H = 2$. By comparing the curve of two-vehicle case with that of the three-vehicle case, it can be concluded that for the difference in flow properties of \bar{U}/U_∞ and u'/U_∞ induced by both preceding vehicles, V2 and V3, the blockage effect of V2 contributes more than 90% of the difference in the flow properties while the blockage of V3 has just a minor effect for less than 10%. This phenomenon in the X - Z plane is similar to that in the X - Y plane which was mentioned in Section 4.3.1.1. In Figures 4.8(a) and 4.9(a) for one- and two-vehicle cases at 30 and 50 km/h, the blockage effect of the preceding vehicle, V2 on \bar{U}/U_∞ is weakened by 50% or more because of the larger vehicle spacing for wake development. The values of u'/U_∞ induced by the presence of V2 are around 5% for both 30 km/h and 50 km/h cases as shown in Figures 4.8(b) and 4.9(b).

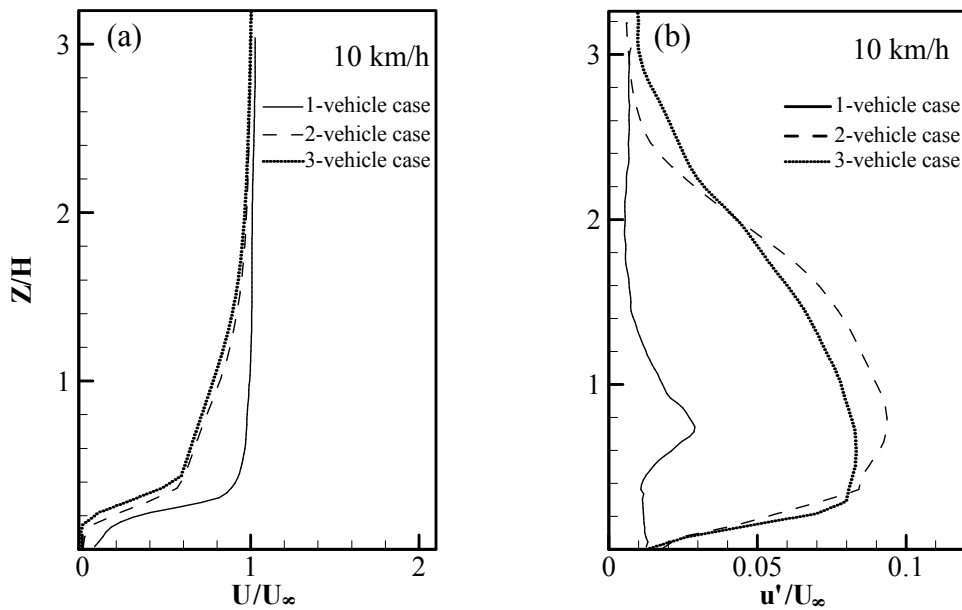


Figure 4.7 (a) \bar{U}/U_∞ and (b) u'/U_∞ profiles in X - Z plane at $1H$ ahead of the last vehicle front, V1 for one-, two- and three-vehicle cases ($\alpha = 25^\circ$) at 10 km/h (Huang et al., 2009a).

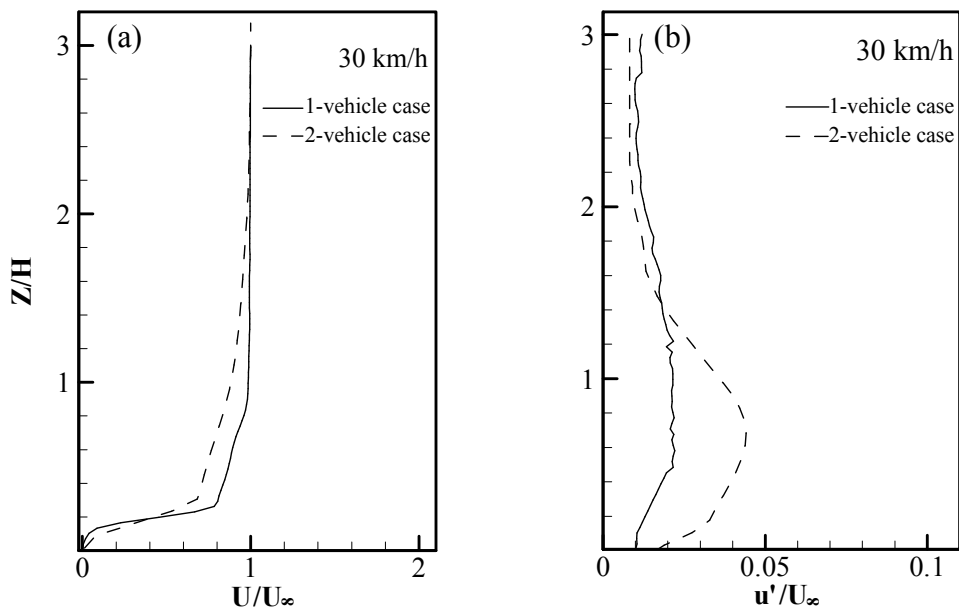


Figure 4.8 (a) \bar{U}/U_∞ and (b) u'/U_∞ profiles in X - Z plane at $1H$ ahead of the last vehicle front, V1 for one- and two-vehicle cases ($\alpha = 25^\circ$) at 30 km/h (Huang et al., 2009a).

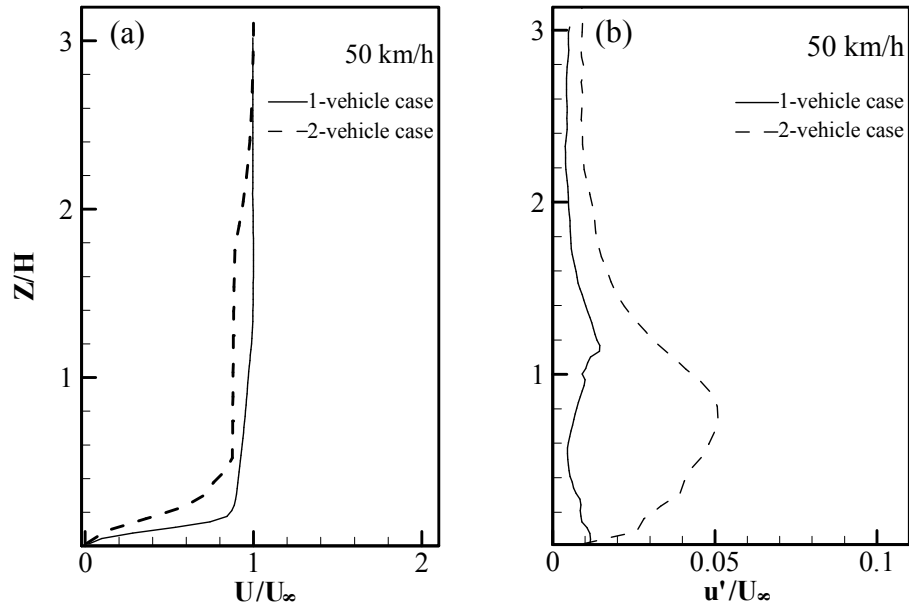


Figure 4.9 (a) \bar{U}/U_∞ and (b) u'/U_∞ profiles in X - Z plane at $1H$ ahead of the last vehicle front, V1 for one- and two-vehicle cases ($\alpha = 25^\circ$) at 50 km/h (Huang et al., 2009a).

Figures 4.10(a) to (c) show the normalized vorticity, $\varpi_y \cdot H/U_\infty$ in X - Z plane for one-, two- and three- vehicle cases at 10 km/h, respectively. The area encircled by solid contour line represents that the air flow here are rotating in counter clockwise direction while the area encircled by the dotted contour line represents that the air flow here are rotating in clockwise direction. The higher the contour value, the faster the rotational speed is. Again the preceding vehicle, V2 makes a more noticeable difference in the value of vorticity than in structure. Peak vorticity values are changed from (-12.1, 7.5) to (-9.8, 7.0) by V2. But the second preceding vehicle, V3 has almost no effect on the vorticity value over the rear slant of V1. Its effect on the positive signed vortex in the lower part of the wake region is still discernible. From Figure 4.10(c), the peak vorticity values for the three preceding vehicle cases are (-9.9, 6.7).

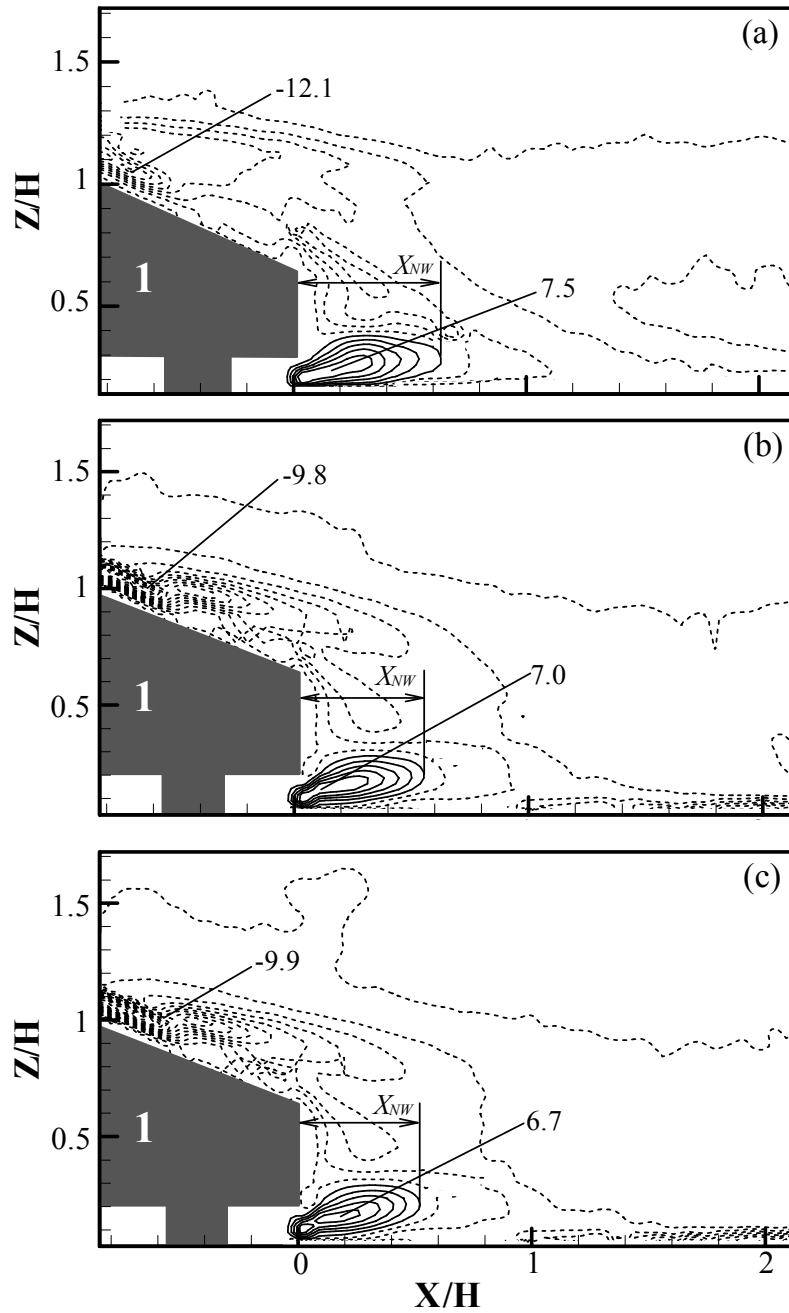


Figure 4.10 Vorticity, $\bar{\omega}_z \cdot H/U_\infty$ contours in X - Z plane for (a) one-vehicle, (b) two-vehicle and (c) three-vehicle cases ($\alpha = 25^\circ$) at 10 km/h (Contour base line = 1, step = 1) (Huang et al., 2009a).

Figures 4.10(a) to (c), it can be concluded that the two preceding vehicles change the lower part of the wake region more severely than the upper part. The normalized circulation values of positive signed vortex structure, $\bar{\Gamma}_y/(U_\infty \cdot H)$

are 2.5, 2.1 and 2.0 for one-vehicle, two-vehicle and three-vehicle cases at 10 km/h, respectively (i.e. 16% reduction by one preceding vehicle, V2 alone or 36% reduction by both preceding vehicles, V2 and V3). The changes in circulation values caused by the preceding vehicles are more prominent than in the peak vorticity values because the vortex sizes are also decreased.

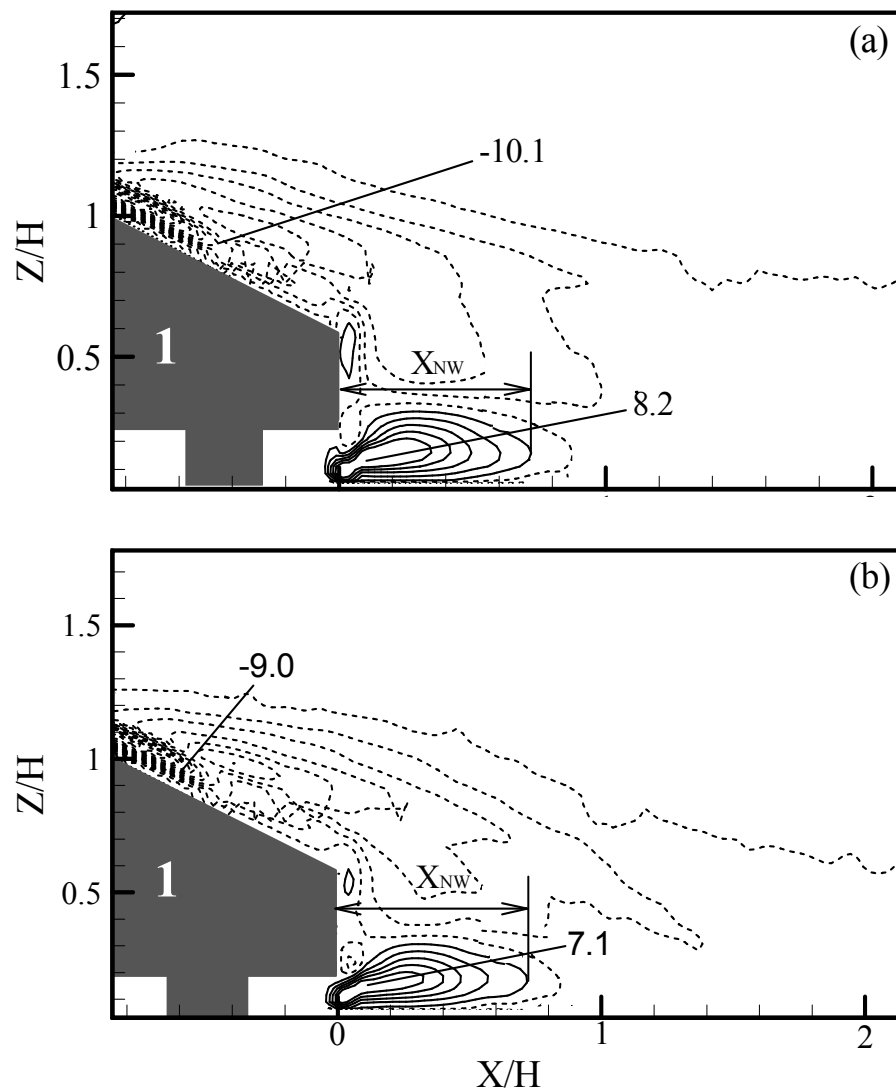


Figure 4.11 Vorticity, $\bar{\omega}_z \cdot H/U_\infty$ contours in X - Z plane for (a) one-vehicle, and (b) two-vehicle cases at 30 km/h (Contour base line = 1, step = 1).

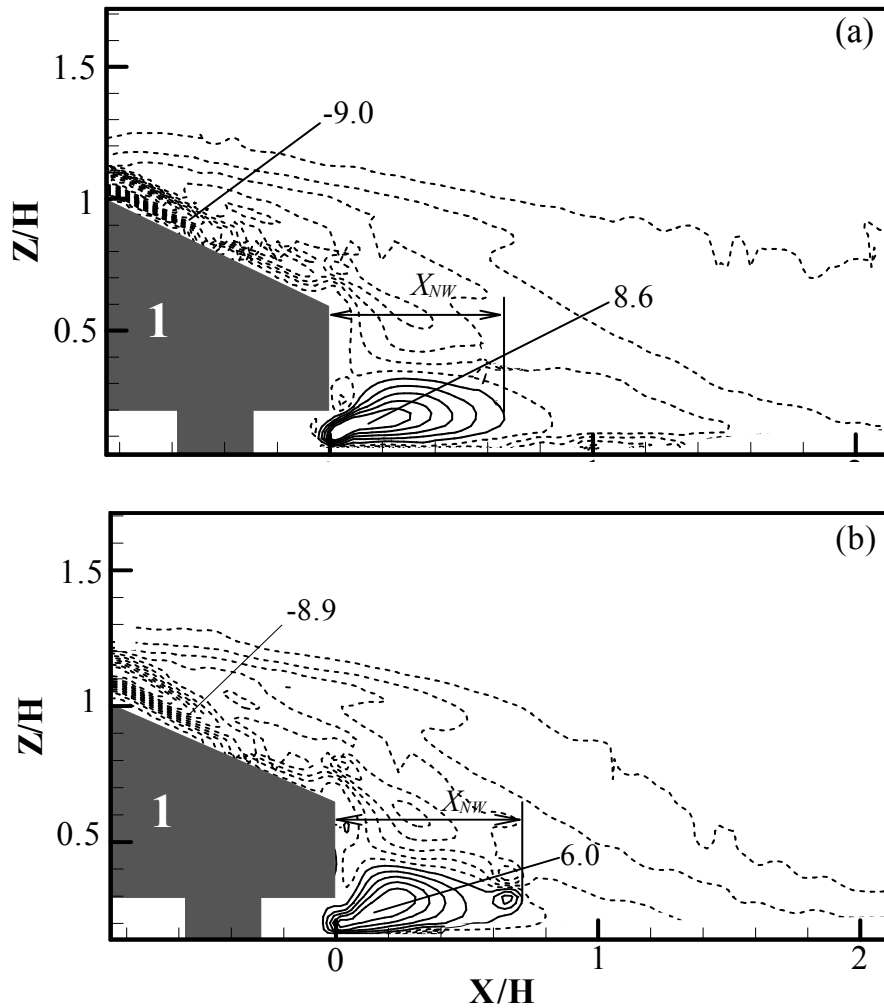


Figure 4.12 Vorticity, $\varpi_z \cdot H/U_\infty$ contours in X - Z plane for (a) one-vehicle (Huang et al., 2009a) and (b) two-vehicle cases at 50 km/h (Contour base line = 1, step = 1).

The extension of near wake separation bubble, X_{NW} was previously reported to be $0.65H$ by experiment (Lienhart and Becker, 2003) or by large eddy simulation (LES) approach (Krajnovic and Davidson, 2005a). The flow structure in Figure 4.10(a) shows that X_{NW} is around $0.64H$ for 10 km/h and remains almost the same for up to 50 km/h as shown in Figures 4.11(a) and 4.12(a). The results presented good agreement with the experimental and numerical results obtained from Lienhart and Becker (2003) and Krajnovic and Davidson (2005a),

respectively for a single vehicle case at these three studied vehicle speeds. Figure 4.10(a) also justifies the removal of a small vortex generated by inadequate resolution in coarse and medium grid using LES approach as described by Krajnovic and Davidson (2005a). They assumed that “the Reynolds number and resolution requirements could be decreased if the positions of the recirculation regions in the flow are defined by the geometry rather than by the viscosity and upstream conditions”. In the present study, the values of X_{NW} remain constant from 10 to 50 km/h for no preceding vehicle case as shown in Figures 4.10(a), 4.11(a) and 4.12 (a), and justify their assumption for single vehicle case. However, the values of X_{NW} will decrease with increasing number of the preceding vehicle(s) in a queue arrangement (e.g., $0.64H$, $0.54H$ and $0.52H$ for one-, two- and three-vehicle cases at 10 km/h, respectively as shown in Figures 4.10(a), (b) and (c), $0.64H$ and $0.61H$ for one- and two-vehicle cases at 30 km/h, respectively as shown in Figures 4.11(a) and (b), or $0.64H$ and $0.62H$ for one- and two-vehicle cases at 50 km/h, respectively as shown in Figures 4.12(a) and (b)). This shrinkage in length of X_{NW} might be caused by the reducing blockage effect of the preceding vehicle(s) in respect to the height over ground as shown in Figures 4.7(a), 4.8(a) and 4.9(a). Generally speaking, the length of X_{NW} decreases with increasing vehicle speed by comparing with and without preceding vehicle(s) cases. The length reduction of X_{NW} is 3% and 16% for vehicle speed at 50 km/h and 10 km/h, respectively.

At higher vehicle speed of 30 km/h or 50 km/h, the preceding vehicle, V2 may reduce the peak vorticity values of $\overline{\omega}_y \cdot H/U_\infty$ from (-10.1, 8.2) to (-9.0, 7.1) or (-9.0, 8.6) to (-8.9, 6.0) respectively, as shown in Figures 4.11 and 4.12. The

corresponding normalized circulation values $\bar{\Gamma}_y / (U_\infty \cdot H)$ for positive signed vortex structure are also reduced from 3.5 to 3.0 (i.e., 14% reduction) or from 3.1 to 2.3 (i.e., 25% reduction), respectively. The changes induced by the preceding vehicle in the $\bar{\omega}_y \cdot H / U_\infty$ contours for these two vehicle speeds are less obvious than for 10 km/h while the positively signed recirculation zone still shows higher sensitivity than other negatively signed parts.

The Reynolds shear stress, $\overline{u'w'} / U_\infty^2$ contours for one-, two and three-vehicle cases at 10 km/h are shown in Figures 4.13(a), (b) and (c). The peak values of $\overline{u'w'} / U_\infty^2$ in the lower wake region consistently decrease from 0.025 to 0.015 and further to 0.011 with the addition of the preceding vehicles, V2 and V3 while the values of $\overline{u'w'} / U_\infty^2$ over the surface of rear slant back remains 0.020 regardless of the presence of the preceding vehicle(s). It should be noted that the occurrence positions of this peak value of $\overline{u'w'} / U_\infty^2$ for 0.020 get much closer to the surface of rear slant back and the pattern of contour lines on top is significantly altered by the preceding vehicle(s). As the exhaust tailpipe of vehicle is often positioned in the lower part of the vehicle rear, it can be inferred that preceding vehicles may have considerable effect on the vehicular exhaust pollutant dispersion by decreasing $\overline{u'w'} / U_\infty^2$ for 40% or more. Future research is recommended for having more thorough understanding of the lower wake region.

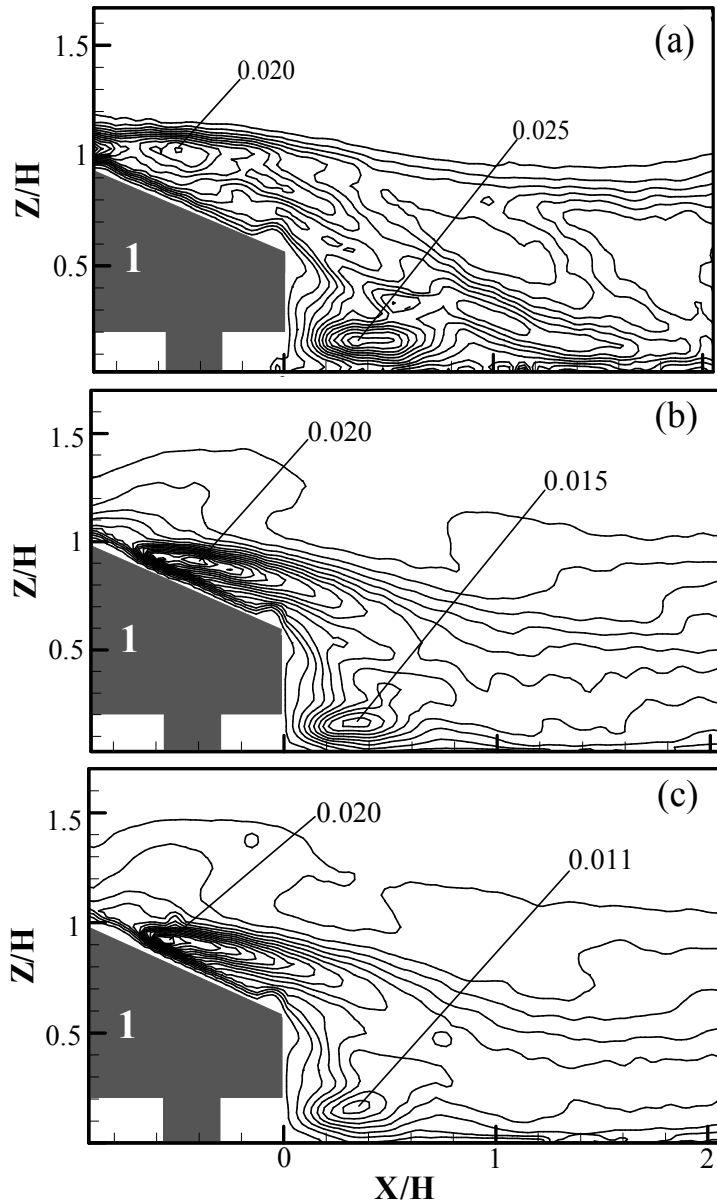


Figure 4.13 Reynolds shear stress, $|\overline{u'w'}|/U_\infty^2$ contours in X - Z plane for (a) one-vehicle, (b) two-vehicle and (c) three-vehicle cases ($\alpha = 25^\circ$) at 10 km/h (Contour base line = 0.0025, step = 0.0025) (Huang et al., 2009a).

The preceding vehicle, V2 also reduces the peak values of Reynolds shear stress $\overline{u'w'}/U_\infty^2$ from (0.030, 0.034) to (0.034, 0.028) or from (0.023, 0.027) to (0.036, 0.025) for 30 and 50 km/h, respectively as shown in Figures 4.14 and 4.15, in the wake of vehicle V1. The changes in $\overline{u'w'}/U_\infty^2$ values and patterns induced

by the preceding vehicles decrease with increasing vehicle spacing. It should be noted that the values of $\overline{u'w'}/U_\infty^2$ are prominently weakened by the preceding vehicles while in contrast the values of $\overline{u'v'}/U_\infty^2$ are strengthened.

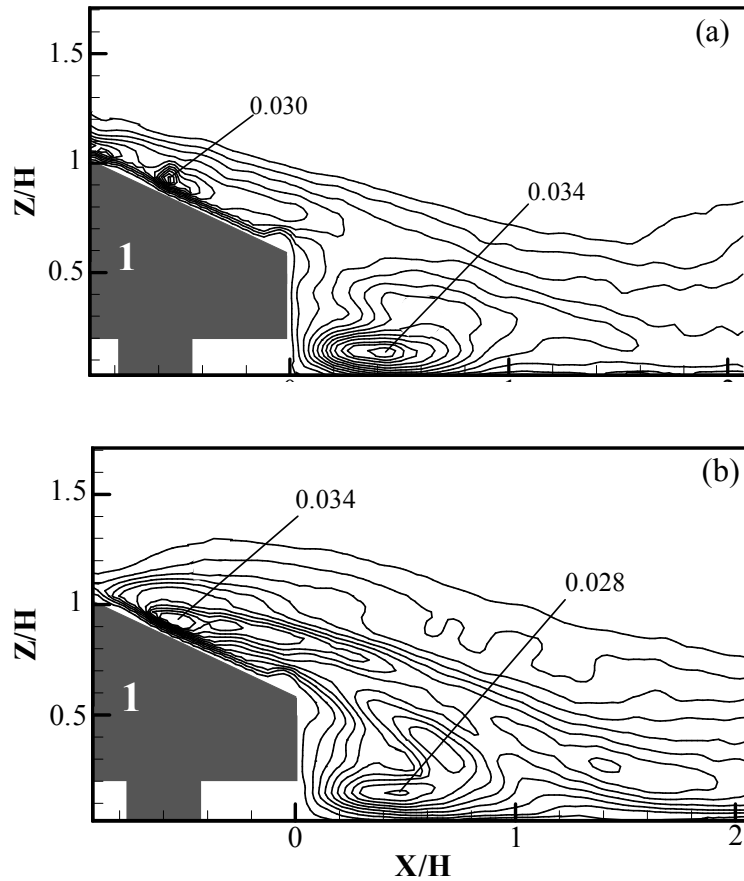


Figure 4.14 Reynolds shear stress, $\overline{|u'w'|}/U_\infty^2$ contours in X - Z plane for (a) one-vehicle and (b) two-vehicle ($\alpha = 25^\circ$) at 30 km/h (Contour base line = 0.0025, step = 0.0025).

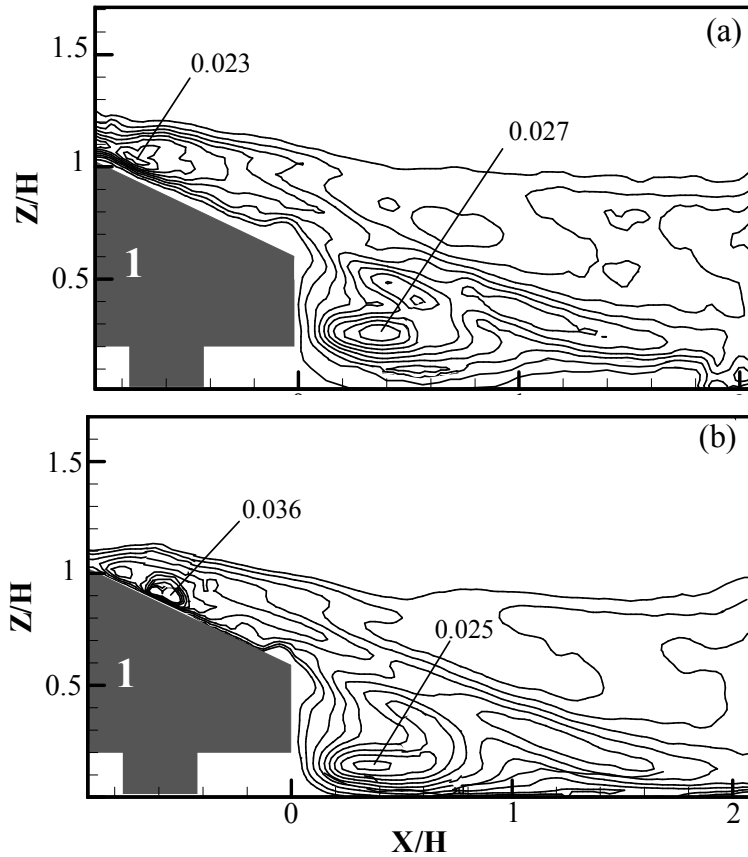


Figure 4.15 Reynolds shear stress, $|\overline{u'w'}|/U_\infty^2$ contours in X - Z plane for (a) one-vehicle and (b) two-vehicle ($\alpha = 25^\circ$) at 50 km/h (Contour base line = 0.0025, step = 0.0025).

4.3.2 Wake structure of one-, two- and three-vehicle cases ($\alpha = 25^\circ$) in Y - Z planes for different vehicle speeds

4.3.2.1 Vorticity contours in Y - Z plane at $X/H = 1$ for the vehicles ($\alpha = 25^\circ$) at different vehicle speeds

Time-averaged vector map in Y - Z plane at downstream distance $X/H = 1$ for one-vehicle ($\alpha = 25^\circ$) was compared with the experimental work of Gosse et al. (2011) as shown in Figure 4.16. Despite of the slightly different studied model vehicles and measurement techniques, the similarity in the locations and shapes of vortex justifies our experimental methodology.

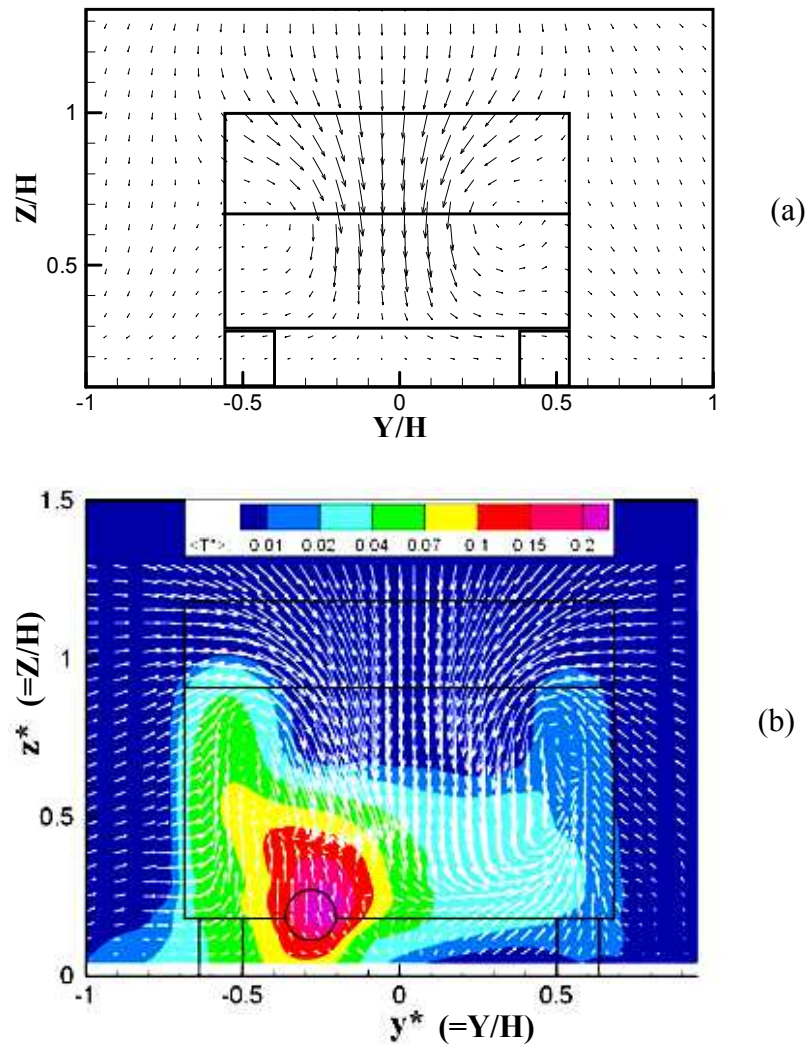


Figure 4.16 Time-averaged vector map in Y - Z plane at the downstream distance $X/H = 1$ for one-vehicle ($\alpha = 25^\circ$) (a) black arrows from the present experimental study measured by PIV at 50 km/h and (b) white arrows from Figure 5(d) of Gosse et al. (2011) measured by LDA at 45 km/h.

Normalized streamwise vorticity, $\bar{\omega}_x \cdot H/U_\infty$ contours in Y - Z plane at $X/H = 1$ for one-vehicle case at 10, 30 and 50 km/h are shown in Figures 4.17(a), (b) and (c), respectively. The flow patterns show good agreement with the results obtained from the experimental fluid dynamics (EFD) by Kozaka et al. (2004) and computational fluid dynamics (CFD) by Chan et al. (2008a). For 10 km/h case, a pair of counter rotating vortices is distributed at $Y/H = \pm 0.25$ and $Z/H = 0.65$ with

the maximum vorticity, $\varpi_x \cdot H/U_\infty$ values (-2.35, 2.77). The first preceding vehicle, V2 at $3.1H$ upstream from the following vehicle, V1 has no noticeable effect on the pattern of $\varpi_x \cdot H/U_\infty$ contours, but reduces its maximum vorticity values to (-2.00, 2.22). The second preceding vehicle, V3 still has no prominent effect on the contour pattern, though it can further reduce the maximum vorticity to (-1.91, 2.16). The corresponding normalized circulation values $\bar{\Gamma}_x / (U_\infty \cdot H)$ for one-, two- and three-vehicle cases at 10 km/h are 3.9, 3.7 and 3.5, respectively (i.e. 4% reduction by the preceding vehicle, V2 alone or 10% reduction by both preceding vehicles, V2 and V3). Therefore it can be concluded that the presence of the preceding vehicles does not have much effect on the wake structure of V1 but has more obvious effect on the values of vorticity and circulation in the $Y-Z$ plane, as in the other two planes (i.e., $X-Y$ and $X-Z$). Contrary to the results of 10 km/h in $X-Z$ plane, the effect of the preceding vehicles is more prominent in peak vorticity than in circulation values in $Y-Z$ plane.

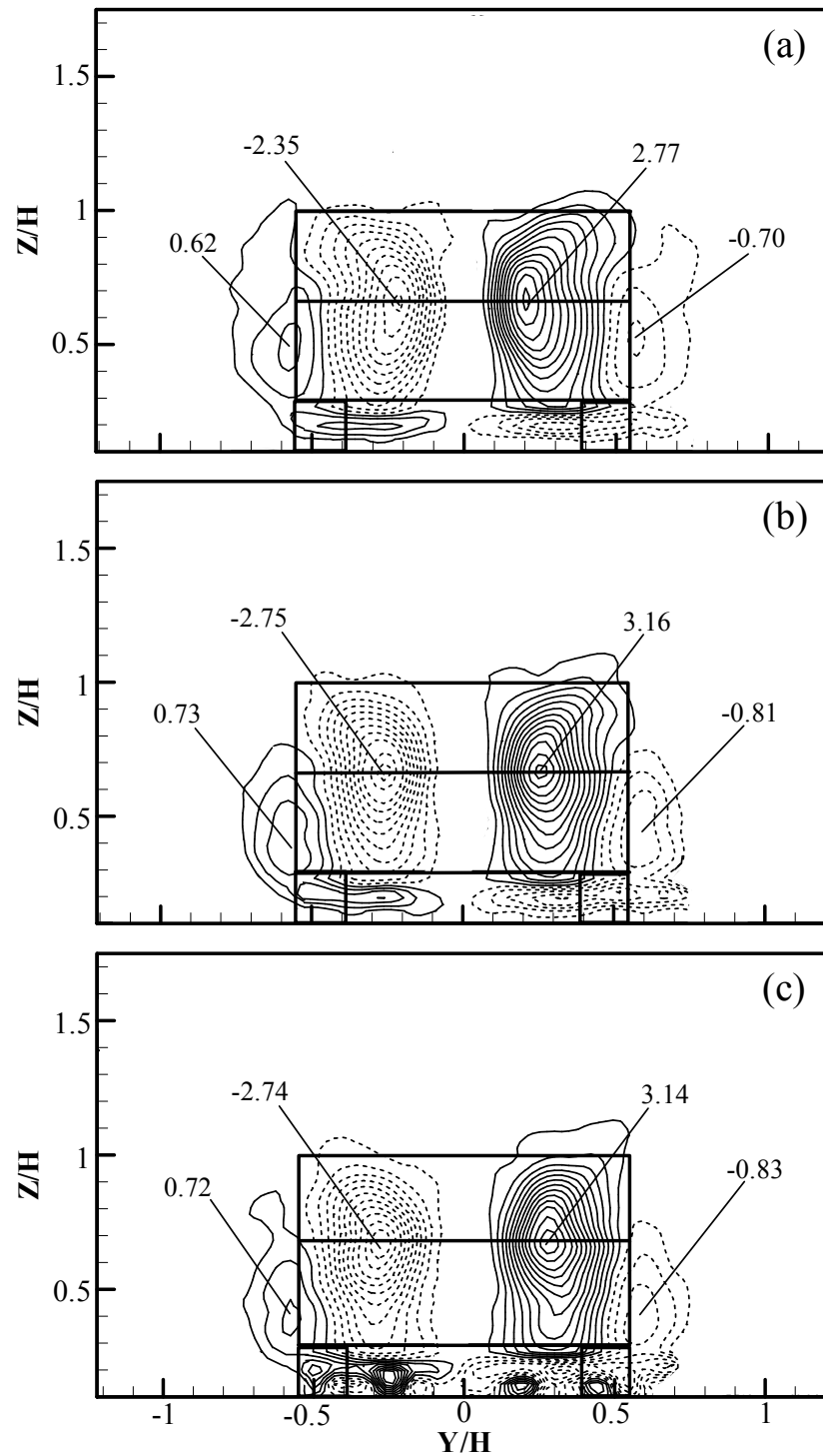


Figure 4.17 Vorticity, $\bar{\omega}_x \cdot H/U_\infty$ contours in $Y-Z$ plane at $X/H = 1$ for one-vehicle case ($\alpha = 25^\circ$) at (a) 10 km/h; (b) 30 km/h and (c) 50 km/h (Contour base line = 0.2, step = 0.2) (Huang et al., 2009a).

In addition to the 10km/h case, the pattern of $\varpi_x \cdot H/U_\infty$ contours is also observed to be independent of the preceding vehicle, V2 for 30 km/h and 50 km/h cases by comparing the contours of $\varpi_x \cdot H/U_\infty$ with and without V2 cases. The effect of the preceding vehicle, V2 is also more obvious in vorticity values than in wake structure of V1. For 30 km/h case, the preceding vehicle, V2 reduces the maximum vorticity value $\varpi_x \cdot H/U_\infty$ of the following vehicle, V1 from (-2.75, 3.16) to (-2.29, 2.34) (i.e. 22% reduction) and the normalized circulation value $\bar{\Gamma}_x / (U_\infty \cdot H)$ from 3.9 to 3.4 (i.e. 13% reduction). For 50 km/h case, the preceding vehicle, V2 reduces the maximum vorticity value of the following vehicle, V1 from (-2.74, 3.14) to (-2.21, 2.61) (i.e. 18% reduction) and the normalized circulation value $\bar{\Gamma}_x / (U_\infty \cdot H)$ from 4.0 to 3.5 (i.e. 14% reduction). It should be noted that the vehicle spacing is almost three times for 30 km/h (i.e., $9.3H$) or five times for 50 km/h (i.e., $15.5H$) long if compared with that of 10 km/h case (i.e., $3.1H$). However, the reduction in maximum vorticity value of the following vehicle, V1 induced by the preceding vehicle(s) (i.e., V2 only or both V2 and V3) is still comparable to the 10 km/h case (around 17% reduction). It reveals that the decreasing effect of the preceding vehicle on the vorticity of trailing vortices from a following vehicle is insensitive to the vehicle spacing. Watkins and Vano (2008) have also recently presented similar findings for the relationship between the vehicle spacing and drag force. The curve of drag coefficient for the following vehicle is almost parallel to that for an isolated vehicle regardless of the large vehicle spacing (i.e., $X/L \geq 1$ or $X/H \geq 3.6$).

4.3.2.2 Vorticity contours in Y - Z plane at $X/H = 3$ for the vehicles ($\alpha = 25^\circ$) at different vehicle speeds

Normalized streamwise vorticity, $\bar{\omega}_x \cdot H/U_\infty$ contours in Y - Z plane at $X/H = 3$ for one-vehicle case at 10, 30 and 50 km/h are shown in Figures 4.18(a), (b) and (c). Because downwash flow is the main stream in the near-wake region of the vehicle at $X/H = 3$, it pushes the longitudinal vortices closer to the ground if compared with the Figure 4.17 at $X/H = 1$. The maximum $\bar{\omega}_x \cdot H/U_\infty$ values of the trailing vortices for one-vehicle case at 10 km/h are (-2.35, 2.77) at $X/H = 1$, (-1.90, 1.94) at $X/H = 2$ and (-1.18, 1.35) at $X/H = 3$. At $X/H = 3$, the presence of the preceding vehicle(s) cannot induce any obvious effect in the wake structure, as happened at $X/H = 1$. However, the reduction in vorticity values induced by the preceding vehicle is still noticeable. The maximum $\bar{\omega}_x \cdot H/U_\infty$ values of the trailing vortices from the vehicle, V1 are reduced from (-1.18, 1.35) to (-1.09, 1.21) (i.e., 9% reduction) by the preceding vehicle, V2 only or reduced from (-1.18, 1.35) to (-0.95, 1.12) (i.e., 19% reduction) by both preceding vehicles, V2 and V3. The corresponding normalized circulation values $\bar{\Gamma}_x / (U_\infty \cdot H)$ for the one-, two- and three-vehicle cases at 10 km/h are 2.9, 2.6 and 2.0, respectively (i.e., 10% reduction by V2 alone or 31% reduction by both V2 and V3).

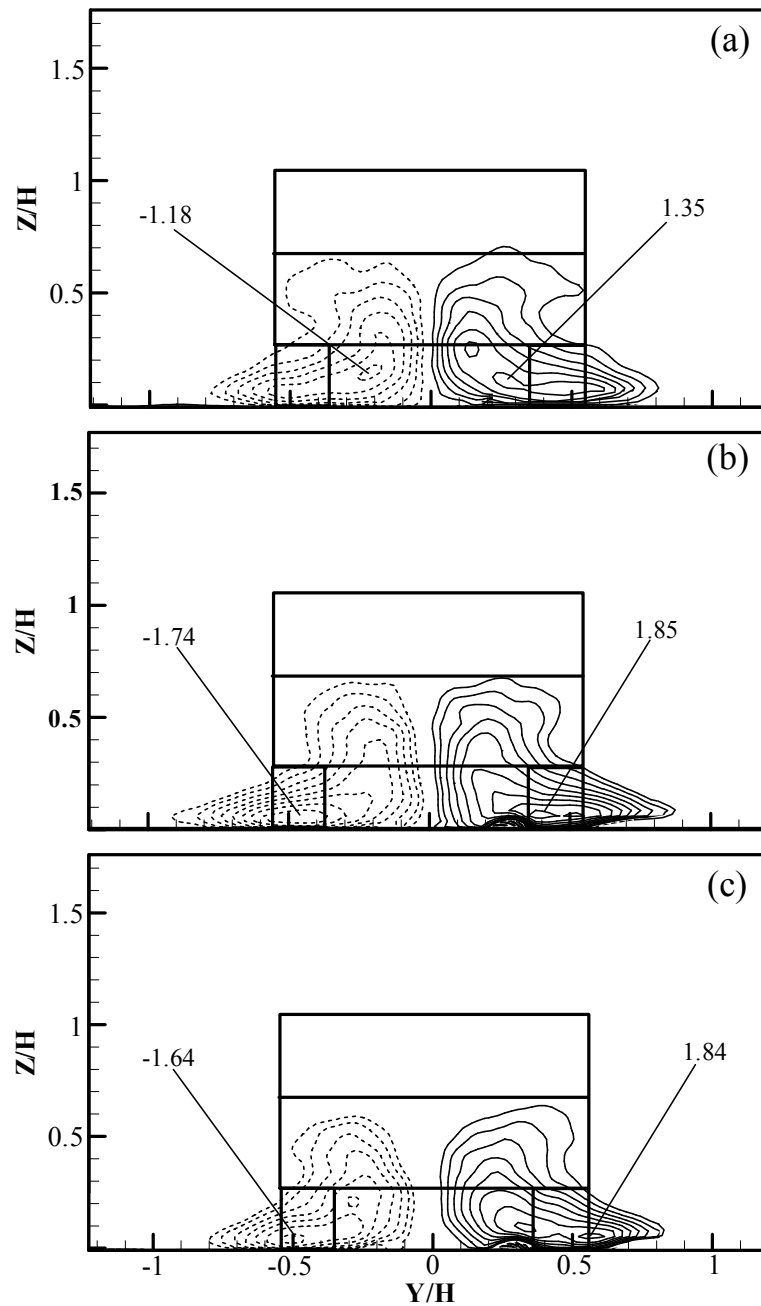


Figure 4.18 Vorticity, $\bar{\omega}_x \cdot H/U_\infty$ contours in Y - Z plane at $X/H = 3$ for one-vehicle case ($\alpha = 25^\circ$) at (a) 10 km/h, (b) 30 km/h and (c) 50 km/h (Contour base line = 0.2, step = 0.2) (Huang et al., 2009a).

The presence of the preceding vehicle, V2 for the 30 and 50 km/h cases still cannot induce any obvious effect in the wake structure at $X/H = 3$ but produces some differences in vorticity values. Therefore only vorticity contours for

one-vehicle cases at these two vehicle speeds are shown in Figures 4.18(b) and (c), respectively. The maximum vorticity values $\bar{\omega}_x \cdot H/U_\infty$ of the trailing vortices from the vehicle, V1 are reduced from (-1.74, 1.85) to (-1.52, 1.82) (i.e., 7% reduction) for 30 km/h or reduced from (-1.64, 1.84) to (-1.66, 1.81) (i.e., 0.3% reduction) for 50 km/h caused by the preceding vehicle, V2. The normalized circulation values $\bar{\Gamma}_x / (U_\infty \cdot H)$ of trailing vortices are reduced by V2 alone from 3.8 to 3.7 (i.e. 3% reduction) for 30 km/h and 4.2 to 3.9 (i.e. 9% reduction) for 50 km/h, respectively.

4.3.3 Summary of the characteristics of maximum vorticity values for trailing vortices at different X/H locations and vehicle speeds for one-, two- and three-vehicle cases ($\alpha = 25^\circ$)

Longitudinal peak vorticity values measured behind the last vehicle, V1 for different vehicle speeds and arrangements of the preceding vehicle(s) are summarized in Table 4.1.

Vehicle speed	Number of the preceding vehicle(s)	$X/H = 1$	$X/H = 2$	$X/H = 3$
10 km/h	0	2.56	1.92	1.27
	1	2.11	1.50	1.25
	2	2.04	1.28	1.04
30 km/h	0	2.96	2.07	1.80
	1	2.31	1.86	1.67
50 km/h	0	2.94	2.08	1.74
	1	2.41	1.83	1.73

Table 4.1 Average longitudinal peak vorticity behind the last vehicle, V1 ($\alpha = 25^\circ$) for different vehicle speeds and arrangements of the preceding model vehicle(s) (Huang et al., 2009a).

4.3.4 Summary conclusions of a queue of vehicles ($\alpha = 25^\circ$)

The three-dimensional flow structures of a queue of vehicles ($\alpha = 25^\circ$) (i.e., one-, two- and three-vehicle cases) were investigated comprehensively in a closed-circuit wind tunnel using particle image velocimetry (PIV) for the typical urban vehicle speeds (i.e., 10, 30 and 50 km/h).

The longitudinal vortices are found to be counter-rotating and moving downstream at relatively low velocity if compared with their surrounding flow. Inside the longitudinal vortices, there are velocity gradients along the vortex radius for the downstream movement, and the lowest downstream velocity occurs at vortex cores. The velocity difference is up to $0.25U_\infty$ between the center and edge of longitudinal vortices.

The wake flow structure of a vehicle queue is mainly dominated by its immediate upstream vehicle rather than the incoming flow altered by the preceding vehicle(s). While the downstream vehicle has the most pronounced effect on the wake flow structure, all the upstream vehicle(s) still has/have some effects. The changes induced by the upstream vehicles in wake flow structure are often within the order of 10%, and at an order of 20% in flow properties (e.g., mean and turbulent velocity, vorticity, shear stress etc.). In the present study, it was observed that the mean and turbulent velocities are more sensitive to vehicle spacing than the shear stress and vorticity.

Cross-sectional turbulence distribution is still non-uniform in the far-wake region. The low turbulence occurs at the center part of the wake flow while the

high turbulence occurs at its two sides. For such a turbulence distribution, it may lead to considerable underestimation on turbulence magnitude if the measurement is only taken along the centerline of the vehicle wake.

4.4 Results and Discussion for Queue Effect of the Studied Vehicles ($\alpha = 60^\circ$) on the Flow Structures in the Vehicle Wake

4.4.1 Wake structure in X - Y plane at $Z/H = 0.5$ for the vehicles ($\alpha = 60^\circ$) at different vehicle speeds

4.4.1.1 Velocity profiles, \bar{U}/U_∞ and u'/U_∞ for the vehicles ($\alpha = 60^\circ$) at 10 km/h

Figures 4.19(a) and (b) show the cross-sectional normalized velocity, \bar{U}/U_∞ and turbulence, u'/U_∞ profiles at $1H$ upstream from the vehicle, V1 and $Z = 0.5H$ above the ground. In Figure 4.19(a), the profile of \bar{U}/U_∞ for one-vehicle case at 10 km/h shows a shallow valley in the middle. Again, the maximum \bar{U}/U_∞ deficit is 12% due to the blockage effect from the vehicle, V1 downstream. For two-vehicle case, the curve shape is significantly altered in the wake region of the preceding vehicle, V2 within $-0.8 \leq Y/H \leq 0.8$. Unlike the vehicles for $\alpha = 25^\circ$ where the longitudinal vortex produces two deep footmarks (marked by two “+”) on the \bar{U}/U_∞ profile as shown in Figure 4.2(a), while the longitudinal vortex is too weak to be determined from the \bar{U}/U_∞ profile and some unclear footmark can be seen from u'/U_∞ profile for the vehicles ($\alpha = 60^\circ$) as shown in Figure 4.19.

The results of two- and three-vehicle cases at 10 km/h in Figure 4.19(a) show that two preceding vehicle case (i.e., both V2 and V3) has some minor

changes in the wake structure if compared with the single preceding vehicle case (i.e., V2 only). The expanded wake from the vehicle, V3 can be observed at the two wider sides of its u/U_∞ curve. The value of mean velocity profile, \bar{U}/U_∞ for its center is reduced from 0.87 to 0.23 (i.e., 74% reduction) which is caused by the single wake effect of V2 alone, and further reduction to 0.15 (i.e., 35% reduction from 0.23) by the double blockage effects of V2 and V3. On the other hand, the value of mean turbulence, u'/U_∞ for these two longitudinal vortex centers is increased from 0.01 (i.e., background level) to 0.13 (i.e., 1200% increment) by the preceding vehicle, V2 alone, and further up to 0.14 (i.e., 7.7% increment from 0.13) by both preceding vehicles, V2 and V3 due to the reduction in U_∞ .

Furthermore, as the shape of curve reflects local flow structure, the spatial coincidence of curves for two- and three-vehicle cases in Figures 4.19(a) and (b) reveals that the preceding vehicle, V3 does not have obvious effect on the wake structure (e.g., the position and diameter of longitudinal vortex) of the following vehicle, V2. It can be inferred that the wake structure behind V1 will not be significantly altered by both V2 and V3.

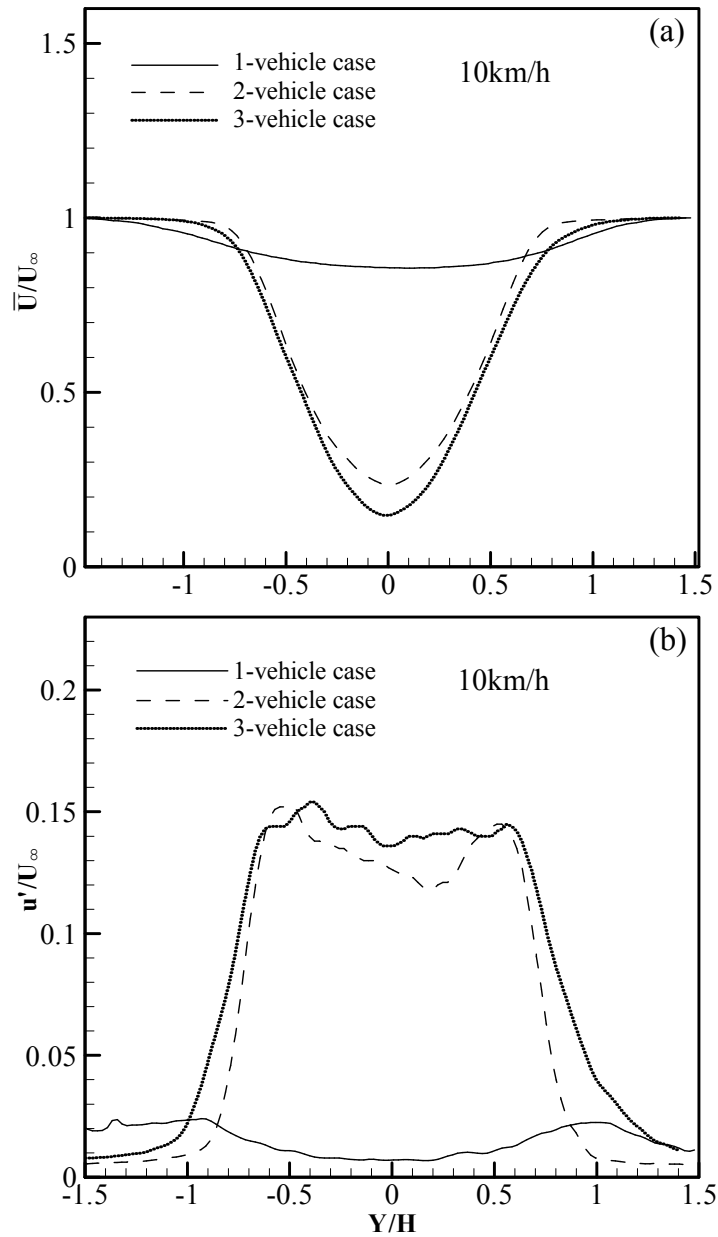


Figure 4.19 Horizontal cross-sectional profiles: (a) \bar{U}/U_∞ and (b) u'/U_∞ at $1H$ ahead of the last vehicle front, $V1$ and $Z = 0.5H$ above the ground for one-, two- and three-vehicle cases ($\alpha = 60^\circ$) at 10 km/h (i.e., $3.1H$ vehicle spacing).

4.4.1.2 Velocity profiles, \bar{U}/U_∞ and u'/U_∞ for the vehicles ($\alpha = 60^\circ$) at 30 km/h

Figures 4.20(a) and (b) show the cross-sectional velocity, \bar{U}/U_∞ and turbulence u'/U_∞ profiles at $1H$ upstream from the last following vehicle, $V1$ and $Z/H = 0.5$ for the vehicle speed at 30 km/h .

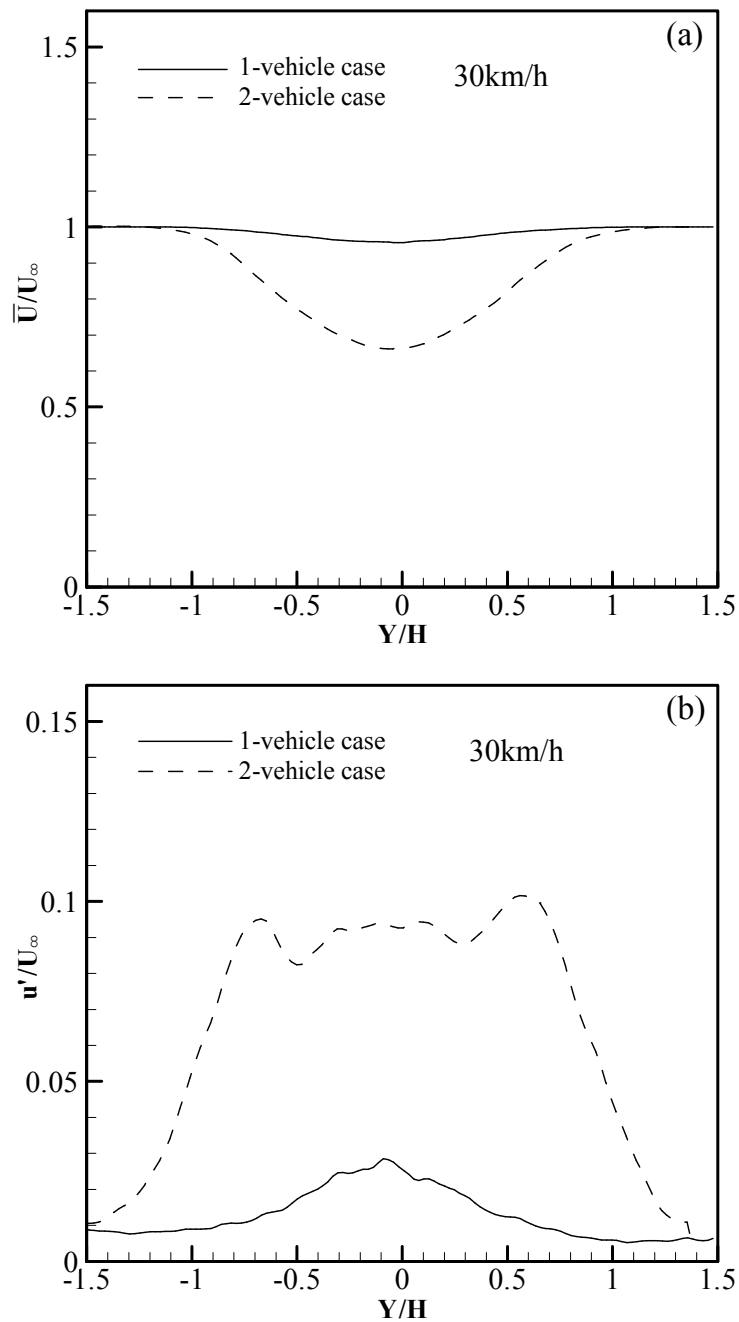


Figure 4.20 Horizontal cross-sectional profiles: (a) \bar{U}/U_∞ and (b) u'/U_∞ at $1H$ ahead of the last vehicle front, $V1$ and $Z = 0.5H$ above the ground for one- and two-vehicle cases ($\alpha = 60^\circ$) at 30 km/h (i.e., $9.3H$ vehicle spacing).

In Figure 4.20(a), the maximum deficit in normalized mean velocity, \bar{U}/U_∞ is decreased from 12% (for 10 km/h case) to 5% (for 30 km/h case) due to the suppression of blockage effect by the faster incoming flow. For the two-vehicle

case, the single valley of the dashed \bar{U}/U_∞ curve induced by the preceding vehicle, V2 is observed to be wider and shallower when it is compared with the two-vehicle case at 10 km/h in Figure 4.19(a). This shallower phenomenon might be caused by the increasing of vehicle spacing from $3.1H$ to $9.3H$.

4.4.1.3 Velocity profiles, \bar{U}/U_∞ and u'/U_∞ for the vehicles ($\alpha = 60^\circ$) at 50 km/h

Figures 4.21(a) and (b) show the cross-sectional velocity, \bar{U}/U_∞ and turbulence, u'/U_∞ profiles at $1H$ upstream from the last following vehicle, V1 and $Z/H = 0.5$ for the vehicle speed at 50 km/h. The values at the centers of \bar{U}/U_∞ curves for one- and two-vehicle ($\alpha = 60^\circ$) cases are 0.92 and 0.78, respectively while one- and two-vehicle ($\alpha = 25^\circ$) cases are 0.97 and 0.92, respectively. For u'/U_∞ curves, the difference between with and without preceding vehicle ($\alpha = 60^\circ$ or 25°) is about 3.3% or 1%, respectively. The center part of vehicle wake has the lowest turbulence intensity which is in sharp contrast to the preceding vehicle cases at 10 and 30 km/h. As the difference in the properties of incoming flow caused by the preceding vehicle can be as large as 14%, the blockage effect of the preceding vehicle cannot be ignored even in engineering applications if the vehicle spacing is less than $15H$. Hence, the preceding vehicle ($\alpha = 60^\circ$) has more impact on the air flow toward the following vehicle than a preceding vehicle with a rear slant angle of 25° (i.e., 0.14 versus 0.05 at 50 km/h for \bar{U}/U_∞).

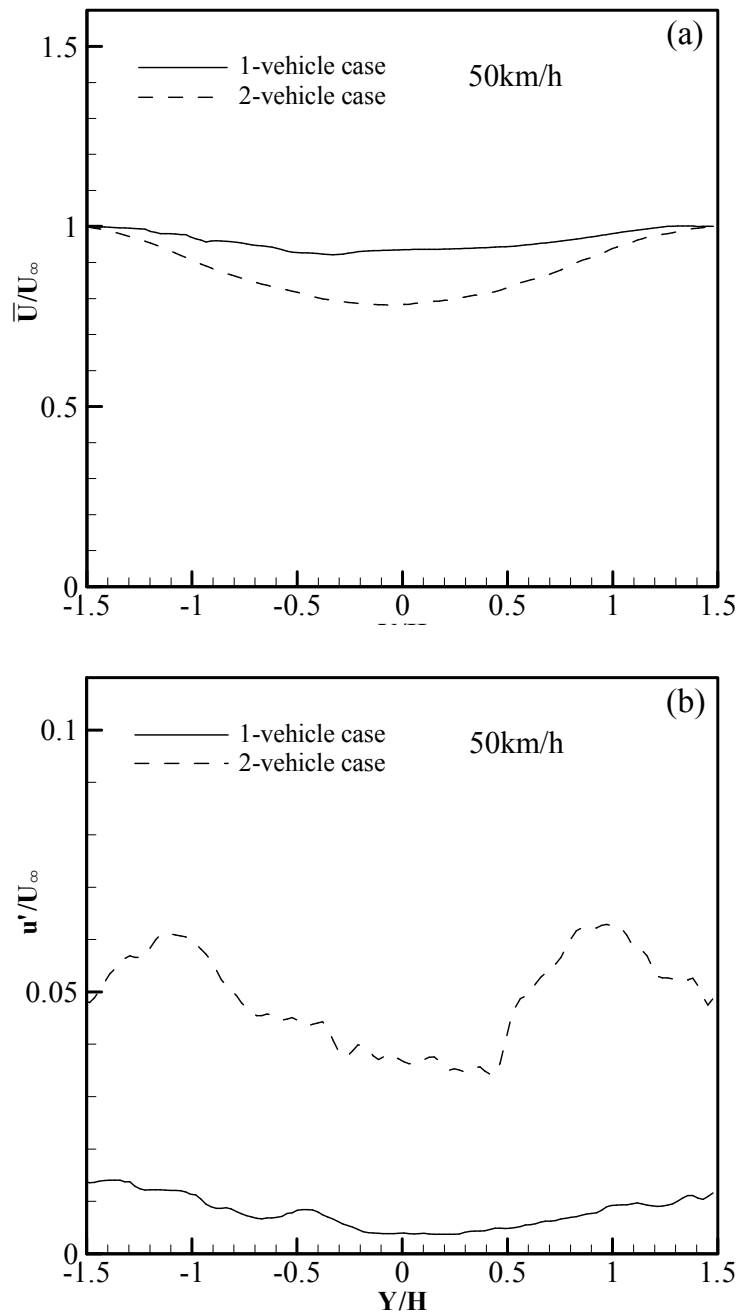


Figure 4.21 Horizontal cross-sectional profiles: (a) \bar{U}/U_∞ and (b) u'/U_∞ at $1H$ ahead the last vehicle front, $V1$ and $Z = 0.5H$ above the ground for one- and two-vehicle cases ($\alpha = 60^\circ$) at 50 km/h (i.e., $15.5H$ vehicle spacing).

The turbulence, u'/U_∞ profile in Figure 4.21(b) is still quite non-uniform even in this far-wake region, i.e. $14.5H$ downstream from the preceding vehicle, $V2$. The lowest turbulence, u'/U_∞ is about 0.038 which occurs at the center part of

the wake while the highest turbulence, u'/U_∞ is about 0.055 which occurs at the two sides. Such high turbulence is believed to be induced by the broken eddies from the trailing vortices. Comparing with the turbulence, u'/U_∞ profiles at downstream $X/H = 8.3$ and $X/H = 14.5$ in Figures 4.20(b) and 4.21(b), it can be observed that when air flows from near-wake region ($X/H < 10$) to far-wake region ($X/H > 10$), the turbulence in wake decreases for the whole cross-section profile, but the width of turbulent wake in the Y -direction has considerably expanded.

4.4.1.4 Streamwise velocity, \bar{U}/U_∞ contours for the vehicles ($\alpha = 60^\circ$) at different vehicle speeds

Figure 4.22 shows the contours of \bar{U}/U_∞ in X - Y plane at $Z/H = 0.5$ behind the last vehicle, V1 for one-vehicle case at 10 km/h. There is an ellipse shaped region of the reverse flow staying between $X/H = 0$ and 1 for all the one-, two- and three-vehicle cases. This region is in sharp contrast with all positive values for the one-, two- and three-vehicle cases ($\alpha = 25^\circ$). In addition, the preceding vehicles do not seem to have a strong effect on the flow structure and speed of wake flow on X - Y plane for the studied vehicle speeds, as shown in Figures 4.22 to 4.24.

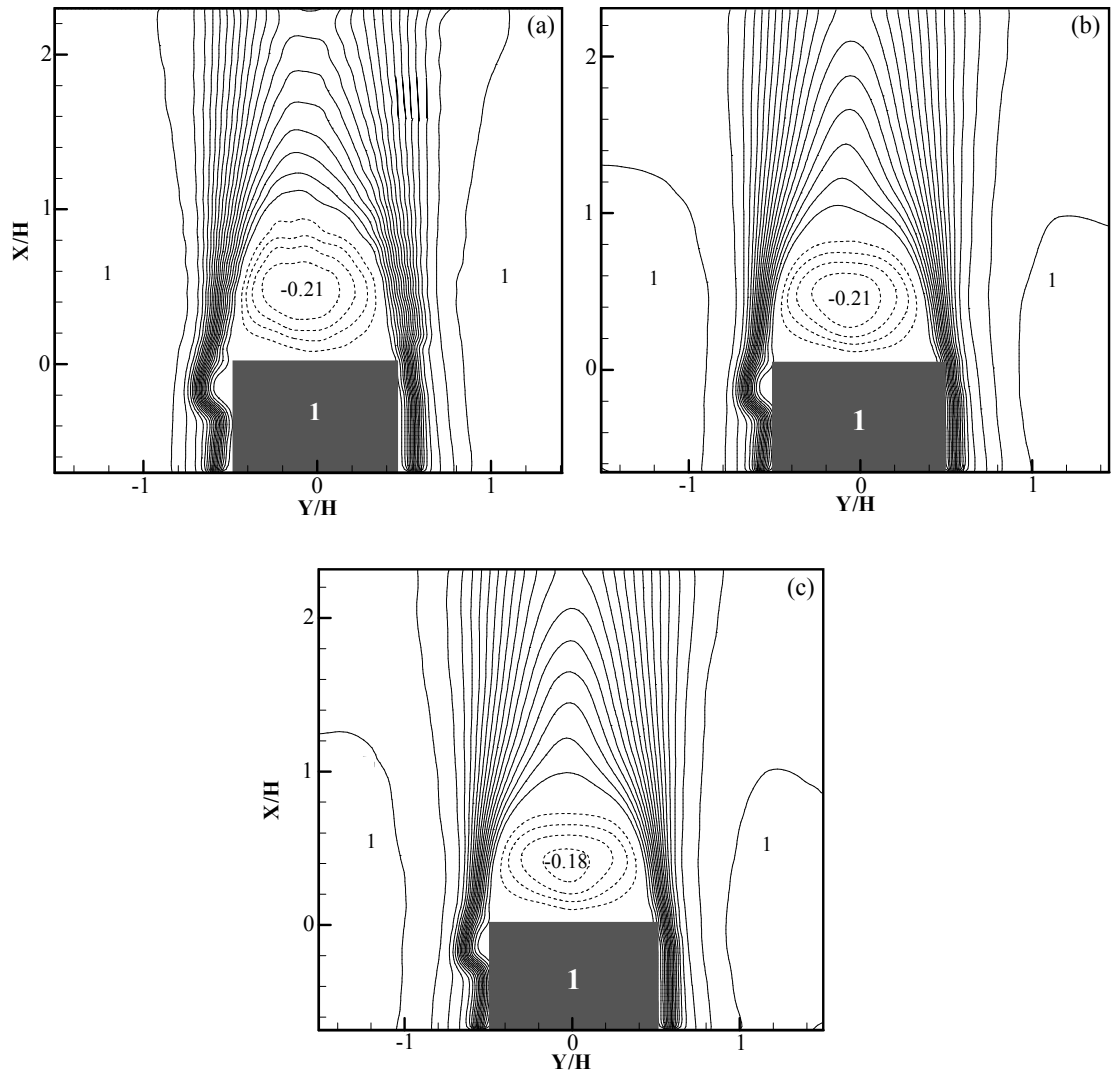


Figure 4.22 Contours of \bar{U}/U_∞ in X - Y plane at $Z/H = 0.5$ for (a) one-, (b) two- and (c) three-vehicle cases ($\alpha = 60^\circ$) at 10 km/h (Contour base line = 0.005, step = 0.005), where the dashed lines represent the negative values.

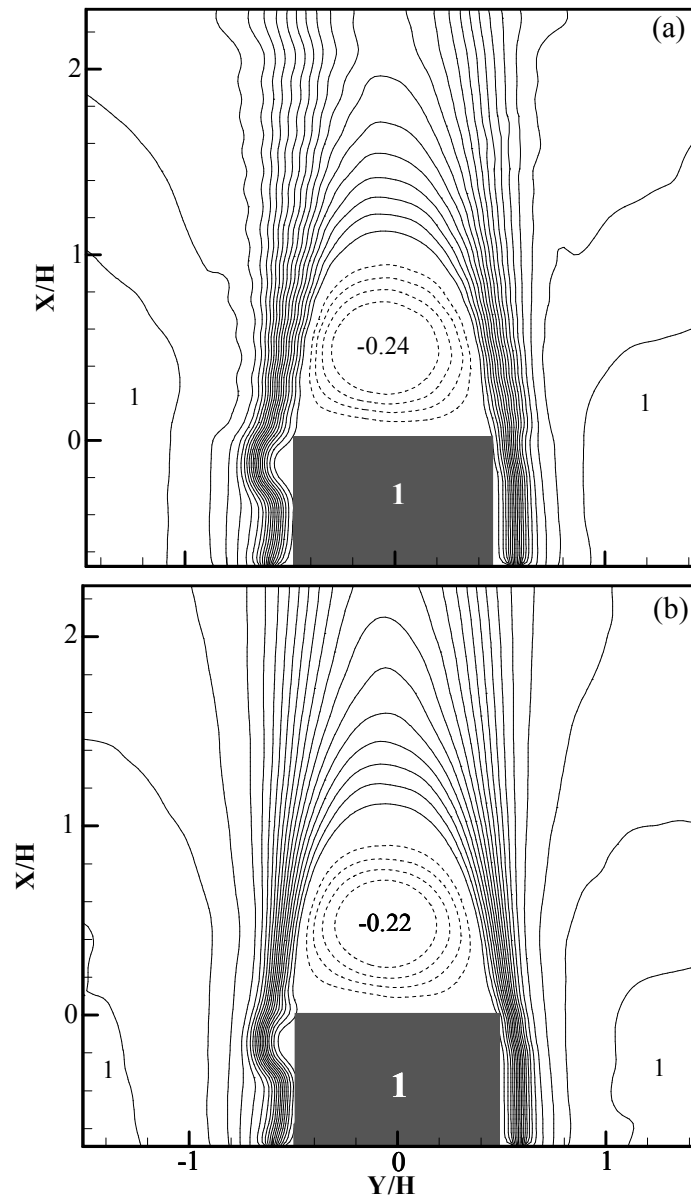


Figure 4.23 Contours of \bar{U}/U_∞ in X - Y plane at $Z/H = 0.5$ for (a) one- and (b) two-vehicle cases ($\alpha = 60^\circ$) at 30 km/h (Contour base line = 0.005, step = 0.005), where the dashed lines represent the negative values.

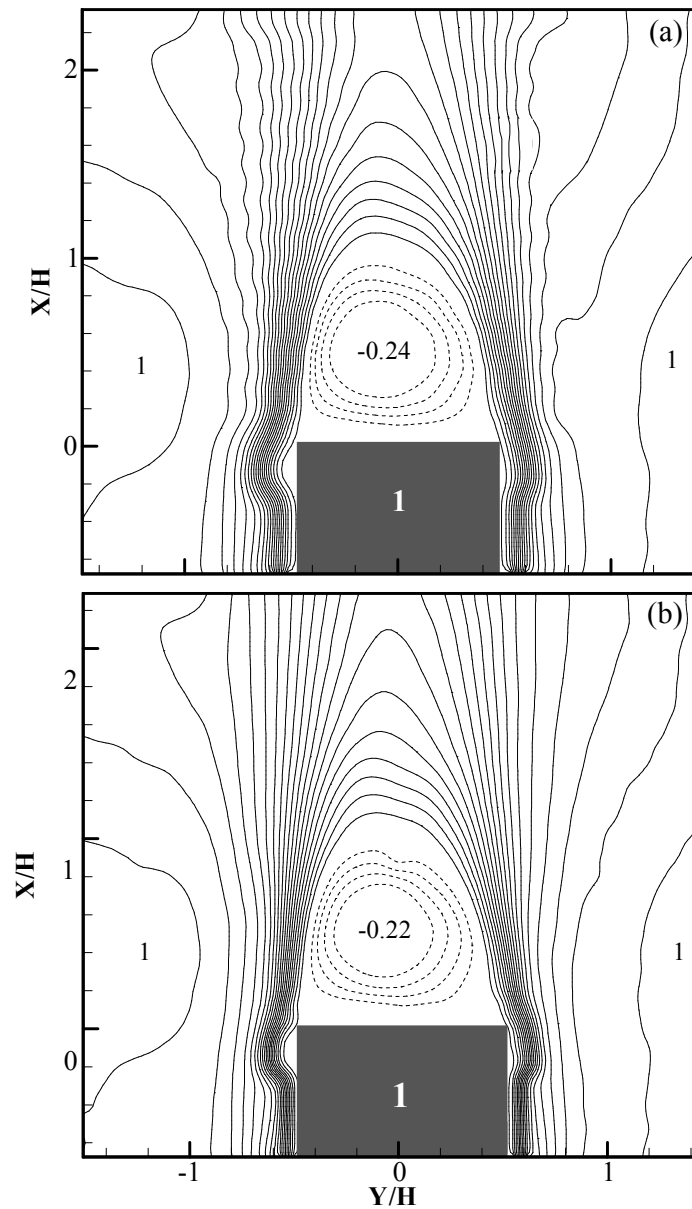


Figure 4.24 Contours of \bar{U}/U_∞ in X - Y plane at $Z/H = 0.5$ for (a) one- and (b) two-vehicle cases ($\alpha = 60^\circ$) at 50 km/h (Contour base line = 0.005, step = 0.005), where dashed lines represent negative values.

4.4.1.5 Wake structure in X - Z plane at $Y/H = 0$ for the vehicles ($\alpha = 60^\circ$) at different vehicle speeds

Normalized \bar{U}/U_∞ and u'/U_∞ profiles along the Z -direction at $1H$ ahead of the last vehicle front, V1 for one-, two- and three- vehicle cases at 10 km/h are shown in Figures 4.25(a) and (b). The preceding vehicle, V2 of two-vehicle case may significantly decrease \bar{U}/U_∞ by 90% and increase u'/U_∞ by 20% for the incoming flow toward the following vehicle, V1. The blockage effect of V2 is obvious for the flow region lower than $Z/H = 1$ but is still noticeable at $Z/H = 2$. By comparing the flow property curves for two-vehicle case with three-vehicle case, it can be concluded that for the difference in flow properties of \bar{U}/U_∞ and u'/U_∞ induced by both preceding vehicles, V2 and V3, the blockage effect of V2 contributes more than 90% of the difference in the flow properties while the blockage of V3 has just a minor effect of less than 10%. This phenomenon in the X - Z plane is similar to that in X - Y plane as mentioned in Section 4.4.1. In Figures 4.26(a) and 4.27(a) for one- and two-vehicle cases at 30 and 50 km/h, the blockage effect of the preceding vehicle, V2 on \bar{U}/U_∞ is weakened by 50% or more for 10 km/h case, because 30 and 50 km/h cases have larger vehicle spacing for the wake development. The values of u'/U_∞ induced by the presence of V2 are between 5% and 10% for both 30 km/h and 50 km/h cases as shown in Figures 4.26(b) and 4.27(b).

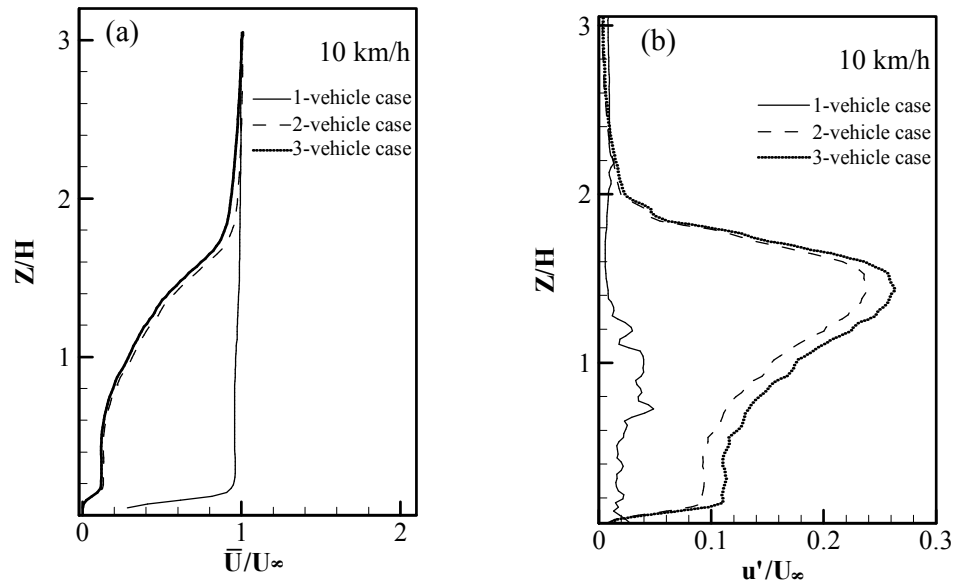


Figure 4.25 (a) \bar{U}/U_∞ and (b) u'/U_∞ profiles in $X-Z$ plane at $1H$ ahead of the last vehicle front, V1 for one-, two- and three-vehicle cases ($\alpha = 60^\circ$) at 10 km/h .

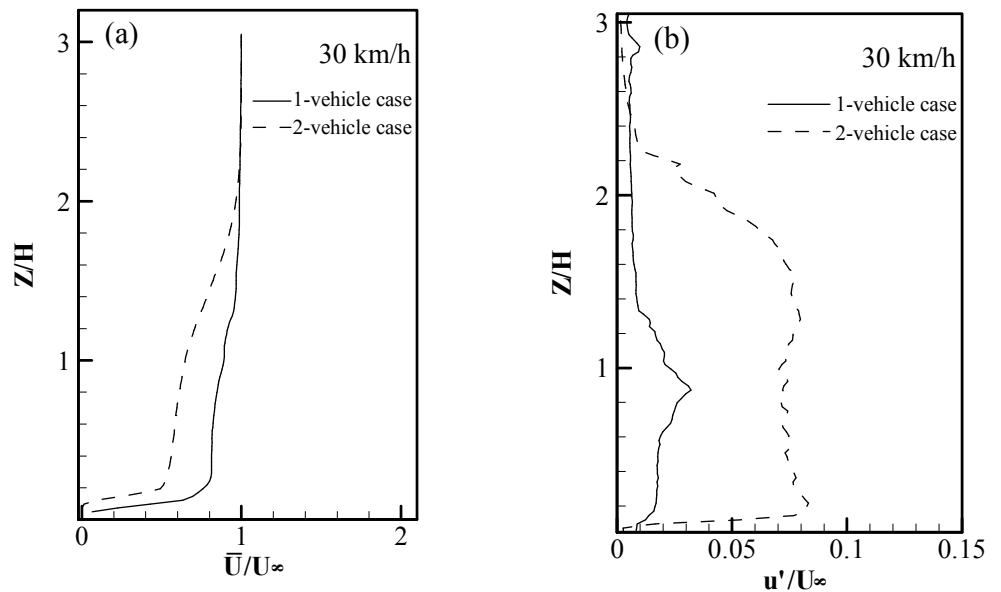


Figure 4.26 (a) \bar{U}/U_∞ and (b) u'/U_∞ profiles in $X-Z$ plane at $1H$ ahead of the last vehicle front, V1 for one- and two-vehicle cases ($\alpha = 60^\circ$) at 30 km/h .

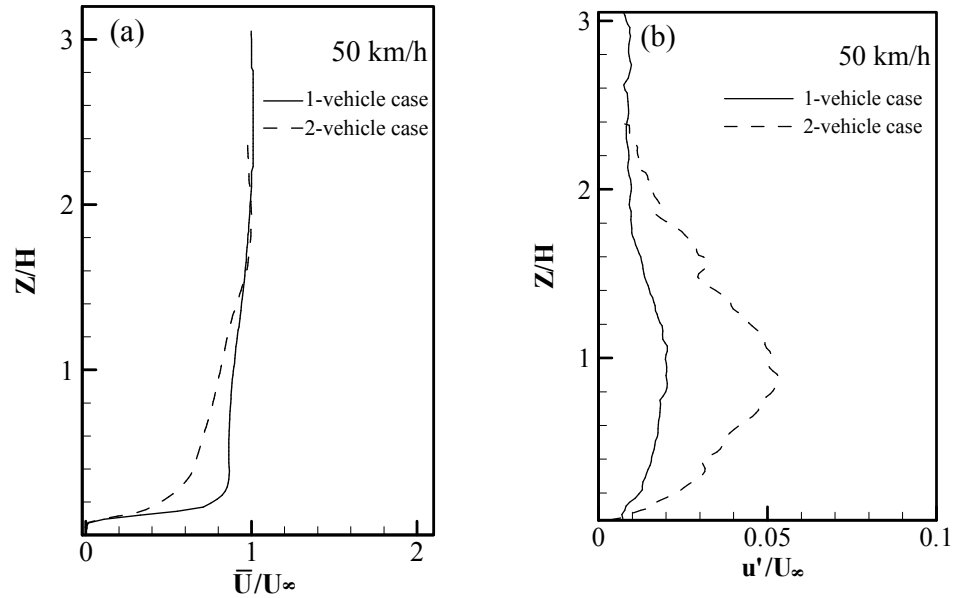


Figure 4.27 (a) \bar{U}/U_∞ and (b) u'/U_∞ profiles in X - Z plane at $1H$ ahead of the last vehicle front, V1 for one- and two-vehicle cases ($\alpha = 60^\circ$) at 50 km/h.

Figures 4.28(a), (b) and (c) show the normalized vorticity, $\bar{\omega}_y \cdot H/U_\infty$ in X - Z plane for one-, two- and three- vehicle cases at 10 km/h, respectively. It should be noted that unlike the vortex structure behind the vehicle(s) ($\alpha = 25^\circ$), there are a pair of smaller sized counter rotating vortices staying right behind the backside of the vehicle(s) ($\alpha = 60^\circ$). Again the preceding vehicle, V2 makes a more noticeable difference in the value of vorticity than in vortex structure. Peak vorticity values (-11.1, 3.4), (-10.5, 2.6) and (-9.8, 2.4) for one- and two- and three-vehicle cases, respectively. Hence, it can be concluded that the preceding vehicle(s) has/have more impact on the lower part of the wake than on the upper part. Because the vorticity values for the vehicle ($\alpha = 60^\circ$) are low which is equal to about one third of the vorticity values for the vehicle ($\alpha = 25^\circ$), therefore the circulation is not calculated for the vehicle ($\alpha = 60^\circ$) to avoid the disturbance which might be caused by the background noise signal.

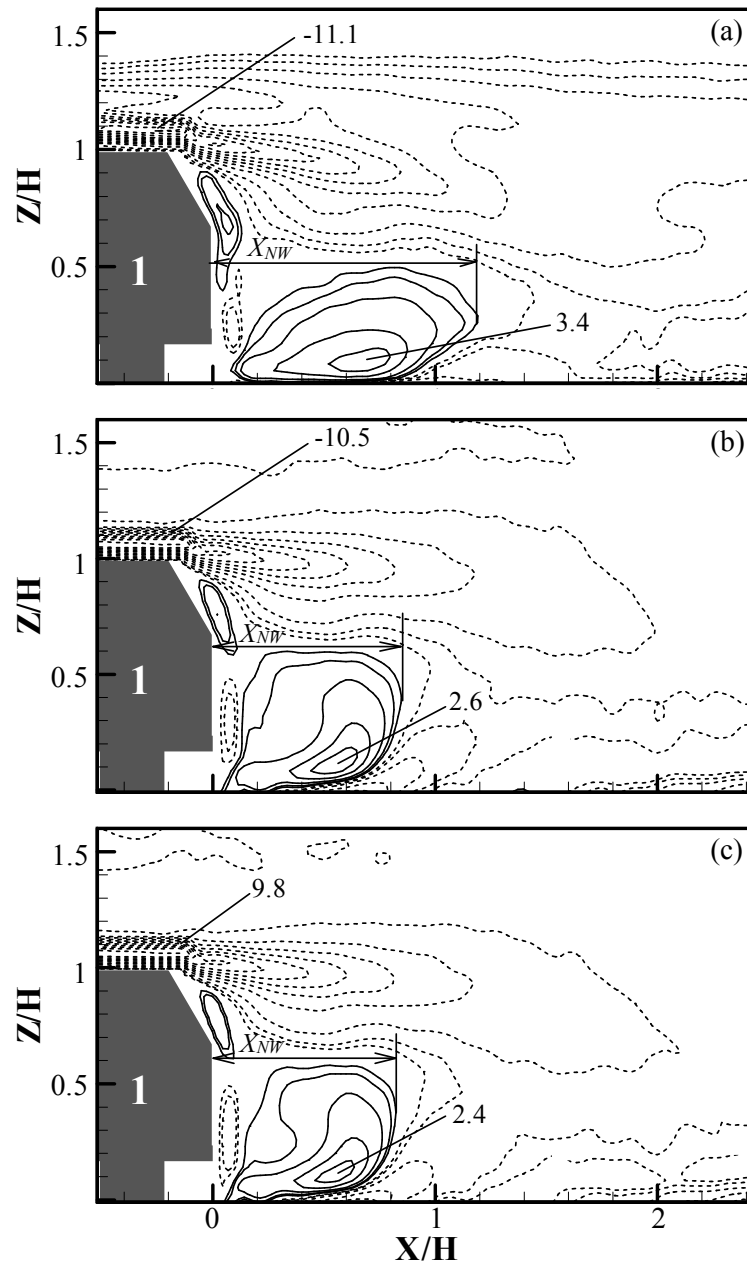


Figure 4.28 Vorticity, $\bar{\omega}_z \cdot H/U_\infty$ contours in X - Z plane for (a) one-vehicle, (b) two-vehicle and (c) three-vehicle cases ($\alpha = 60^\circ$) at 10 km/h (Contour base line = 0.5, step = 1).

The extension of near-wake separation bubble, X_{NW} for the vehicle ($\alpha = 25^\circ$) was previously reported to be $0.65H$ by experiment (Lienhart and Becker, 2003) or by LES approach (Krajnovic and Davidson, 2005a) as well as the present study of

the vehicle ($\alpha=25^\circ$) discussed in Section 4.3.1.5. On the other hand, the length of X_{NW} for the vehicle ($\alpha=60^\circ$) has not been clearly reported in the literature. From Figure 4.28, it can be determined that the length of X_{NW} is around $1.20H$, $0.85H$, and $0.82H$ for one-, two- and three-vehicle cases at 10 km/h, respectively. For 30 km/h case, the length of X_{NW} is around $1.32H$ and $1.12H$ for one- and two-vehicle cases, respectively, as shown in Figures 4.29(a) and (b). For 50 km/h, the length of X_{NW} is around $1.30H$ and $1.05H$ for one- and two-vehicle cases, respectively, as shown in Figures 4.30(a) and (b). Unlike the case for the vehicle ($\alpha=25^\circ$), the length of X_{NW} is not constant to the studied vehicle speeds for the vehicle ($\alpha=60^\circ$).

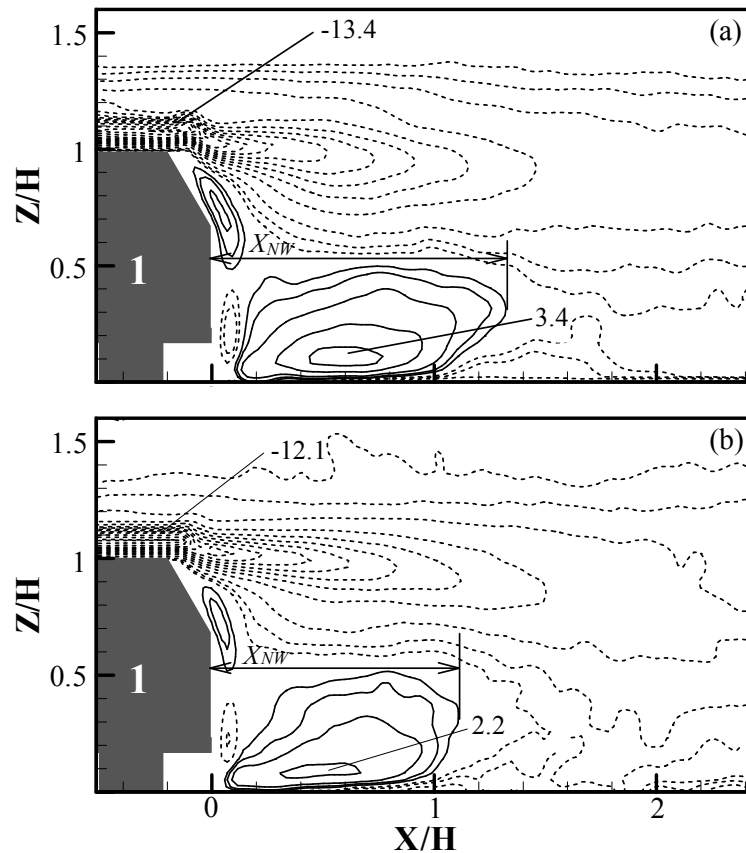


Figure 4.29 Vorticity, $\bar{\omega}_z \cdot H/U_\infty$ contours in X - Z plane for (a) one-vehicle and (b) two-vehicle cases ($\alpha=60^\circ$) at 30 km/h (Contour base line = 0.5, step = 1).

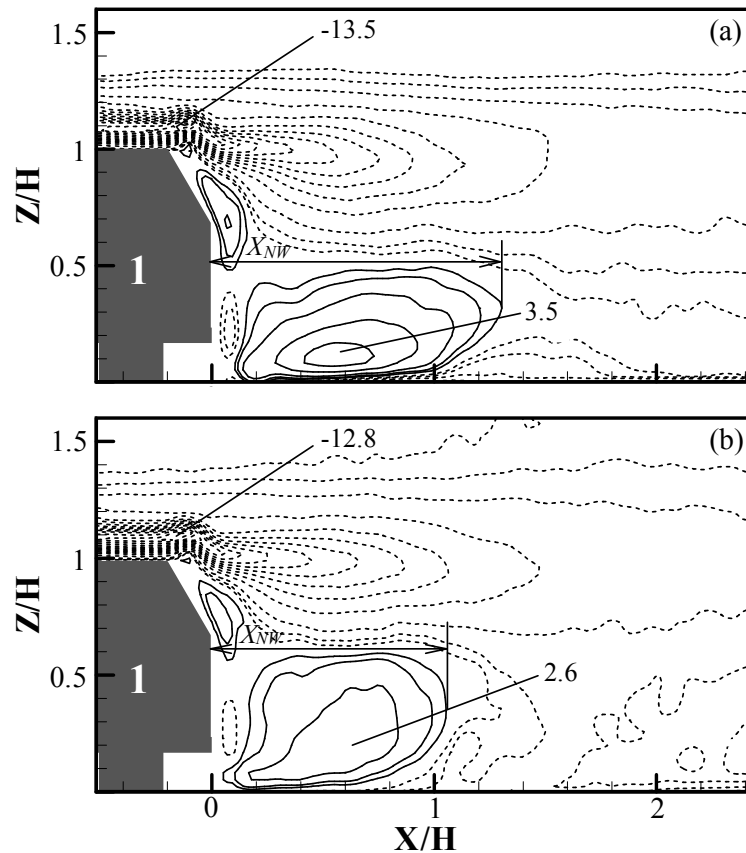


Figure 4.30 Vorticity, $\varpi_z \cdot H/U_\infty$ contours in X - Z plane for (a) one-vehicle and (b) two-vehicle cases ($\alpha = 60^\circ$) at 50 km/h (Contour base line = 0.5, step = 1).

At higher vehicle speed of 30 km/h or 50 km/h, the preceding vehicle, V2 may reduce the peak vorticity values of $\varpi_y \cdot H/U_\infty$ from (-13.4, 3.4) to (-12.1, 2.2) or (-13.5, 3.5) to (-12.8, 2.6), respectively. The changes induced by the preceding vehicle in the $\varpi_y \cdot H/U_\infty$ contours for these two vehicle speeds are less obvious than for 10 km/h while the positively signed recirculation zone still shows higher sensitivity than other negatively signed zones.

4.4.2 Wake structure of one-, two- and three-vehicle cases ($\alpha = 60^\circ$) in Y - Z planes for different vehicle speeds

4.4.2.1 Vorticity contours in Y - Z plane at $X/H = 1$ for the vehicles ($\alpha = 60^\circ$) at different vehicle speeds

Normalized streamwise vorticity, $\bar{\omega}_x \cdot H/U_\infty$ contours in Y - Z plane at $X/H = 1$ for one-vehicle case at 10, 30 and 50 km/h are shown in Figures 4.31(a), (b) and (c), respectively. A pair of counter-rotating vortices is distributed at $Y/H = \pm 0.45$ and $Z/H = 0.35$ with the maximum vorticity, $\bar{\omega}_x \cdot H/U_\infty$ values (-0.724, 0.801). It is worth pointing out that the value of maximum $\bar{\omega}_x \cdot H/U_\infty$ generated by a vehicle ($\alpha = 60^\circ$) is less than one third of that generated by the vehicle ($\alpha = 25^\circ$). This is one of the reasons why the wake flow behind the vehicle with a rear slant angle larger than 30° is sometimes considered as a quasi-two-dimensional flow. Similar to the case for $\alpha = 25^\circ$, the preceding vehicle, V2 at $3.1H$ upstream from the following vehicle, V1 does not change the pattern of $\bar{\omega}_x \cdot H/U_\infty$ contours (contours of $\bar{\omega}_x \cdot H/U_\infty$ with the preceding vehicle(s) not shown because of their similarity), but reduces the maximum vorticity values to (-0.685, 0.632). The second preceding vehicle, V3 still has no prominent effect on the contour pattern, though it can further reduce the maximum vorticity to (-0.558, 0.562). Therefore it can be concluded that the presence of the preceding vehicle(s) does not have much effect on the vortical structure of V1 but has more prominent effect on the values of vorticity in the Y - Z plane, as in the other two planes (i.e., X - Y and X - Z).

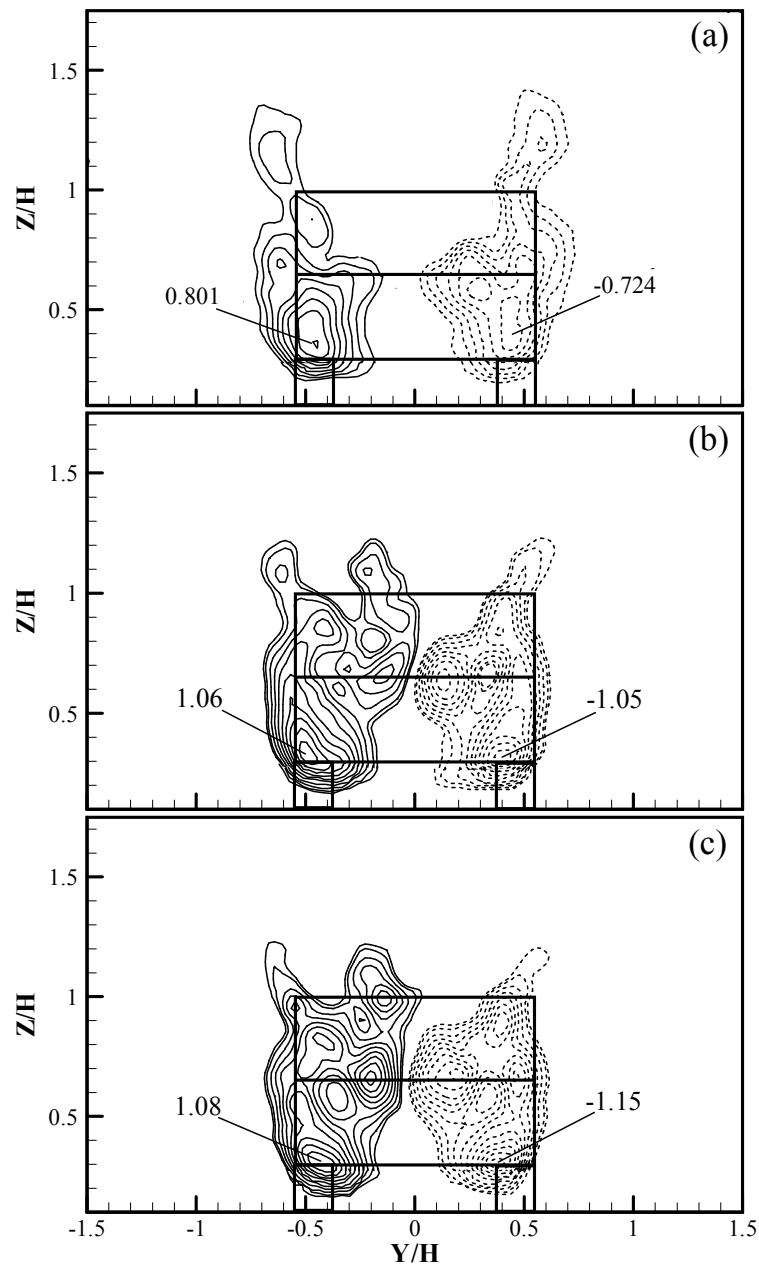


Figure 4.31 Vorticity, $\bar{\omega}_x \cdot H/U_\infty$ contours in Y - Z plane at $X/H = 1$ for one-vehicle case ($\alpha = 60^\circ$) at (a) 10 km/h, (b) 30 km/h and (c) 50 km/h (Contour base line = 0.2, step = 0.1).

In addition to the 10km/h case, the pattern of vorticity, $\bar{\omega}_x \cdot H/U_\infty$ contours is also observed to be almost independent of the preceding vehicle, V2 for 30 km/h and 50 km/h cases by comparing the contours of vorticity with or without

V2. The effect of V2 is also more obvious in the peak vorticity values than in the wake structure of V1. For 30 km/h case, the preceding vehicle, V2 reduces the maximum vorticity value of the following vehicle, V1 from (-1.05, 1.06) to (-0.875, 0.889) (i.e., 16% reduction). For 50 km/h case, the preceding vehicle, V2 reduces the maximum vorticity value of V1 from (-1.15, 1.08) to (-0.945, 0.830) (i.e. 20% reduction). It should also be noted that the vehicle spacing is almost three times longer for 30 km/h case (i.e., $3.1H$ to $9.3H$) and five times longer for 50 km/h case (i.e., $3.1H$ to $15.5H$) when compared with that of 10 km/h case. However, about 15% reduction of maximum vorticity value of the following vehicle, V1 induced by the preceding vehicle(s) (i.e, V2 only or both V2 and V3) is still comparable to the 10 km/h case. It reveals that for the vehicle ($\alpha = 60^\circ$), the reduction in the vorticity of trailing vortices generated by the following vehicle, V1 is insensitive to the vehicle spacing between V1 and its preceding vehicle, V2.

4.4.2.2 Vorticity contours in Y - Z plane at $X/H = 3$ for the vehicles ($\alpha = 60^\circ$) at different vehicle speeds

Normalized streamwise vorticity, $\bar{\omega}_x \cdot H/U_\infty$ contours in Y - Z plane at $X/H=3$ for one-vehicle case at 10, 30 and 50 km/h are shown in Figures 4.32(a), (b) and (c), respectively. In the near-wake region of the vehicle ($\alpha = 60^\circ$) at $X/H = 3$, the wake flow does not push the longitudinal vortices vertically closer to the ground, unlike the case for the vehicle ($\alpha = 25^\circ$).

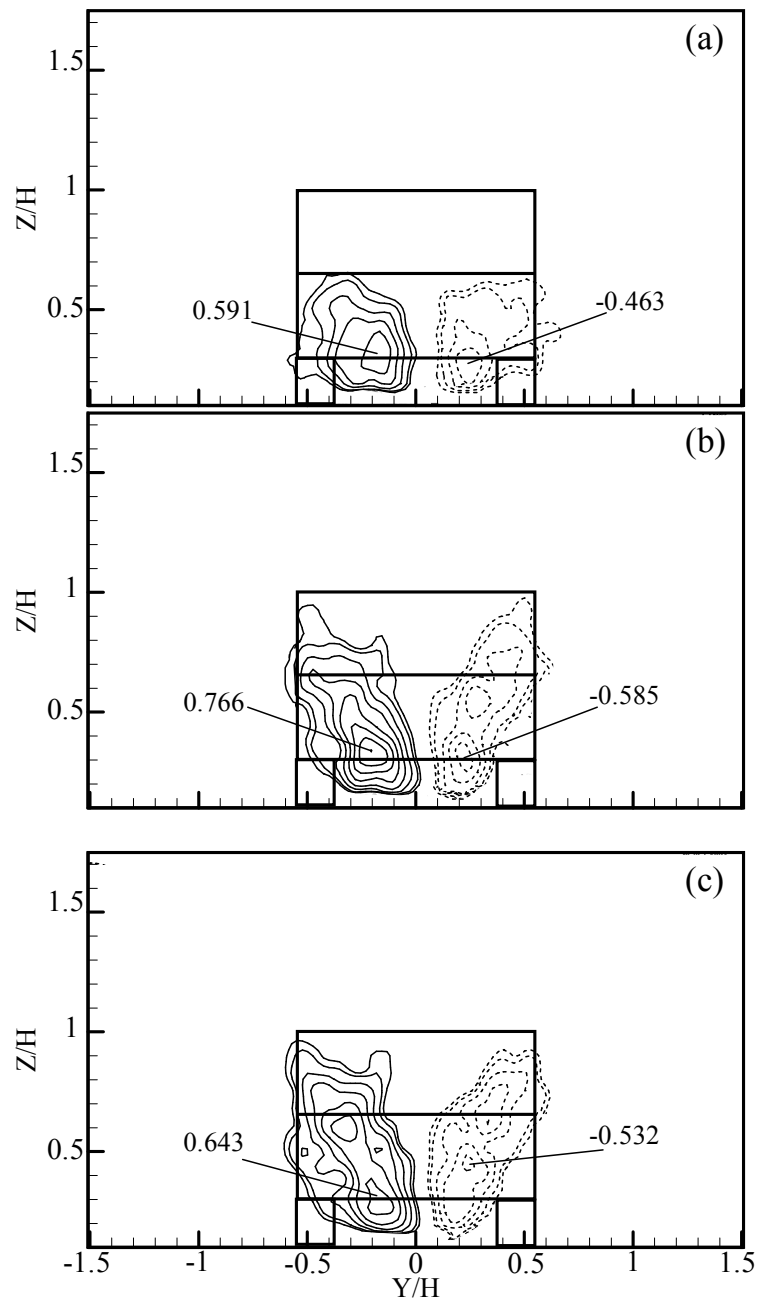


Figure 4.32 Vorticity, $\bar{\omega}_x \cdot H/U_\infty$ contours in Y - Z plane at $X/H = 3$ for one-vehicle case ($\alpha = 60^\circ$) at (a) 10 km/h, (b) 30 km/h and (c) 50 km/h (Contour base line = 0.2, step = 0.1).

For one-vehicle case at 10 km/h, the maximum $\bar{\omega}_x \cdot H/U_\infty$ values of the trailing vortices are (-0.724, 0.801) at $X/H = 1$, (-0.598, 0.630) at $X/H = 2$ (figures not shown) and (-0.463, 0.591) at $X/H = 3$. At $X/H = 3$, the presence of the

preceding vehicle(s) cannot induce any obvious effect in the vortical structure, as happened at $X/H = 1$. However, the reduction of vorticity values induced by the preceding vehicle(s) is/are still noticeable. The maximum $\bar{\omega}_x \cdot H/U_\infty$ values of the trailing vortices from the vehicle, V1 for 10 km/h are reduced from (-0.463, 0.591) to (-0.422, 0.436) (i.e., 19% reduction) and (-0.463, 0.591) to (-0.410, 0.419) (i.e., 21% reduction) by the preceding vehicle, V2 only and both preceding vehicles, V2 and V3, respectively.

The presence of the preceding vehicle, V2 for the 30 and 50 km/h cases still cannot induce any obvious effect in the wake structure at $X/H = 3$ but produces some differences in vorticity values. Therefore only the vorticity contours for one-vehicle cases at three studied speeds, respectively are shown in Figure 4.32. The maximum $\bar{\omega}_x \cdot H/U_\infty$ values of the trailing vortices from the vehicle, V1 for 30 km/h and 50 km/h cases are reduced by the preceding vehicle, V2 from (-0.585, 0.766) to (-0.487, 0.536) (i.e., 24% reduction) and (-0.532, 0.643) to (-0.551, 0.473) (i.e., 13% reduction), respectively.

4.4.3 Summary for the characteristics of maximum vorticity values for trailing vortices at different X/H locations and vehicle speeds for one-, two- and three-vehicle cases ($\alpha = 60^\circ$)

Longitudinal peak vorticity values measured behind the last vehicle, V1 for different vehicle speeds and arrangements of the preceding vehicle(s) are summarized in Table 4.2.

Vehicle speed	Number of the preceding vehicle(s)	$X/H = 1$	$X/H = 2$	$X/H = 3$
10 km/h	0	0.763	0.614	0.527
	1	0.659	0.546	0.429
	2	0.560	0.478	0.415
30 km/h	0	1.06	0.659	0.678
	1	0.882	0.590	0.512
50 km/h	0	1.11	0.712	0.588
	1	0.888	0.613	0.512

Table 4.2 Average longitudinal peak vorticity behind the last vehicle, V_1 ($\alpha = 60^\circ$) for different vehicle speeds and arrangements of the preceding vehicle(s).

4.5 Summary of Chapter

The three-dimensional flow structures of a queue of vehicles ($\alpha = 60^\circ$) (i.e., one-, two- and three-vehicle cases) were investigated comprehensively in a closed-circuit wind tunnel using PIV for the typical urban vehicle speeds (i.e., 10, 30 and 50 km/h).

A pair of weak longitudinal vortices moves downstream with their surrounding flow. The vortices are so weak that they almost have no impact on the wake flow after a downstream movement of $X/H = 2.1$. The evidence of the existence of longitudinal vortices cannot be found in the \bar{U}/U_∞ curve. However, some small waves between $Y/H = (-0.5, 0.5)$ can be observed in u/U_∞ curve of Figure 4.19(b). These small waves are in similar frequency but with a much smaller amplitude if compared with the corresponding waves in u'/U_∞ curve of

Figure 4.2(b) for the vehicles ($\alpha = 25^\circ$). Therefore these small waves in Figure 4.19(b) can be considered as the slight footprint of the weak longitudinal vortices.

For the vehicles ($\alpha = 60^\circ$), the wake flow structure of a vehicle queue is mainly dominated by the last vehicle rather than the incoming flow altered by the preceding vehicle(s). The following vehicle has the most pronounced effect on the wake flow structure while the preceding vehicle(s) still can have some minor effects. The changes induced by the preceding vehicle(s) in wake flow structure are often within the order of 10%, and at an order in between 10% and 20% of their flow properties (e.g., mean and turbulent velocity, vorticity, shear stress etc.). In the present study, it is observed that the mean and turbulent velocities are more sensitive to the vehicle spacing than the trailing vorticities.

Cross-sectional turbulence distribution is still non-uniform in the far-wake region of the vehicle(s) ($\alpha = 60^\circ$). The low turbulence occurs at the center part of the wake flow while the high turbulence occurs at its two sides. For such turbulence distribution, it may lead to considerable underestimation on turbulence magnitude if the measurement is only taken along the centerline of the vehicle wake. It should be also noted this situation is reversed in the near-wake region of the vehicle(s) for $\alpha = 60^\circ$.

**Chapter 5 Vehicle Queue Effect on the Characteristics of
Air Flow, and Exhaust Scalar Dispersion and
Distribution Fields in the Vehicle Wake****5.1 Introduction**

The major source of air pollution is the on-road vehicle exhaust emissions in most urban cities (Mayer, 1999). Due to their serious impacts on urban air quality and public health, many experiments and numerical models for the pollutant dispersion of on-road vehicles or the pollutant dispersion in urban street canyons/street transport environments have been performed for the monitoring and improvement of urban air quality in the past decades (Sharma and Khare, 2001; Chan et al. 2002; Ketzel et al. 2003; Corsmeiera et al. 2005; Li et al. 2006; Wang et al. 2006a; Lai et al. 2009; Valerio et al. 2009; Claudia et al. 2009; Chang et al. 2009b; Carpentieri et al. 2011; Kudo et al. 2011; Rhys-Tyler et al. 2011). On the contrary, the pollution in close vicinity of on-road vehicles (e.g., the vehicular exhaust pollutant dispersion and concentration in a relatively short distance behind vehicle(s)) has received less attention. This kind of pollutant dispersion behavior not only has a direct impact on human health in urban microenvironments, particularly to those high peak exposures of ground vehicle drivers and passengers, bicyclists, motorcyclists, pedestrians and people passing, working or living nearby (Dong and Chan, 2006, Wang et al., 2006a & b, Uhrner et al., 2007, Esber et al. 2007, Chan et al. 2008a & 2008b, 2010a & 2010b, Claudia et al. 2009, Prashant et al. 2009, Albriet et al, 2010, Liu et al. 2011), but also constitutes a major fraction of the total pollutant dispersion (Venkatram et al., 1999).

Richards et al. (2000) studied numerically the pollution dispersion in the near wake of a vehicle. Chan et al. (2001) developed a two-dimensional nitrogen oxides dispersion from a vehicular exhaust plume and its sensitivity studies. Wang et al. (2006b) have developed a three-dimensional pollutant (i.e., carbon monoxide) concentration dispersion from a vehicular exhaust plume in the real atmosphere. Kanda et al. (2006a & b) have investigated the velocity and concentration fields behind vehicle model(s) and have found that the concentration field of exhaust gas has strong relationship with the flow behavior behind the vehicle(s). Sahlodin et al. (2007) incorporated vehicle-induced turbulence together with atmosphere-induced turbulence into a simple Gaussian dispersion model for predicting the pollutant dispersion near roadways. Uhrner et al. (2007) developed a physical model by combining a computational fluid dynamics (CFD) model with an aerosol fine particle model to account for the effects of dilution, nucleation, condensation and coagulation on particle formation and growth in the exhaust plume of a diesel fuelled vehicle. Dong and Chan (2006) and Chan et al. (2008a) have developed a three-dimensional large eddy simulation (LES) of flow structures and pollutant dispersion in the near-wake regions of a ground vehicle for different urban driving conditions. Chan et al. (2008b) have also investigated the effect of rear slant angle on the flow structures, and pollutant dispersion and concentration fields in the wake of a scaled model vehicle. Albriet et al. (2010) coupled a CFD code to a modal aerosol model to simulate the tailpipe plume of a vehicle with aerosol emissions corresponding to urban driving conditions. Recently, Chan et al. (2010a) have first investigated numerically the effects of the aerosol characteristics and behavior in the wake of ground vehicle for stationary and lower vehicle speed

conditions. Furthermore, Chan et al. (2010b) have investigated the interaction effects of different sulfur contents, relative humidities, driving modes and vehicular exhaust tailpipe exit conditions on the three-dimensional exhaust gas-to-nanoparticle conversion and concentration distribution in the wake region of a typical bus-shaped vehicle. Liu et al. (2011) have simulated numerically the three-dimensional exhaust particle dispersion and concentration fields in the near-wake region of the studied ground vehicle. All these literatures have well documented the pollutant dispersion and concentration fields for a single vehicle.

On the other hand, urban traffic density has been increasing significantly with shortened interval distance between the consecutive vehicles (i.e., vehicle spacing) especially for the most dense urban areas which have considerably slower average vehicle speeds or encountered slow traffic under road congestion. Watkins and Viro (2008) have recently discussed the application of modern traffic technologies (i.e., intelligent transport systems) for further reduction on the vehicle spacing. Here rises a question: how much of our knowledge gained from a single vehicle can still be applied to the case like a queue of multiple vehicles? Up to now, very few research works concerning the interaction effect of flow structures, and scalar (i.e., pollutant) or aerosol particle dispersion and concentration fields from a queue of multiple vehicles have been performed. Clifford et al. (1996) identified that 75% of the total received pollution for a following vehicle comes from the preceding one. Recently, Kanda et al. (2006b) have found that the pollutant dispersion for a queue of vehicles is dominated by the symmetric vehicle wake other than the offset positioned exhaust tailpipe. It can be concluded that the wake

flow of a queue of vehicles affects not only their aerodynamic properties but also the pollutant dispersion and concentration level behind the vehicles. A better understanding of the interactions between the flow structures, and scalar (i.e., pollutant) dispersion and distribution fields from a queue of vehicles becomes essential but has not been well documented.

Among a queue of vehicles, the air flow characteristics, and pollutant dispersion and concentration fields behind the vehicle are highly dependent on the arrangement of the preceding and following vehicles which have pronounced effects on the incoming flow and the wake flow, as discussed in Chapter 4. The aim of the present study is to experimentally study (a) the spatial evolution of flow structures, and scalar (i.e., pollutant) dispersion and distribution fields for different downstream distances within near-wake region; and (b) how the evolution is affected by the presence of the preceding vehicle(s) for typical urban driving conditions (i.e., 10, 30 and 50 km/h).

5.2 Experimental Set-up

The present study was performed in a closed circuit wind tunnel with a test section of $0.6 \times 0.6 \times 2\text{m}$ (width \times height \times length) and 0.5% background turbulence intensity for different incoming flow velocities, U_∞ . The size of all studied vehicles is $0.09 \times 0.081 \times 0.18\text{ m}$ ($W \times H \times L$) with a rear slant angle, $\alpha = 25^\circ$ (vehicle **A**) or 60° (vehicle **B**) which is similar to our previous work of Chan et al. (2008b) as shown in Figure 5.1. Two different rear slant angles were chosen to cover the critical rear slant angle, 30° whereas two-dimensional wake flow ($\alpha > 30^\circ$) or

three-dimensional wake flow ($\alpha < 30^\circ$) could be generated accordingly (Ahmed et al. 1984; Chan et al., 2008a and 2008b).

In order to avoid the possible perturbation of the flow by the heated air injection system, a small flexible pressured air tube was inserted through the left front tire of the vehicle and connected to the heating element device and produced the necessary hot air jet exit condition as shown in Figure 3.3(b). The vehicular exhaust tailpipe scalar (i.e., pollutant) concentration of on-road vehicle was simulated using a heated air jet at certain temperature, T_j and velocity, U_j through a small tailpipe exit of diameter, $d = 3 \times 10^{-3}$ m for the scaled-down vehicles **A** and **B**. The exhaust tailpipe exit was located at the rear side of the vehicle (i.e., $Y/H = 0.278$ and $Z/H = 0.222$). The heating element device was placed inside the vehicle to maintain constant T_j using a dedicated feedback and temperature control system. For the present study, the potential core temperature of the heated exhaust air jet, T_j and ambient air in wind tunnel, T_α were maintained constant (Chan et al., 2008b and Huang et al. 2009b). The exit jet velocity, U_j of the vehicle was then determined by the conservation of the mass flow rates from the vehicular exhaust tailpipe conditions of the real and scale-model vehicles for different vehicle speeds (Chan et al., 2008b).

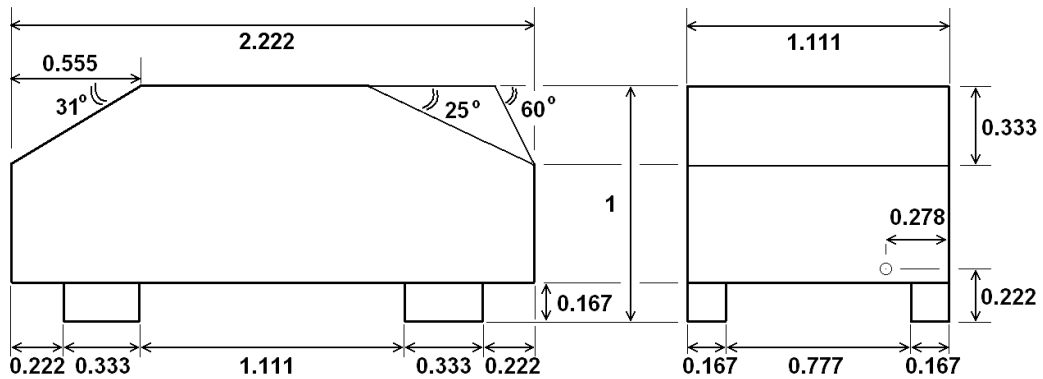


Figure 5.1 Two studied scale-model vehicles of a rear slant angle, $\alpha = 25^\circ$ (vehicle **A**) and 60° (vehicle **B**) where the dimension is normalized by the vehicle height, $H = 81$ mm, respectively (Chan et al. 2008b). The small circle on the backside of the vehicle, V1 represents the location of exhaust tailpipe.

The x-axis is oriented in the direction of the main stream flow, U_∞ , the y-axis is perpendicular both to the side wall of the studied vehicle and the main stream flow, and the z-axis is represented for the spanwise direction, as shown in Figure 3.3(b). The vehicle was set on a designed ground plane (2.0 m in length \times 0.59 m in width \times 0.02 m in thickness) from the wind-tunnel floor as shown in Figure 3.3(c) in order to limit the boundary layer thickness (Narasimha et al. 1994). The details of boundary layer thickness and rms velocity values of this designed flat plate can be referred to the experimental methodology of Chapter 3. A single model vehicle or a queue of model vehicles was placed in-line on this horizontal designated flat plate to simulate the effect of a single moving vehicle or a queue of multiple moving vehicles on the flow structure and scalar (i.e., pollutant) dispersion and distribution fields in the vehicle wake region. Since the vehicle speeds of 30 and 50 km/h of a single studied vehicle have shown similar results as described in Chan et al. (2008b), therefore only the 10 and 30 km/h driving speeds were studied and presented. Their corresponding Reynolds numbers, $Re_H = U_\infty \times H / \nu$ equals to 1.48×10^4 and 4.44×10^4 ,

respectively, where H is the height of vehicle ($H = 81$ mm) and ν is the kinematic viscosity of ambient air. For a queue of vehicles, the “vehicle spacing” between the rear of the preceding vehicle and the front of the following one was fixed to allow for two seconds of the vehicle movement (i.e., vehicle spacing = $U_\infty \times 2$ s). Hence, the corresponding vehicle spacing was $3.1H$ and $9.3H$ in respect to the vehicle speed of 10 and 30 km/h, respectively as shown in Figure 5.2. The origin point of Cartesian coordinate system was fixed on the flat plate under the center point of the rear side on last vehicle (i.e., vehicle No. 1, V1). The X -axis was in the direction of main free stream flow, Y -axis was in the direction of vehicle width, and Z -axis was in the direction of the vehicle height. The velocity components, U , V and W correspond to the X , Y and Z axes, respectively. In the present study, all experimental results were normalized (e.g., X/H , U/U_∞ etc.). Normalized mean temperature excess (i.e., scalar), $\bar{T}^* = (T_i - T_a)/(T_j - T_a)$ where T_i is the measured average local temperature, and T_a is the background air temperature inside the wind tunnel and T_j is the exhaust jet exit temperature. It should be noted that only the last vehicle, V1 for a queue of vehicles was installed the heating element device with an exhaust air heated jet exit inside itself while other preceding vehicles, V2 and V3 are treated as bluff bodies. The reason for such vehicle arrangement is because the research target of the present study is to investigate the wake flow effect of the preceding vehicle(s) (i.e., V2 only or both V2 and V3) on the characteristics of scalar (i.e., pollutant) dispersion and distribution fields behind the last polluted vehicle, V1.

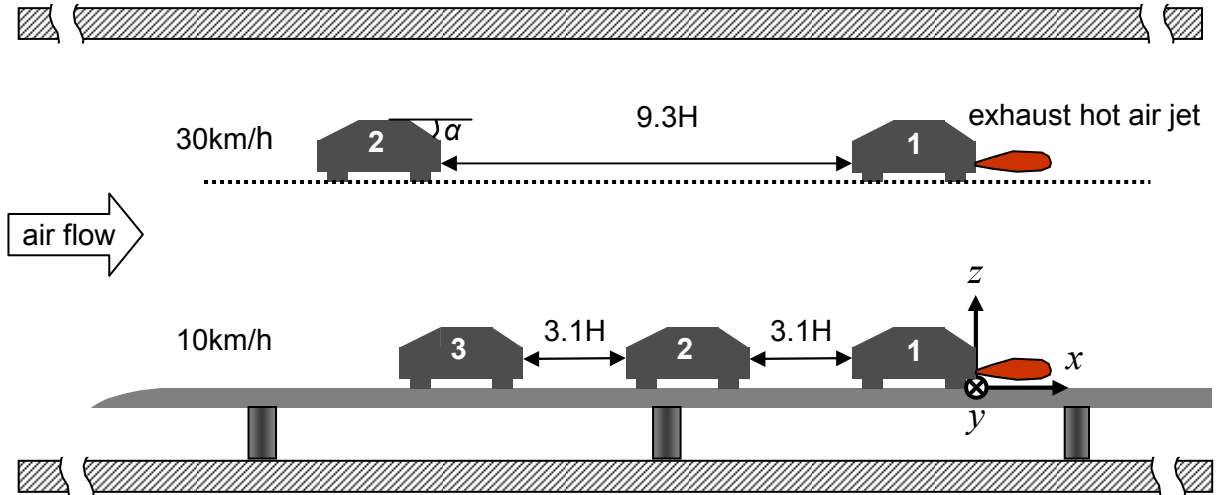


Figure 5.2 Experimental setup and coordinate system inside the wind tunnel facility for a queue of vehicle arrangement at the speed of 10 and 30 km/h.

A customer-made probe combined with a cold-wire and X hot-wire sensors was positioned behind the vehicle No. 1 to measure the temperature (or passive scalar) distribution and air flow vectors, respectively in the cross-sectional Y - Z planes at the downstream distances $X/H = 2, 4, 6$ and 8 . The cold-wire sensor was made of Wollaston (Pt-90%Rh-10%) wire with $1.27 \mu\text{m}$ diameter and 2.5 mm effective length, operated with 0.1 mA constant current. The hot-wire sensors were made of Wollaston (Pt-90%Rh-10%) wire with $5 \mu\text{m}$ diameter and 5 mm effective length, operated at a constant temperature. A low operational temperature for hot-wire sensors was chosen to minimize the heat noise signal transferred to the neighboring cold-wire while they can still maintain a good performance of flow detection. All the voltages from cold- and hot-wire sensors were measured through a 16-channel 12-bit A/D board into a personal computer. The data acquisition for every test point was set to be 5 seconds long with a 2 kHz sampling frequency yielding 10,000 samples. About 1,890 test points were equally spaced by 4 mm

distance on every tested Y - Z plane which are equal to a cross-section area, 324×122 mm ($W \times H$) (i.e. $4H$ wide \times $1.5H$ high) at the downstream distances, $X/H = 2, 4, 6,$ and 8 . Because the X hot-wire sensors can only measure two flow components (e.g. U and V components) each time for Y - Z plane, the X hot-wire sensors will then be rotated by 90° to measure the two components (e.g., U and W components) and repeat the testing procedure for the same Y - Z plane. Thus all three flow components, U , V and W together with temperature excess, T_i for every test point can be acquired.

5.3 Results and Discussion

5.3.1 Air flow characteristics, and exhaust scalar dispersion and distribution fields behind a queue of vehicles ($\alpha = 25^\circ$) in the downstream

The incoming flow toward a moving vehicle will be significantly altered by the presence of the preceding vehicle(s), thus the wake flow behind the last vehicle, $V1$ will also be changed accordingly. The change in flow characteristics could have significant impact on the pollutant (i.e., scalar) dispersion behind the vehicle(s). Since the downstream velocity component, U has no contribution to the scalar dispersion in Y - Z plane, only the lateral velocity component, V and vertical velocity component, W will be presented in figures below. Normalized mean lateral and vertical velocity components, \bar{V}/U_∞ and \bar{W}/U_∞ , and normalized mean temperature excess, \bar{T}^* (i.e., mean scalar distribution) contours for the vehicle(s) ($\alpha = 25^\circ$) in the cross-sectional Y - Z plane at $X/H = 2$ for one-, two- and three-vehicle cases at 10 km/h are shown in Figure 5.3(a), (b) and (c), respectively.

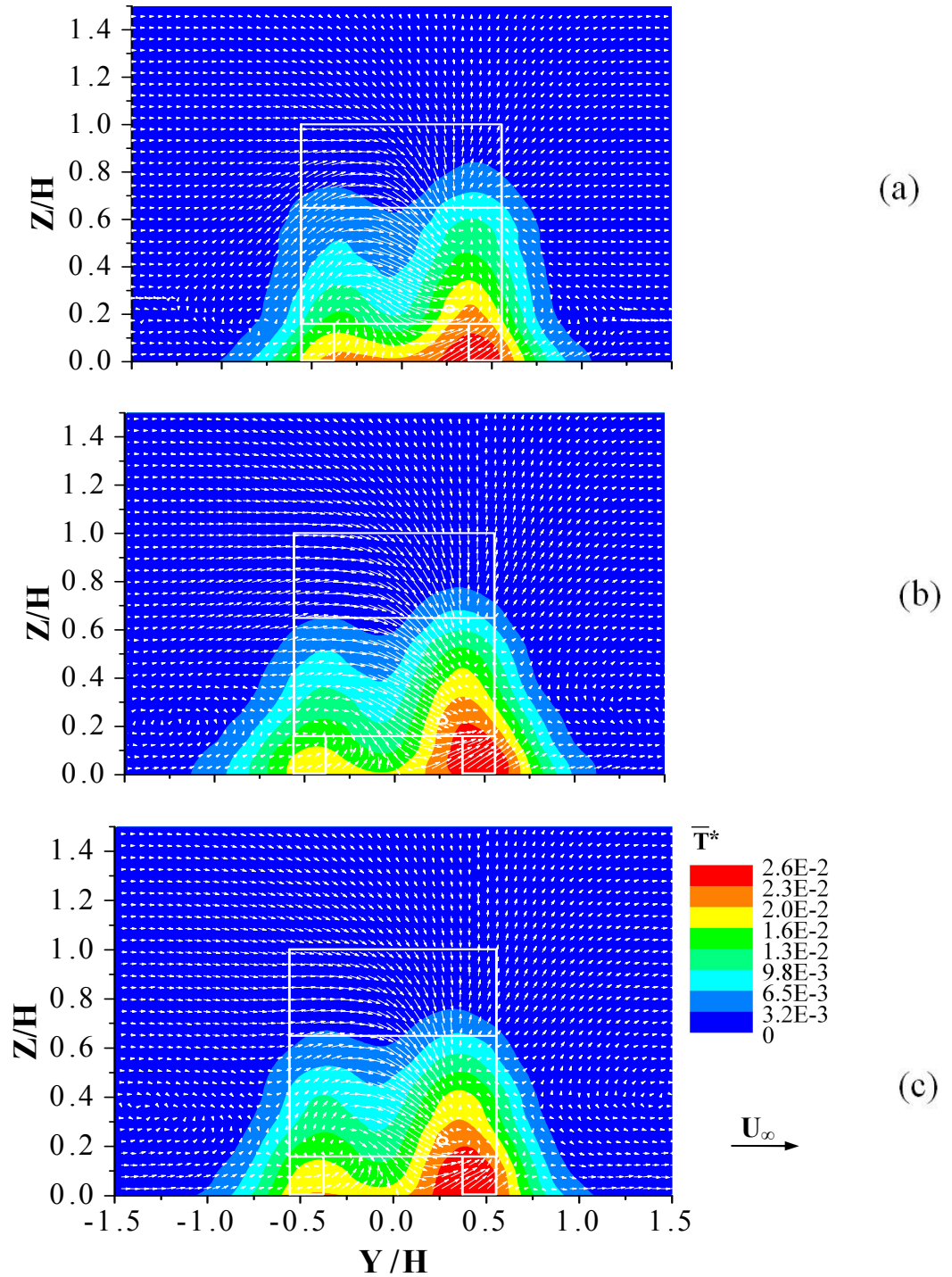


Figure 5.3 Normalized mean temperature excess, \bar{T}^* and normalized mean vector, \overline{VW}^* in Y-Z plane at $X/H = 2$ behind the vehicle(s) ($\alpha = 25^\circ$) at 10 km/h for (a) one-vehicle, (b) two-vehicle and (c) three-vehicle cases.

The vectors form two counter rotating vortices behind the vehicle, V1, as shown in Figure 5.3 indicating that the wake flow is a complex three-dimensional flow because of the large \overrightarrow{VW}^* vectors and their asymmetric pattern. This flow pattern is generally in good agreement with the findings in Chan et al. (2008b).

The symmetry of wake flow structure is slightly disturbed by the jet exit flow, thus the \overrightarrow{VW}^* component is stronger on the right-hand side than the left-hand side one behind the vehicle as shown in Figure 5.3(a). The vortex centers are located at around $Y/H = \pm 0.4$ and $Z/H = 0.3$ as shown in Figure 5.3. Exhaust hot air is mainly trapped and rotated inside these two trailing vortices (or known as the longitudinal vortices in some literatures) and thus the dual peak regions in the mean scalar, \bar{T}^* distribution field are formed. The vortex on the right-hand side of the vehicle (i.e, the same side of tailpipe exit) shares a larger portion of exhaust hot air and forms a peak scalar region (i.e. the contour region of the highest scalar value) with a larger size and higher temperature than the left-hand side one. When the trapped exhaust hot air rotates to the lowest region of vortex and touches ground, the “peak scalar region” is formed within $0.25 < Y/H < 0.6$ and $0 < Z/H < 0.2$ because its rotation is slowed down by the ground and thus heat is accumulated in this small zone. Similarly, the vortex on the left-hand side of the vehicle forms the second peak scalar region within $-0.25 < Y/H < -0.6$ and $0 < Z/H < 0.1$ by its clockwise rotation. Such a scalar (i.e., pollutant) distribution pattern indicates that the flow pattern dominates the dispersion of mean scalar distribution field in near-wake region and forms two non-symmetrical peak scalar regions by a pair of trailing vortices. The offset location of exhaust tailpipe accounts for the

non-symmetrical left-right handed scalar distribution. These two peak scalar regions locate almost over the two footprints of the vehicle tires. For either side of the vehicle, the highest scalar value occurs at the location where the trailing vortex touches the ground. With the addition of preceding vehicle(s), two main differences can be observed from Figures 5.3(a) to (c). The first difference is the unbalance between the left- and right-handed mean scalar distribution regions. The vortex on the right-hand side (i.e., the same side of tailpipe exit) shares a larger portion of exhaust hot air and forms a larger and higher scalar region with increasing number of the preceding vehicle(s). One reason of this change can be referred to Figure 4.7(a). It indicates that the incoming flow of the averaged flow velocity, \bar{U}/U_∞ increases with the height above the ground toward this vehicle. Since the exhaust tailpipe is located at the lower part above the ground of the right-hand side, the interaction between jet and wake flows is weakened by the smaller flow velocity, i.e., the jet can maintain its characteristics for a longer developing region which favors the hot air supply of right trailing vortex. In Figure 4.7(a), the average velocity curves, \bar{U}/U_∞ for two-vehicle and three-vehicle cases are very close, thus the heat dispersion patterns for two-vehicle and three-vehicle cases in Figures 5.3(b) and (c) are very similar. On the contrary, Figure 4.7(b) indicates that the turbulence, u'/U_∞ in the incoming flow is considerably increased by the preceding vehicle(s). Generally speaking, turbulence is in the favor of a homogeneous scalar distribution. Therefore from the increasingly unbalanced scalar distribution patterns, it can be concluded that the importance of average velocity well exceeds that of turbulence for the heat (i.e. scalar) dispersion. Another reason of the unbalance between the left- and

right-handed scalar regions is the vorticity of trailing vortices which decrease with increasing number of the preceding vehicle(s) as summarized in Table 4.1. Smaller vorticity value implies a lower vortex rotation speed. The vortex on the right-hand side may transfer the heat at a lower rate to the interface between these two vortices, which diminishes the heat transport rate to the vortex of the lower scalar (i.e. lower temperature) on the left-hand side. The evidence is that a thin orange zone of \bar{T}^* distribution lying over $Y/H=0$ where two vortices interface in Figure 5.3(a). The disappearance of orange zone of \bar{T}^* distribution in Figure 5.3(b) and (c) implies that less quantity of heat is transferred to that region by the presence of the preceding vehicle(s). With less heat quantity received by the left-handed vortex, it becomes a lower scalar, \bar{T}^* region. The second difference is that the vertical height of these two high scalar, \bar{T}^* regions on each side gets lower with increasing number of the preceding vehicle(s). The two high scalar, \bar{T}^* region heights (i.e., left- and right-handed peak regions) at Z/H are (0.73, 0.84) for no preceding vehicle, (0.63, 0.76) for one preceding vehicle, and (0.64, 0.75) for two preceding vehicles, respectively, as shown in Figures 5.3(a) to (c). For the cases of one and two preceding vehicle(s), there is almost no difference in the scalar distribution field and this indicates that the number of the preceding vehicle(s) is a less dominant factor than no preceding vehicle case. The reason to this change can also be referred to Figure 4.7(a) which indicates that the velocity profile of incoming flow toward the vehicle(s) is not uniformly vertical above the ground. After the incoming flow passes through the vehicle rear, the relatively stronger upper flow will result in a stronger downwash thus further pushing the wake structure to the ground as shown in Figure 4.10. For the topmost dashed curve, its

rightmost ending point in Figure 4.10(b) and (c) for two-vehicle and three-vehicle cases, respectively is obviously lower than in Figure 4.10(a) for one-vehicle case. One more phenomenon deserving attention is that for all the one-, two-, and three-vehicle cases, the bases of all mean scalar distribution regions are of the same width in the range of $-1 < Y/H < +1$, unlike their heights which decrease with the increasing number of the preceding vehicle(s). From Figure 4.7(a), one or two preceding vehicle(s) not only decreases the velocity of incoming flow but also leads to the unbalance of the incoming flow in the vertical profile of \bar{U}/U_∞ along the downstream. For the effect of reduction on incoming velocity, it does not lead to any obvious change in wake structure because as discussed in Chapter 4, the wake structure is quite independent of the incoming flow velocity. For the effect of vertically unbalanced \bar{U}/U_∞ , it can lead to the pushing effect on the wake structure as above-mentioned. However, the preceding vehicle(s) cannot induce any unbalance effect on the incoming flow in the horizontal profile (assuming the vehicle body is symmetrical on both sides), therefore the wake structure can maintain its horizontal stability with the presence of the preceding vehicle(s). It can be observed that the flow structure is pushed down due to the effect of the preceding vehicle(s) as shown in Figures 4.10(a) to (c). Similarly in Figures 5.3(b) and (c), it can be observed that heat (i.e., \bar{T}^* or scalar) dispersion region is pushed down due to the effect of the preceding vehicle(s) as well. This similarity suggests that the wake flow is the crucial factor for the scalar dispersion and distribution field of the exhausted jet behind vehicle, V1 at $X/H = 2$. Since there will be no other strong disturbance source along the downstream, it can be inferred

that the wake flow will continue to be the crucial factor for the formation of scalar dispersion and distribution of exhaust jet behind the vehicle, V1 for $X/H \geq 2$.

Figures 5.4 show the comparison of \bar{T}^* contours and \overrightarrow{VW}^* vectors in the cross-sectional $Y-Z$ plane at $X/H = 2$ for the vehicle ($\alpha = 25^\circ$), (a) for 30 km/h in the present study and (b) for 45 km/h in Gosse et al. (2011). Although the studied vehicle shape, tailpipe location and some other parameters (e.g. vehicle speed) are slightly different, the overall dual-peak contour distribution can still be observed and confirmed in both experimental studies. One peak is taller than the other peak on the side of tailpipe exit and the dual-peaks are almost left-right symmetrically located behind the vehicle. Secondly the high \bar{T}^* contour regions in red/purple and yellow color in Figures 5.4(a) and (b) are in similar trend, i.e. both almost rise to 80% and 40% of their vehicle heights and vehicle widths, respectively on the side of tailpipe exit. The overall \bar{T}^* contour distribution and the high \bar{T}^* contour region of these two studies are quite comparable to each other. The present experimental methodology was further extended from a single vehicle to a queue of vehicles.

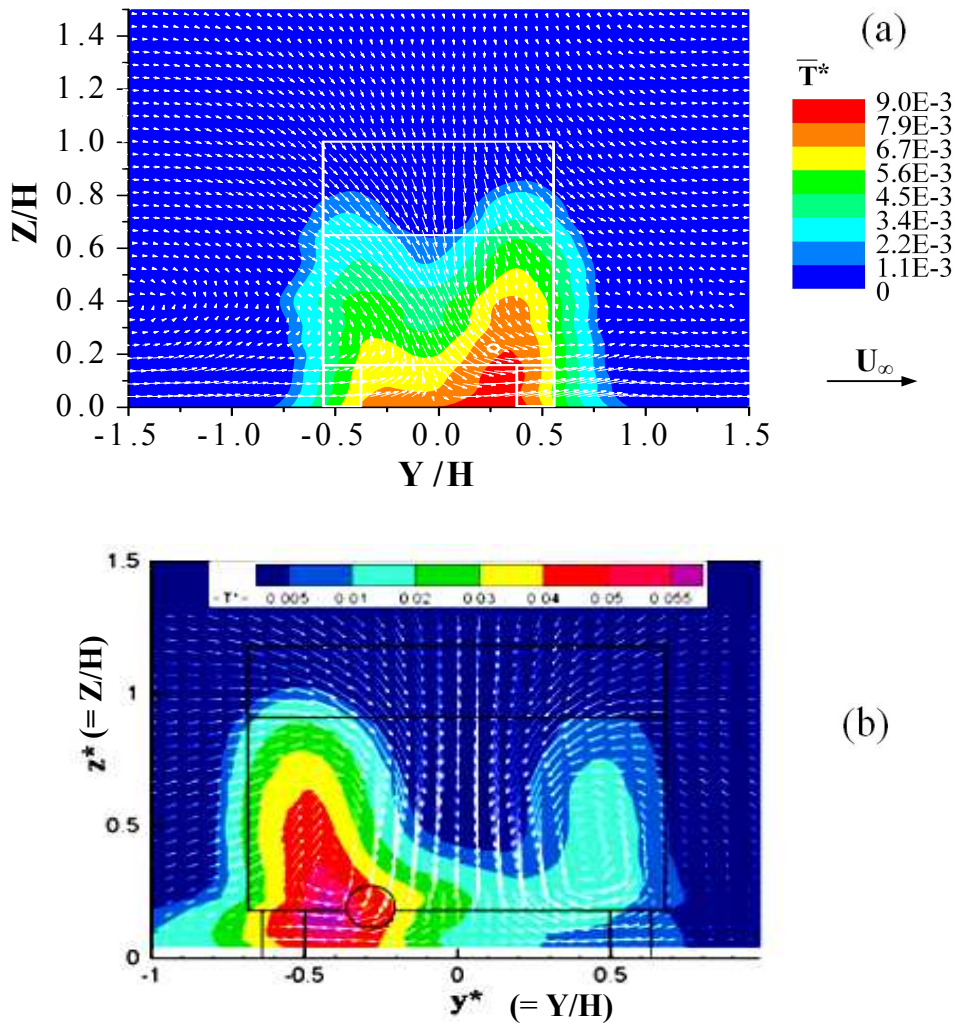


Figure 5.4 Normalized mean temperature excess, \bar{T}^* and normalized mean vector, \overline{VW}^* in Y - Z plane at $X/H = 2$ behind the vehicle(s) ($\alpha = 25^\circ$) for (a) one-vehicle at 30 km/h and (b) one-vehicle at 45 km/h (Figure 5(e) of Gosse et al. (2011)).

Figures 5.5(a) and (b) show \bar{T}^* contours and \overline{VW}^* vectors in the cross-sectional Y - Z plane at $X/H = 2$ for the vehicle(s) ($\alpha = 25^\circ$) at 30 km/h for one- and two-vehicle cases. Because the mechanisms of wake generation and heat distribution are not drastically different from that of 10 km/h, the flow structure, and mean scalar, \bar{T}^* distribution patterns are similar to those of 10 km/h in many aspects. If the scalar distribution of 30 km/h is compared with that of 10 km/h for

one-vehicle case, it can be noted that the dual peaks of the scalar distribution field persists but the difference between the heights of these dual peaks is smaller, and it is possibly because the wake flow is stronger at 30 km/h than at 10 km/h. The saddle point in the outer edge of scalar dispersion region between these two peak scalar regions is located higher for 30 km/h than that for 10 km/h, i.e. $Z/H = 0.65$ versus 0.62, which may suggest a faster turbulent mixing process of the jet scalar dispersion. For 30 km/h, the peak values of scalar distribution regions also decrease but not as much as that for 10 km/h with the preceding vehicle case, because the unbalance in incoming flow induced by the preceding vehicle in vertical velocity profile of 30 km/h (in Figure 4.8(a)) is not as much as of 10 km/h (in Figure 4.7(a)). At this higher vehicle speed, the scalar dispersion region is decreased in width when comparing with the corresponding case of 10 km/h. In addition, the size of the peak scalar region is also increased by the presence of preceding vehicle(s), as occurred to the corresponding case of 10 km/h.

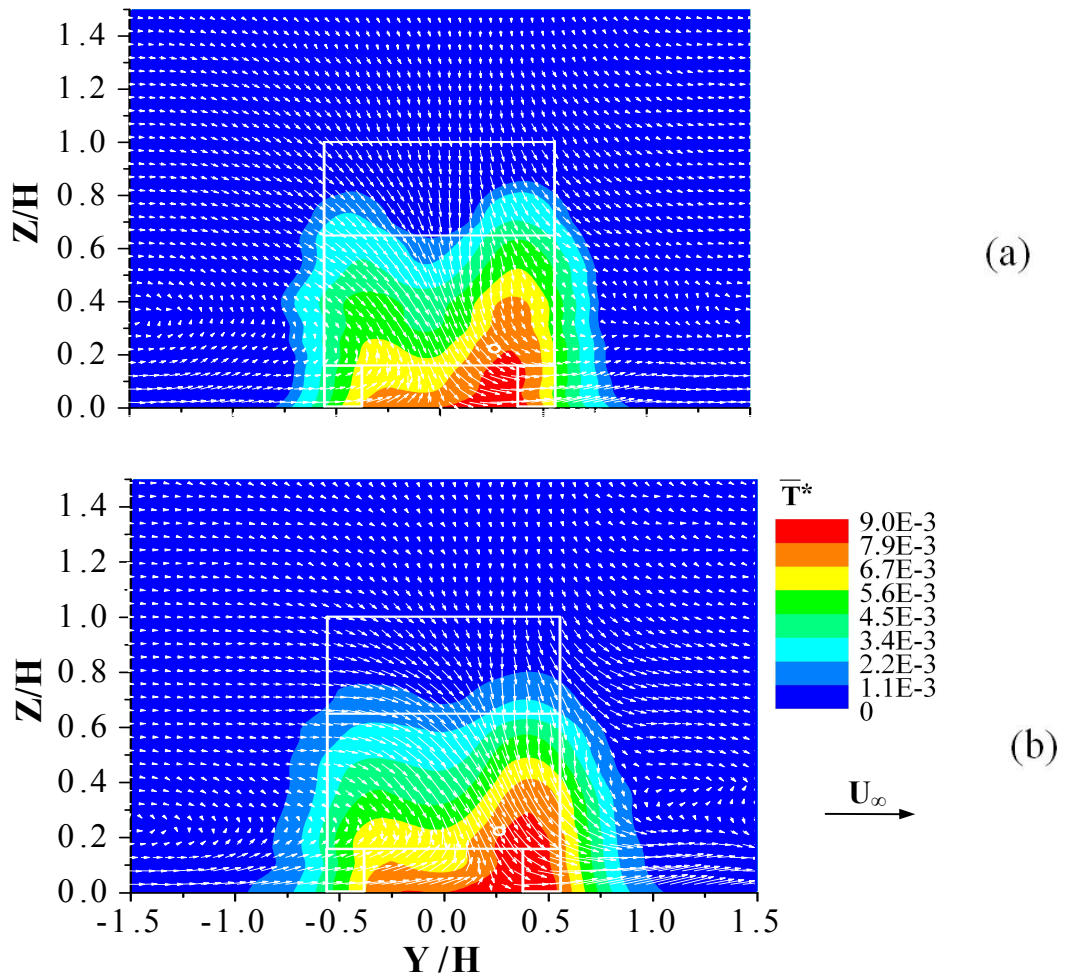


Figure 5.5 Normalized mean temperature excess, \bar{T}^* and normalized mean vector, \overline{VW}^* in $Y-Z$ plane at $X/H = 2$ behind the vehicle(s) ($\alpha = 25^\circ$) at 30 km/h for (a) one-vehicle and (b) two-vehicle cases.

Normalized mean \overline{VW}^* vectors and normalized mean temperature excess, \bar{T}^* (i.e., mean scalar distribution) contours for the vehicle(s) ($\alpha = 25^\circ$) in the cross-sectional $Y-Z$ plane at $X/H = 4$ at 10 km/h for one- two- and three-vehicle cases are shown in Figures 5.6(a) to (c), respectively.

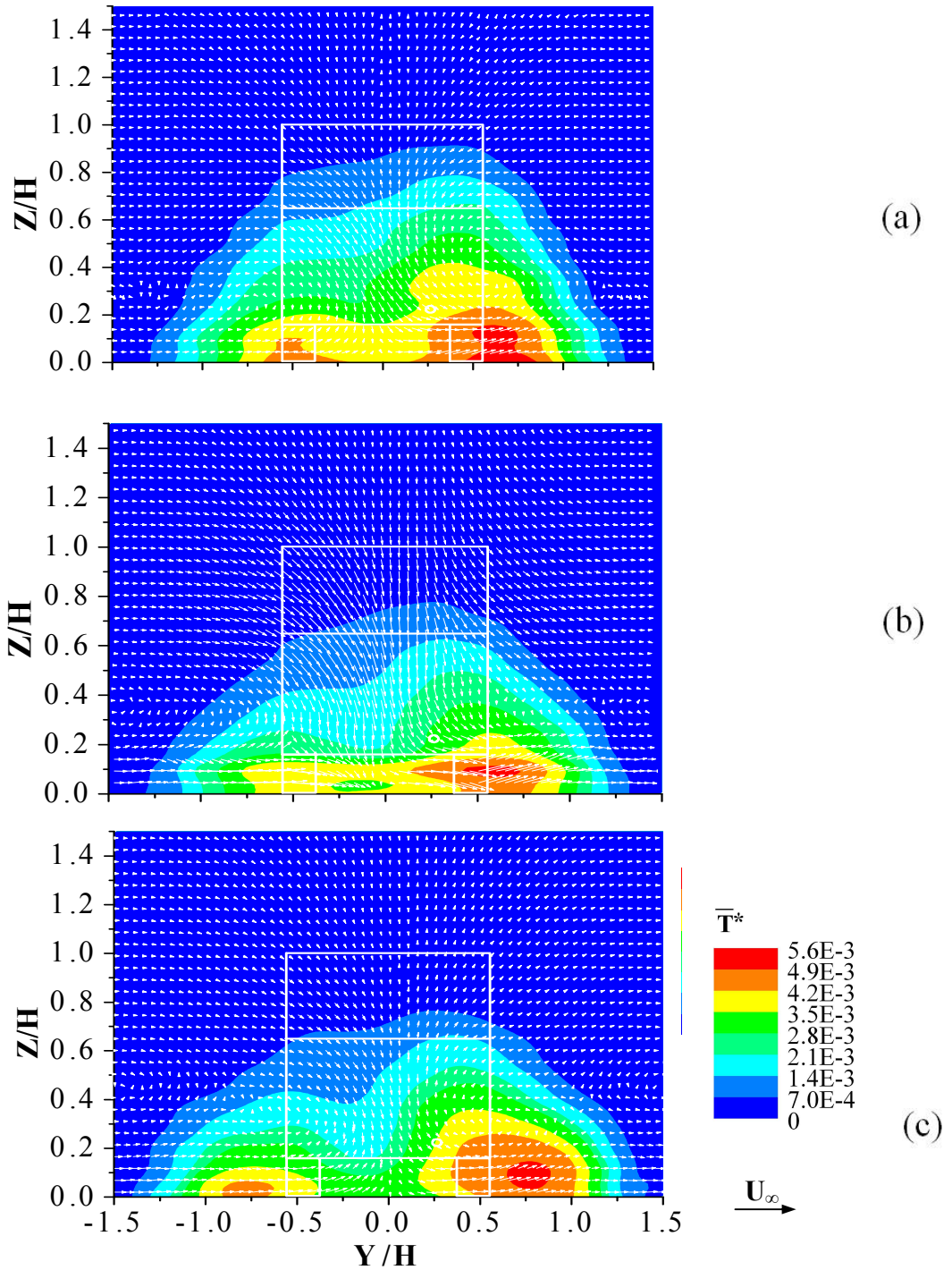


Figure 5.6 Normalized mean temperature excess, \bar{T}^* and normalized mean vector, \overline{VW} in Y-Z plane at $X/H=4$ behind the vehicle(s) ($\alpha=25^\circ$) at 10 km/h for (a) one-vehicle, (b) two-vehicle (Huang et al. 2009b) and (c) three-vehicle cases.

The vectors of a pair of counter rotating vortices behind the vehicle are still discriminable in Figure 5.6. The saddle point in the outer edge of scalar dispersion regions between the left- and right-hand side of scalar distribution is not as discernible as at $X/H = 2$ (in Figure 5.3). The vortex centers are located at around $Y/H = \pm 0.5$ and $Z/H = 0.3$. The peak scalar region is located at around $0.5 < Y/H < 0.8$ and $Z/H < 0.14$ on the right-hand side of the vehicle while the second peak scalar region is located at around $-0.2 < Y/H < -0.7$ and $Z/H < 0.05$ on the left-hand side of the vehicle. For the bases of the full scalar distribution regions, they are all expanded from $-1.05 \leq Y/H \leq 1.05$ at $X/H = 2$ to $-1.27 \leq Y/H \leq 1.29$ at $X/H = 4$ due to the evolution of wake flow behind the vehicle. The topmost points of scalar distribution regions are also elevated from $Z/H = (0.84, 0.76 \text{ \& } 0.75)$ at $X/H = 2$ to $Z/H = (0.92, 0.85 \text{ \& } 0.78)$ at $X/H = 4$ for one-, two- and three-vehicle cases, respectively.

Figures 5.7(a) and (b) show \bar{T}^* contours and \overrightarrow{VW}^* vectors in the cross-sectional $Y-Z$ plane at $X/H = 4$ for the vehicle(s) ($\alpha = 25^\circ$) at 30 km/h for one- and two-vehicle cases, respectively. The air flow vectors of a pair of counter rotating vortices behind the vehicle are still discriminable at $X/H = 4$. The saddle point in the outer edge of the full scalar dispersion region between the left- and right-hand side of scalar distribution, however, is not as discernible as at $X/H = 2$ (in Figure 5.5) because the valley in between is almost flat. The almost equal magnitude on the left- and right-hand sides of the full scalar dispersion region for one-vehicle case change to obviously left-hand short and right-hand tall for two-vehicle case, indicating that the preceding vehicle has more prominent effect

on the unbalance of scalar distributions at $X/H = 4$ than at $X/H = 2$. For the bases of the full scalar distribution regions, they are expanded from $-0.95 \leq Y/H \leq 1.05$ at $X/H = 2$ to $-1.41 \leq Y/H \leq 1.41$ at $X/H = 4$ due to the evolution of wake flow behind the vehicle. The topmost points of the scalar distribution regions are lowered from $Z/H = (0.86 \text{ \& } 0.81)$ at $X/H = 2$ to $Z/H = (0.84 \text{ \& } 0.78)$ at $X/H = 4$ for one- and two-vehicle cases, respectively.

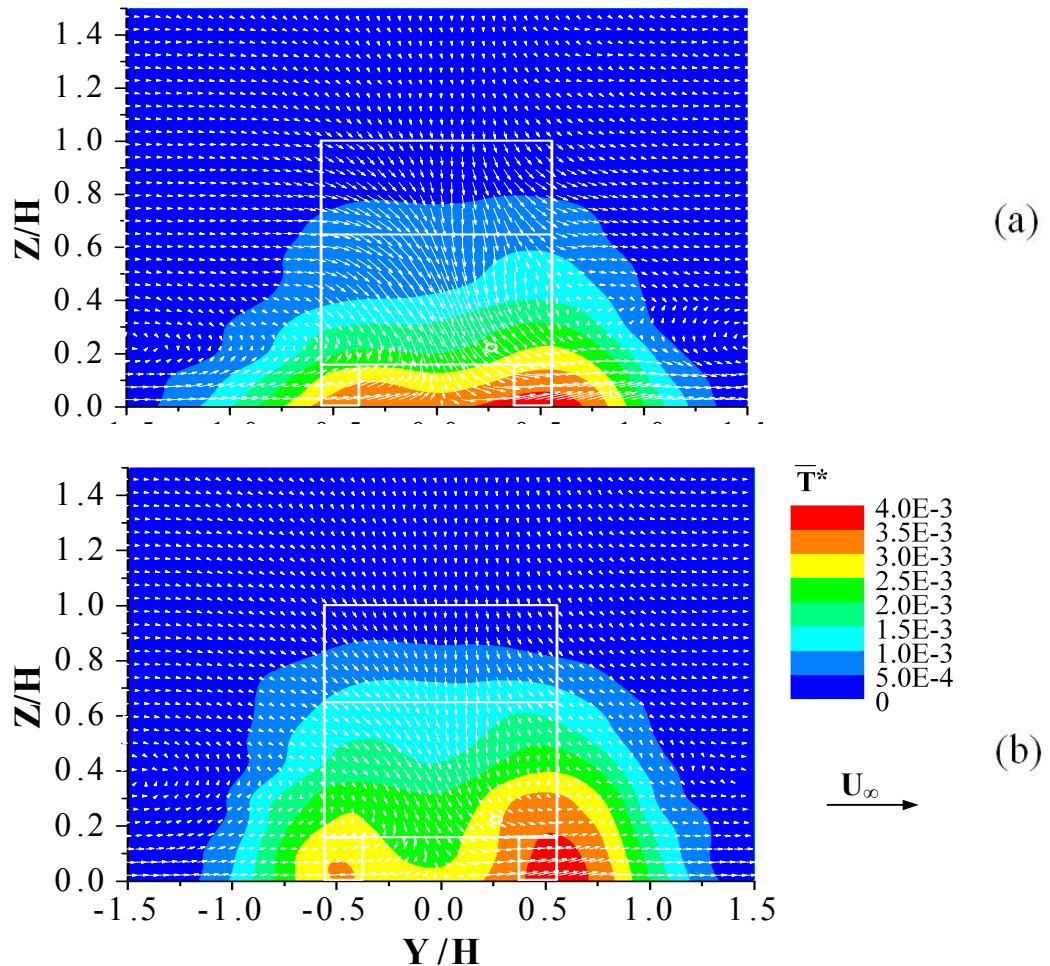


Figure 5.7 Normalized mean temperature excess, \bar{T}^* and normalized mean vector, \overline{VW}^* in Y-Z plane at $X/H = 4$ behind the vehicle(s) ($\alpha = 25^\circ$) at 30 km/h for (a) one-vehicle and (b) two-vehicle cases (Huang et al. 2009b).

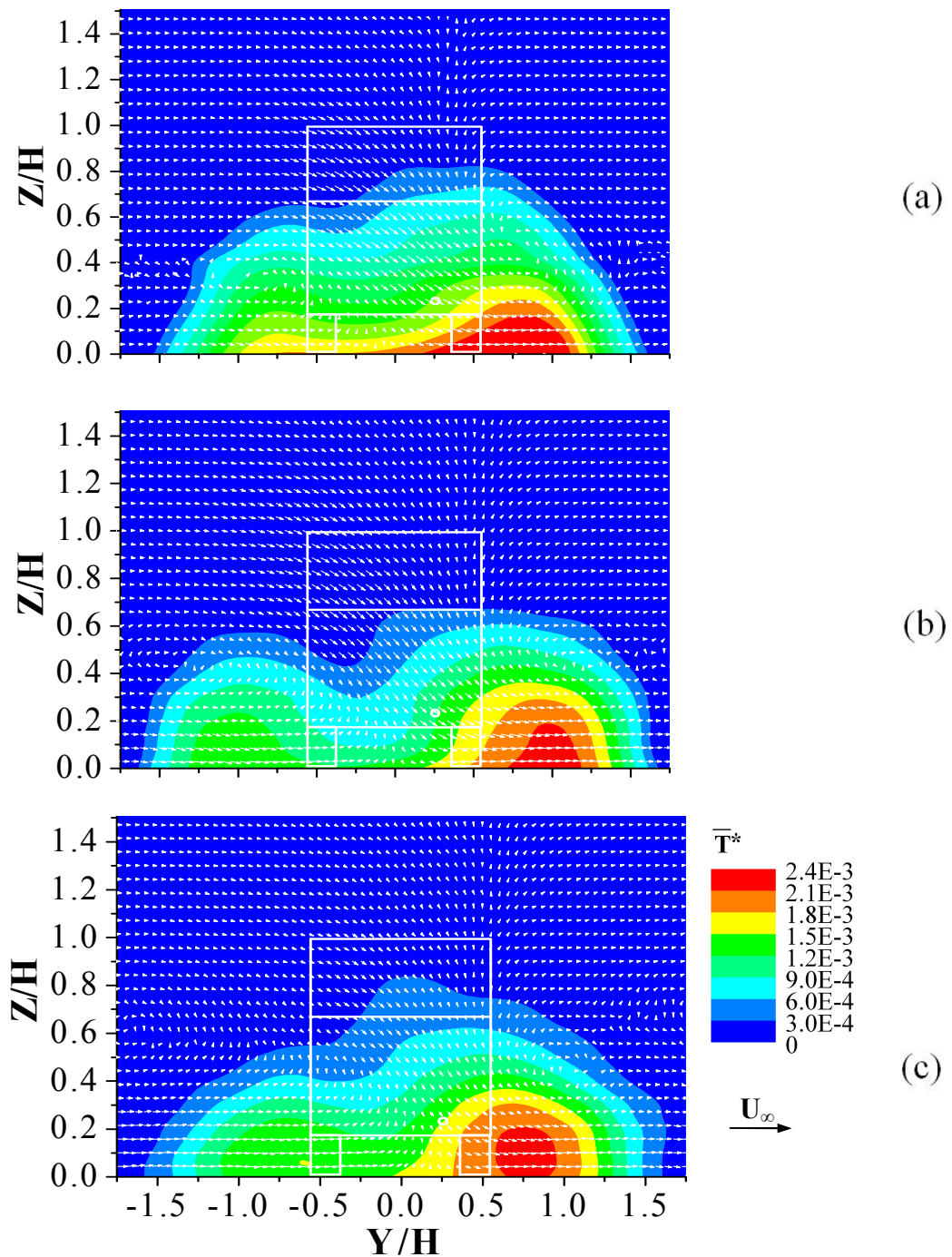


Figure 5.8 Normalized mean temperature excess, \bar{T}^* and normalized mean vector, \overline{VW}^* in Y-Z plane at $X/H = 6$ behind the vehicle(s) ($\alpha = 25^\circ$) at 10 km/h for (a) one-vehicle, (b) two-vehicle and (c) three-vehicle cases.

Normalized lateral and vertical velocity components, \overrightarrow{VW}^* and normalized mean temperature excess, \bar{T}^* contours for the vehicle(s) ($\alpha = 25^\circ$) in the cross-sectional Y - Z plane at $X/H = 6$ at 10 km/h for one- two- and three-vehicle cases are shown in Figures 5.8(a) to (c), respectively. The vectors of trailing vortices are not as discriminable as at $X/H = 2$ and 4. The peak scalar region is located at around $0.7 < Y/H < 1.1$ and $Z/H < 0.2$ which is further away from the vehicle centerline at $X/H = 6$ than at $X/H = 4$ due to the expansion of wake structure. The full scalar distribution region decreases in height by the downwash flow but their bases are expanded from around $Y/H = \pm 1.28$ at $X/H = 4$ to $Y/H = \pm 1.58$ at $X/H = 6$. The effect of the preceding vehicle(s) still obviously increases the size of the dual peak scalar regions and unbalances the dual scalar distribution fields in between the vortices on the left- and right-hand sides, as at earlier X/H locations.

Figures 5.9(a) and (b) show \bar{T}^* contours and \overrightarrow{VW}^* vectors in the cross-sectional Y - Z plane at $X/H = 6$ for the vehicle(s) ($\alpha = 25^\circ$) at 30 km/h for one- and two-vehicle cases. The peak scalar region is located at around $0.25 < Y/H < 0.8$ and $Z/H < 0.2$ for $X/H = 6$ while it was at around $0.25 < Y/H < 0.75$ and $Z/H < 0.2$ for $X/H = 4$. Their bases of full scalar distribution field also expand from $Y/H = \pm 1.41$ at $X/H = 4$ to $Y/H = \pm 1.55$ at $X/H = 6$. For the dual peak scalar regions on the left- and right-hand sides, these two regions are further away from the vehicle centerline by a distance, $Y/H = 0.1$ if compared with their previous Y/H locations at $X/H = 4$ in Figure 5.7. Similar to the case at $X/H = 4$, the unbalance of

the scalar dispersion and distribution regions in between the vortices on the left- and right-hand sides is enhanced by the presence of the preceding vehicle.

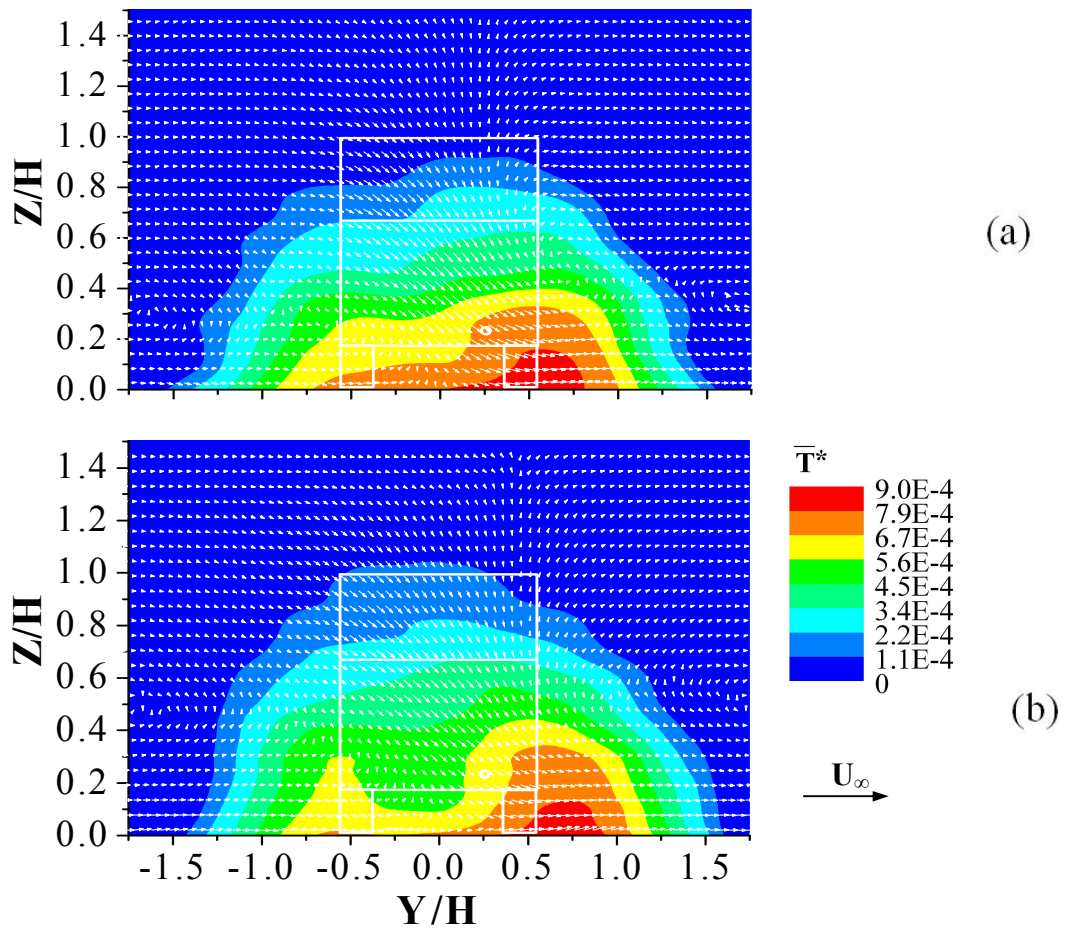


Figure 5.9 Normalized mean temperature excess, \bar{T}^* and normalized mean vector, \overline{VW}^* in Y - Z plane at $X/H = 6$ behind the vehicle(s) ($\alpha = 25^\circ$) at 30 km/h for (a) one-vehicle and (b) two-vehicle cases.

Figures 5.10(a) to (c) show \bar{T}^* contours and \overline{VW}^* vectors in cross-sectional Y - Z plane at $X/H = 8$ for the vehicle(s) ($\alpha = 25^\circ$) at 10 km/h for one-, two- and three-vehicle cases.

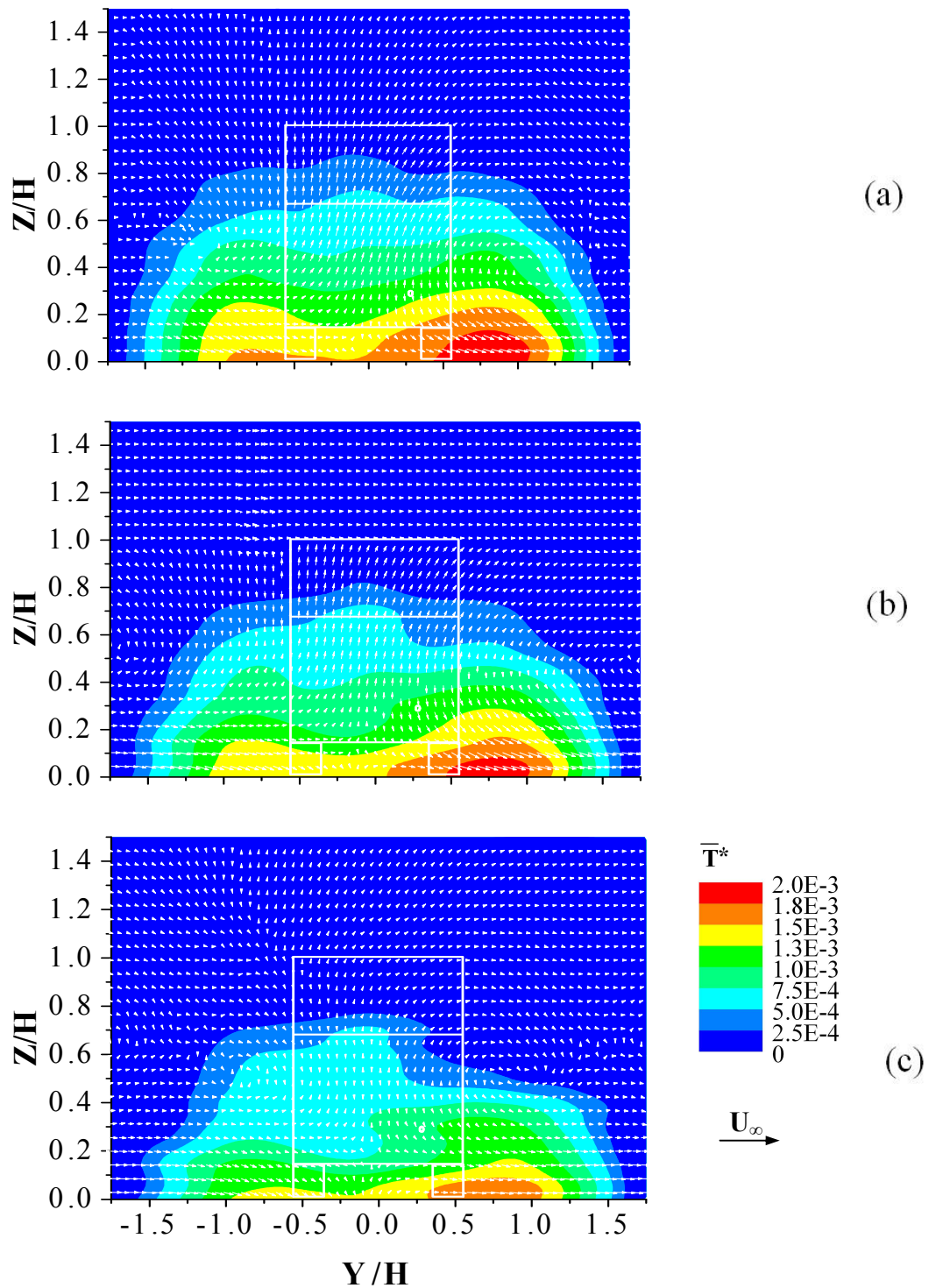


Figure 5.10 Normalized mean temperature excess, \bar{T}^* and normalized mean vector, \overline{VW}^* in Y - Z plane at $X/H = 8$ behind the vehicle(s) ($\alpha = 25^\circ$) at 10 km/h for (a) one-vehicle, (b) two-vehicle (Huang et al. 2009b) and (c) three-vehicle cases.

Figure 5.10(a) shows that the center location of the peak scalar region remains at $Y/H = 0.83$ which is the same to the one-vehicle case in Figure 5.8(a). This suggests that the vehicular exhaust jet almost follows a straight trajectory in parallel to X axis in between $X/H = 6$ and 8 or the natural expanding rate of wake structure is much slower after $X/H = 6$. From $X/H = 0$ to 8, the center of the peak scalar region shifts from $Y/H = 0.4$ to 0.65, 0.65 to 0.8 and 0.8 to 0.8 when it moves from $X/H = 2$ to 4, 4 to 6 and 6 to 8, respectively at low vehicle speed (e.g., 10 km/h). But the rightmost edge of the full scalar distribution region occurs at $Y/H = 1.6$ for $X/H = 8$. If compared with $Y/H = 1.25$ at $X/H = 6$, it indicates that the peak scalar region is still growing in size while its center moves aside at a much slower pace. This downstream location at $X/H = 8$ is close to the end of near-wake region of vehicle (i.e., $0 < X/H < 10$, as defined by Baker, 2001) where the large trailing vortices break into small eddies. The peak scalar region on the left-hand side of the vehicle wake noticeably diminishes with the addition of preceding vehicle(s) as shown in Figures 5.10(a) to (c).

Figures 5.11(a) and (b) show \bar{T}^* contours and \overrightarrow{VW}^* vectors in the cross-sectional $Y-Z$ plane at $X/H = 8$ for the vehicle(s) ($\alpha = 25^\circ$) at 30 km/h for one- and two-vehicle cases. The dual peak scalar regions on the left- and right-hand sides at this downstream location, $X/H = 8$, slightly decrease in height and maintain almost the same in width when compared with that at $X/H = 6$. These slight changes indicate that the scalar dispersion has reached its steady flow at the near end of the near-wake region. The stronger downwash flow induced by the

presence of the preceding vehicle splits the original connected dual peak scalar regions into two separate regions.

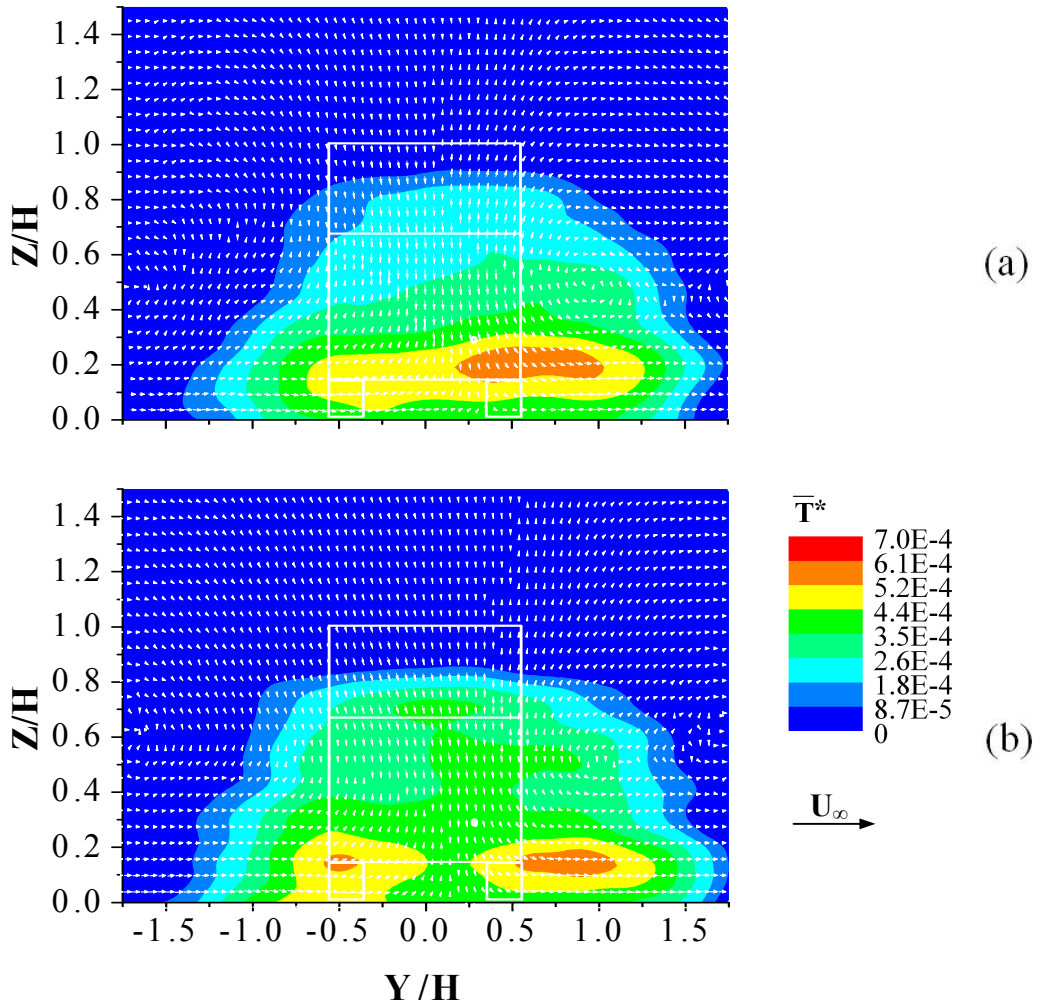


Figure 5.11 Normalized mean temperature excess, \bar{T}^* and normalized mean vector, \overline{VW}^* in Y-Z plane at $X/H = 8$ behind the vehicle(s) ($\alpha = 25^\circ$) at 30 km/h for (a) one-vehicle and (b) two-vehicle cases (Huang et al. 2009b).

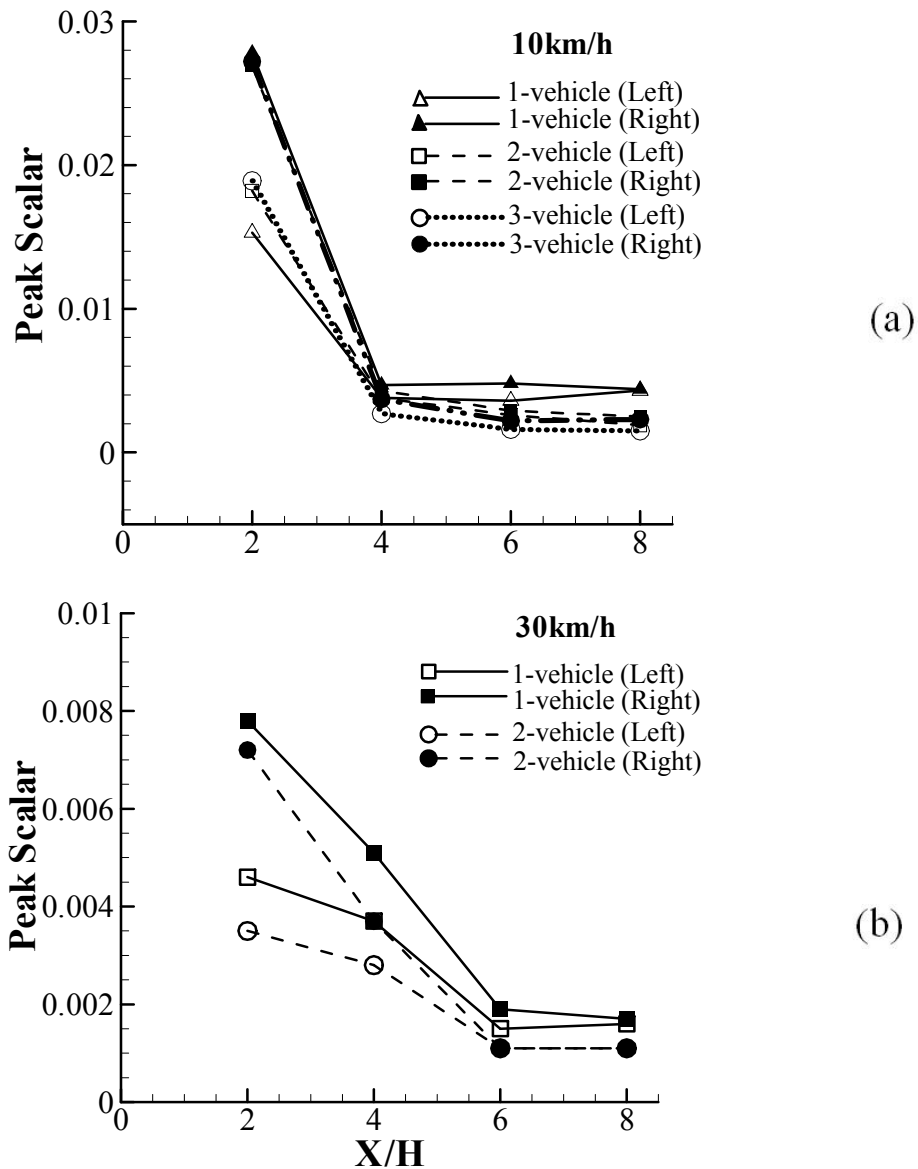


Figure 5.12 Peak scalar, \bar{T}_{\max}^* behind the studied vehicle(s) ($\alpha = 25^\circ$) for the left- and right-hand regions along the downstream distance, X/H at 10 km/h and 30 km/h.

The peak scalar values of \bar{T}_{\max}^* along the downstream distance, X/H behind both the left- and right-hand sides of the vehicle(s) ($\alpha = 25^\circ$) are shown in Figures 5.12(a) and (b). It clearly shows that the right-hand scalar dispersion region always provides a higher peak scalar value than the left-hand region for the present study due to the tailpipe exit location on the right-hand side of vehicle. On the other hand,

Chang et al. (2009b) demonstrated that if the tailpipe exit is located at the center of vehicle, a left-right symmetric scalar dispersion pattern can be observed (as shown in Figure 6(c) of Chang et al. (2009b)). In the present study, it can be further concluded that the vehicle queue effect on the peak scalar value is more sensitive for $X/H \leq 4$ at 10 km/h, and $X/H \leq 6$ at 30 km/h, respectively.

The modified crosswind finite line source Gaussian formula from Equation (2-21) was adopted to calculate a single finite line scalar, T distribution behind the vehicle(s) ($\alpha = 60^\circ$) in the downwind distance which is expressed as:

$$T = \frac{Q}{2\pi\sigma_y\sigma_zU} \left[\exp\left(-\frac{(y-y_0)^2}{2\sigma_y^2}\right) \right] \left\{ \exp\left[-\frac{(z-z_0)^2}{2\sigma_z^2}\right] + \exp\left[-\frac{(z+z_0)^2}{2\sigma_z^2}\right] \right\} \quad (5-1)$$

where Q is the strength of a finite temperature line source; U is wind speed; y_0 and z_0 are the horizontal (in Y -axis) and vertical (in Z -axis) locations of source, respectively; and σ_y and σ_z are horizontal (in Y -axis) and vertical (in Z -axis) dispersion parameters, respectively. For the present study specifically, the spatial variables were normalized by the vehicle height, $H = 0.081$ m, and the mean temperature excess, \bar{T} was normalized by the temperature excess of exhaust jet, T_j .

Equation (5-1) can be expressed as follows:

$$\bar{T}^* = \frac{Q_0/T_j}{2\pi\sigma_y\sigma_zU} \left[\exp\left(\frac{-(y/H-y_0/H)^2}{2(\sigma_y/H)^2}\right) \right] \left\{ \exp\left[\frac{-(z/H-z_0/H)^2}{2(\sigma_z/H)^2}\right] + \exp\left[\frac{-(z/H+z_0/H)^2}{2(\sigma_z/H)^2}\right] \right\} \quad (5-2)$$

where Q_0 is the strength of a single finite temperature line source for the studied vehicle(s) ($\alpha = 60^\circ$).

For the dual finite line sources (i.e., the studied vehicles ($\alpha = 25^\circ$), Equation (5-1) was further modified from a single finite line source to the Equation (5-3) of dual finite line sources (i.e., left- and right-hand finite line sources are subscripted by 1 and 2, respectively) to calculate a finite line scalar, T distribution behind the studied vehicle(s) ($\alpha = 25^\circ$) in the downwind distance as:

$$T = \frac{Q_1}{2\pi\sigma_{y_1}\sigma_{z_1}U} \left[\exp\left(\frac{-(y-y_1)^2}{2\sigma_{y_1}^2}\right) \right] \left\{ \exp\left[\frac{-(z-z_1)^2}{2\sigma_{z_1}^2}\right] + \exp\left[\frac{-(z+z_1)^2}{2\sigma_{z_1}^2}\right] \right\} \\ + \frac{Q_2}{2\pi\sigma_{y_2}\sigma_{z_2}U} \left[\exp\left(\frac{-(y-y_2)^2}{2\sigma_{y_2}^2}\right) \right] \left\{ \exp\left[\frac{-(z-z_2)^2}{2\sigma_{z_2}^2}\right] + \exp\left[\frac{-(z+z_2)^2}{2\sigma_{z_2}^2}\right] \right\} \quad (5-3)$$

For the present study specifically, the spatial variables were normalized by the vehicle height, $H = 0.081$ m, and the mean temperature excess, \bar{T} was normalized by the temperature excess of exhaust jet, \bar{T}_j . Equation (5-3) can be expressed as follows:

$$\bar{T}^* = \frac{Q_1/\bar{T}_j}{2\pi\sigma_{y_1}\sigma_{z_1}U} \left[\exp\left(\frac{-(y/H-y_1/H)^2}{2(\sigma_{y_1}/H)^2}\right) \right] \left\{ \exp\left[\frac{-(z/H-z_1/H)^2}{2(\sigma_{z_1}/H)^2}\right] + \exp\left[\frac{-(z/H+z_1/H)^2}{2(\sigma_{z_1}/H)^2}\right] \right\} \\ + \frac{Q_2/\bar{T}_j}{2\pi\sigma_{y_2}\sigma_{z_2}U} \left[\exp\left(\frac{-(y/H-y_2/H)^2}{2(\sigma_{y_2}/H)^2}\right) \right] \left\{ \exp\left[\frac{-(z/H-z_2/H)^2}{2(\sigma_{z_2}/H)^2}\right] + \exp\left[\frac{-(z/H+z_2/H)^2}{2(\sigma_{z_2}/H)^2}\right] \right\} \quad (5-4)$$

where y_1 and z_1 , y_2 and z_2 are the locations of left- and right-hand sources, respectively; σ_{y_1} , σ_{z_1} , σ_{y_2} and σ_{z_2} are the left- and right-hand dispersion parameters in horizontal (in Y -axis) and vertical (in Z -axis), respectively; Q_1 and Q_2 are the strengths of dual finite temperature line sources for the studied vehicles ($\alpha = 25^\circ$) from the left- and right-hand regions, respectively.

The fitted values of variables in Equation (5-4) based on the normalized mean temperature excess distributions obtained from the results of Figures 5.3 to 5.11 for the studied vehicle(s) ($\alpha = 25^\circ$) cases at different locations in the downwind distance are summarized in Table 5.1. Because the fitted values of z_1 and z_2 are normally less than 10^{-3} , they can be neglected and are not included in Table 5.1. It means that the peaks of left and right scalar dispersion regions are very close to ground, as shown in Figures 5.3(a) to (c).

$\alpha = 25^\circ$ $X/H = 2$	$\frac{Q_1/T_j}{2\pi\sigma_{y_1}\sigma_{z_1}U}$	$\frac{y_1}{H}$	$\frac{\sigma_{y_1}}{H}$	$\frac{\sigma_{z_1}}{H}$	$\frac{Q_2/T_j}{2\pi\sigma_{y_2}\sigma_{z_2}U}$	$\frac{y_2}{H}$	$\frac{\sigma_{y_2}}{H}$	$\frac{\sigma_{z_2}}{H}$
1-vehicle 10 km/h	0.01531	-0.3010	0.3017	0.3256	0.0278	0.3665	0.2974	0.5427
2-vehicle 10 km/h	0.01821	-0.3962	0.3362	0.3415	0.02689	0.3882	0.2955	0.3785
3-vehicle 10 km/h	0.01885	-0.3798	0.3105	0.3194	0.02717	0.3695	0.2849	0.3696
1-vehicle 30 km/h	0.00461	-0.2970	0.2917	0.4733	0.00784	0.3493	0.2922	0.3990
2-vehicle 30 km/h	0.00346	-0.2694	0.2701	0.4354	0.0072	0.4021	0.3034	0.3564

$\alpha = 25^\circ$ $X/H = 4$	$\frac{Q_1/T_j}{2\pi\sigma_{y_1}\sigma_{z_1}U}$	$\frac{y_1}{H}$	$\frac{\sigma_{y_1}}{H}$	$\frac{\sigma_{z_1}}{H}$	$\frac{Q_2/T_j}{2\pi\sigma_{y_2}\sigma_{z_2}U}$	$\frac{y_2}{H}$	$\frac{\sigma_{y_2}}{H}$	$\frac{\sigma_{z_2}}{H}$
1-vehicle 10 km/h	0.00379	-0.5063	0.4581	0.3773	0.00473	0.5490	0.4496	0.4682
2-vehicle 10 km/h	0.00378	-0.5420	0.4633	0.2786	0.00429	0.5836	0.4474	0.3744
3-vehicle 10 km/h	0.00265	-0.7544	0.5006	0.3164	0.00369	0.7617	0.4587	0.3413
1-vehicle 30 km/h	0.00366	-0.3615	0.3945	0.3754	0.00506	0.4815	0.4334	0.3965
2-vehicle 30 km/h	0.00284	-0.4856	0.3819	0.4219	0.00366	0.5461	0.3945	0.3754

$\alpha = 25^\circ$ $X/H = 6$	$\frac{Q_1/T_j}{2\pi\sigma_{y_1}\sigma_{z_1}U}$	$\frac{y_1}{H}$	$\frac{\sigma_{y_1}}{H}$	$\frac{\sigma_{z_1}}{H}$	$\frac{Q_2/T_j}{2\pi\sigma_{y_2}\sigma_{z_2}U}$	$\frac{y_2}{H}$	$\frac{\sigma_{y_2}}{H}$	$\frac{\sigma_{z_2}}{H}$
1-vehicle 10 km/h	0.00359	-0.7750	0.5401	0.3373	0.00483	0.7811	0.5113	0.3706
2-vehicle 10 km/h	0.00258	-0.7605	0.5067	0.2434	0.00293	0.7837	0.5797	0.3194
3-vehicle 10 km/h	0.00155	-0.9589	0.4397	0.3085	0.00221	0.9773	0.5506	0.3171
1-vehicle 30 km/h	0.00154	-0.5106	0.5696	0.4255	0.00185	0.5730	0.5974	0.4142
2-vehicle 30 km/h	0.00108	-0.5642	0.4898	0.4978	0.00108	0.7271	0.6076	0.4493

$\alpha = 25^\circ$ $X/H = 8$	$\frac{Q_1/T_j}{2\pi\sigma_{y_1}\sigma_{z_1}U}$	$\frac{y_1}{H}$	$\frac{\sigma_{y_1}}{H}$	$\frac{\sigma_{z_1}}{H}$	$\frac{Q_2/T_j}{2\pi\sigma_{y_2}\sigma_{z_2}U}$	$\frac{y_2}{H}$	$\frac{\sigma_{y_2}}{H}$	$\frac{\sigma_{z_2}}{H}$
1-vehicle 10 km/h	0.00431	-0.8178	0.6721	0.4617	0.00435	0.8156	0.6059	0.4175
2-vehicle 10 km/h	0.00188	-0.8694	0.6698	0.5156	0.00246	0.8013	0.6096	0.3906
3-vehicle 10 km/h	0.00149	-0.7769	0.6298	0.4123	0.00226	0.7689	0.6103	0.3504
1-vehicle 30 km/h	0.00159	-0.4273	0.5654	0.4520	0.00172	0.6378	0.6905	0.3979
2-vehicle 30 km/h	0.00109	-0.4934	0.6032	0.5246	0.00109	0.8456	0.8368	0.4893

Table 5.1 Fitted values of variables in the dual finite line source Gaussian equation (5-4) for the studied vehicles ($\alpha = 25^\circ$).

From Table 5.1 for the studied queue vehicles ($\alpha = 25^\circ$) of different vehicle speeds, the ratios of left-hand and right-hand line source strengths,

$$\frac{Q_1/T_j}{2\pi\sigma_{y_1}\sigma_{z_1}U} \bigg/ \frac{Q_2/T_j}{2\pi\sigma_{y_2}\sigma_{z_2}U}$$

were found to be around 48% to 70% at $X/H = 2$, 72% to 88% at $X/H = 4$, 70 to 100% at $X/H = 6$ and 66% to 100% at $X/H = 8$, respectively. This trend clearly indicates that the most significant change in source

strength takes place within range $X/H < 6$, therefore this range requires special attention for the future studies of pollutant dispersion from moving vehicles. The presence of preceding vehicle(s) will make the source strength change occur faster. From the spatial parameters, y , σ_y and σ_z , it can be seen that additional preceding vehicle(s) make the left and right scalar regions more symmetrical in y -axis (i.e., y_1 and y_2) of the studied vehicle(s) while the size and strength of the scalar region locating at tailpipe side are higher.

5.3.2 Exhaust scalar dispersion and distribution fields behind a queue of the studied vehicles ($\alpha = 60^\circ$) in the downstream

Figures 5.13(a) to (c) show \overline{T}^* contours in the cross-sectional Y - Z plane at $X/H = 2$ for the vehicle(s) ($\alpha = 60^\circ$) at 10 km/h for one-, two- and three-vehicle cases. The wake structure of the vehicle ($\alpha = 60^\circ$) has a pair of counter-rotating trailing vortices whose magnitude of vorticity is about one-third of the vehicle ($\alpha = 25^\circ$). As the trailing vortices are weak, they do not have much effect on the wake flow and scalar distribution, hence the wake region behind the vehicle ($\alpha = 60^\circ$) is considered to be quasi two-dimensional (Ahmed et al. 1984; Chan et al. 2008b). Because \overline{VW}^* vectors for the vehicle(s) ($\alpha = 60^\circ$) are relatively small for the present studied range, $X/H = 2$ to 8, the \overline{VW}^* vectors are only shown in Figure 5.13 for $X/H = 2$ while other \overline{VW}^* vectors for $X/H = 4$ to 8 will not be presented to leave their scalar distribution fields in neat.

Even at this short distance from the exhaust tailpipe, $X/H = 2$, the wake flow generated at the centerline is strong enough to suppress the exhaust jet flow and trap almost all hot air to the central zone of the vehicle wake. The effect of offset exhaust jet flow is to shift the full scalar region away from the centerline of vehicle wake and toward the side of tailpipe exit by almost $Y/H = 0.1$, as shown in Figure 5.13(a). From the vertical profiles of \bar{U}/U_∞ for the two- and three-vehicle cases as shown in Figure 4.25(a), it can be observed that about 70~80% and 10~60% of the incoming flow is blocked by the preceding vehicle(s) for $Z/H < 1$ and $1 < Z/H < 2$, respectively. Therefore as observed for the vehicle ($\alpha = 25^\circ$), the downwash flow is enhanced by the preceding vehicle(s) and the peak scalar region is pushed downward to the ground in Figures 5.13(b) and (c). However, similar to the cases of vehicle(s) ($\alpha = 25^\circ$), the size of peak scalar region also decreases with the addition of preceding vehicle(s). Interestingly though, the peak scalar region moves downward by the presence of the preceding vehicle(s), the top of full scalar distribution region rises from $Z/H = 1.2$ to 1.4. In Figure 4.25(b), the u'/U_∞ turbulence profile indicates that the incoming flow has a high turbulence for $Z/H > 1$. Since the high turbulence favors heat and mass transfer, and may transport a small portion of scalar (i.e., pollutant) from its lower region, making the edge of scalar distribution region higher.

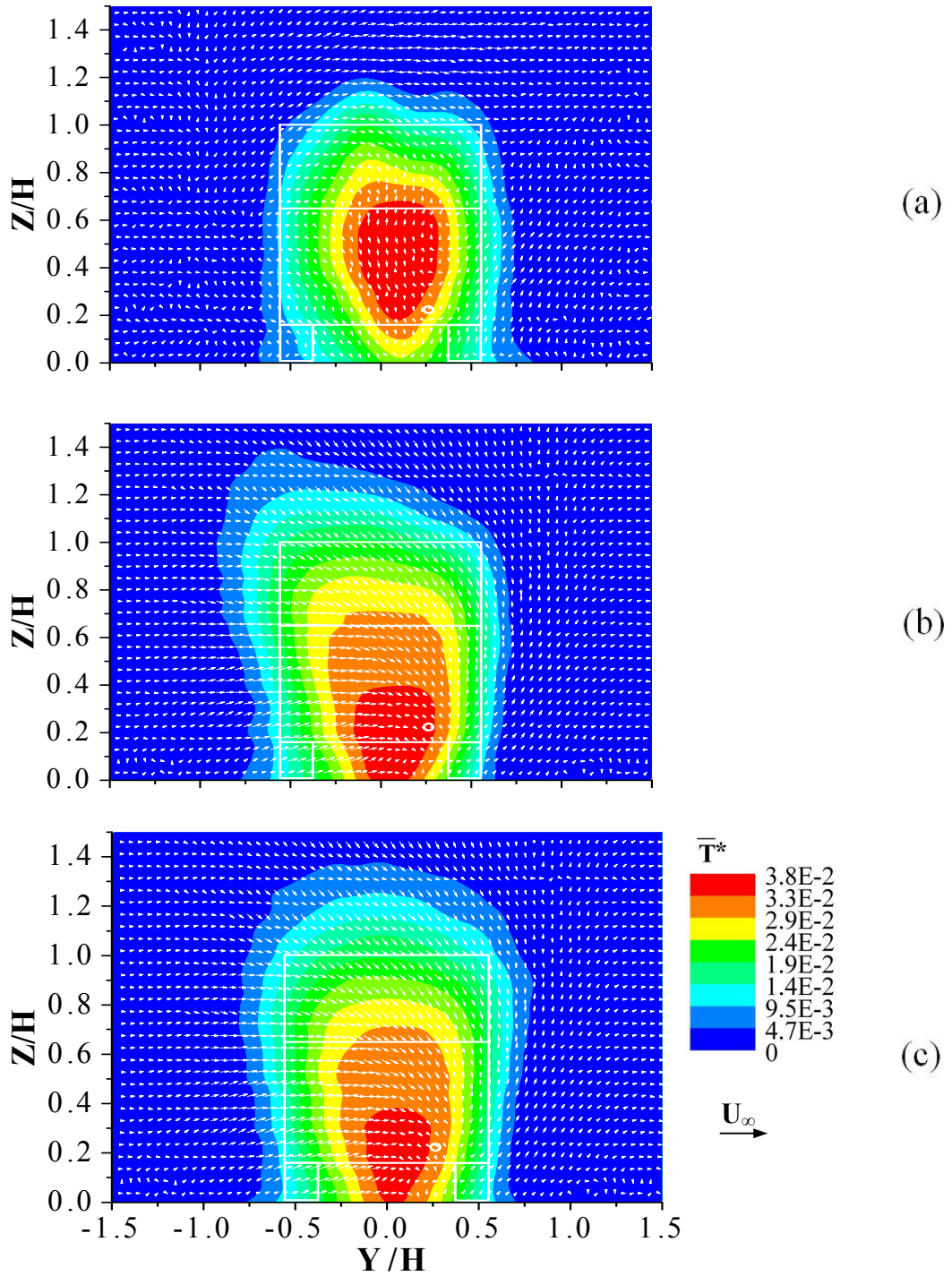


Figure 5.13 Normalized mean temperature excess, \bar{T}^* and normalized mean vector, \overline{VW}^* in Y-Z plane at $X/H = 2$ behind the vehicle(s) ($\alpha = 60^\circ$) at 10 km/h for (a) one-vehicle, (b) two-vehicle and (c) three-vehicle cases.

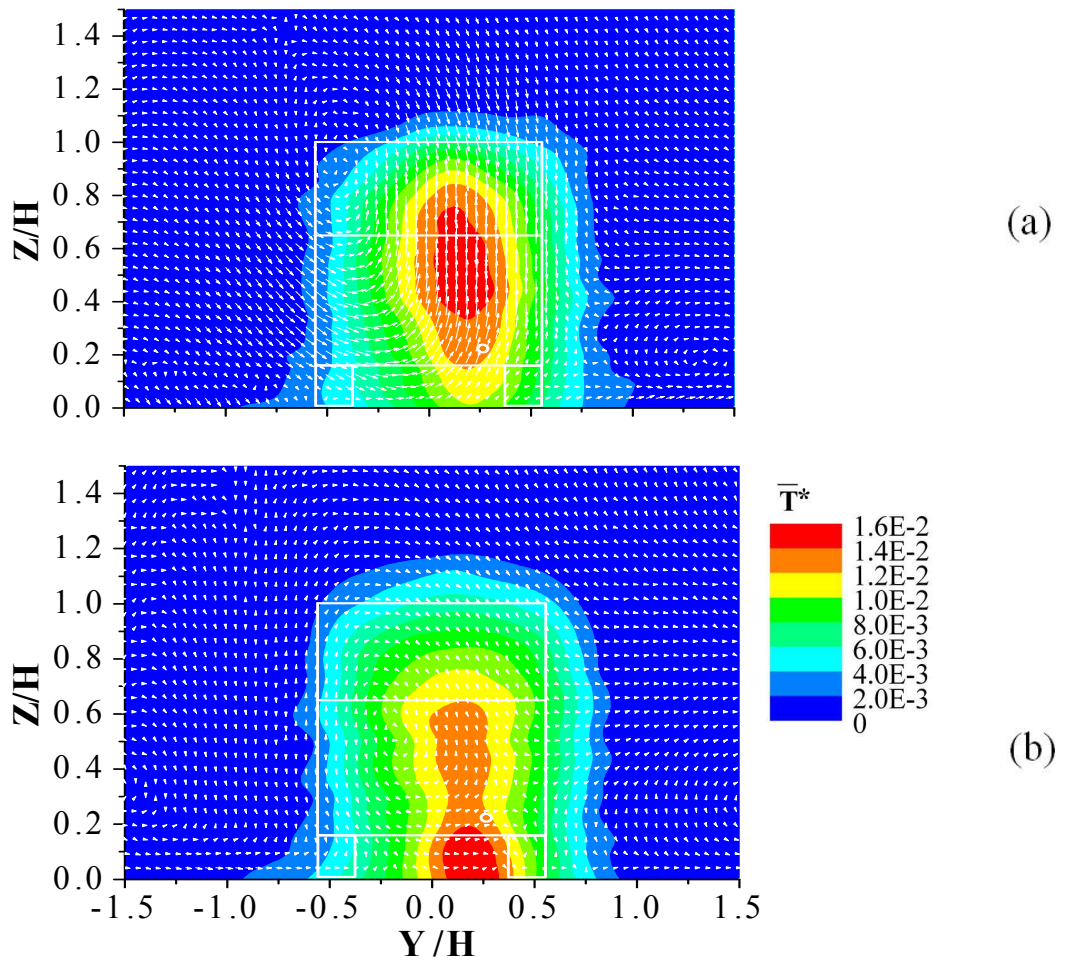


Figure 5.14 Normalized mean temperature excess, \bar{T}^* and normalized mean vector, \overline{VW}^* in Y - Z plane at $X/H = 2$ behind the vehicle(s) ($\alpha = 60^\circ$) at 30 km/h for (a) one-vehicle and (b) two-vehicle and three-vehicle cases.

Figures 5.14(a) and (b) show \bar{T}^* contours in the cross-sectional Y - Z plane at $X/H = 2$ for the vehicle(s) ($\alpha = 60^\circ$) at 30 km/h for one- and two-vehicle cases. Similar to the vehicle speed of 10 km/h cases, the scalar distribution patterns of 30 km/h cases are also slightly offset to the exhaust jet exit and the left-right region is almost symmetrical. The position of peak scalar region is very sensitive to the presence of the preceding vehicle which also raises the extreme edge of scalar distribution region from $Z/H = 1.1$ to 1.2, and similar to the previous 10 km/h cases.

It should be noted that the preceding vehicle(s) can lower the peak scalar region, but cannot change the overall structure of scalar dispersion and distribution region, for both 10 and 30 km/h.

Figures 5.15(a) to (c) show scalar \bar{T}^* contours in the cross-sectional $Y-Z$ plane at $X/H = 4$ for the vehicle(s) ($\alpha = 60^\circ$) at 10 km/h for one-, two- and three-vehicle cases, respectively. The sizes of full scalar distribution regions are increased for all the three studied cases which are 1.1 times higher and 1.4 times wider when compared with the corresponding regions at $X/H = 2$ for 10 km/h. But the peak scalar region becomes more slim for a single vehicle case at $X/H = 4$. For two- and three-vehicle cases, the difference in the highest scalar region pattern for $X/H = 4$ is even larger than no preceding vehicle case, and this suggests that the effect of the preceding vehicle(s) has more impact on the scalar distribution region than the downstream distance does. The sizes of peak scalar regions at $X/H = 4$ are nearly half of the location at $X/H = 2$. They are almost inversely proportional to the downstream distance. It should be noted that the region of the highest scalar distribution overlaps seemingly a direct jet flow path from its tailpipe exit as shown in Figure 5.15(c). That is believed to be a coincidence which is pushed down by the stronger downwash flow from Figure 5.15(b).

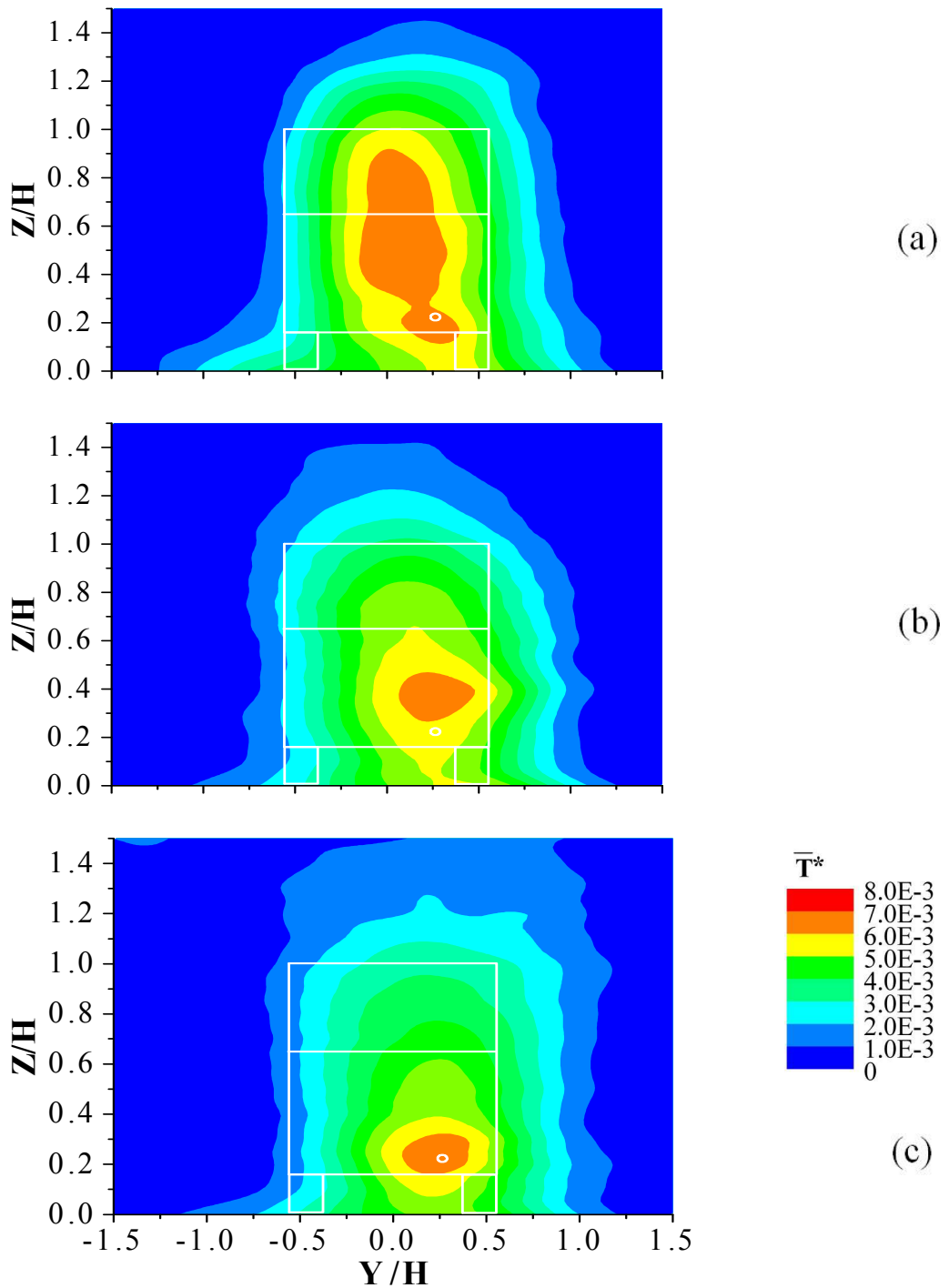


Figure 5.15 Normalized mean temperature excess, \bar{T}^* in Y - Z plane at $X/H = 4$ behind the vehicle(s) ($\alpha = 60^\circ$) at 10 km/h for (a) one-vehicle; (b) two-vehicle (Huang et al. 2009b) and (c) three-vehicle cases.

Figures 5.16(a) and (b) show \bar{T}^* contours in the cross-sectional Y - Z plane at $X/H = 4$ for the vehicle(s) ($\alpha = 60^\circ$) at 30 km/h for one- and two-vehicle cases. At this higher vehicle speed, the peak scalar region has an approximately $0.2H$ diameter size which is centered at $Y/H = 0.1$ and $Z/H = 0.4$, indicating that the offset exhaust jet flow has been almost completely suppressed by the wake flow at this higher vehicle speed. If the vehicle is preceded by another one, the enhanced downwash flow will stretch the peak scalar distribution region to a shape of vertical ellipse.

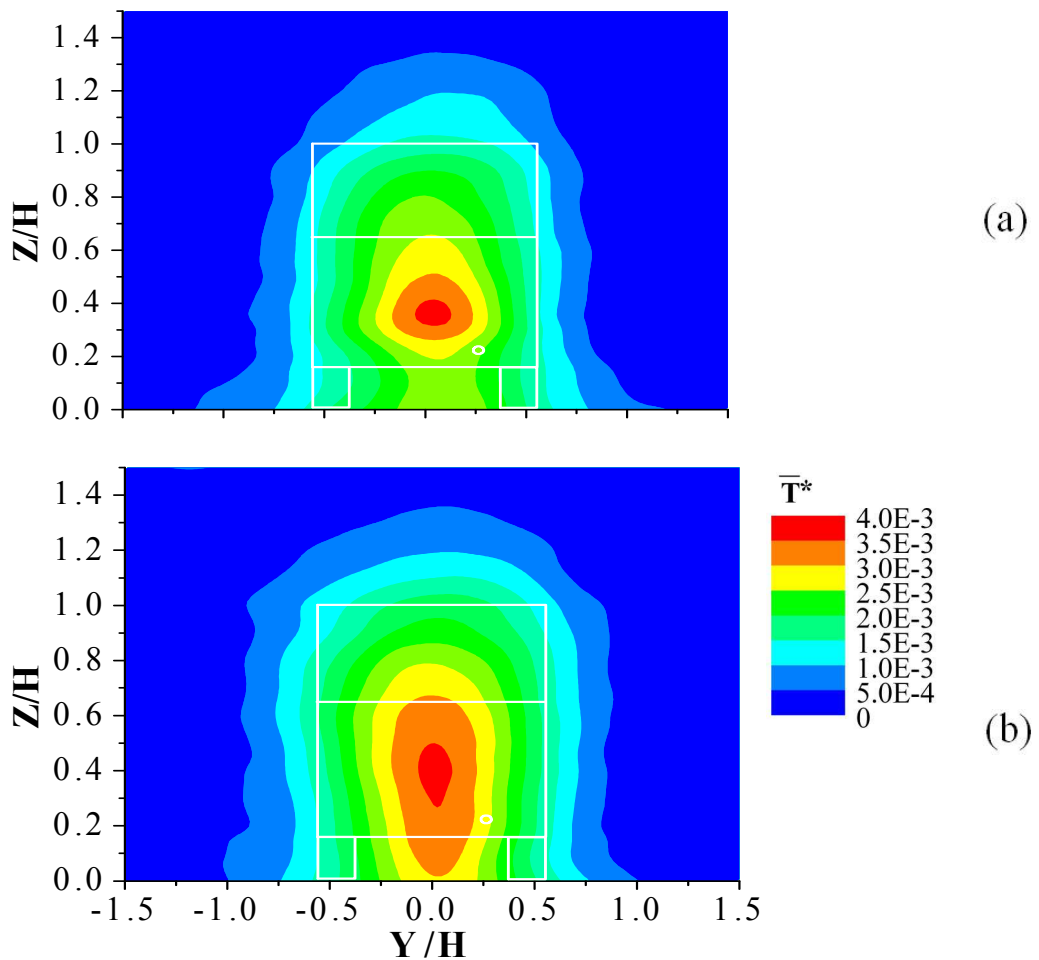


Figure 5.16 Normalized mean temperature excess, \bar{T}^* in Y - Z plane at $X/H = 4$ behind the vehicle(s) ($\alpha = 60^\circ$) at 30 km/h for (a) one-vehicle and (b) two-vehicle (Huang et al. 2009b).

Figures 5.17(a) to (c) show \bar{T}^* contours in the cross-sectional Y - Z plane at $X/H = 6$ for the vehicle(s) ($\alpha = 60^\circ$) at 10 km/h for one-, two- and three-vehicle cases, respectively. The vertical ellipse of the peak scalar region is well centered at around $Y/H = 0.1$ and $Z/H = 0.4$ for a single vehicle case. The downwash flow becomes stronger with the addition of the preceding vehicle(s) and will push the peak scalar region slightly downward indicating that the preceding vehicle effect is diminishing along the downstream distance. If compared with that at the location, $X/H = 4$, the sizes of full scalar distribution regions show not much difference, indicating that scalar distribution pattern of the vehicle(s) ($\alpha = 60^\circ$) reaches the steady state at around $X/H = 6$.

Figures 5.18(a) and (b) show \bar{T}^* contours in the cross-sectional Y - Z plane at $X/H = 6$ for the vehicle(s) ($\alpha = 60^\circ$) at 30 km/h for one- and two-vehicle cases. When compare Figure 5.18(a) with Figure 5.16(a), it can be seen that the centers of the peak scalar distribution region remain at the same Y/H and Z/H locations, indicating that the center of wake structure follows an almost straight trajectory in parallel to X axis for $X/H \geq 6$, which is the same as the vehicle(s) ($\alpha = 25^\circ$). The width of full scalar dispersion is expanded from about $1.5H$ for $X/H = 4$ to about $2.0H$ for $X/H = 6$. With the addition of the preceding vehicle (i.e., two-vehicle case), the peak scalar distribution region is entirely pushed to the ground by the stronger downwash flow.

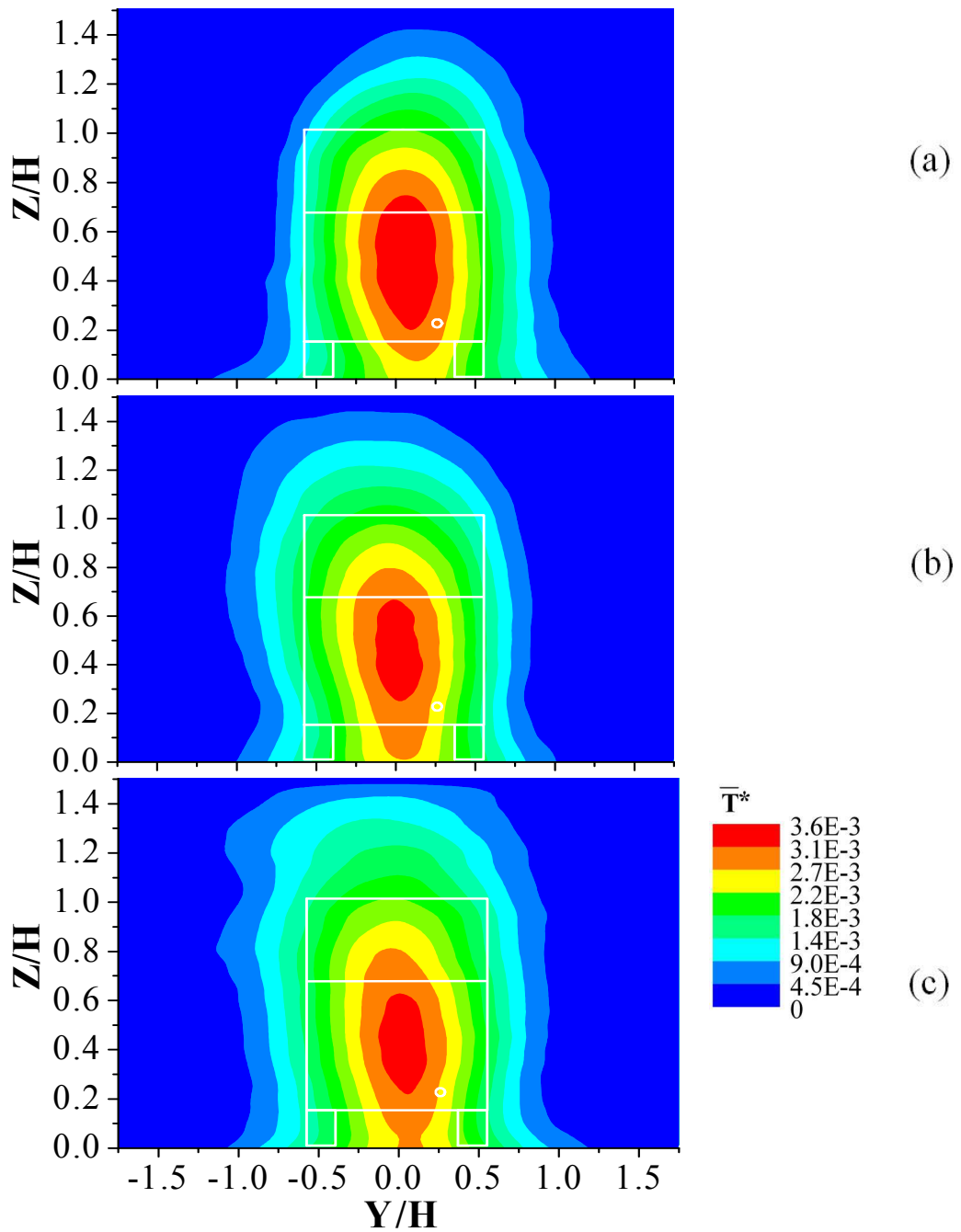


Figure 5.17 Normalized mean temperature excess, \bar{T}^* in Y - Z plane at $X/H = 6$ behind the vehicle(s) ($\alpha = 60^\circ$) at 10 km/h for (a) one-vehicle, (b) two-vehicle and (c) three-vehicle cases.

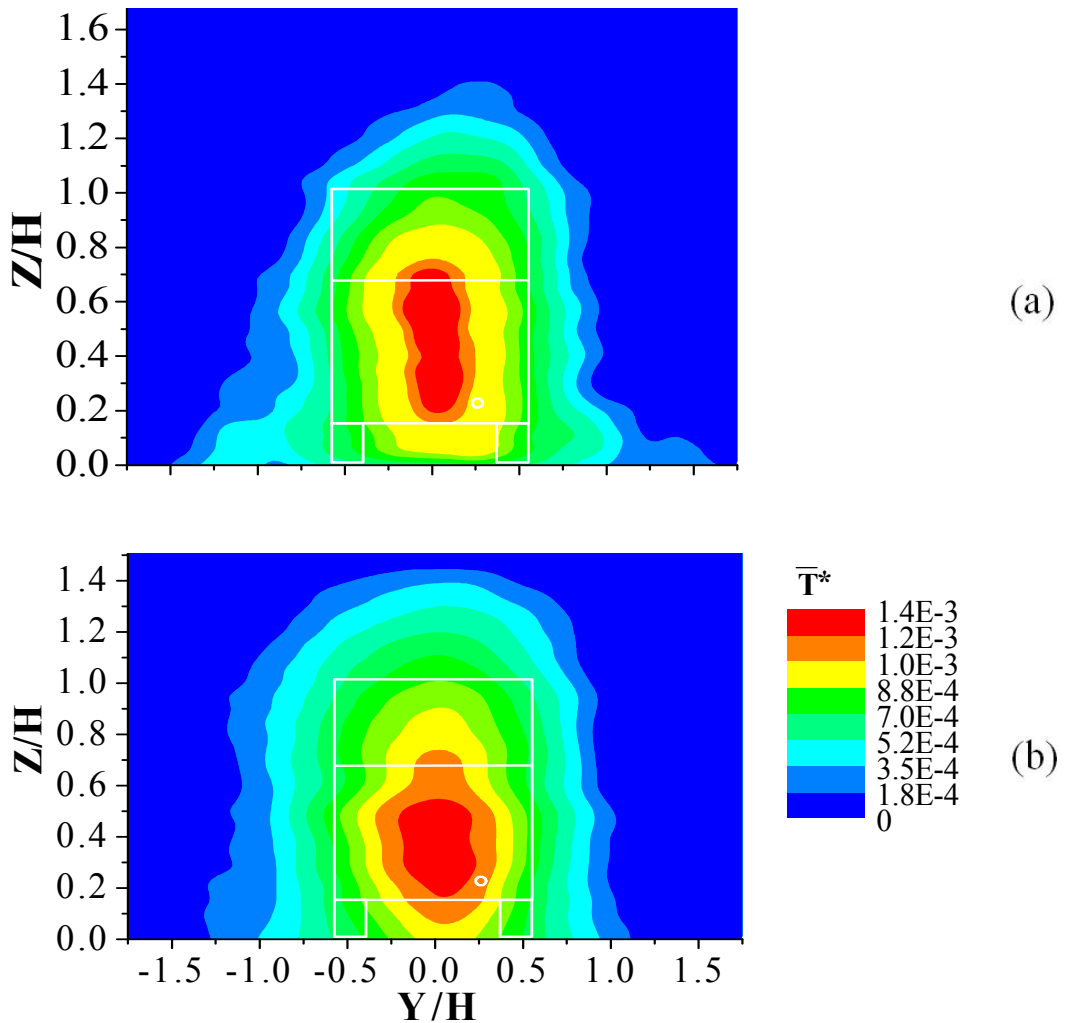


Figure 5.18 Normalized mean temperature excess, \bar{T}^* in Y - Z plane at $X/H = 6$ behind the vehicle(s) ($\alpha = 60^\circ$) at 30 km/h for (a) one-vehicle and (b) two-vehicle cases.

Figures 5.19(a) to (c) show \bar{T}^* contours in the cross-sectional Y - Z plane at $X/H = 8$ for the vehicle(s) ($\alpha = 60^\circ$) at 10 km/h for one- two- and three-vehicle cases. When compared with the downstream location at $X/H = 6$, the width of full scalar distribution region is expanded from about $2.0H$ for $X/H = 6$ to about $2.8H$ for $X/H = 8$. The centers of all peak scalar distribution regions are not higher than $Z/H = 0.12$ due to the effect of continuous pushing down by the downwash flow which can be enhanced by the preceding vehicle(s). At the end of the near-wake

region, the overall scalar distribution pattern is still horizontally symmetric along the centerline of the vehicle as shown in Figure 5.19.

Figures 5.20(a) and (b) show \bar{T}^* contours in the cross-sectional Y - Z plane at $X/H = 8$ for the vehicle(s) ($\alpha = 60^\circ$) at 30 km/h for one- and two-vehicle cases. If compared with a single vehicle of 30 km/h at $X/H = 6$, the scalar (i.e., \bar{T}^*) distribution patterns, they look similar except larger in width and height of their scalar distribution regions. It confirms our previous conclusion that the scalar distribution pattern of the vehicle(s) ($\alpha = 60^\circ$) reaches the steady state at around $X/H = 4$. One major difference between Figures 5.19 and 5.20 for 10 and 30 km/h at $X/H = 8$ is that the extreme edge of scalar distribution region for 30 km/h is not as regular shape as 10 km/h, due to its low signal level of \bar{T}^* . This comparison also confirms another conclusion that the scalar dissipation rate is more sensitive to the vehicle speed than to the downstream distance with or without the preceding vehicle(s).

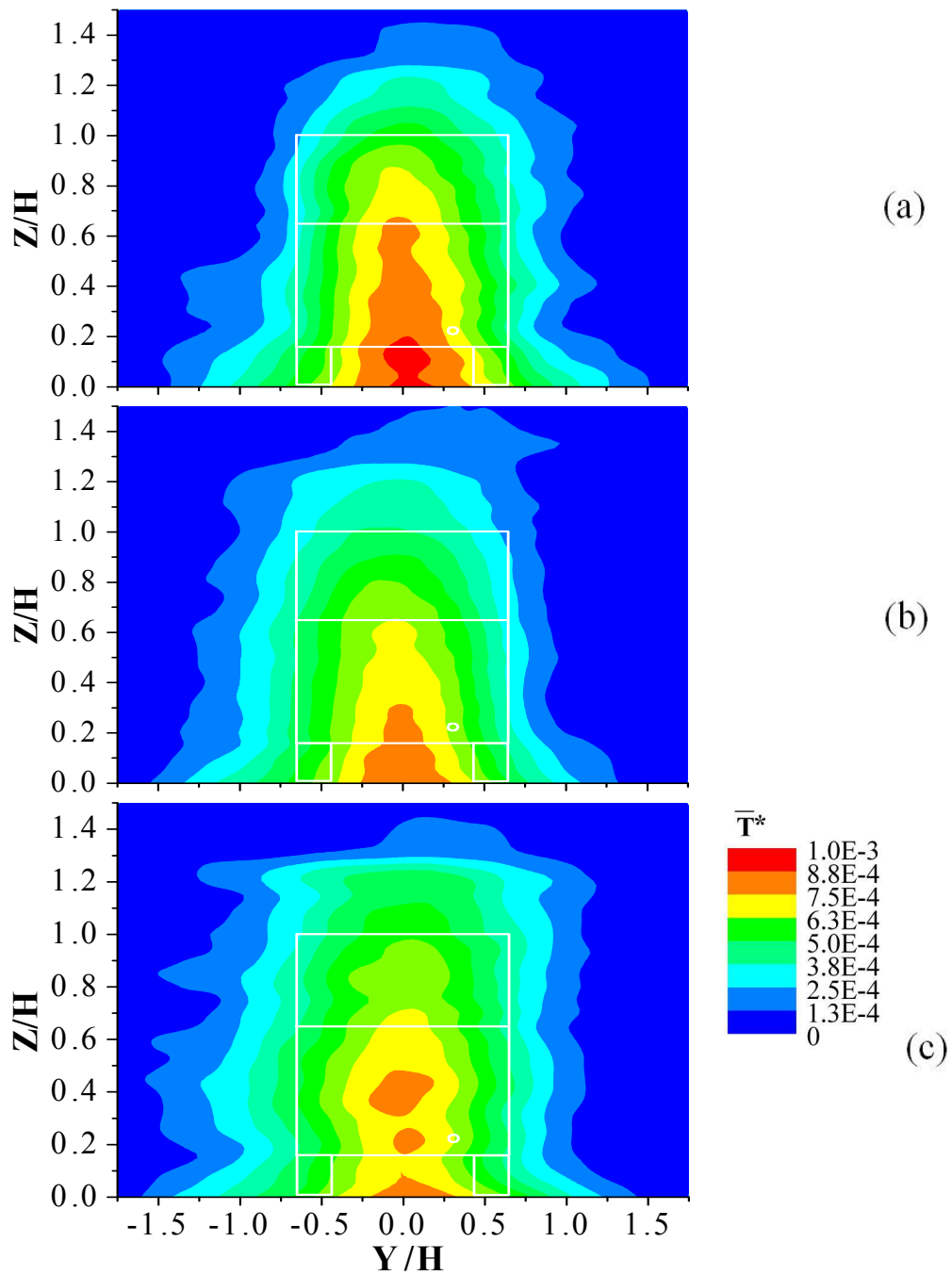


Figure 5.19 Normalized mean temperature excess, \bar{T}^* in Y - Z plane at $X/H = 8$ behind the vehicle(s) ($\alpha = 60^\circ$) at 10 km/h for (a) one-vehicle, (b) two-vehicle (Huang et al. 2009b) and (c) three-vehicle cases.

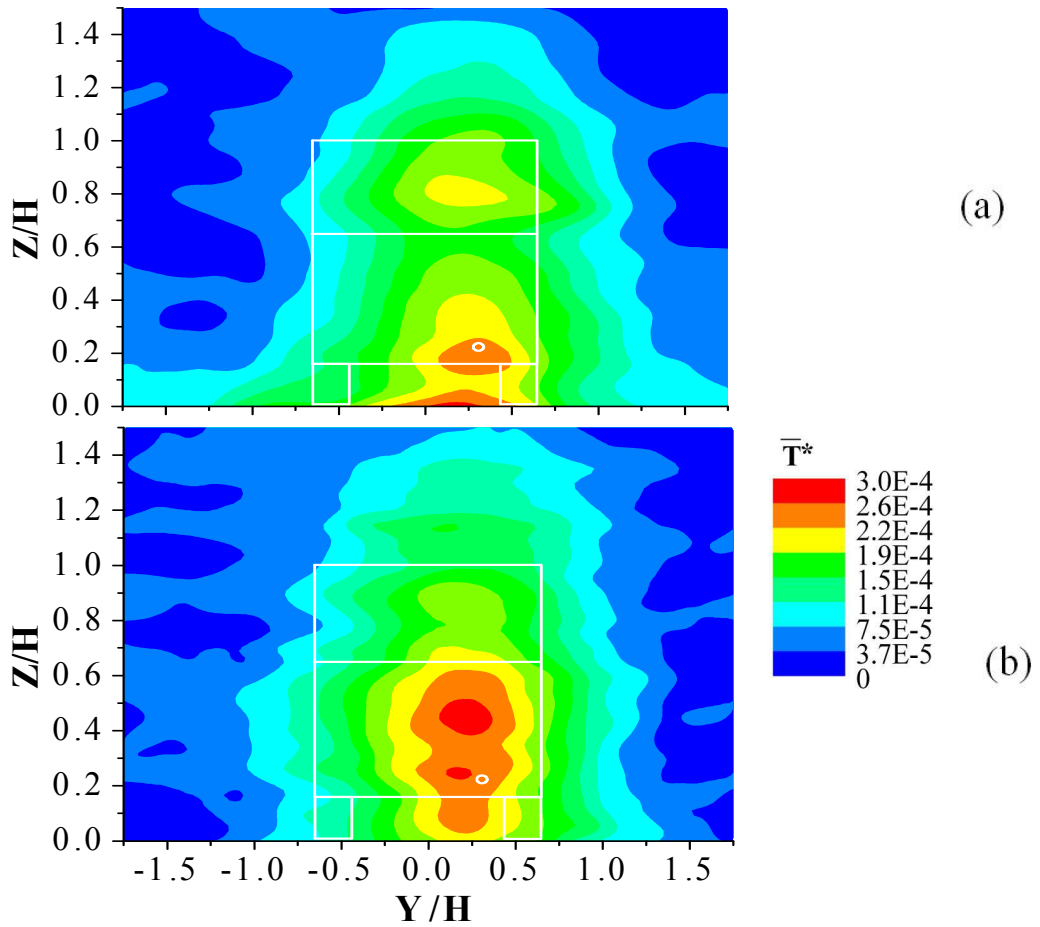


Figure 5.20 Normalized mean temperature excess, \bar{T}^* in $Y-Z$ plane at $X/H = 8$ behind the vehicle(s) ($\alpha = 60^\circ$) at 30 km/h for (a) one-vehicle and (b) two-vehicle cases (Huang et al. 2009b).

The peak scalar values of \bar{T}_{\max}^* along the downstream distance, X/H behind the vehicle(s) ($\alpha = 60^\circ$) are shown in Figure 5.21. It clearly shows that the peak scalar dispersion regions are sensitive to the decreasing number of the preceding vehicles at the studied vehicle speeds. The scalar dispersion value decreases with increasing the vehicle speed but it reaches steadily to $X/H = 4$ for such two-dimensional wake flow.

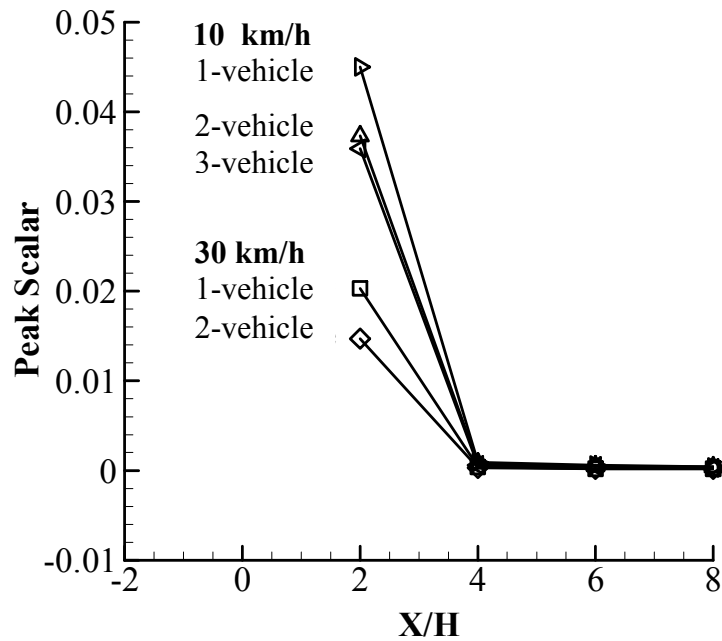


Figure 5.21 Peak scalar, \bar{T}_{\max}^* behind the studied vehicle(s) ($\alpha = 60^\circ$) along the downstream distance, X/H at 10 km/h and 30 km/h.

Because the scalar distribution contours behind the vehicles ($\alpha = 60^\circ$) follow a single peak pattern, therefore the traditional finite line source Gaussian formula in Equation (5-2) was adopted to calculate the normalized scalar, \bar{T}^* distribution.

The fitted values of variables in Equation (5-2) based on the normalized mean temperature excess distributions, \bar{T}^* obtained from the results of Figures 5.13 to 5.20 for the studied vehicle(s) ($\alpha = 60^\circ$) cases at different locations in the downwind distance are summarized in Table 5.2.

$\alpha = 60^\circ$ $X/H = 2$	$\frac{Q_0/T_j}{2\pi\sigma_y\sigma_zU}$	$\frac{y_0}{H}$	$\frac{z_0}{H}$	$\frac{\sigma_y}{H}$	$\frac{\sigma_z}{H}$
1-vehicle 10 km/h	0.04505	0.06764	0.4586	0.3484	0.3796
2-vehicle 10 km/h	0.03729	-0.00627	0.3996	0.3994	0.4901
3-vehicle 10 km/h	0.03958	0.01476	0.4006	0.3933	0.5080
1-vehicle 30 km/h	0.02028	0.1490	0.4465	0.3411	0.3812
2-vehicle 30 km/h	0.01469	0.1401	0.3322	0.3749	0.4807

$\alpha = 60^\circ$ $X/H = 4$	$\frac{Q_0/T_j}{2\pi\sigma_y\sigma_zU}$	$\frac{y_0}{H}$	$\frac{z_0}{H}$	$\frac{\sigma_y}{H}$	$\frac{\sigma_z}{H}$
1-vehicle 10 km/h	0.0009	0.1226	0.4515	0.4244	0.5544
2-vehicle 10 km/h	0.0008	0.1848	0.3722	0.4578	0.5199
3-vehicle 10 km/h	0.0006	0.2200	0.2092	0.4373	0.6596
1-vehicle 30 km/h	0.0004	0.0236	0.3863	0.3833	0.4507
2-vehicle 30 km/h	0.0003	0.0068	0.3920	0.3994	0.4768

$\alpha = 60^\circ$ $X/H = 6$	$\frac{Q_0/T_j}{2\pi\sigma_y\sigma_zU}$	$\frac{y_0}{H}$	$\frac{z_0}{H}$	$\frac{\sigma_y}{H}$	$\frac{\sigma_z}{H}$
1-vehicle 10 km/h	0.0006	0.0820	0.4562	0.4353	0.4945
2-vehicle 10 km/h	0.0005	-0.0237	0.4522	0.4519	0.5150
3-vehicle 10 km/h	0.0005	-0.0024	0.4529	0.4700	0.5637
1-vehicle 30 km/h	0.0002	0.0370	0.1140	0.5066	0.6722
2-vehicle 30 km/h	0.0002	-0.0103	0.4273	0.5248	0.5328

$\alpha = 60^\circ$ $X/H = 8$	$\frac{Q_0/T_j}{2\pi\sigma_y\sigma_zU}$	$\frac{y_0}{H}$	$\frac{z_0}{H}$	$\frac{\sigma_y}{H}$	$\frac{\sigma_z}{H}$
1-vehicle 10 km/h	0.0004	0.0228	0.1848	0.5145	0.6703
2-vehicle 10 km/h	0.0004	-0.0685	0.0899	0.5399	0.7329
3-vehicle 10 km/h	0.0003	-0.0311	0.3053	0.5873	0.6777
1-vehicle 30 km/h	0.0002	0.2252	0.0287	0.5660	0.8542
2-vehicle 30 km/h	0.0002	0.1829	0.3409	0.5237	0.6085

Table 5.2 Fitted values of variables in the single finite line source Gaussian equation (5-2) for the studied vehicles ($\alpha = 60^\circ$).

From Table 5.2 for the studied queue vehicles ($\alpha = 60^\circ$) of different vehicle speeds, it can be seen that the preceding vehicle(s) make the scalar (i.e. pollutant) distribution region larger in size, lower in height and weaker in strength. The most rapid decay in source strength takes place within range $X/H < 4$ and this decay is unchanged by the presence of preceding vehicle(s). Comparing the parameters in

Table 5.1 with Table 5.2, it can be noted that though the initial overall line source strength is similar for the two vehicle rear types, the decay rate along the downstream distance for vehicle rear type ($\alpha = 25^\circ$) is more sensitive to the vehicle speed than the other vehicle category ($\alpha = 60^\circ$). Hence, more different vehicle speeds need to be studied for vehicle category ($\alpha = 25^\circ$) than for vehicle category ($\alpha = 60^\circ$). The efficient distributions of measurement grids behind vehicles should be different for the two vehicle rear categories (i.e., $\alpha < 30^\circ$ or $\alpha > 30^\circ$). They imply that a lower and wider grid profile for vehicle ($\alpha < 30^\circ$) and a higher and slimmer profile for vehicle ($\alpha > 30^\circ$) should be used.

5.4 Summary of Chapter

Experimental investigations for the queue effect of the studied vehicle(s) on flow structures, and scalar (i.e., \bar{T}^*) dispersion and distribution fields from the heated air exhaust jet in the vehicle wake for typical urban driving conditions (i.e., 10 and 30 km/h) were performed in a closed-circuit wind tunnel using the combined X hot-wire and cold-wire technique.

The wake structure behind a queue of vehicle(s) is mainly dominated by the last vehicle, V1. The preceding vehicle(s) has/have more prominent effect on the flow characteristics (e.g., velocities, turbulence etc.) than the wake structure region.

The preceding vehicle(s) will lead to a stronger downwash flow in the wake region of vehicle queue for the rear slant angles ($\alpha = 60^\circ$ and 25°) at different vehicle speeds. The stronger downwash flow will push the top of the scalar distribution regions lower, in particular for the vehicle ($\alpha = 60^\circ$), its highest scalar distribution regions are pushed from half of the vehicle height to near ground. It will also push the top edge of scalar dispersion regions closer to the ground for the vehicles having a rear slant angle smaller than the critical angle (i.e., $\alpha < 30^\circ$) or raise the top edge of scalar distribution regions for the vehicle(s) having a rear slant angle (i.e., $\alpha > 30^\circ$).

For the vehicle(s) ($\alpha > 30^\circ$), the offset positioned tailpipe exit will slightly shift the full scalar dispersion and distribution region to its right-hand side. For the vehicle(s) ($\alpha < 30^\circ$), the offset positioned tailpipe exit will lead to the unbalance of scalar dispersion and distribution region in the wake flow. The wake flow on the same side of tailpipe exit will share a larger portion of scalar dispersion and distribution region than the left-hand side, and the unbalanced scalar sharing can be enhanced by the addition of preceding vehicle(s).

Vehicle exhaust scalar (i.e. pollutant) distribution field undergoes relatively fast changes within the downstream distance, $X/H \leq 6$ for both vehicle rear shapes (i.e., $\alpha > 30^\circ$ or $\alpha < 30^\circ$) and this characteristic shows no dependence on the category of vehicle wake flow (i.e. two-dimensional or three-dimensional wake flow). After $X/H=6$, the exhaust jet scalar dispersion pattern will become relatively stable and gradually expand in size and decay in its scalar. The scalar dispersion

rate of the exhaust jet is more sensitive to the downstream distance than to the vehicle speed.

Preceding vehicle(s) enhances the overall scalar (i.e., pollutant) dispersion and distribution field while reduces the peak scalar (i.e., pollutant) level. A preceding vehicle does not noticeably enhance the pollutant dispersion and distribution region behind the last vehicle ($\alpha < 30^\circ$), but does so for the last vehicle ($\alpha > 30^\circ$).

For the vehicle(s) ($\alpha < 30^\circ$) which has/have a pair of trailing vortices in wake flow, the exhaust jet scalar will be mainly trapped inside these two trailing vortices and fills in an “m-shaped” region behind the vehicle. Additional preceding vehicle(s) will not change the flow structure but enhance the scalar of one side of the “m-shape” which is located on the same side of the tailpipe exit while diminishing the scalar of the other side. For the vehicle(s) ($\alpha > 30^\circ$), its wake flow is simple, going from four sides of the vehicle rear end toward the perpendicular bisector of the vehicle end. Exhaust jet scalar will be carried by such a wake flow to form an “n-shaped” region standing behind the vehicle. The high scalar concentration region is located at the center of an “n-shape” and is slightly inclined to the ground. Additional preceding vehicle(s) will increase the inclination angle of high scalar concentration region toward the ground and push the high scalar region to touch the ground much earlier than without the preceding vehicle.

In the near-wake region of a three-dimensional flow generated by the vehicle(s) ($\alpha < 30^\circ$), the vehicular exhaust jet forms a dual peak scalar dispersion

and distribution region where the first and second peak scalar dispersion and distribution regions lie just outside the two footprints of vehicle tires. Additional preceding vehicle(s) will also make the scalar dispersion and distribution region slightly wider. The assumption that vehicular exhaust jet flow can be considered as a line source is acceptable for the vehicle(s) ($\alpha > 30^\circ$). However for the vehicle(s) ($\alpha < 30^\circ$), there is significant unbalance in jet scalar dispersion and distribution field between the left- and right-hand sides of the vehicle. Therefore, it may cause some errors which can be worse in the vehicle queue cases and needs a better description for two possible line sources (e.g., the heavy scalar weights from a line source on the side of tailpipe exit and the other low scalar weights from a line source on the side without tailpipe exit).

Chapter 6 **Conclusions and Recommendations for Future Work**

6.1 **Conclusions for the Vehicle Queue Effect on the Characteristics of Air Flow in the Vehicle Wake**

In the present study, the characteristics of air flow in the near-wake region of a scaled-down vehicle which was placed alone or behind the preceding vehicle(s) in a wind tunnel facility were experimentally investigated with the particle image velocimetry (PIV) for the selected urban vehicle speeds at 10, 30 and 50 km/h (i.e., Reynolds numbers $Re_H = 1.48 \times 10^4$, 4.44×10^4 and 7.40×10^4 , respectively).

It was found that the wake flow structures behind the vehicle are only determined by the rear profile of the vehicle (i.e., rear slant angle). The shape of vehicle front and body does not have any noticeable impact on the wake flow structures behind the vehicle. In the present study, the front and body of all studied vehicles are of the same shape except for different rear slant angles ($\alpha = 25^\circ$ or 60°) in order to generate the three-dimensional or a quasi two-dimensional wake flow behind the vehicle, respectively.

6.1.1 **Conclusions for the characteristics of air flow around a single vehicle ($\alpha > 30^\circ$)**

The main structure of wake flow behind the studied vehicle ($\alpha > 30^\circ$) contains two kinds of vortices, namely a recirculation vortex and a pair of counter rotating trailing vortices stretching backward. On the vertical streamwise central plane behind the vehicle, the cross-section of the recirculation vortex shape looks

like a horizontal but slightly tilted vertical ellipse and it starts immediately behind the vehicle rear in the downstream distance till $X/H = 1.2\sim 1.3$ and $0.6H$ above the ground surface. Within the present studied range from 10 to 50 km/h, the vehicle speed cannot change the length of recirculation bubble or its normalized vorticity (i.e., its absolute vorticity is proportional to the vehicle speed) behind the vehicle.

A pair of trailing vortices at the cross-sectional planes along the downstream distance, X/H which is parallel to the end plane of the vehicle look like two vertical ellipses with the left one rotating clockwise and the right one rotating counter clockwise. The two vortices each occupies almost symmetrically half of the projection region of the vehicle rear. Though weak in vorticity, the trailing vortices can maintain their flow structures almost unchanged for certain distance, suggesting their weak interaction with the surrounding air. The trajectory of trailing vortices can be imagined as two parallel straight tubes horizontally stretching backward at one third of the vehicle height over ground.

The normalized vorticity of the trailing vortices decays along the downstream distance. There is a turning point for the relationship between the decay rate of vorticity and the vehicle speed. When the trailing vortices move from $X/H = 1$ to 2, the decay rate of vorticity is around 20%, 36% and 38%, respectively for 10, 30 and 50 km/h cases with a turning point at around 30 km/h. When the vortices move from $X/H = 2$ to 3, the decay rate of vorticity for different vehicle speeds do not show much prominent effect. This phenomenon suggests that the decay rate of trailing vortices is sensitive to both vehicle speed (with a turning

point at 30 km/h) and the downstream location (with a turning point at $X/H = 2$) in an initial flow development.

6.1.2 Conclusions for the characteristics of air flow around a queue of vehicles ($\alpha > 30^\circ$)

If there is a preceding vehicle ($\alpha > 30^\circ$) in the upstream, the incoming flow toward a following vehicle will be altered, especially for a short vehicle spacing (i.e., 3 times of its vehicle height) with a 86% reduction of its incoming mean flow velocity. The blockage effect slowly decreases for a longer vehicle spacing (i.e., 9 times of vehicle height) with a 30% reduction of incoming mean flow velocity or a 20% reduction of incoming mean flow velocity for an even longer vehicle spacing (i.e., 15 times of vehicle height). The second or more preceding vehicles almost cannot induce further reduction to its mean velocity of incoming flow, e.g. one preceding vehicle induced 86% reduction while two preceding vehicles induced 87% reduction for a short vehicle spacing (i.e., 3 times of its vehicle height). Therefore, if the studies are mainly related to the mean flow velocity, one preceding vehicle is enough for full consideration, but not for studies which have relation to the turbulence. The second preceding vehicle can still enhance an additional 20% turbulence which cannot be considered to be a negligible value. For the flow region affected by the preceding vehicle(s), the velocity deficit is more obvious in the low region (i.e. lower than one vehicle height) while the turbulence increment is more obvious than in the high region (i.e. higher than one vehicle height). If a vehicle follows behind the type of the vehicle(s) ($\alpha > 30^\circ$), the following vehicle will benefit most from its/their obvious flow blockage effect and

save the maximal motor fuels. Therefore, the vehicle following such type of vehicle(s) on the road is strongly recommended.

For the recirculation bubble, though its extension of near-wake separation bubble length, X_{NW} has demonstrated the vehicle speed independence in the single vehicle cases. But the separation bubble length shows dependence on the spacing of vehicle queue for a short vehicle spacing (i.e., 3 times of its vehicle height) with a 50% reduction of its length and for a longer vehicle spacing (i.e., 9 times or more of its vehicle height) with about 15 to 20% reduction of its length. It has demonstrated that the uniformity of the vertical velocity profile for the incoming flow may play an important role for the sensitivity of the near-wake separation bubble length and vehicle spacing. The longer the vehicle spacing is, the more uniform the vertical velocity profile and the less difference in its separation bubble length will be. The normalized vorticity of the recirculation bubble can be reduced to about 20 to 30% by the first preceding vehicle and further 6% reduction by the second preceding vehicle. It indicates that two preceding vehicles are good enough for certain simulations of a queue of moving vehicles with a rear slant angle ($\alpha > 30^\circ$). The reduction in recirculation vorticity is independent of its vehicle speed and spacing, but is only dependent on the number of the preceding vehicles. The independence is attributed to the peak vorticity regions which always occur near the ground surface, thus becomes insensitive to the uniformity of the vertical velocity profile.

For a pair of trailing vortices, their flow structures show almost insensitivity to the arrangements of the preceding vehicle(s) and its vehicle spacing. Because the preceding vehicle(s) and its vehicle spacing do not affect the left-right balance of the horizontal velocity profile for the incoming flow. This symmetric velocity profile may favor the stability of this left-right distributed vortex structures. The normalized vorticity of trailing vortices, however shows its sensitivity to both the preceding vehicle(s) and its vehicle spacing. At the downstream location behind the vehicle, $X/H = 1$, the normalized vorticity can be reduced by 17% and further reduced 15% by one and two preceding vehicles, respectively. Surprisingly, the longer vehicle spacing can induce a large reduction of vorticity (i.e., 14%, 17% and 20% reduction of vorticity for the vehicle spacing equals to 3 times, 9 times and 15 times of the vehicle height, respectively.) In common sense, the longer vehicle spacing between two consecutive vehicles is similar to a single vehicle case, thus it should induce a smaller decrement. The physical explanation is that the trailing vortices are still developing and the factor of vehicle spacing has not been fully shown at such close location yet. The reduction of vorticity induced by the preceding vehicle(s) is also sensitive to the downstream distance, X/H . The highest vorticity reduction occurs at $X/H = 2$ where a 33% vorticity reduction is induced by a preceding vehicle. In addition, almost 17% vorticity reduction is induced by a preceding vehicle at either $X/H = 1$ or $X/H = 3$. The sensitivity of the vorticity to the downstream distance suggests that the trailing vortices undergo fast developing at $X/H = 2$.

6.1.3 Conclusions for the characteristics of air flow around a single vehicle ($\alpha < 30^\circ$)

The main structure of wake flow behind the studied vehicle ($\alpha < 30^\circ$) also contains two kinds of vortices, namely a recirculation vortex and a pair of counter rotating trailing vortices stretching backward. Its normalized vorticity is 2 times and 3 times stronger than the counterparts of the vehicle ($\alpha > 30^\circ$) for a recirculation vortex and a pair of trailing vortices, respectively, suggesting a much stronger three-dimensional flow movement takes place behind the vehicle ($\alpha < 30^\circ$). On the vertical streamwise at the central plane of the vehicle, the cross-section of the recirculation vortex shape looks like a horizontal but slightly tilted vertical ellipse, but is much smaller than that of the vehicle ($\alpha > 30^\circ$) which is almost half of both its length and height. The near-wake separation bubble length of the recirculation vortex starts immediately behind the vehicle rear and lasts to the downstream distance at $X/H = 0.64$, floating between one third of the vehicle height and the ground surface. Within the present studied range from 10 to 50 km/h, the separation bubble length of the recirculation vortex does not vary with the vehicle speeds.

A pair of trailing vortices at the cross-sectional planes along the downstream distance, X/H which is parallel to the end plane of the vehicle ($\alpha < 30^\circ$) looks like two vertical ellipses where the left one rotates clockwise and the right one rotates counter clockwise, which are contrary to their rotating directions for the vehicle ($\alpha > 30^\circ$). The two vortices each occupies almost symmetrically half of the projection region of the vehicle back. Unlike the trailing vortices of a vehicle ($\alpha > 30^\circ$), the trailing vortices of the vehicle ($\alpha < 30^\circ$) change

their flow structures quickly along the downstream distance because the downwash flow in wake region is stronger for this type of vehicle. The trajectory of trailing vortices can be imagined as two straight tubes horizontally stretching backward and being pushed by the downwash flow against the ground surface to an increasingly flat pattern in the downstream direction. Under such flow resistance from each other, the extension of these two trailing vortices is mainly outward.

The normalized vorticity of trailing vortices decays with the downstream distance. There is a turning point for the relationship between the decay rate of vorticity and the vehicle speed. When the trailing vortices move from $X/H = 1$ to 2, the decay rate of vorticity is around 25, 30 and 29%, respectively for 10, 30 and 50km/h cases. However, when the trailing vortices move from $X/H = 2$ to 3, the decay rate of vorticity is around 34%, 13% and 16%, respectively for 10, 30 and 50km/h cases. It can be seen that the vehicle speed at 10 km/h following a decay trend is different from that of 30 and 50 km/h cases. This phenomenon suggests that the decay rate of trailing vortices in normalized vorticity is sensitive to the vehicle speed (with a turning point at 30 km/h). Within the present studied range, the turning point in the downstream distance is not observed.

6.1.4 Conclusions for the characteristics of air flow around a queue of vehicles ($\alpha < 30^\circ$)

If there is a preceding vehicle ($\alpha < 30^\circ$) in the upstream, the incoming flow toward a following vehicle will be altered, especially for a short vehicle spacing (i.e., 3 times of the vehicle height) with a 34% reduction of incoming mean flow velocity. The blockage effect slowly decreases for a longer vehicle spacing (i.e.,

9 times of vehicle height) with a 29% reduction of the incoming mean flow velocity or 23% reduction of the incoming mean flow velocity for an even longer vehicle spacing (i.e., 15 times of its vehicle height). More preceding vehicles almost will not induce further reduction to the mean velocity of incoming flow, e.g. one preceding vehicle induced 34% reduction while two preceding vehicles induced 36% reduction for a short vehicle spacing (i.e., 3 times of the vehicle height). Therefore for studies mainly related to the mean flow velocity, one preceding vehicle is enough for full consideration, but not for studies which have relation to the turbulence. The second preceding vehicle can still enhance an additional 22% turbulence which cannot be considered to be a negligible value. For the flow region affected by the preceding vehicle(s), the velocity deficit and turbulence increment are more obvious in the low region (i.e. lower than one vehicle height). If a vehicle follows behind the type of vehicle(s) with a rear slant angle ($\alpha < 30^\circ$), the following vehicle will benefit from its/their less obvious flow blockage effect and save some motor fuels. Therefore, the vehicle following such type of vehicle(s) on the road is also highly recommended.

For the recirculation bubble, though its extension of near-wake separation bubble length, X_{NW} has demonstrated the vehicle speed independence in the single vehicle cases. However, the separation bubble length shows dependence on the spacing of vehicle queue for a shorter vehicle spacing (i.e., 3 times of its vehicle height) with about 16% reduction of its length and a longer vehicle spacing (i.e., 9 times or more of its vehicle height) with about 5% reduction of its length while they are much less than their counterparts for about 50% and 20% reduction of their lengths, respectively for the vehicles ($\alpha > 30^\circ$). It has also demonstrated

that the uniformity of the vertical velocity profile for the incoming flow plays an important role in the sensitivity of the near-wake separation bubble length and vehicle spacing. The normalized vorticity of the recirculation bubble can be reduced to 7% at 10 km/h, 13% at 30 km/h or 30% at 50 km/h by the one preceding vehicle, and further reduced another 4% at 10 km/h by the two preceding vehicles, respectively. The decreasing trend in normalized vorticity violates the common sense that the longer vehicle spacing between two consecutive vehicles is more close to a single vehicle case and less interference between the consecutive vehicles is expected, suggesting that a three-dimensional flow is more complex than it may be thought. For such closer vehicle spacing, the one preceding vehicle can cause 7% reduction difference in the normalized vorticity and the two preceding vehicles can cause 11% reduction which is still considered a prominent effect when compared with one preceding vehicle case, suggesting more preceding vehicles are necessary to achieve good simulation accuracy for a queue of vehicles ($\alpha < 30^\circ$).

For a pair of trailing vortices, their structures show almost insensitivity to the arrangements of the preceding vehicle(s) and its vehicle spacing. The reason may be the same to the above-mentioned for the vehicles ($\alpha > 30^\circ$) where the symmetric horizontal velocity profile of the incoming flow may favor the stability of this left-right distributed vortex structures. The normalized vorticity of trailing vortices shows its insensitivity to both the number of the preceding vehicle and its vehicle spacing. At the downstream location behind the vehicle, $X/H = 1$, the normalized vorticity can be reduced by 20% and further reduced another 3% by one preceding vehicle and two preceding vehicles, respectively. For the present

studied vehicle spacings (i.e., 3 times, 9 times and 15 times of the vehicle height), they all induce about 20% reduction in the normalized vorticity of trailing vortices indicating the independence of vehicle spacing. Like the vehicles ($\alpha > 30^\circ$), the vorticity reduction induced by the preceding vehicle(s) ($\alpha < 30^\circ$) is also sensitive to the downstream distance. The highest sensitivity also occurs at the downstream location, $X/H = 2$ where a 30% reduction in vorticity is induced by a preceding vehicle regardless of the vehicle spacing. At $X/H = 3$, a preceding vehicle can induce a large reduction of vorticity (i.e., 17%, 10% and 5% reduction of vorticity for the vehicle spacing equals to 3 times, 9 times and 15 times of the vehicle height, respectively). This trend is back to the common sense that the longer vehicle spacing of two consecutive vehicles is similar to a single vehicle case and should induce smaller changes. The trailing vortices for the vehicles ($\alpha < 30^\circ$) seem to be not fully developed until $X/H = 3$. Before that they are still under development and cannot exactly show their potentials.

6.2 Conclusions for the Vehicle Queue Effect on the Characteristics of Exhaust Scalar Dispersion and Distribution Fields in the Vehicle Wake

After the study of the vehicle queue effect on the characteristics of air flow in vehicle wake mentioned in Section 6.1, the characteristics of vehicular exhaust scalar (i.e., pollutant) dispersion and distribution fields in the near-wake region of a scaled-down vehicle which was placed alone or behind the preceding vehicle(s) in a wind tunnel facility were experimentally investigated with the cold- and hot-wires anemometers for the selected urban vehicle speeds at 10 and 30 km/h (i.e., Reynolds numbers $Re_H = 1.48 \times 10^4$ and 4.44×10^4 , respectively).

6.2.1 Conclusions for the characteristics of exhaust scalar dispersion and distribution fields behind a single vehicle ($\alpha > 30^\circ$)

As discussed in Section 6.1.1, a quasi two-dimensional wake flow containing a pair of weak trailing vortices will be generated behind the studied vehicle ($\alpha > 30^\circ$). The trailing vortices are so weak that their flow effect on the vehicular exhaust jet dispersion pattern from the vehicle cannot be observed. Driven by such a quasi two-dimensional wake flow, this kind of vehicular exhaust jet scalar dispersion is relatively simple, filling in a turbulent air cavity left by the vehicle penetrating in still air. At the beginning of the studied downstream distance (i.e. $X/H = 2$), the cross-section of the filled turbulent air cavity is almost identical to that of the vehicle. As downstream distance increases, the cross-section of the hole will grow larger and rotate in upward direction forming an “n-shaped” region which will grow to about 1.5 times of the vehicle height where the highest scalar contour region stays at about half of the vehicle height (i.e., close to the height level of human inhalation zone) and 2 times of the vehicle width near the end of the near-wake region. It should be noted that when the n-shape of scalar dispersion and distribution field grows larger with increasing downstream distance, the highest scalar contour region still remains at the center of the vehicle rear projection, indicating that the high scalar contour region does not overlap the geometric center of scalar dispersion region though it seems so in the early half of near wake.

6.2.2 Conclusions for the characteristics of exhaust scalar dispersion and distribution fields behind a queue of vehicles ($\alpha > 30^\circ$)

As discussed in Section 6.1.2, the wake structures are insensitive to the studied preceding vehicle(s) ($\alpha > 30^\circ$). With the presence of the preceding vehicle(s), the size and shape of the “scalar profile” would not be changed too much, but the highest scalar contour region will be lowered from half of the vehicle height toward the ground surface (i.e., stay away from the height level of human inhalation zone). Therefore, such type of vehicle queue on the road is strongly recommended.

6.2.3 Conclusions for the characteristics of exhaust scalar dispersion and distribution fields behind a single vehicle ($\alpha < 30^\circ$)

As discussed in Section 6.1.3, a three-dimensional wake flow containing a pair of counter rotating trailing vortices will be generated behind the studied vehicle ($\alpha < 30^\circ$). The trailing vortices are the main driven force for the lateral jet scalar dispersion. The amount of scalars (i.e. pollutants) are mainly trapped inside these two trailing vortices and formed the cross-section of exhaust scalar distribution region behind the vehicle which looks like an “m-shape” region standing on the ground. This “m-shape” is initially about 0.5 times of the vehicle height and 1.5 times of the vehicle width, and will grow to about 0.8 times of the vehicle height and 3 times of the vehicle width near the end of the near-wake region in a horizontal expansion primarily.

At the beginning of the studied downstream distance, the m-shaped region is about 0.5 times of the vehicle height and 1.5 times of the vehicle width. At the

end of the near-wake region (i.e., $X/H \geq 8$), the “m-shape” will grow to about 0.8 times of the vehicle height and 3 times of the vehicle width in a horizontal expansion primarily. The vehicular exhaust jet is not uniformly distributed in the m-shaped scalar dispersion region where these two high scalar distribution regions are located at the two sides of the “m-shape” and stay near the ground which is not higher than the adult knees (i.e., away from the height level of human inhalation zone). The side of the “m-shape” which is behind the vehicle tailpipe will share the main portion of exhaust jet scalar, thus this side of the vehicle rear has a much higher scalar distribution region and is 50% taller but not obviously wider than the other side. Each side of the “m-shape” has a high scalar distribution region for itself which is located on the ground surface between the feet of the “m-shape”. As the downstream distance increases, the two high scalar distribution regions will gradually move outwards along with the expansion of the “m-shaped” region.

6.2.4 Conclusions for the characteristics of exhaust scalar dispersion and distribution fields behind a queue of vehicles ($\alpha < 30^\circ$)

For the studied vehicles ($\alpha < 30^\circ$), the wake flow structures are also almost unchanged by the presence of the preceding vehicle(s). The size of the “m-shaped” scalar distribution regions for the vehicle queue cases does not change much from those for a single vehicle cases. But as a stronger downwash flow in wake region is induced by the preceding vehicle(s), the downwash flow acts as a cutting force and induces the difficulties for the vehicular exhaust jet scalar to transport to the other side of the wake region. Therefore, the unbalanced scalar distribution field between the two sides of the “m-shaped” region will be enhanced for vehicle queue cases. As the side closer to tailpipe exit will have a much higher jet scalar dispersion than

the other side of the vehicle, therefore the driver in the following vehicle should avoid opening the window on the preceding vehicle tailpipe side or keep away from this side if possible (i.e. high scalar region). The air intake for the vehicle ventilation system is also suggested to be located at the front corner on the other side of the tailpipe exit in order to stay away from the high scalar distribution regions either in the vehicle center (for the vehicles with $\alpha > 30^\circ$) or shifted to the vehicle side of tailpipe exit (for the vehicles with $\alpha < 30^\circ$).

6.3 Recommendation for Future Work

Having performed the experimental investigation of the vehicle queue effect on the characteristics of air flow and exhaust scalar dispersion and distribution fields in the vehicle wake, some of the future research work are recommended as follows:

1. to have a better understanding of the physics of a tailpipe exit immediately behind the vehicle, the initial interaction between the exhaust jet scalar and wake flows, and how this exhaust jet scalar disperses into this very near-wake region.
2. in addition to the traditional experimental approach, the computational fluid dynamics (CFD) approach has become an increasingly popular research tool in recent years due its effectiveness and efficiency. It can provide answers and insights for many air flow characteristics in a full commercial CFD package, unlike experimental tests which need to be repeated with

different dedicated measurement instruments for investigating different air flow characteristics. CFD can provide the researchers with a reasonable idea of the objective(s) which they are going to study beforehand, therefore they can better plan their experiments to focus mainly on their research interests and aspects. According to the literature reviews and findings obtained from my Chief Supervisor's research group, the air flow characteristics behind the vehicle with a rear-slant angle ($\alpha > 30^\circ$) is easier to be simulated by CFD with a good accuracy because it has a relatively simple and quasi two-dimensional wake flow. However, the air flow characteristics behind a queue of vehicles ($\alpha < 30^\circ$) are still a challenging research work because it has a complex three-dimensional wake flow. The present experimental findings could serve as a good dataset for the numerical model validation. For CFD approaches, more attention should be paid to the region from the beginning of vehicle rear to the downstream distance of two vehicle heights. This is not only because the air flow undergoes the most rapid changes in such closer region for the whole test section, but also because the evolution of air flow in this region governs the main structure of wake flow and the vehicle exhaust dispersion pattern.

Appendix Equipment Specifications

I-1 Closed-loop Wind Tunnel Facility (Model No.: LW-8565H)

Manufacturer:	Long Win Science & Technology Co. Ltd., Taiwan
Wind speed range:	1 to 40 m/s
Overall dimension:	Length × width × height = 10.1 × 2.4 × 5.1 m
Dimension of test section:	L × W × H = 2400 × 600 × 600 mm
Contraction ratio:	9:1
Power :	AC380V, 60Hz, 60Hp
Driven type:	Step-motor and axial fan
Speed control:	Step-motor inverter model : Dynagen S36-4060-686-90 Control resolution: 0.01Hz/0.3rpm/0.00085m/s
Control correlation:	Wind speed (m/s) = control frequency (Hz) × 0.845 + 0.12 m/s

I-2 Flowmap PIV System Hub (Model No.: 9080N0601)

Manufacturer:	Dantec Dynamics A/S, Denmark
Dimension:	Length × Width × Height = 466 × 486 × 185 mm
Weight:	14 kg
Operating environment:	+5 to +40 °C, humidity < 85%
Power :	AC 100-240 V, 47-63 Hz, 150-300 W
Network:	100Mbit/s Ethernet
TCP/IP address:	10.10.100.200 Subnet mask 255.0.0.0

Data buffer size:	1.0 gigabyte
Camera signal input:	Up to 4 channels of P-n-P camera kits
Analogue signal input:	4 channels, BNC connector, $\pm 10\text{V}$, 12 bits
TTL signal output:	4 channels, 25-pin D-sub connector, $\pm 5\text{V}$, programmable delay and duration per channel

I-3 Hisense 4M PIV Camera (Model: 80C79)

Manufacturer:	Dantec Dynamics A/S, Denmark
Dimension:	Length \times Width \times Height = 160 \times 90 \times 75 mm
Weight:	1.3 kg
Operating environment:	0 \sim +40 $^{\circ}\text{C}$, humidity $<$ 85%
Power :	AC 100-240 V, 47-63 Hz, 70 W
CCD sensor :	Type : progressive scan interline Active area: 8.6 \times 6.9 mm Number of pixels : 2048 \times 2048 Pixel pitch 6.7 \times 6.7 μm Dynamic range : >60 dB Maximum frame rate : 9 Hz Frame interval rage: 0.0002 \sim 110 ms

I-4 Gemini PIV Laser

Manufacturer:	New Wave Research Inc., USA
Laser head dimension:	Length \times width \times height = 560 \times 360 \times 220 mm
Laser type:	Nd: YAG, Q-switch
Cooling:	Deionized water, 5 L/min, built-in circulation pump
Weight:	15 kg
Power supply dimension:	Length \times width \times height = 400 \times 320 \times 480 mm

Appendix

Cooling:	Air
Weight:	25 kg
Operating environment:	+5 ~ +40 °C, humidity < 85%
Power :	AC 200-250 V, 47-63 Hz, 6.5 A
Laser beam :	Diameter 5 mm, beam divergence < 1 mrad Wavelength 532 nm Maximum energy output 200 mJ @ 532 nm Energy stability \pm 3.5%

I-5 Three Dimensional Mechanical Traverse (Model No.: 5751-1)

Manufacturer:	Dantec Dynamics A/S, Denmark
Movement range:	$X \times Y \times Z = 1520 \times 620 \times 720$ mm
Movement speed:	Maximum 15mm/s
Calibration factor:	160 pluses/mm
Weight:	85 kg
Operating environment:	0 ~ +40 °C, humidity < 85%
Loading capacity :	Maximum 60 kg
Motor controller :	three motor amplifiers, RS232 control
Power :	AC 200-240 V, 50/60 Hz, 700 W

I-6 SPT Smoke Generator for PIV Seeding

Manufacturer: Dantec Dynamics A/S, Denmark.

Dimension:	Length \times width \times height = 440 \times 230 \times 210 mm
Air supply:	Maximum 1.5 m ³ /s
Weight:	8 kg
Compressor:	Built in

Appendix

Power :	AC 200-240 V, 50/60 Hz, 6.3 A
Smoke oil:	Paraffin oil, type Ondina 15 from Shell Oil Company
Smoke droplets:	Diameter: mean 1.56 μm , rms 0.68 μm
Smoke concentration:	$> 10^7 /\text{cm}^3$

I-7 StreamLine Hot-wire Anemometer

Manufacturer:	Dantec Dynamics A/S, Denmark
Dimension:	Length \times Width \times Height = 354 \times 386 \times 215 mm
Weight:	12 kg
Operating environment:	+5 to +40 $^{\circ}\text{C}$, humidity $<$ 85%
Power :	AC 100-240 V, 47-63 Hz, 150-300 W
Network:	100Mbit/s Ethernet
TCP/IP address:	10.10.100.100 Subnet mask 255.0.0.0
Data buffer size:	1.0 megabyte
Hot-wire signal output:	Up to 2 channels
Analogue signal output:	2 channels, BNC connector, ± 10 V
Control signal output:	15-pin RS-232 connector, ± 5 V

I-8 Cold-wire Anemometer

Manufacturer:	Department of Mechanical Engineering, University of Newcastle, N.S.W, 2308, Australia
Dimension:	Length \times width \times height = 500 \times 350 \times 200 mm
Weight:	5 kg
Operating environment:	+5 to +40 $^{\circ}\text{C}$, humidity $<$ 85%.
Power :	AC 100-240 V, 47-63 Hz, 150-300 W.

Appendix

Cold-wire signal output:	4 channels
Analogue signal Amplifier:	4 channels, BNC connector, ± 10 V

I-9 Micro-manometer, model: FCO510

Manufacturer:	Furness Controls Ltd., England, UK
Dimension:	Length \times Width \times Height = 95 \times 44 \times 37 mm
Weight:	1.6 kg
Operating environment:	-10 \sim +50 $^{\circ}$ C, humidity < 95%
Power :	AC 90-240 V, 50/60 Hz, 9 W; or DC 12 V, 0.5 A
Differential pressure range :	< 2000 Pa
Velocity range:	0 \sim 20 m/s
Signal output:	5-digit LCD display; RS232 to printer or computer

I-10 Data acquisition board, model NI PCI-6070E

Manufacturer:	National Instruments, USA.
Dimension:	Length \times Width \times Height = 175 \times 107 \times 23 mm
Computer bus:	PCI
Operation System:	Windows 9X, XP, NT
Number of channels:	16 channels
Sample rate:	1.25 MHz
Resolution	12 bit
Voltage range:	± 10 V
Range accuracy:	14.4 mV
I/O connector:	68-pin male D-type

References

- Al-Garni A.M., 2004. Experimental investigation of the flow around a generic SUV. *Society of Automotive Engineers (SAE) Technical Paper*, 2004-01-0228.
- Al-Garni A.M., Bernal L.P., 2010. Experimental study of a pickup truck near wake. *Journal of Wind Engineering and Industrial Aerodynamics*, Vol. 98, pp. 100-112.
- Ahmed S. R., 1981. Wake structure of typical automobile shapes. *Journal of Fluids Engineering*, Vol. 103, pp. 162-169.
- Ahmed S.R., Ramm G., Faltin G., 1984. Some salient features of the time-averaged ground vehicle wake. *Society of Automotive Engineers (SAE) Technical Paper*, 840300.
- Alam M.M., Zhou Y., Wang X.W., 2011. The wake of two side-by-side square cylinders. *Journal of Fluid Mechanics*, Vol. 669, pp. 432–471.
- Alexander L.B., Walter F.D., 2003. Modeling Ventilation and Dispersion For Covered Roadways, *Journal of Wind Engineering and Industrial Aerodynamics*, Vol. 95, pp. 593-608.
- Alonso-Estebanez A., Pascual-Munoz P., Yague C., Laina R., Castro-Fresno D., 2012. Field experimental study of traffic-induced turbulence on highways. *Atmospheric Environment*, Vol. 61, pp. 189-196.
- Amato F., Pandolfi M., Moreno M., Furger M., Pey J., Alastuey A., Bukowiecki N., Prevot A.S.H., Baltensperger U., Querol X., 2011. Sources and variability of inhalable road dust particles in three European cities. *Atmospheric Environment*, Vol. 45, pp. 6777-6787.
- Amatya D.M., Longmire E.K., 2010. Simultaneous measurements of velocity and deformation in flows through compliant diaphragms. *Journal of Fluids and Structures*, Vol. 26, pp. 218-235.
- Ashok K.L., Patil R.S. 1989. A general finite line source model for vehicular pollution dispersion. *Atmospheric Environment*, Vol. 23, pp. 555–562.
- Baker C.J., 1996. Outline of a novel method for the prediction of atmospheric pollution dispersal from road vehicles. *Journal of Wind Engineering and Industrial Aerodynamics*, Vol.65, pp. 395-404.
- Baker C.J., 2001. Flow and dispersion in ground vehicle wakes. *Journal of Fluids and Structures*, Vol. 15, pp. 1031-1060.
- Baker C.J., Hargreaves D.M., 2001. Wind tunnel evaluation of a vehicle pollution dispersion model. *Journal of Wind Engineering and Industrial Aerodynamics*, Vol. 89, pp. 187-200.

References

- Ball S.J., Ashforth-Frost S., Jambunathan K., Whitney C.F., 1999. Appraisal of a hot-wire temperature compensation technique for velocity measurements in non-isothermal flows. *International Journal of Heat and Mass Transfer*, Vol. 42, pp. 3097-3102.
- Baroud C.N., Brendan B.P., Harry L. Swinney, Zhen S.S., 2003. Scaling in three-dimensional and quasi-two-dimensional rotating turbulent flows. *Physics of Fluids* Vol. 15, pp. 2091-2014.
- Baumer D., Vogel B., Fiedler F., 2005. A new parameterization of motorway-induced turbulence and its application in a numerical model. *Atmospheric Environment*, Vol. 39, pp. 5750-5759.
- Bearman P.W., Beer D.D., Hamidy E., Harvey J.K., 1989. The effect of a moving floor on wind tunnel simulation of road vehicles. *Society of Automotive Engineers (SAE) Technical Paper*, 880245.
- Benedict L.H., Gould R.D., 1996. Towards better uncertainty for turbulence statistics. *Experiments in Fluids*, Vol. 22, pp. 129-136.
- Benson P.E., 1979. A versatile dispersion model for predicting air pollutant levels near highways and arterial streets. Department of Transportation, California State, USA.
- Benson, P.E., 1992. A review of the development and application of the CALINE 3 and 4 models. *Atmospheric Environment*, Vol. 26, pp. 379–390.
- Berajeklian A., Mydlarski L., 2011. Simultaneous velocity-temperature measurements in the heated wake of a cylinder with implications for the modeling of turbulent passive scalars. *Physics of Fluids*, Vol. 23, Article No. 055107.
- Bishop G.A., Stedman D.H., 1990. On-road carbon monoxide emission measurement comparisons for the 1988-1989 Colorado oxy-fuel program. *Environmental Science and Technology*, Vol. 24, pp. 843-847.
- Bishop G.A., Stedman D.H., 1996. Measuring the emissions of passing cars. *Accounts of Chemical Research*, Vol. 29, pp. 489-495.
- Boulter P.G., 1999. Remote sensing of vehicle emissions near traffic calming measures in Gloucester. Transport Research Laboratory, Crowthorne, Berkshire, Research Report No. 423.
- Brillant G., Husson S., Bataille F., 2008. Experimental study of the blowing impact on a hot turbulent boundary layer hot cold wire. *International Journal of Heat and Mass Transfer*, Vol. 51, pp. 1996-2005.
- Britt A.H., Debbie A.N, 1998. Characterizing the effects of driver variability on real-world vehicle emissions, *Transportation Research Part D.*, Vol. 3, pp. 117-128.

References

- Cadle S., Chock J., Heuss J., Monson P., 1976. Results of the general motors sulfate dispersion experiments. *General Motors Research Publication*, GMR-2107.
- CalTrans, 1989. CALINE4-A dispersion model for predicting the air pollution concentration near roadways. Department of Transportation, California State, USA.
- Camussi R. and Felice F.D., 2006. Statistical properties of vortical structures with spanwise vorticity in zero pressure gradient turbulent boundary layers. *Physics of Fluids*, Vol. 18, Article No. 035108.
- Carissimo B., Dupont E., Musson G.L., Marchand O., 1995. Note de principe du code MERCURE version 3.1. EDF-DER, HE-3395007B.
- Carpentieri M., Kumar P., 2011. Ground-fixed and on-board measurements of nanoparticles in the wake of a moving vehicle. *Atmospheric Environment*, Vol. 45, pp. 5837-5852.
- Carpentieri M., Kumar P., Robins A., 2011. An overview of experimental results and dispersion modelling of nanoparticles in the wake of moving vehicles. *Environmental Pollution*, Vol. 159, pp. 685-693.
- Carpentieri M., Kumar P., Robins A., 2012. Wind tunnel measurements for dispersion modelling of vehicle wakes. *Atmospheric Environment*, Vol. 62, pp. 9-25.
- Casarsa L., Giannattasio P., 2008. Three-dimensional features of the turbulent flow through a planar sudden expansion. *Physics of Fluids*, Vol. 20, Article No. 015103.
- Chan T.L., 2002. On-Road Remote Sensing of Automobile Emissions. Air Pollution Control in Hong Kong, Seminar Proceedings, Department of Mechanical Engineering, The Hong Kong Polytechnic University, May 28, 2002.
- Chan T.L., Dong G., Leung C.W., Cheung C.S., Hung W.T., 2002a. Validation of a two-dimensional pollutant dispersion model in an isolated street canyon. *Atmospheric Environment*, Vol. 36, pp. 861-872.
- Chan T.L., Leung C.W., Jambunathan K., Ashforth-Frost S., Zhou Y., Liu M.H., 2002b. Heat transfer characteristics of a slot jet. *International Journal of Heat and Mass Transfer*, Vol. 45, pp. 993-1006.
- Chan T.L. and Dong G., 2005. Large eddy simulation of flow structures and pollutant dispersion in the near-wake region of light-duty diesel vehicle, *Atmospheric Environment*, Vol. 40, pp. 1104-1116.
- Chan T.L., Ning Z., Wang J.S., Cheung C.S., Leung C.W., Hung W.T., 2007. Gaseous and particle emission factors from the selected on-road petrol/gasoline, diesel and liquefied petroleum gas vehicles. *Energy Fuels*, Vol. 21, pp. 2710-2718.

- Chan T.L., Luo D.D., Cheung C.S., Chan C.K., 2008a. Large eddy simulation of flow structures and pollutant dispersion in the near-wake region of the studied ground vehicle for different driving conditions. *Atmospheric Environment*, Vol. 42, pp. 5317-5339.
- Chan T.L., Gosse K., Zhou Y., Lee S.C., Wang X.W., Huang, J.F., 2008b. Effect of rear slant angle on flow structures and pollutant dispersion in the wake of the studied model vehicle. *International Journal of Heat and Mass Transfer*, Vol. 51, pp. 6180-6193.
- Chan T.L., Liu Y.H., Chan C.K., 2010a. Direct quadrature method of moments for exhaust particle formation and evolution in the wake of the studied ground vehicle. *Journal of Aerosol Science*, Vol. 41, pp. 553-568.
- Chan T.L., Zhou K., Lin J.Z., Liu C.H., 2010b. Vehicular exhaust gas-to-nanoparticle conversion and concentration distribution in the vehicle wake region. *International Journal of Nonlinear Sciences and Numerical Simulation*, Vol. 11, pp. 581-593.
- Chang V.W.C., Hildemann L.M., Chang C.H., 2009a. Wind tunnel measurements of the dilution of tailpipe emissions downstream of a car, a light-duty truck, and a heavy-duty truck tractor head. *Journal of the Air & Waste Management Association*, Vol. 59, pp. 704-714.
- Chang V.W.C., Hildemann L.M., Chang C.H., 2009b. Dilution rates for tailpipe emissions: Effects of vehicle shape, tailpipe position, and exhaust velocity. *Journal of the Air & Waste Management Association*, Vol. 59, pp. 715-724.
- Charron A., Harrison R.M., 2003. Primary particle formation from vehicle emissions during exhaust dilution in the road side atmosphere. *Atmospheric Environment*, Vol. 37, pp. 4109-4119.
- Chock D.P., Cadle S.H., Monson P.R., Heuss J.M., 1977. General motors sulfate dispersion experiment: experimental procedures and results. *Journal of Air Pollution Control Association*, Vol. 27, pp. 33-38.
- Chock D.P., 1977. General motors sulfate dispersion experiment- An overview of the wind, temperature, and concentration fields. *Atmospheric Environment*, Vol. 11, pp. 553-559.
- Chock D.P., 1978. A Simple Line source model for dispersion near roadways. *Atmospheric Environment*, Vol. 12, pp. 823-829.
- Chok C., Parameswaran S., Sun R., Gleason M., 1994. Numerical investigation of the effects of base slant on the wake pattern and drag of three-dimensional bluff bodies with a rear blunt end. *Journal of Wind Engineering and Industrial Aerodynamics*, Vol. 51, pp. 269-285.
- Choy Y.S., Huang J.F., Huang L.X., Zhou Y., 2007. An experimental study of flow induced vibration on a tensioned membrane, *Journal of Mechanical Science and Technology*, Vol. 21, pp. 1359-1366.

References

Claudia S.H., Mattias H., Evert L., Maria S., Jan B.C.P., 2009. A new approach to in-situ determination of roadside particle emission factors of individual vehicles under conventional driving conditions. *Atmospheric Environment*, Vol. 43, pp. 2481-2488.

Clifford M.J., Clarke R., Riffat S.B., 1997. Local aspects of vehicular pollution. *Atmospheric Environment*, Vol. 31, pp. 271-276.

Colls J.J. and Micallef A., 1999. Measured and modeled concentrations and vertical profiles of airborne particulate matter within the boundary layer of a street canyon. *The Science of Total Environment*, Vol.235, pp. 221-233.

Corsmeier U., Imhof D., Kohler M., Kühlwein J., Kurtenbach R., Petrea M., Rosenbohm E., Vogel B., Vogt U., 2005. Comparison of measured and model-calculated real-world traffic emissions. *Atmospheric Environment*, Vol. 39, pp. 5760-5775.

Depardon S., Lasserre J.J., Brizzi L.E., Boree J., 2006. 1/4 scale vehicle wake pattern analysis using near-wall PIV. *Society of Automotive Engineers (SAE) Technical Paper 2006-01-1027*.

Dong G. and Chan T.L., 2006. Large eddy simulation of flow structures and pollutant dispersion in the near-wake region of a light-duty diesel vehicle. *Atmospheric Environment*, Vol. 40, pp. 1104-1116.

Ehrhard J., Khatib I.A., Winkler C., Kunz R., Moussiopoulos N., Ernst G., 2000. The microscale model mimo: development and assessment. *Journal of Wind Engineering and Industrial Aerodynamics*, Vol. 85, pp. 163-176.

Eichhorn J., 1995. Validation of a microscale pollution dispersal model. *Proceeding of 21st International Meeting on Air Pollution Modeling and its Application*, Baltimore, USA.

Esber L.A., El-Fadel M., Nuwayhid I., Saliba N., 2007. The effect of different ventilation modes on in-vehicle carbon monoxide exposure. *Atmospheric Environment*, Vol. 41, pp. 3644-3657.

Eskridge R.E. and Hunt J.C.R., 1979a. Highway modeling part 1: Prediction of velocity and turbulence fields in the wake of vehicles. *Journal of Applied Meteorology*, Vol. 18, pp. 387-400.

Eskridge R.E., Binkowski F.S., Hunt J.C.R., Clark T.L., Demerjian K.L., 1979b. Highway modeling part 2: Advection and diffusion of SF6 tracer gas. *Journal of Applied Meteorology*, Vol. 18, pp. 401-412.

Eskridge R.E. and Thompson R.S., 1982. Experimental and theoretical study of the wake of a block-shaped vehicle in a shear-free boundary flow. *Atmospheric Environment - Part A General Topics* Vol. 16, pp. 2821-2836.

References

- Farell C., Guven O., Carrasquel S., Patel V.C., 1977. Effect of wind tunnel walls on the flow past circular cylinders and cooling tower models. *Journal of Fluids Engineering*, Vol. 99, pp. 470-479.
- Feng L.H., Wang J.J., Pan C., 2010. Effect of novel synthetic jet on wake vortex shedding modes of a circular cylinder. *Journal of Fluids and Structures*, Vol. 26, pp. 900-917.
- Ganapathisubramani B., Longmire E.K., Marusic I., 2006. Experimental investigation of vortex properties in a turbulent boundary layer. *Physics of Fluids*, Vol. 18, 055105.
- Geers L.F.G., Tummers M.J., Hanjalic K., 2005. Particle imaging velocimetry-based identification of coherent structures in normally impinging multiple jets. *Physics of Fluids*, Vol. 17, Article No. 055105.
- Gidhagen L., Johansson C., Strom J., Kristensson A., Swietlicki E., Pirjola L., Harkonen J., Valkonen E., Kukkonen J., Rantakrans E., Jalkanen L., Lahtinen K., 1995. An operational dispersion model for predicting pollution from a road. *International Journal of Environment and Pollution*, Vol.5, pp. 602-610.
- Gifford F.A., 1968. "An outline of theories of diffusion in lower layers of the atmosphere," *Meteorology and Atomic Energy*, U.S Atomic Energy Commission, Oak Ridge, Tenn., USA.
- Gillieron P., Leroy A., Aubrun S., Audier P., 2010. Influence of the slant angle of 3D bluff bodies on longitudinal vortex formation. *Journal of Fluids Engineering*, Vol. 132, AN 051104: pp. 1-9.
- Gillies J.A., Etyemezian V., Kuhns H., Nikolic D., Gillette D.A., 2005. Effect of vehicle characteristics on unpaved road dust emissions. *Atmospheric Environment*, Vol. 39, pp. 3241–2347.
- Gong R., Waring P., 1996. Investigation of emission behavior in an urban driving cycle with a remote sensing system. *The Second Conference on Urban Transport and Environment*, ed. by Sucharov L.J. et al., pp. 199-208.
- Gosman A.D., 1999. Developments in CFD for industrial and environmental applications in wind engineering. *Journal of Wind Engineering and Industrial Aerodynamics*, Vol. 81, pp. 21-39.
- Gosse K., Paranthoen P., Patte-Rouland B., Gonzalez, M., 2006a. Dispersion in the near wake of idealized car model. *International Journal of Heat and Mass Transfer*, Vol. 49, pp. 1747-1752.
- Gosse K., Patte R.B., Gonzalez M., Paranthoen P., 2006b. Scalar dispersion in the near wake of a simplified model car. *Experiments in Fluids*, Vol. 40, pp. 135-140.
- Gosse K., Gonzalez M., Paranthoen P., 2011. Mixing in the three-dimensional wake of an experimental modelled vehicle. *Environmental Fluid Mechanics*, Vol. 11, pp. 573-589.

References

- Gryning S.E., Holtslag A.A.M., Irwing J.S., Sievertsen B., 1987. Applied dispersion modelling based on meteorological scaling parameters. *Atmospheric Environment*, Vol. 21, pp. 79-89.
- Guenther P.L., Stedman D.H., Bishop G.A., Stuart P.B., James H.B., Richard W.Q., 1994. A HC detector for the remote sensing for vehicle exhaust emissions. *Review of Scientific Instruments*, Vol. 66, pp. 3024-3029.
- Guilmineau E., 2008. Computational study of flow around a simplified car body. *Journal of Wind Engineering and Industrial Aerodynamics*, Vol. 96, pp. 1207-1217.
- Hackett J.E., Williams J.E., Baker J.B., Wallis S.B., 1987. On the influence of ground movement and wheel rotation in the test on modern car shapes. *Society of Automotive Engineers (SAE) Technical Paper 870245*.
- Hall J.W., Ziada S., Weaver D.S., 2003. Vortex-shedding from single and tandem cylinders in the presence of applied sound. *Journal of Fluids and Structures*, Vol. 18, pp. 741-758.
- Hall R.C., 2001. Modelling of dense gas dispersion in tunnels, prepared by Atkins W.C. consultants limited for the Health and Safety Executive, Contract Research Report, 359/2001.
- Hallmark S.L., Guensler R., Fomunung I., 2003. Characterizing on-road variables that affect passenger vehicle model operation. *Transportation Research Part D*, Vol. 7, pp. 81-98.
- Hansen J.Q, Winther M, Sorenson S.C. 1995. The influence of driving patterns on petrol passenger car emissions. *The Science of Total Environment*, Vol. 169, pp. 129-139.
- Hansson H.C., 2003. Model simulation of ultra-fine particles inside a road tunnel. *Atmospheric Environment*, Vol.37, pp. 2023-2036.
- Harkonen J., Valkonen E., Kukkonen J., Rantakrans E., Jalkanen L., Lahtinen K., 1995. An operational dispersion model for predicting pollution from a road. *International Journal of Environmental Pollution*, Vol. 5, pp. 602–610.
- Harrison R.M., Jones M., Collins G., 1999. Measurements of the physical properties of particles in the urban atmosphere. *Atmospheric Environment*, Vol. 33, pp. 309-321.
- Harrison R.M., Jones A.M., Barrowcliffe R., 2004. Field study of the influence of meteorological factors and traffic volumes upon suspended particle mass at urban roadside sites of differing geometries. *Atmospheric Environment*, Vol. 38, pp. 6361-6369.
- Hawley J.G., Brace C.J., Cox A., Ketcher D., Stark R., 2003. Influence of time-alignment on the calculation of mass emissions on a chassis rolls dynamometer. *Society of Automotive Engineers (SAE) Technical Paper 2003-01-0395*.

References

- Hider Z.E., Hibberd S., Baker C.J., 1997. Modelling particulate dispersion in the wake of a vehicle. *Journal of Wind Engineering and Industrial Aerodynamics*, Vol. 67, pp. 733-744.
- Hitchins J., Morawska L., Wolff R., Gilbert D., 1999. Concentrations of sub-micrometer particles from vehicle emissions near a major road. *Atmospheric Environment*, Vol. 34, pp. 51-59.
- Hong Kong Census and Statistics Department, 2011. The Government of the Hong Kong Special Administrative Region.
- Hong Kong Transport Department, 2011. The Government of the Hong Kong Special Administrative Region.
- Huang J.F., Zhou Y., Zhou T., 2006. Three-dimensional wake structure measurement using a modified PIV technique, *Experiments in Fluids*, Vol. 40, pp. 884-896.
- Huang J.F., Chan T.L., Zhou Y., 2009a. Three-dimensional flow structure measurements behind a queue of studied model vehicles. *International Journal of Heat and Fluid Flow*, Vol. 30, pp. 647-657.
- Huang J.F., Chan T.L., Zhou Y., 2009b. Flow structures and pollutant dispersion and concentration fields from a queue of studied model vehicles. Environment and Transport-Transport and Air Pollution 2009 (ETTAP 2009), Paper No.: 063. *Proceedings of the 17th Transport and Air Pollution Symposium and 3rd Environment and Transport Symposium*, June 2-4, 2009, Toulouse, France.
- Huang J.F. and Chan T.L., 2012. Vehicle queue effect on the characteristics of air flow, and exhaust scalar dispersion. *International Journal of Heat and Mass Transfer*, Vol. 55, 7981-7990.
- Ingalls M.N., Garbe R.J., 1982. Ambient pollutant concentration from mobile sources in microscale situations. *Society of Automotive Engineers (SAE) Technical Paper 820787*.
- Iungo G.V. and Buresti G., 2009. Experimental investigation on the aerodynamic loads and wake flow features of low aspect-ratio triangular prisms at different wind directions. *Journal of Fluids and Structures*, Vol. 25, pp. 1119-1135.
- Jamriska M. and Morawska L., 2001. A Model for Determination of Motor Vehicle Emission Factors from On-Road Measurements with a Focus On Sub-Micrometer Particles. *The Science of Total Environment*, Vol. 264, pp. 241-255.
- Jones J.W., Ripberger C.T., Vescio N., 2001. An investigation of remote sensing devices for chemical characterization of motor vehicle exhaust. Office of Research and Development, EPA, U.S.

References

- Jung Y.W., Park S.O., 2005. Vortex-shedding characteristics in the wake of an oscillating airfoil at low Reynolds number. *Journal of Fluids and Structures*, Vol. 20, pp. 451–464.
- Kanda I., Uehara K., Yamao Y., Yoshikakwa Y., Morikawa T., 2006a. A wind tunnel study on exhaust gas dispersion from road vehicles- Part I: Velocity and concentration fields behind single vehicles. *Journal of Wind Engineering and Industrial Aerodynamics*, Vol. 94, pp. 639-658.
- Kanda I., Uehara K., Yamao Y., Yoshikakwa Y., Morikawa T., 2006b. A wind tunnel study on exhaust gas dispersion from road vehicles- Part II: Effect of vehicle queues. *Journal of Wind Engineering and Industrial Aerodynamics*, Vol. 94, pp. 659-673.
- Karim M.M., 1999. Traffic pollution inventories and modeling in metropolitan Dhaka, Bangladesh. *Transportation Research Part D.*, Vol. 4, pp. 291-312.
- Karppinen A., 2001. Meteorological pre-processing and atmospheric dispersion modelling of urban air quality and applications in the Helsinki metropolitan area. Department of Engineering Physics and Mathematics, Helsinki University of Technology, Finland.
- Katz J., 1995. Race-Car Aerodynamics. Robert Bentley Inc., Cambridge, MA. ISBN 0837601428.
- Kennedy I.M., Moody M.H., 1998. Particle dispersion in a turbulent round jet. *Experimental Thermal and Fluid Science*, Vol. 18, pp. 11-26.
- Ketzel M., Wahlin P., Berkowicz R., Palmgren F., 2003. Particle and trace gas emission factors under urban driving conditions in Copenhagen based on street and roof-level observations. *Atmospheric Environment*, Vol. 37, pp. 2735-2749.
- Khalighi B., Zhang S., Koromilas C., Balkanyi S.R., Bernal L.P., Iaccarino G., Moin P., 2001. Experimental and computational study of unsteady wake flow behind a bluff body with a drag reduction device. *Society of Automotive Engineers (SAE) Technical Paper 2001-01-1042*.
- Khare M., Sharma P., 1999. Performance evaluation of general finite line source model for Delhi traffic conditions. *Transportation Research Part D.*, Vol. 4, pp. 65-70.
- Kim D.H., Gautam M., Gera D., 2001. On the prediction of concentration variations in a dispersing heavy-duty truck exhaust plume using k-epsilon turbulent closure. *Atmospheric Environment*, Vol. 35, pp. 5267-5275.
- Kozaka E.O., Ozkan G., Ozdemir I.B., 2004. Turbulent structure of three-dimensional flow behind a model car: 1. Exposed to uniform approach flow. *Journal of Turbulence*, Vol. 5, pp. 1-22.

References

- Krajnovic S., Davidson L., 2004. Large eddy simulation of the flow around simplified car model. *Society of Automotive Engineers (SAE) Technical Paper* 2004-01-0227.
- Krajnovic S., Davidson L., 2005a. Flow around a simplified car, Part 1: Large eddy simulation. *Journal of Fluids Engineering*, Vol. 127, pp. 901-918.
- Krajnovic S., Davidson L., 2005b. Flow around a simplified car, Part 2: Understanding the flow. *Journal of Fluids Engineering*, Vol. 127, pp. 919-928.
- Krajnovic S., Davidson L., 2005c. Influence of floor motion in wind tunnels on the aerodynamics of road vehicles. *Journal of Wind Engineering and Industrial Aerodynamics*, Vol. 93, pp. 677-696.
- Kruger M., Luders H., Luers B., Kaufmann R., Koch W., 1997. Influence of exhaust gas aftertreatment on particulate characteristics of vehicle diesel engine. *Motortechnische Zeitschrift*, Vol. 59, pp. 442-447.
- Kudo S., Sekiguchi K., Kim K.H., Sakamoto K., 2011. Spatial distributions of ultrafine particles and their behavior and chemical composition in relation to roadside sources. *Atmospheric Environment*, Vol. 45, pp. 6403-6413.
- Kukkonen J., Härkönen J., Karppinen A., Pohjola M., Pietarila H., Koskentalo T., 2001. A semi-empirical model for urban PM10 concentrations, and its evaluation against data from an urban measurement network. *Atmospheric Environment*, Vol. 35, pp. 4433-4442.
- Kukkonena J., Partanen L., Karppinen A., Walden J., Kartastenpää R., Aarnio P., Koskentalo T., Berkowicz R., 2003. Evaluation of the OSPM model combined with an urban background model against the data measured in 1997 in Runeberg Street, Helsinki. *Atmospheric Environment*, Vol. 37, pp. 1101-1112.
- Kumar P., Alan R., Rex B., 2009. Fast response measurements of the dispersion of nanoparticles in a vehicle wake and a street canyon. *Atmospheric Environment* 43, pp. 6110–6118.
- Lai C.H., Chang C.C., Wang C.H., Shao M., Zhang Y.H., Wang J.L., 2009. Emissions of liquefied petroleum gas (LPG) from motor vehicles. *Atmospheric Environment*, Vol. 43, pp. 1456-1463.
- Lajos T., Preszler L., Finta L., 1986. Effect of moving ground simulation on the flow past bus models. *Journal of Wind Engineering and Industrial Aerodynamics*, Vol. 22, pp. 271-277.
- Levi A., Sini J.F., 1992. Simulation of diffusion within an urban street canyon. *Journal of Wind Engineering*, Vol. 52, pp. 114-119.
- Li X.X., Liu C.H., Leung Y.C., Lam K.M., 2006. Recent progress in CFD modelling of wind field and pollutant transport in street canyons. *Atmospheric Environment*, Vol. 40, pp. 5640-5658.

References

- Lienhart H., Becker S., 2003. Flow and turbulent structure in the wake of a simplified car model. *Society of Automotive Engineers (SAE) Technical Paper* 2003-01-0656.
- Liu C.H., Cheng W.C., Leung T.C.Y., Leung D.Y.C., 2011a. On the mechanism of air pollutant re-entrainment in two-dimensional idealized street canyon streets. *Atmospheric Environment*, Vol. 45, pp. 4763-4769.
- Liu Y.H., He Z., Chan T.L., 2011b. Three-dimensional simulation of exhaust particle dispersion and concentration fields in the near-wake region of the studied ground vehicle. *Aerosol Science and Technology*, 45, pp. 1019-1030.
- Longley I.D., Gallagher M.W., Dorsey J.R., Flynn M., Allan J.D., Alfarra M.R., Inglis D., 2003. A case study of aerosol ($4.6 \text{ nm} < D_p < 10 \text{ nm}$) number and mass size distribution measurements in a busy street canyon in Manchester, UK. *Atmospheric Environment*, Vol. 37, pp. 1563-1571.
- Luo Z.W., Li Y.G., William W.N., 2010. Intake fraction of nonreactive motor vehicle exhaust in Hong Kong. *Atmospheric Environment*, Vol. 44, pp. 1913-1918.
- Marcelo C., Marcelo G., Miguel S., 2003. Intercomparison of atmospheric dispersion models. *Atmospheric Environment*, Vol. 37, pp. 2435-2449.
- Mathissen M., Scheer V., Kirchner U., Vogt R., Benter T. 2012. Non-exhaust PM emission measurements of a light duty vehicle with a mobile trailer. *Atmospheric Environment*, Vol. 59, pp. 232-242.
- Matsuda T., Sakakibara J., 2005. On the vortical structure in a round jet. *Physics of Fluids*, Vol. 17, Article No. 025106.
- Matsui H., Karim M.M., 1998a. A mathematical model of wind flow, vehicle wake, and pollutant concentration in urban road microenvironments. Part I: Model description. *Transportation Research Part D*, Vol. 3, pp. 81-92.
- Matsui H., Karim M.M., 1998b. A mathematical model of wind flow, vehicle wake, and pollutant concentration in urban road microenvironments. Part II: Model results. *Transportation Research Part D*, Vol. 3, pp. 171-191.
- Mayer H. 1999. Air pollution in cities. *Atmospheric Environment*, Vol. 33, pp. 4029-4037.
- McKain D.L., Nigel N.C., McDaniel T.I., Hoppie J.A., 1998. Chassis test cycle development for heavy-duty engine emissions test compliance, *Society of Automotive Engineers (SAE) Technical Paper* 980407.
- McKain D.L., Clark N.N., 1999. Speed and power regressions for quality control of heavy duty vehicle chassis dynamometer research, *Society of Automotive Engineers (SAE) Technical Paper* 1999-01-0614.

References

- Mi J., Nathan G. J., 2005. Statistical analysis of the velocity field in a mechanical precessing jet flow. *Physics of Fluids*, Vol. 17, Article No. 015102.
- Micallef A., Deuchar C.N., Colls J.J., 1998. Indoor and outdoor measurements of vertical concentration profiles of airborne particulate matter. *The Science of Total Environment*, Vol. 215, pp. 209-216.
- Mohamed F.Y., 2013. A wind tunnel study on the effect of thermal stability on flow and dispersion of rooftop stack emissions in the near wake of a building. *Atmospheric Environment*, Vol. 65, pp. 89-100.
- Molnar P., Janhall S., Hallquist M., 2002. Roadside measurements of fine and ultrafine particles at a major road north of Gothenburg. *Atmospheric Environment*, Vol. 36, pp. 4115-4123.
- Morris J.A., Bishop G.A., Stedman D.H., 1999. Remote sensing and comparison of emissions from heavy-duty diesel trucks. *Proceedings for the 9th CRC on-road vehicle emission workshop*, SD, California, April 19-21, pp. 4-29-4-39.
- Mouhammad E.H., Amina M., Kamel A.M., 2011. Experimental investigation of the flow in the near-field of a cross-shaped orifice jet. *Physics of Fluids*, Vol. 23, Article No. 045101.
- Nagata K., Yasuhiko S., Satoru K., 2011. Effects of small-scale freestream turbulence on turbulent boundary layers with and without thermal convection. *Physics of Fluids*, Vol. 23, Article No. 065111.
- Nagendra S.M.S., Mukesh K., 2002. Line source emission modeling. *Atmospheric Environment*, Vol. 36, pp. 2083-2098.
- Namdeo A.K., Colls J.J., Baker C.J., 1999. Dispersion and re-suspension of fine and coarse particulates in an urban street canyon. *The Science of Total Environment*, Vol. 235, pp. 3-13.
- Narasimha R., Prasad S.N., 1994. Leading edge shape for flat plate boundary layer studies. *Experiments in Fluids*, Vol. 17, pp. 358-360.
- Nelson Peter F., Anne R. Tibbett, Stuart J. Day, 2008. Effects of vehicle type and fuel quality on real world toxic emissions from diesel vehicles. *Atmospheric Environment*, Vol. 42, pp. 5291-5303.
- Noger C., 2005. Investigation of the transient aerodynamic phenomena associated with passing maneuvers. *Journal of Fluids and Structures*, Vol. 21, pp. 231-241.
- Noll K.E., Miller T.L., Claggett M., 1977. A comparison of three line source dispersion models. *Atmospheric Environment*, Vol. 12, pp. 1323-1329.
- Onorato M., Costelli A.F., Garrone A., Viassone L., 1986. Experimental analysis of vehicle wakes. *Journal of Wind Engineering and Industrial Aerodynamics*, Vol. 22, pp. 317-330.

- Pacione M., 2003. Urban environmental quality and human wellbeing- a social geographical perspective. *Landscape and Urban Planning*, Vol. 65, pp. 19-30.
- Paranthoen P., Gilles G., Franck W., Michel G., 2004. Counter gradient diffusion vs “counter diffusion” temperature profile? *International Journal of Heat and Mass Transfer*, Vol. 47, pp. 819–825.
- Park C.W., Lee S.J., 2003. Flow structure around two finite circular cylinders located in an atmospheric boundary layer: side-by-side arrangement. *Journal of Fluids and Structures*, Vol. 17, pp. 1043-1058.
- Parka C.W., Lee S.J., 2004. Effects of free-end corner shape on flow structure around a finite cylinder. *Journal of Fluids and Structures*, Vol. 19, pp. 141-158.
- Pearce W., Baker C.J., 1997. Wind-tunnel investigation of the effect of vehicle motion on dispersion in urban canyons. *Journal of Wind Engineering and Industrial Aerodynamics*, Vol. 69-71, pp. 915-926.
- Petersen W.B., 1980. User's guide for HIWAY-2, highway air pollution model, 3–17, EPA-600/8-80-018. Environmental Science Research Laboratory, Office of Research and Development US Environmental Protection Agency, Research Triangle Park, NC, 27711.
- Petit C., Jerphanion D., Brou M., 2000. Analyse de sensibilité d'un logiciel d'évaluation des immissions liées au trafic automobile, au niveau de aa rue. le cas de STREET 3.1. *Ninth International Symposium "Transport and Air Pollution"*, Avignon, France, June 2000.
- Petri T., Taisto R., Jarkko T., Tarja Y.T., Ari L., Jaakko K., Jari H., Ari K., 2002. Measurements and modelling of PM_{2.5} concentrations near a major road in Kuopio, Finland, *Atmospheric Environment*, Vol. 36, pp. 4057-4068.
- Pino C.D., Parras L., Felli M., Fernandez F.R., 2011. Structure of trailing vortices: Comparison between particle image velocimetry measurements and theoretical models. *Physics of Fluids*, Vol. 23, Article No. 013602.
- Pokharel S.S., Bishop G.A., Stedman D.H., 2002. An on-road motor vehicle emissions in inventory for Denver: An efficient alternative to modeling. *Atmospheric Environment*, Vol. 36, pp. 5177-5184.
- Rafia A., Hassan M.N., Ibrahim N.A., 2003. Review of air pollution and health impacts in Malaysia, *Environmental Research*, Vol. 92, pp. 71-77.
- Rahai H. R. and LaRue J. C., 1992. Decay of temperature variance in the presence of nonhomogeneous strain. *Journal of Fluids Engineering*, Vol. 114, pp. 155-160.
- Rajagopalan A.G., Tong C.N., 2003. Experimental study of the blowing impact on a hot turbulent boundary layer. *Physics of Fluids*, Vol. 15, pp. 227-244.
- Rao S.T., Keenan M.T., 1980. Suggestions for improvement of the EPA-HIWAY model. *Air Pollution Control Association*, Vol. 30, pp. 247-256.

References

- Recktenwald Weller T., Schroder W., Oberlack M., 2007. Comparison of direct numerical simulations and particle-image velocimetry data of turbulent channel flow rotating about the streamwise axis. *Physics of Fluids*, Vol. 19, Article No. 085114.
- Rhys-Tyler G.A., Legassick W., Bell M.C., 2011. The significance of vehicle emissions standards for levels of exhaust pollution from light vehicles in an urban area. *Atmospheric Environment*, Vol. 45, pp. 3286-3293.
- Richards K.A., Wright N.G., Baker C.J., Baxendale A.J., 2000. Computational modelling of pollution dispersion in the near wake of a vehicle. *Proceedings of the MIRA International Conference on Vehicle Aerodynamics*, Ruby, UK.
- Richards K.A., 2002. Computational modelling of pollution dispersion in the near wake of a vehicle. University of Nottingham, PhD thesis.
- Ryan A., 2000. Wake surveys behind a passenger car subjected to a transient cross-wind gust. *Society of Automotive Engineers (SAE) Technical Paper* 2000-01-0874.
- Sahlodin A.M., Sotudeh G.R., Zhu Y.F., 2007. Modeling of dispersion near roadways based on the vehicle-induced turbulence concept. *Atmospheric Environment*, Vol. 41, pp. 92-102.
- Scanlon T.J., 1997. A numerical analysis of flow and dispersion around a cube, *Proceedings of IBPSA conference*, Prague, September 1997.
- Schacher G.E. and Fairall C.W., 1979. Frequency response of cold wires used for atmospheric turbulence measurements in the marine environment. *Review of Scientific Instruments*, Vol. 50, pp. 1463-1466.
- Seaton A., MacNee W., Donaldson, K., Godden, D., 1985. Particulate air Pollution and acute health effects. *The Lancet*, Vol. 345, pp. 176-178.
- Sharma P., Khare M., 2001. Modeling of vehicle exhausts - A review. *Transportation Research Part D.*, Vol. 6, pp. 179-198.
- Sharma N., Chaudhry K.K., Chalapati R., 2004. Vehicular pollution prediction modeling: A review of highway dispersion models. *Transport Reviews*, Vol. 24, pp. 409-435.
- Shen S., Jaques P.A., Zhu Y.F., Geller M.D., Sioutas C., 2002. Evaluation of the SMPS-APS system as a continuous monitor for measuring PM_{2.5}, PM₁₀ and coarse (PM_{2.5-10}) Concentrations. *Atmospheric Environment*, Vol. 36, pp. 3939-3950.
- Shozo I., Hitoshi K., 1990. A micro-scale dispersion model for motor vehicle exhaust gas in urban areas- OMG volume- source model. *Atmospheric Environment*, Vol. 24, pp. 243-251.
- Shridhar G., Bruce M.A., Joseph K., 2004. The structure of a jet in cross flow at low velocity ratios. *Physics of Fluids*, Vol. 16, Article No. 2067.

References

- Silva C.M., Costa M., Farias T.L., Santos H., 2006. Evaluation of SI engine exhaust gas emissions upstream and downstream of the catalytic converter, *Energy Conversion and Management*, Vol. 47, pp. 2811-2828.
- Sideridis G.A., Kastrinakis E.G., Nychas S.G., Rapsomanikis S., 2011. Scalar transport from a planar source in a turbulent boundary layer. *International Journal of Heat and Mass Transfer*, Vol. 54, pp. 5337-5347.
- Sigmund Cohn, 2011. <http://www.sigmundcohn.com/pdf/EN/precious%20metal%20wire.pdf>
- Sims-Williams D.B., 2001. An investigation into large scale unsteady structures in the wake of real and idealized hatchback car models. *Society of Automotive Engineers (SAE) Technical Paper 2001-01-1041*.
- Singha A., Balachandar R., 2011. Structure of wake of a sharp-edged bluff body in a shallow channel flow. *Journal of Fluids and Structures*, Vol. 27, pp. 233-249.
- Sivacoumar R. and Thanasekaran K., 1999. Line source model for vehicular pollution prediction near roadways and model evaluation through statistical analysis. *Environmental Pollution*, Vol. 104, pp. 389-395.
- Sivacoumar R. and Thanasekaran, K., 2002. Comparison and performance evaluation of models used for vehicular pollution prediction. *Journal of Environment Engineering*, Vol. 127, pp. 524-530.
- Sjodin A., Andreasson K., 2000. Multi-year remote-sensing measurements of gasoline light-duty vehicle emissions on a freeway ramp. *Atmospheric Environment*, Vol. 34, pp. 4657-4665.
- Song J., Shuya Y., Takuma K. and Yasuaki K., 2006. Characteristics of flow behind passenger vehicle. *Society of Automotive Engineers (SAE) Technical Paper 2006-01-1030*.
- Sotiris V., Bernard E.A.F., Norbet G.F., Koulis P., 2002. Model sensitivity and uncertainty analysis using roadside air quality measurements. *Atmospheric Environment*, Vol. 36, pp. 2121-2134.
- Stone V. and Donladson K., 1998. Small particles- big problems. *The Aerosol Society Newsletter* No. 33, Sept. 1998.
- Uhrner U., Lowis S. von, Vehkamaki H., Wehner B., Brasel S., Hermann M., Stratmann F., Kulmala M., Wiedensohler A., 2007. Dilution and aerosol dynamics within a diesel car exhaust plume- CFD simulations of on-road measurement conditions. *Atmospheric Environment*, Vol. 41, pp. 7440-7461.
- Valerio F., Stella A., Pala M., Balducci D., Piccardo M.T., Cipolla M., 2009. The effect of EURO-0 vehicle substitution on polycyclic aromatic hydrocarbon and carbon monoxide concentrations in an urban area. *Atmospheric Environment*, Vol. 43, pp. 1520-1526.

References

- Vardoulakis S., Bernard E.A., Fisher, Koulis P., Norbert G. F., 2003. Modelling air quality in street canyons: A review. *Atmospheric Environment*, Vol. 37, pp. 155-182.
- Venkatram A., Fitz D., Bumiller K., Du S.M., Boeck., Ganguly C., 1999. Using a dispersion model to estimate emission rates of particulate matter from paved roads. *Atmospheric Environment*, Vol. 33, pp. 1093-1102.
- Verbeek R.P., Baarbe H.L., Gombel P.V., Sloten P.V., 1993. Chassis dynamometer in-use compliance method for European 13-mode test. *Society of Automotive Engineers* (SAE) Technical Paper 937158.
- Vignati E., Berkowicz R., Palmgren F., Lyck E., Hummelshoj P., 1999. Transformation of size distributions of emitted particles in streets. *The Science of the Total Environment*, Vol. 235, pp. 37-49.
- Vino G., Watkins S., Mousley P., 2003. The passenger vehicle wake under the influence of upstream turbulence. *Society of Automotive Engineers* (SAE) Technical Paper 2003-01-0650.
- Wang D.H. and Tong C.N., 2002. Conditionally filtered scalar dissipation, scalar diffusion, and velocity in a turbulent jet. *Physics of Fluids*, Vol. 14, pp. 2170-2185.
- Wang Z.J., Zhou Y., Xu Y.L., Huang J.F., 2004. Water rivulet effects on the near wake of an inclined cylinder. *Proceeding of International Conference on Flow-induced Vibration*, Paris France, July 2004. Vol. 2, pp. 449-454.
- Wang Z.J., Zhou Y., Huang J.F., Xu Y.L., 2005. Fluid dynamics around an inclined cylinder with running water rivulets, *Journal of Fluids and Structures*, Vol. 21, pp. 49-64.
- Wang J.S., Chan T.L., Cheung C.S., Leung C.W., Hung W.T., 2006a. Three-dimensional pollutant concentration dispersion of a vehicular exhaust plume in the real atmosphere. *Atmospheric Environment*, Vol. 40, pp. 484-497.
- Wang J.S., Chan T.L., Ning, Z., Leung C.W., Cheung C.S., Hung W.T., 2006b. Roadside measurement and prediction of CO and PM_{2.5} dispersion from on-road vehicles in Hong Kong. *Transportation Research Part D- Transport and Environment*, Vol. 11, pp. 242-249.
- Ward C.E., Ranzieri A.J., Earl C.S., 1977. CALINE 2- an improved micro-scale model for the dispersion of air pollutants from a line source. *Federal Highway Administration Report*, FHWA-RD-77-74, Washington, DC.
- Watkins S., Vino G., 2008. The effect of vehicle spacing on the aerodynamics of a representative car shape. *Journal of Wind Engineering and Industrial Aerodynamics*, Vol. 96, pp. 1232-1239.

- Wehner B., Birmili W., Gnauk T., Wiedensohler A., 2002. Particle number size distributions in a Street canyon and their transformation into the urban-air background: measurements and a Simple model study. *Atmospheric Environment*, Vol. 36, pp. 2215-2223.
- Wong C.P., Chan T.L., Leung C.W., 2003. Characterisation of diesel exhaust particle number and size distributions using mini-dilution tunnel and ejector-diluter measurement techniques. *Atmospheric Environment*, Vol. 37, pp. 4435-4446.
- Wu C.F., Yost M.G., Hashmonay R.A., Tsai M.Y., 2003. Path concentration profile reconstruction of optical remote sensing measurements using polynomial curve fitting procedures. *Atmospheric Environment*, Vol. 37, pp. 1879-1888.
- Xia J.Y. and Leung D.Y.C., 2001. Pollutant dispersion in urban street canopies. *Atmospheric Environment*, Vol. 35, pp. 2033-2043.
- Yu L., 1998. Remote vehicle exhaust emission sensing for the traffic simulation and optimization models. *Transportation Research Part D*, Vol.3, pp. 337-347.
- Zhang K.M., Wexler A.S., 2004a. Evolution of particle number distribution near roadways- Part I: analysis of aerosol dynamics and its implications for engine emission measurement. *Atmospheric Environment*, Vol. 38, pp. 6643-6653
- Zhang K.M., Wexler A.S., Zhu Y.F., Hinds W.C., Sioutas C., 2004b. Evolution of particle number distribution near roadways- Part II: the 'Road-to-Ambient' process. *Atmospheric Environment*, Vol. 38, pp. 6655-6665.
- Zhang Y., Donald H.S., Bishop G.B., Guenther P.L., Beaton S.P., Peterson J.E., 1993. On-road hydrocarbon remote sensing in the Denver area. *Environmental Science & Technology*, Vol. 27, pp. 1885-1891.
- Zhang Y., Stedman D.H., Bishop G.A., Beaton S.P., Guenther P.L., 1996. On-road evaluation of inspection/maintenance effectiveness. *Environment Science & Technology*, Vol. 30, pp. 1445-1450.
- Zhang K., Stuart B., Francois D., 2011. Vehicle emissions in congestion: Comparison of work zone, rush hour and free-flow conditions. *Atmospheric Environment*, Vol. 45, pp. 1929-1939.
- Zhou T., Wang H., Razali S.F.M., Zhou Y., Cheng L., 2010. Three-dimensional vorticity measurements in the wake of a yawed circular cylinder. *Physics of Fluids*, Vol. 22, Article No. 015108.
- Zimmerman J.R., Thompson R.S., 1975. User's guide for Highway, a highway air pollution model. EPA-650/4-74-008.